MICROSTRUCTURATION OF NONLINEAR OPTICAL MATERIALS: METHODOLOGIES, CHARACTERIZATION, AND APPLICATIONS

Raj Kumar Golconda

Dipòsit Legal: T. 55-2013

UNIVERSITAT ROVIRA I VIRGILI
MICROSTRUCTURATION OF NONLINEAR OPTICAL MATERIALS:
METHODOLOGIES, CHARACTERIZATION, AND APPLICATIONS
Raj Kumar Golconda
Dipòsit Legal: T. 55-2013

Microstructuration of nonlinear optical materials: methodologies, characterization, and applications

Raj Kumar Golconda

This thesis discusses results based on the fabrication of 1D and 2D microstructures on the surface of the nonlinear optical materials such as $KTiOPO_4$, $RbTiOPO_4$, by ultrafast laser ablation and $LiNbO_3$ by selective chemical etching. The linear and nonlinear diffraction properties as well as the structural modifications of these materials were analyzed in detail. The possible application of these microstructures has been explored for the development of RGBY laser phosphor displays by embedding luminescent nanoparticles into microstructures inscribed on the surface of nonlinear optical materials. In this way, multicolor light emissions can also be controlled spatially at the micro-meter scale.

Raj Kumar Golconda Microstructuration of nonlinear optical materials: methodologies, characterization, and applications

UNIVERSITAT ROVIRA I VIRGILI

Microstructuration of nonlinear optical materials: methodologies, characterization, and applications

Raj Kumar Golconda

Doctoral Thesis

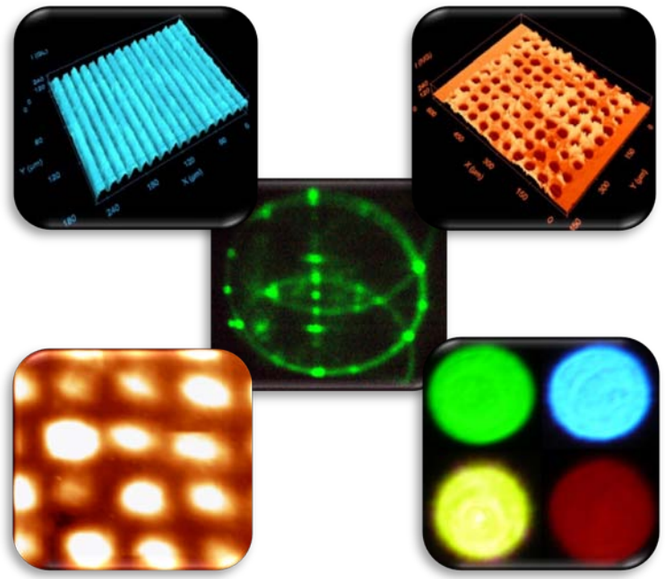

Supervised by:
Dr. Joan Josep Carvajal
Prof. Dr. Magdalena Aguiló

Tarragona, 2012

UNIVERSITAT ROVIRA I VIRGILI
MICROSTRUCTURATION OF NONLINEAR OPTICAL MATERIALS:
METHODOLOGIES, CHARACTERIZATION, AND APPLICATIONS
Raj Kumar Golconda
Dipòsit Legal: T. 55-2013

Microstructuration of nonlinear optical materials: methodologies, characterization, and applications

Doctoral Thesis

Submitted by:
Raj Kumar Golconda

Supervised by:
Dr. Joan Josep Carvajal
Prof. Dr. Magdalena Aguiló

Departament de Química Física i Inorgànica
Física i Cristal·lografia de Materials i Nanomaterials
(FiCMA-FiCNA)

Tarragona
2012

UNIVERSITAT ROVIRA I VIRGILI
MICROSTRUCTURATION OF NONLINEAR OPTICAL MATERIALS:
METHODOLOGIES, CHARACTERIZATION, AND APPLICATIONS
Raj Kumar Golconda
Dipòsit Legal: T. 55-2013

Microstructuration of nonlinear optical materials: methodologies, characterization, and applications

Raj Kumar Golconda

Física i Cristal·lografia de Materials i Nanomaterials (FiCMA-FiCNA)
Departament de Química Física i Inorgànica
Universitat Rovira i Virgili
Campus Sescelades
C/Marcel·lí Domingo, s/n
E-43007, Tarragona (Spain)

UNIVERSITAT ROVIRA I VIRGILI
MICROSTRUCTURATION OF NONLINEAR OPTICAL MATERIALS:
METHODOLOGIES, CHARACTERIZATION, AND APPLICATIONS
Raj Kumar Golconda
Dipòsit Legal: T. 55-2013

UNIVERSITAT ROVIRA I VIRGILI
DEPARTAMENT DE QUÍMICA FÍSICA I INORGÀNICA
Campus Sescelades
Marcel·lí Domingo, s/n
43007 Tarragona
Tel. +34 977 55 81 37
Fax +34 977 55 95 63
www.quimica.urv.es

Dr. Joan Josep Carvajal Martí, i Prof. Dr. Magdalena Aguiló Díaz, del Departament de Química Física i Inorgànica de la Universitat Rovira i Virgili,

CERTIFIQUEM:

Que aquest treball titulat "Microstructuration of nonlinear optical materials: methodologies, characterization, and applications", que presenta el Sr. Raj Kumar Golconda per l'obtenció del títol de Doctor, ha estat realitzat sota la nostra direcció al Departament de Química Física i Inorgànica d'aquesta universitat i que acompleix els requeriments per poder optar a Menció Europea.

Tarragona, 24 de juliol de 2012

UNIVERSITAT ROVIRA I VIRGILI
MICROSTRUCTURATION OF NONLINEAR OPTICAL MATERIALS:
METHODOLOGIES, CHARACTERIZATION, AND APPLICATIONS
Raj Kumar Golconda
Dipòsit Legal: T. 55-2013

UNIVERSITAT ROVIRA I VIRGILI
MICROSTRUCTURATION OF NONLINEAR OPTICAL MATERIALS:
METHODOLOGIES, CHARACTERIZATION, AND APPLICATIONS
Raj Kumar Golconda
Dipòsit Legal: T. 55-2013

Abstract

Microstructuration of nonlinear optical materials: methodologies, characterization, and applications

Femtosecond laser pulses have been successfully used for the microstructuring of diverse materials by ultrafast laser ablation. In particular, the fabrication of diffraction gratings on the surface of different materials using this technique, is an attractive field of research. The fabrication of these diffractive elements on the surface of nonlinear optical materials is immensely attractive for the development of technological applications. So that, nonlinear optical materials are presently an attractive targets for ultrafast lasers to enhance the nonlinear behavior of these materials.

We fabricated one dimensional (1D) and two dimensional (2D) microstructures on the surface of different nonlinear optical materials such as $KTiOPO_4$, $RbTiOPO_4$, and $LiNbO_3$ to understand the potential diffractive properties that can be obtained with them, associated with the nonlinear optical properties. We investigated the linear and nonlinear diffraction properties of the microstructured nonlinear optical materials in detail.

We also explored a possible application for these structures as it is the development of RGBY laser phosphor displays. To do that, we embedded luminescent nanoparticles doped with lanthanide ions into the micro-meter feature sized structures inscribed on the surface of the nonlinear optical crystals. In this way, multicolor light emissions can be controlled spatially at the micro-meter scale.

Key words: Ultrafast laser ablation, nonlinear optical materials, diffraction gratings, laser phosphor displays.

UNIVERSITAT ROVIRA I VIRGILI
MICROSTRUCTURATION OF NONLINEAR OPTICAL MATERIALS:
METHODOLOGIES, CHARACTERIZATION, AND APPLICATIONS
Raj Kumar Golconda
Dipòsit Legal: T. 55-2013

UNIVERSITAT ROVIRA I VIRGILI
MICROSTRUCTURATION OF NONLINEAR OPTICAL MATERIALS:
METHODOLOGIES, CHARACTERIZATION, AND APPLICATIONS
Raj Kumar Golconda
Dipòsit Legal: T. 55-2013

Preface

The Ph.D investigation contained in this thesis has been carried out at the group of *Física i Cristal·lografia de Materials i Nanomaterials (FiCMA-FiCNA)* at the *Departament de Química Física i Inorgànica* of the *Universitat Rovira i Virgili* in Tarragona (Spain), and was supervised by Dr. Joan Josep Carvajal and the Prof. Dr. Magdalena Aguiló.

This thesis has also involved active collaboration with the following groups: Grupo de Microprocesado de Materiales con Láser, group led by Prof. Pablo Moreno at the University of Salamanca, Salamanca (Spain), the Nano electronic and Photonic systems group (NePhos), group led by Prof. Lluis Marsal, the Dept. Enginyeria Electronica of the Universitat Rovira i Virgili, Tarragona (Spain), the Organic nanostructured photovoltaics, group led by Prof. Jordi Martorell at the ICFO-Institut de Ciències Fotòniques, Barcelona (Spain), and the Matériaux, Optique Nonlinéaire et Plasmonique, group led by Prof. Benoit Boulanger at the Institut Néel, Centre National de la Recherche Scientifique (CNRS), Grenoble (France).

This work was financed by

This work was partially funded by the European Commission under the Seventh Framework Program under Project Cleanspace FP7-SPACE-2010-1-GA-263044, by the Spanish Government under Projects MAT 2008–06729-C02-02/NAN, MAT 2010-11402-E, MAT 2011-29255-C02-02, TEC 2010-21574-C02-02, HF 2008-0045, DE 2009-0002, PI09/90527, and by the Catalan Government under project 2009SGR235 by the Research Center on Engineering of Materials and Systems (EMaS) of the URV.

Raj Kumar Golconda
Tarragona, 2012

UNIVERSITAT ROVIRA I VIRGILI
MICROSTRUCTURATION OF NONLINEAR OPTICAL MATERIALS:
METHODOLOGIES, CHARACTERIZATION, AND APPLICATIONS
Raj Kumar Golconda
Dipòsit Legal: T. 55-2013

UNIVERSITAT ROVIRA I VIRGILI
MICROSTRUCTURATION OF NONLINEAR OPTICAL MATERIALS:
METHODOLOGIES, CHARACTERIZATION, AND APPLICATIONS
Raj Kumar Golconda
Dipòsit Legal: T. 55-2013

Acknowledgements

This thesis has been kept on track and has been through to completion with the support and encouragement of numerous people including my friends, colleagues and various institutions. At the end of my thesis I would like to thank all those people who made this thesis possible and unforgettable experience for me. It is a pleasant task to express my thanks to all those who contributed in many ways to success of this investigation and made it an unforgettable experience for me.

In the first place I would like to express my sincere gratitude to my group head Prof. Dr. Francesc Díaz for giving me an opportunity to join in the FiCMA-FiCNA group and providing necessary infrastructure and resources to accomplish my research work. I am much thankful to him for picking me up as a student at the critical stage of my Ph.D. I always admire him for dedication towards work, discussions, and his valuable suggestions.

Secondly, I am extremely grateful to my thesis directors, Prof. Dr. Magdalena Aguiló and Dr. Joan Josep Carvajal for their support, guidance and encouragement throughout the tenure of my doctoral thesis. At this moment of accomplishment, I express my sincere thanks to Dr. Joan Josep Carvajal for his extraordinary patience on my thesis progress, and his valuable suggestions. His dedication and conviction towards research work will always inspire me and I hope to continue to work with his noble thoughts. I can only say sincere thanks to him through my future work. I also gratefully acknowledge Dr. Jaume Massons for his advices, supervision, and crucial contribution for performing laser experiments in the laboratory.

This thesis would also not have been possible without the help of the technicians of this group. I would like to thank Agustí Montero and Nicolette Bakker for cutting and polishing of my crystals. I would also like to thank Laura Escorihuela for her great help in doing experiments in the laboratory and taking care of my furnaces during my absence.

I gratefully thank to the other senior members of the FiCMA-FiCNA group Dra. Josefina Gavaldà, Dra. Ma Rosa Solé, Dra. Maria Cinta Pujol, Dr. Xavier Mateos, and

Isabel Parreu for their support during my research in this group. I sincerely acknowledge Dra. Maria Cinta Pujol for all her help, suggestions, and friendly discussions.

I would like to thank all my colleagues Montserrat Galceran, Western Bolaños, Venkatesan Jambunathan, Martha Segura, Jaume Cugat, William Barrera, Muhammad Usman Qadri, Oleksandr Bilousov, Ali Butt, Carla Jose Berrospe, Oleksandr Savchuk, Mina Moeini for their support and humorous conversations.

This thesis would not have also been possible without the help of Dr. Patricia Segonds, Neél Institut, Grenoble. I will forever be thankful to her for giving me an opportunity for my three months stay to carry out the laser experiments and devoting her valuable time for my laser experiments in Neél Institut. I also thank Cohin who helped and provided me necessary components to perform laser experiments in the laboratory.

It is my great pleasure to acknowledge my Indian friends in Tarragona for their kindness, help, and funny talks during get together. My sincere thanks to Subba Rao, Purushotham, Chandan, Suryakanth, Siddam Venkat, Sunil, Lakshmi Tumung, and Shikha for their support and their friendship. I am very grateful to acknowledge my friends Bagvanth Reddy, Suresh, Narsimha, Khadar Basha, Sita lakshmi, Deepak, Srinivasa Reddy, Vara Prasad, and Venkatesh who supported and helped me during my studies.

Last but not least I would like to thank my family members Amma, Akka, Chelli, Mama, Athamma, Raghava, Pandu, Niharika, and Nikhil for their love and affection throughout these years.

UNIVERSITAT ROVIRA I VIRGILI
MICROSTRUCTURATION OF NONLINEAR OPTICAL MATERIALS:
METHODOLOGIES, CHARACTERIZATION, AND APPLICATIONS
Raj Kumar Golconda
Dipòsit Legal: T. 55-2013

To my family & friends…….

UNIVERSITAT ROVIRA I VIRGILI
MICROSTRUCTURATION OF NONLINEAR OPTICAL MATERIALS:
METHODOLOGIES, CHARACTERIZATION, AND APPLICATIONS
Raj Kumar Golconda
Dipòsit Legal: T. 55-2013

List of publications

This doctoral thesis is partially based on the work contained in the following papers, referred by roman numerals in the text:

Paper I

J.J. Carvajal, A. Peña, **R. Kumar**, M.C. Pujol, X. Mateos, M. Aguiló, F. Díaz, J.R. Vázquez de Aldana, C. Méndez, P. Moreno, L. Roso, T. Trifonov, A. Rodríguez, R. Alcubilla, Z. Král, J. Ferré-Borrull, J. Pallarès, L.F. Marsal, S. Di Finizio, R. Macovez, J. Martorell "*New approaches for the fabrication of photonic structures of nonlinear optical materials*", Journal of Luminescence, **129**, 1441-1447 (2009).

Paper II

G. Raj Kumar, J.J. Carvajal, M.C. Pujol, X. Mateos, M. Aguiló, F. Díaz, J.R. Vázquez de Aldana, C. Méndez, P. Moreno, L. Roso, T. Trifonov, A. Rodríguez, R. Alcubilla, Z. Král, J. Ferré-Borrull, J. Pallarès, L.F. Marsal, S. Di Finizio, R. Macovez, J. Martorell, *"Fabrication and characterization of photonic structures in crystals of the KTiOPO4 family"*, Óptica Pura y Aplicada, **42,** 147-152 (2009).

Paper III

G. Raj Kumar, J.J. Carvajal, M.C. Pujol, X. Mateos, M. Aguiló, F. Díaz, J.R. Vázquez de Aldana, C. Romero, C. Méndez, P. Moreno, L. Roso, J. Ferré-Borrull, J. Pallarès, L.F. Marsal, R. Macovez, J. Martorell, *"Analysis of linear and nonlinear optical properties of diffraction gratings inscribed on the surface of single crystals of the KTiOPO4 family"*, Proceedings of SPIE, **7728**, 77817-1-10 (2010).

Paper IV

Raj Kumar Golconda, J.J. Carvajal, M.C. Pujol, X. Mateos, M. Aguiló, F. Díaz, J.R. Vázquez de Aldana, C. Romero, C. Méndez, P. Moreno, L. Roso, *"Fabrication of photonic structures in crystals of the $KTiOPO_4$ family by ultrafast laser ablation"*, Physics Procedia, **8**, 126-135 (2010).

Paper V

G. Raj Kumar, J.J. Carvajal, M.C. Pujol, X. Mateos, J. Grau, J. Massons, J.R. Vázquez de Aldana, C. Méndez, P. Moreno, L. Roso, J. Ferré-Borrull, J. Pallarès, L.F. Marsal, M. Aguiló, F. Díaz, *"Surface ablation of $RbTiOPO_4$ by femtosecond laser"*, Optical Materials, **34**, 207-214 (2011).

Paper VI

R.K. Golconda, J.J. Carvajal, M.C. Pujol, X. Mateos, J. Massons, J.R. Vázquez de Aldana, C. Méndez, P. Moreno, L. Roso M. Aguiló, F. Díaz. *"Luminescent nano particles embedded in conical pores in $KTiOPO_4$ single crystals"* Appl. Phys. Exp. (to be submitted).

Paper VII

J. J. Carvajal, **R.K. Golconda**, , M.C. Pujol, X. Mateos, J. Massons, , J.R. Vázquez de Aldana, C. Méndez, P. Moreno, L. Roso, F. Díaz, M. Aguiló, *"Polycrystalline $RbTiOPO_4$ and TiO_2 formed on structured surfaces of $RbTiOPO_4$ single crystals by ultrafast laser ablation"*, Cryst. Eng. Comm. (to be submitted).

Paper VIII

Joan Josep Carvajal, **Raj Kumar Golconda**, Maria Cinta Pujol, Xavier Mateos, Maria de la O Ramírez, Luisa Bausá, Marco Bettinelli, Magdalena Aguiló, and Francesc Díaz, *"Interparticle energy migration-mediated upconversion in oxide nanoparticles"*, Advanced Materials (to be submitted).

Paper IX

R.K. Golconda, J.J. Carvajal, M.C. Pujol, X. Mateos, J. Massons, A. Ruiz de la cruz, J.S. Céspedes, M. Aguiló, F. Diaz, *"Multi-colour emission from luminescent nanoparticles embedded into micro-structures of $KTiOPO_4$ for RGBY laser phosphor display devices"*, Advanced Functional Materials (to be submitted).

UNIVERSITAT ROVIRA I VIRGILI
MICROSTRUCTURATION OF NONLINEAR OPTICAL MATERIALS:
METHODOLOGIES, CHARACTERIZATION, AND APPLICATIONS
Raj Kumar Golconda
Dipòsit Legal: T. 55-2013

CONTENTS

UNIVERSITAT ROVIRA I VIRGILI
MICROSTRUCTURATION OF NONLINEAR OPTICAL MATERIALS:
METHODOLOGIES, CHARACTERIZATION, AND APPLICATIONS
Raj Kumar Golconda
Dipòsit Legal: T. 55-2013

CHAPTER ONE

Introduction

The control of the optical properties of matter has been one of the major interesting tasks of research in recent years. Progress in photonics science has been intimately related to the development of optical materials by analyzing the light matter interaction. So that, presently, surface structuring by short laser pulses through nonlinear interactions with matter, for instance, is increasingly interesting for the development of new devices in photonics. This is especially true for nonlinear optical materials, that play a crucial role for the development of frequency conversion technologies where little research has been developed to analyze the structuring of their surfaces by ultrafast laser ablation.

The structuration of the surface of these nonlinear optical materials allows to develop optical components such as diffraction gratings. Thus, the characterization of these structured materials in terms of their potential functionality is another important field of research. The diffraction properties of micro-structured nonlinear optical materials could allow to develop new photonic devices presenting large nonlinearities

and satisfying at the same time all the technological requirements for applications such as wide transparence range, fast response, and high damage threshold.

Finally, the combination these surface structured nonlinear optical materials with luminescent nanoparticles, might allow to develop new functional devices that encompasses the benefits of the two types of materials. Those are the basic lines followed in the present thesis.

1.1. Ultrafast laser ablation

Femtosecond (fs) pulsed lasers have open a wide range of exciting new possibilities in the processing of semiconductors [1,2], transparent materials [3], polymers [4,5] and tissues [6], in information technology, telecommunication technology, biotechnology, and medicine industry, and defense industry [7,8]. Materials processing by fs lasers have distinct advantages over conventional processing methods. This technique allows for instance, direct writing of structures on the surface of the material, higher processing speeds due to effective optical coupling, minimal contamination of the processed material due to the ultrashort pulse width, athermal processing, spatial resolutions in the submicron regime, and reproducibility [9]. A fs laser pulse fundamentally changes the laser-material interaction mechanism compared with a long pulse, due to its high peak power, which is powerful enough for ionization of any material.

In particular, the highly nonlinear-laser matter interaction conditions produced by ultrafast laser pulses are conductive to the processing of hard-to-machine materials such as wide band gap materials, difficult to process by conventional tools. Normally, wide band gap materials are transparent to visible and near-infrared light as the photon energy is insufficient to excite an electron from the valence band to the conduction band by linear absorption. However, the extremely high intensities created by amplified ultrafast laser pulses cause nonlinear effects which lead to significant absorption of the photons.

The energy transport in femtosecond laser ablation can be separated into two stages: a first part in which the photon energy is absorbed by electrons and a second part where the absorbed energy is distributed to the lattice, leading to material removal. Photon absorption can be classified as linear absorption and nonlinear

absorption. Linear absorption generally obeys the Lamberts-Beer law [10], according to which the absorption of a specific wavelength through a material is a function of the material path length and it is independent of the incident laser intensity. Using ultrafast lasers, nonlinear absorption is significant in all materials, no matter it is transparent or opaque to a particular wavelength. The schematic view of these mechanisms is shown in Figure 1.1. Two physical mechanisms are involved for free electron generation [11] in femtosecond laser ablation: avalanche ionization (collisional impact ionization) and photoionization (multiphoton ionization or tunnel ionization). The kinetic energy of a free electron becomes sufficiently high by absorbing photons. Part of the energy may transfer to a bound electron by collisions to overcome the ionization potential [12]. This process is called collisional impact ionization [13]. Consequently, the free electrons absorb photons and produce more free electrons from bound electrons. Such series of the impact ionization processes is called avalanche ionization [14], that depends on the free electron density and is exponentially proportional to the laser intensity. The avalanche ionization process can occur for wide band gap materials at an intensity of laser below 10^{12} W/cm^2.

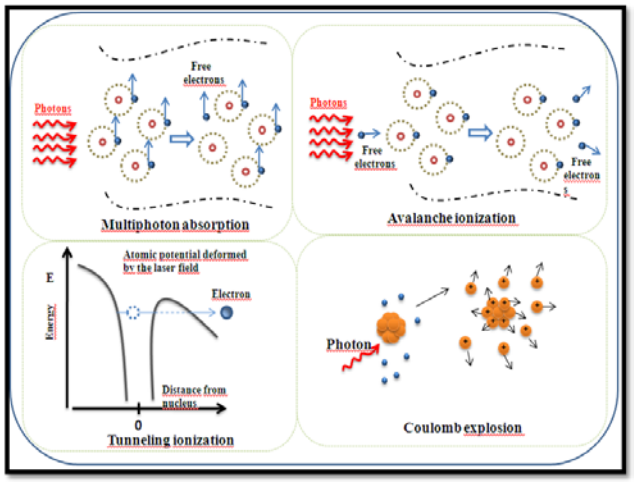

Figure 1.1. *Schematic view of the mechanisms involved in the femtosecond laser ablation process*

Multiphoton ionization occurs when a bound electron gets free from the valence band by absorbing several photons with a total energy of photons greater than the ionization potential [15]. Multiphoton ionization can be significant when the laser intensity is above 10^{13}W/cm^2. Tunneling ionization can be considered when the intensity is higher than 10^{15}W/cm^2 [16, 17]. Free electron density is assumed to

saturate at a critical density n_{cr}, at which ablation occurs [18], and it is taken as the free electron density at which plasma oscillation frequency equals the laser frequency:

$$n_{cr} = \pi m_e c^2/e^2\lambda^2 \qquad \text{Eq. 1.1}$$

where m_e is the electron mass, c is the speed of light, e is the electrical charge of the electron, and λ is the laser wavelength. At critical density, transparent wide band gap materials are completely opaque, and the laser energy is absorbed mainly through inverse Brehmstralhung in a similar way electrons do in metals.

During the femtosecond pulse duration, electrons have no time to transfer energy to other ions or out of the bulk material. Most of the pulse energy is firstly deposited into electrons in a small depth of the material by the laser electric field, what is called the skin layer l_s, that can be estimated by:

$$l_s = \alpha \frac{c}{2\omega}\left(1 + \frac{1}{r} + \frac{1}{2r^2}\right) \qquad \text{Eq.1.2}$$

where α is the absorption coefficient at the critical density, ω is the laser frequency, and r is the refractive index at the critical density. The absorption coefficient can be estimated from the Fresnel formula

$$\alpha = \frac{4r}{(1+r)^2 + r^2} \qquad \text{Eq. 1.3}$$

Where the refractive index can be calculated as

$$r = \sqrt{\frac{\omega_{pe}}{2\omega}\left(1 + \frac{\omega^2}{\omega_{pe}^2}\right)^{-1}} \qquad \text{Eq. 1.4}$$

Where ω_{pe} is the electron plasma frequency, apart from the avalanche ionization and the photoionization, there are two other mechanisms involved in the femtosecond laser ablation: thermal vaporization [19], where the electron-phonon collisions increase the local temperature above the vaporization point, and Coulomb explosion [20], where excited electrons escape from the bulk material and form a strong electric field which pulls out the ions within the impact area. In thermal vaporization the emitted species are likely to have similar kinetic energies, the volume of the material removed per pulse is of the order of micrometers, and the ablated surface generated is

rough. In Coulomb explosion, ions of different materials have similar momenta, the majority of the removed ions have a faster speed than those removed in thermal vaporization, the volume of material removed is of the order of tens of nanometers, and the ablated surface tends to be smooth.

Another parameter that we have to take into account is that in wide band gap materials, laser ablation can occur only when the fluence is higher than a certain value at a given pulse width. The threshold fluence is the laser fluence at which lattice instabilities of such magnitude are induced that the system is irreversibly damaged and at least a mono layer of material is removed [21]. A significant characteristic of femtosecond laser ablation of dielectrics is that its threshold fluence is higher than the predicted by the law of the square root of the pulse width [22].

$$F_{th} = \sqrt{\tau_p} \qquad \text{Eq. 1.5}$$

where F_{th} is the threshold fluence and τ_p is the laser pulse width.

This is because the femtosecond laser ablation of wide band gap material is dominated by ionization. Thus, the electron temperature dominates over the electron-phonon temperature, and the heated volume is governed by the photon absorption depth instead of thermal diffusion depth. Since the photon absorption depth is not proportional to the square of the pulse width, the threshold fluence deviates from this law.

According to this assumption, that the laser ablation initiated when the free electron density reaches to the critical density, the threshold fluence can be considered as the minimal fluence required to create the critical density. Based on this assumption, the theoretical threshold (F_{th}) logarithmically depends on the value of the critical density [23]:

$$F_{th} = \frac{2}{\alpha} ln\left(\frac{n_{cr}}{n_0}\right) \qquad \text{Eq. 1.6}$$

where n_0 is the number of seed electrons generated by the multiphoton ionization process, determined by

$$n_0 = \int_0^{\infty} P(I)dt \qquad \text{Eq.1.7}$$

where *P(I)* is the photoionization expressed as:

$$P(I) = \delta_N \left(\frac{I}{\hbar\omega}\right)^N N_s \qquad \text{Eq. 1.8}$$

where δ_N is the cross section of the N-photon ionization process, ħ is reduced plank constant, and N_s is the atoms density in the solid.

From the material removal mechanisms, in Coulomb explosion, it is assumed that the threshold fluence is the minimal fluence required to create an electric field high enough for electrons to overcome the summation of the binding energy of ions in the lattice (ε_b), density of conductive electrons (n_e), and the ionization potential (U_{PI}). According to this assumption, the threshold fluence in wide band gap materials can be expressed as:

$$F_{th} = \frac{3}{4}\left(\varepsilon_b + U_{PI}\right)\frac{l_s n_s}{\alpha} \qquad \text{Eq. 1.9}$$

The ablation depth is governed by the photon absorption depth, that is typically longer than the thermal diffusion depth during the femtosecond pulse. It is assumed that the actual fluence at the ablation depth *d is* equal to the absorbed threshold fluence, $F(z=d) = (1-r)F_{th}$. Based on this assumption, the ablation depth can be estimated by:

$$d = \frac{1}{\alpha} ln\left(\frac{F}{F_{th}}\right) \qquad \text{Eq. 1.10}$$

where *F* is the laser fluence.

In this thesis, femtosecond laser pulses are utilized for the surface patterning of nonlinear optical dielectric materials.

1.2. Diffraction gratings

Diffraction is the apparent bending of waves around small obstacles and the spreading out of waves through small openings. The same effects occur when light waves travel through a medium with a varying refractive index while diffraction occurs whenever propagating waves encounter such changes. Its effects are generally

most pronounced for waves where the wavelength is roughly similarly to the dimensions of the diffracting objects. If the obstructing object provides multiple, closely spaced openings, a complex pattern of varying intensity can result. This is due to the interference of different waves generated at the obstructing objects, each of one converted to a wave front. The word diffraction was firstly introduced by F.M. Grimaldi to record accurate observations of the phenomenon in 1665 [24]. The first diffraction grating was made by the American astronomer David Rittenhouse in 1785, who reported the fabrication of a half-inch wide grating with fifty-three apertures [25].

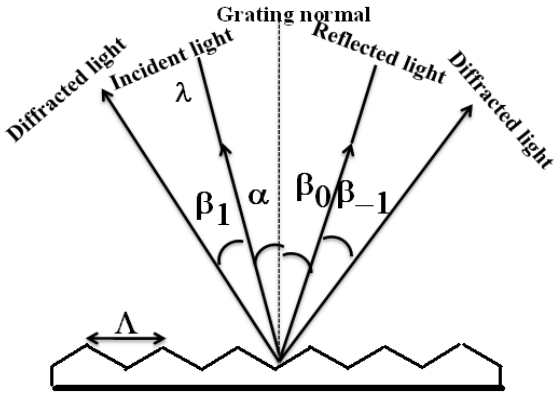

***Figure 1.2**. Schematic view of reflection grating containing the incident beam and different diffracted beams*

A diffraction grating is an optical element with a precise pattern of microscopic periodic structures that is used to diffract light. Usually this pattern is a corrugated surface of grooves (surface-relief grating), though some gratings are formed by the periodic variation of the refractive index inside the grating itself. Diffraction gratings play an important role in the field of science and technology, including laboratory spectroscopy, optical telecommunications, filtering, etc.

When a monochromatic light is incident on a grating surface, it is diffracted into discrete directions. The light diffracted by each groove combines to form set of diffracted wave fronts. The usefulness of a grating depends on the fact that there exists a unique set of discrete angles along which, for a given spacing Λ between grooves, the diffracted light from each facet is in phase with the light diffracted from any other facet, leading to constructive interference.

Diffraction by a grating can be visualized from the geometry displayed in Figure 1.2 which shows a ray of light of wavelength λ incident at an angle α and diffracted by a grating (of groove spacing Λ, also called pitch) along a set of angles (β_m). These angles are measured from the grating normal, which is shown as the dashed line perpendicular to the grating surface at its centre. The sign convention for these angles depends on whether the light is diffracted on the same side or the opposite side of the grating normal to respect the incident light. In Figure 1.2, which shows a schematic representation of a reflection grating and defines the typical angles used in their optics, the angles $\alpha > 0$ and $\beta_1 > 0$ (since they are measured counter-clockwise from the grating normal) while the angles $\beta_0 < 0$ and $\beta_{-1} < 0$ (since they are measured clockwise from the grating normal).

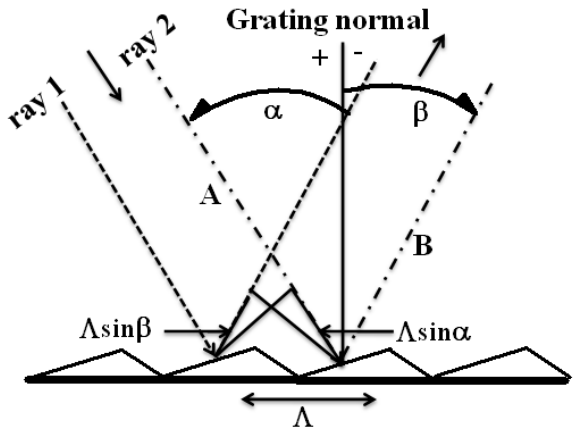

Figure 1.3. *Schematic view of diffraction, for planar wavefronts. Two parallel rays, labeled 1 and 2, are incident on the diffraction grating with groove spacing* Λ at wave front A. U*pon diffraction, the principle of constructive interference implies that these rays are in phase at diffracted wave front B if the difference in their path lengths,* Λsinα + Λsinβ*, is an integral number of wavelengths.*

If we analyze the interference of two parallel rays (ray 1 and ray 2 in Figure 1.3) of light incident on a surface-relief diffraction grating in a reflection configuration, the geometric path difference between light from adjacent grooves is seen to be Λsinα + Λsinβ. Since $\beta < 0$, in this case the term Λsinβ is negative, as can be seen in Figure 1.3. The principle of constructive interference dictates that only when this difference equals the wavelength of light, or some integral multiple thereof, light from adjacent grooves will be in phase (leading to constructive interference). At all other angles the waves originating from the groove faces will interfere destructively.

The grating equation can be written as:

$$m\lambda = \Lambda(\sin\alpha + \sin\beta) \qquad \text{Eq. 1.11}$$

This equation governs the angular locations of the principal intensity maxima when light of wavelength λ is diffracted from a grating of groove spacing Λ. Here m is the diffraction order (or spectral order), which is an integer. For a particular wavelength λ, all values of m for which $m\lambda/\Lambda < 2$ correspond to propagating diffraction orders.

Generally several integers m will satisfy the grating equation. We call each of these values a diffraction order. The physical significance of this is that the constructive reinforcement of wavelengths diffracted by successive grooves merely requires each ray be retarded in phase with each other; this phase difference must therefore correspond to a real distance (path difference) which equals an integral multiple of the wavelength. This happens, for example, when the path difference is equal to one wavelength, in which case we speak of the positive first diffraction order ($m = 1$) or the negative first diffraction order ($m = -1$), depending on whether the rays are advanced or retarded as we move from groove to groove

As we have seen, the grating equation allows light of wavelength λ to be diffracted into both negative and positive orders as well. Explicitly, spectra of all orders m exist for which

$$-2\Lambda < m\lambda < 2\Lambda, \qquad \text{Eq. 1.12}$$

This sign convention for m requires that $m > 0$ if the diffracted ray lies to the counter-clockwise side of the zero order ($m = 0$), and $m < 0$ if the diffracted light lies to the clockwise side of the zero order.

Diffraction gratings can be classified according to several criteria: the geometry of light incidence and collection, the material with which they have been fabricated, their efficiency behavior, the manufacturing method, their working spectra interval, etc. Here we will use only reflection and transmission gratings fabricated on the surface of nonlinear optical dielectric materials by the ultrafast laser ablation and chemical etching methods. The gratings are considered as phase-only gratings to analyze the modulation shapes they produce on the diffracted beams. Such gratings work by retarding the wavefronts as a function of position and these gratings absorb

no light energy. So that the total amount of diffracted light can reach 100% when summed over all the orders.

Reflection gratings are much more common than transmission grating systems. Optical systems can be folded with reflection gratings, which reflect as well as disperse, whereas transmission grating systems are in-line and therefore usually of greater length. Moreover, reflection gratings are not limited by the transmission properties of the grating substrate, and can operate at much higher angles of diffraction. Reflection gratings provide much higher resolving power than equivalent transmission gratings, since the path difference between neighboring beams (i.e., separated by a single groove) is higher in the case of reflection gratings.

In certain types of instrumentation, transmission gratings are much more convenient to use than reflection gratings. The most common configuration involves converting cameras into simple spectrographs by inserting a grating in front of the lens. Another application, where high speed lenses and transmission gratings can be combined advantageously, is in the determination of spectral sensitivity of photographic emulsions. However, transmission gratings are limited to spectral regions where the materials from which they are fabricated are transparent. Their main drawback is that they do not fold the optical path conveniently as reflection gratings do. Moreover, to avoid total internal reflection, their diffraction angles cannot be extreme. Even though the surface of the substrate is usually antireflection coated, internal reflections from grating-air interfaces leads to some backward-propagating orders (i.e., the transmission grating will also behave as a weak reflection grating), and this limits the maximum efficiency achievable in these gratings to about 80 %.

Diffraction from gratings is of capital importance in the fields of integrated optics, holography, optical data processing, and spectral analysis. The diffraction gratings have applications in beam coupling, beam coding, beam deflection, beam expansion, beam shaping, beam splitting, coherent light generation, data processing and modulation, multiple beam generation, pulse shaping, pulse compression, multiplexing, de-multiplexing, Q-switching, mode locking, signal processing, and spatial light modulators among others. [26-35.]

1.3. Nonlinear optics

Nonlinear optics is the study of optical effects arising from the interaction of intense coherent optical radiation with matter in the nonlinear regime. Optical frequency conversion was the first of these phenomena, firstly discovered by Franken and co-workers in a quartz crystal illuminated by a ruby laser at a wavelength of 694.2 nm in 1961 [36]. This was an important milestone experiment for the investigation of several nonlinear optical effects, including sum-frequency generation, stimulated Raman scattering, self-focusing, optical rectification, four-wave mixing, and many others that rise same to novel concepts and applications such as fiber optics, optical spectroscopy, optical switching, quantum optics, telecommunications, signal processing, etc.

In an optical medium, electrons are displaced from their normal orbits by the oscillating electric field ($\tilde{\vec{E}}$) of an incident light wave, generating in this way oscillating dipoles formed by the electrons and the remaining ions. The macroscopic manifestation of the oscillating dipoles is the oscillating polarization or dipole moment per unit volume $\tilde{\vec{P}}$. In regime of conventional optics, the $\tilde{P}$ is simply assumed to be linearly proportional to $\tilde{\vec{E}}$:

$$\tilde{P}(t) = \varepsilon_0 \chi^{(1)} \tilde{E}(t) \qquad \text{Eq. 1.13}$$

where ε_0 is the free-space permittivity, and $\chi^{(1)}$ is the susceptibility of a given medium. Shortly after discovery of second harmonic generation (SHG), several other coherent optical frequency mixing effects (such as optical sum-frequency generation, optical difference frequency generation, and optical third harmonic generation) were observed. All these new effects could be reasonably explained by replacing the linear term on the right hand side of Equation 1.13 by a power series

$$\tilde{P}(t) = \varepsilon_0 \left[\chi^{(1)} \tilde{E}^2(t) + \chi^{(2)} \tilde{E}^2(t) + \chi^{(3)} \tilde{E}^3(t) \right]$$
$$= \tilde{P}^{(1)}(t) + \tilde{P}^{(2)}(t) + \tilde{P}^{(3)}(t) + ... \qquad \text{Eq. 1.14}$$

where, $\chi^{(1)}$, $\chi^{(2)}$, and $\chi^{(3)}$ are the first-order, second-order, and third-order susceptibilities and so on, respectively. For simplicity we take the fields $\tilde{P}(t)$ and $\tilde{E}(t)$ to be scalar quantities. In general, the nonlinear susceptibilities depend on the frequencies of the applied fileds, but under present assumption we take them to be constants.

Sum-frequency generation (SFG) is a nonlinear optical process in which from two input photons incident of low energy on nonlinear medium, a new high energy photon can be generated. If an incident intense optical field contains two monochromatic components of frequency ω_1, ω_2 and propagate through a second order nonlinear crystal, a coherent radiation at the sum frequency of $\omega_3 = \omega_1 + \omega_2$ may be obtained.

Figure 1.4 describes this process.

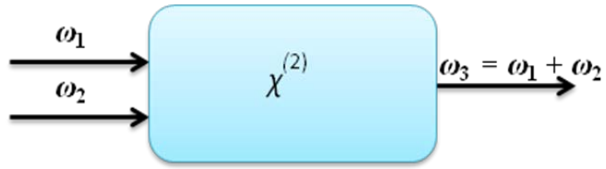

Figure 1.4. *Geometry of the sum frequency generation*

For a laser beam whose electric filed strength is expressed as

$$\tilde{E}(t) = Ee^{-i\omega t} + c.c \qquad \text{Eq. 1.15}$$

The nonlinear polarization component can be expressed as according to equation 1.14 or explicitly as

$$\tilde{P}^{(2)}(t) = 2\varepsilon_0 \chi^{(2)} EE^* + (\varepsilon_0 \chi^{(2)} E^2 e^{-i2\omega t} + c.c.) \qquad \text{Eq. 1.16}$$

The second order polarization consists of a contribution at zero frequency (the first term) and a contribution at frequency 2ω (the second term). The second term contribution can lead to the generation of radiation at the second harmonic frequency and the first term contribution does not lead to the generation of electromagnetic radiation because its second time derivative vanishes.

In this process, a special case is when the two input photons have the same frequency i.e., $\omega_1 = \omega_1 = \omega$, then the SHG occurs: $\omega + \omega = 2\omega$.

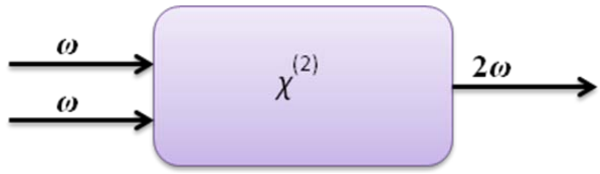

Figure 1.5. *Geometry of the second harmonic generation*

Figure 1.5 shows a schematic representation of the SHG process.

We assume that the medium is lossless both at the fundamental frequency ω_1 and at the second harmonic frequency $\omega_2 = 2\omega_1$. The total electric field within the nonlinear medium to be given by

$$\tilde{E}(z,t) = \tilde{E}_1(z,t) + \tilde{E}_2(z,t) \qquad \text{Eq. 1.17}$$

Where each component is expressed in terms of complex amplitude $E_j(z)$ and slowly varying amplitude $A_j(z)$ according to

$$\tilde{E}_j(z,t) = E_j(z)e^{-i\omega_j t} + c.c., \qquad \text{Eq. 1.18}$$

where $$E_j(z) = A_j(z)e^{ik_j z} \qquad \text{Eq. 1.19}$$

where the k_j is the propagation constant and refractive index are given b

$$k_j = n_j\omega_j/c,\ n_j = [\epsilon^{(1)}\omega_j]^{1/2} \qquad \text{Eq. 1.20}$$

The nonlinear polarization is expressed as

$$\tilde{P}^{NL}(z,t) = P_1(z,t) + \tilde{P}_2(z,t) \qquad \text{Eq. 1.21}$$

and $$\tilde{P}_j(z,t) = \tilde{P}_j(z)e^{-i\omega_j t} + c.c., \qquad j = 1,2 \qquad \text{Eq. 1.22}$$

The expressions for the polarization amplitudes are

$$P_1(z) = 4\varepsilon_0 d_{eff} E_2 E_1^* = 4\varepsilon_0 d_{eff} A_2 A_1^* e^{i(k_2 - k_1)z} \qquad \text{Eq. 1.23}$$

$$P_2(z) = 2\varepsilon_0 d_{eff} E_1^2 = 2\varepsilon_0 d_{eff} A_1^2 e^{2ik_1 z} \qquad \text{Eq. 1.24}$$

The solution of coupled –amplitude equation for sum frequency generation, we find that

$$\frac{dA_1}{dz} = \frac{2i\omega_1^2 d_{eff}}{k_1 c^2} A_2 A_1^* e^{-i\Delta kz} \qquad \text{Eq. 1.25}$$

$$\frac{dA_2}{dz} = \frac{i\omega_2^2 d_{eff}}{k_2 c^2} A_1^2 e^{i\Delta kz} \qquad \text{Eq. 1.26}$$

where $\Delta k = 2k_1 - k_2$ Eq. 1.27

From the slowly varying amplitude approximation

$$\frac{dA_3}{dz} = \frac{2i\omega_3^2 d_{eff}}{k_3 c^2} A_1 A_2 e^{i\Delta kz} \qquad \text{Eq. 1.28}$$

In phase matching consideration, the amplitudes A_1 and A_2 of the input fields can be taken as constants on the right hand side of the equation 1.28. This assumption is valid whenever the conversion of the input fields into the sum frequency field is not too large.

For a special case $\Delta k = 0$ Eq. 1.29

The amplitude A_3 of the sum-frequency wave increases linearly with z, and consequently that its intensity increases quadratically with z. This condition is known as perfect phase matching. When the condition (equation 1.29) is not satisfied, the intensity of the emitted radiation is smaller than for the case of $\Delta k = 0$.

The amplitude of the second harmonic frequency at the exit plane of the nonlinear medium is given by equation 1.28 from $z = 0$ to $z = L$, then

$$A_3(L) = \frac{2id_{eff}\omega_3^2 A_1^2}{k_3 c^2}\int_0^L e^{i\Delta kz}dz \qquad \text{Eq. 1.30}$$

Where intensity of the second harmonic wave is given by the time averaged poynting vector, which for our definition of field amplitude is given by

$$I_i = 2n_i\varepsilon_0 c|A_i|^2 \qquad \text{Eq. 1.31}$$

The intensity of the second harmonic wave along the length L is given by

$$I_{2\omega} = \frac{2\omega^2 d_{eff}^2 L^2}{n_{2\omega}n_\omega^2 c^3\varepsilon_0} I_1^2(\omega)\left(\frac{\sin\Delta kL/2}{\Delta kL/2}\right)^2 \qquad \text{Eq. 1.32}$$

From this equation it can be seen that the intensity is maximized for the phasematched condition $\Delta k = 0$. If the process is not phasematched, the driving polarization at 2ω goes in and out of phase with the generated wave $\tilde{E}(2\omega)$ and conversion oscillates as a function of L with a period: $L_c = \pi/\Delta k$, the parameter L_c, defining the length of the nonlinear medium providing the maximum SHG efficiency (coherence length).

The phase drift naturally resulting from the difference in phase velocities due to material dispersion must be compensated by some phasematching means. Birefringent phasematching (BPM) and quasi-phasematching (QPM) are the two different methods used to achieve phase matching in nonlinear materials. The first time a nonlinear process showed efficient SHG was using birefringence phasematching [37, 38], in which the difference in phase velocity of two orthogonally polarized waves was used to balance the difference due to dispersion. An alternative approach, QPM was suggested independently by Armstrong et al. and Franken et al [39, 40]. QPM uses a periodic modification of the properties of the nonlinear medium to correct the relative phase at regular intervals without matching phase velocities. A particularly effective structure is one in which the sign of the nonlinear susceptibility is periodically reversed throughout the medium. By changing the sign of the nonlinear susceptibility after every coherence length, the phase change of nonlinear polarization wave is shifted by π, effectively rephasing the interaction and leading to monotonic power flow into the harmonic wave.

An alternative to these processes is the use of gratings that are not simply periodic in either the propagation or transverse directions allowing tailoring of the nonlinear interaction in ways that are not possible in BPM media, and generating the second harmonic through new mechanisms such as non-collinear schemes [41], as will be described in the next section.

1.4. Diffraction in nonlinear optical materials

In connection with nonlinear optics, there are some other subjects also studied, i.e., nonlinear transmission, reflection, refraction, and absorption. Along with these there is an interesting phenomenon, diffraction in nonlinear optical materials, or nonlinear diffraction, also to be included in nonlinear optics. Nonlinear diffraction [42] is a kind of non-collinear phase matching [43] that is observed in pure form when the reciprocal lattice vector describing the spatial modulation of the nonlinear susceptibility of the medium does not coincide with the direction of propagation of the fundamental and the generated radiations. This is based on the QPM phenomenon, and was firstly demonstrated in a NaH_4Cl multi-domain sample with periodic spatial modulation of the nonlinear susceptibility, where effective SHG in non-collinear directions was observed by Freund in 1968 [44]. In that case SHG occurs at angles of incidence and diffraction for which the nonlinear analogue of Bragg´s law is satisfied:

$$k_{2\omega} - 2k_{\omega} - G_{p,q} = 0 \qquad \text{Eq. 1.33}$$

where $G_{p,q}$ is the reciprocal lattice vector, with p, q $\in$ Z. For each reciprocal vector $G_{p,q}$ and a prescribed k_{ω}, there is at most a unique angle of propagation for the SH such that Eq. 1.33 is satisfied. In the 1D case for a real space lattice period Λ of the reciprocal lattice has a period of $2\pi/\Lambda$.

The experimental study was carried out in naturally laminated crystals exhibiting non regularity and dispersion of nonlinear domains [45-46], as well as in artificially created nonlinear one-dimensional $\chi^{(2)}$ gratings [47-49] and annular $\chi^{(2)}$ gratings [50, 51]. Nonlinear diffraction has also been reported in the second and third harmonic generation in the presence of a transient optical induced one dimensional (1D) grating [52]. Efficient backward SHG was observed by the nonlinear diffraction phenomenon in a 3D silicon-opal photonic crystal [53]. By employing the concept of nonlinear Bragg diffraction, second harmonic conical waves were generated by two

dimensional annular nonlinear photonic structures [54]. Bragg diffraction occurs at incident angles close to the Bragg angle, in contrast Raman-Nath diffraction occurs at an arbitrary angle of incidence. Nonlinear Bragg diffraction with multi-order generation of second harmonics in contribution to the Raman-Nath diffraction has been observed in a periodically poled 1D lithium niobate crystal [55]. In Figure 1.6, the additional spots are observed only in a nonlinear diffraction grating by longitudinal phase matching conditions which are contributed by the Raman Nath diffraction. The angular positions of the additional spots are defined only by the ratio of the wavelength to the grating period as in Raman-Nath diffraction.

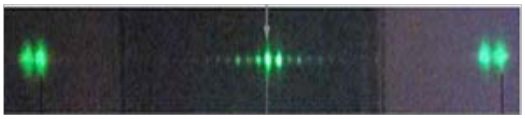

Figure 1.6. *Nonlinear diffraction patterns generated in a 1D QPM grating in a periodically poled lithium niobate crystal* [55].

Recently, nonlinear diffraction was produced by a virtual fundamental beam in 1D and two dimensional (2D) dimensional quadratic gratings of lithium niobate and lithium tantalate crystals [56], and also in random nonlinear photonic structures of strontium tetraborate [57].

In the case of surface relief diffraction gratings, a periodic modulation of the second order susceptibility $\chi^{(2)}$, and a periodic modulation of the linear susceptibility $\chi^{(1)}$ associated to a periodic modulation of the refractive index, can be obtained.

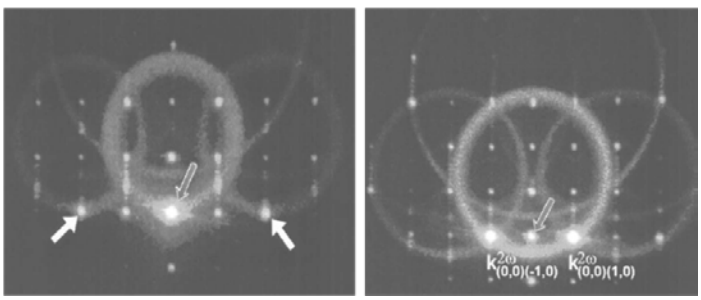

(a) (b)

Figure 1.7. *Images of the SHG for different incident angles θ_0 (a) $\theta_0 = 0^o$ (b)$\theta_0 = 0.7^o$ in a surface relief diffraction grating fabricated by ultrafast alser ablation in a KH_2PO_4 crystal* [58].

In this type of diffraction gratings it has been demonstrated that by changing the incident angle of the fundamental beam, collinear (see Figure 1.7 (a)) or non-collinear phasematching (see Figure 1.7(b)) can be achieved among certain diffraction orders [58]. The several second harmonic rings generated by non-collinear phasematching between fundamental scattered light within and at the surface of the crystal.

Similarly, it has been reported the generation of multiple second harmonic beams on diffraction gratings inscribed on β-BaB_2O_4 crystal by femtosecond laser ablation [59], and the corresponding recorded image is shown Figure 1.8. The brightest ±1 diffraction orders are generated due to the noncollinear phasematching conditions and ±2 diffraction orders of the second harmonic beam are overlapped with the ± 1 diffraction orders of the fundamental beam.

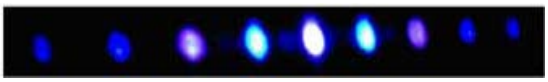

Figure 1.8. *Multiple second harmonic beams generated in a surface relief diffraction grating fabricated by ultrafast laser ablation on a β-BaB_2O_4 crystal* [59].

The control of laser radiation can be obtained by patterning the micro-structures on 1D and 2D diffraction gratings by femtosecond laser ablation on a Nd-doped $LiNbO_3$ crystal was also reported by G.A.Torchia et al [60].

1.5. Localized emission with luminescent nanoparticles

In recent years, control and localization of electromagnetic radiation is of increasing interest for the development of compact, versatile and multifunctional devices through micro-structured patterned materials in the field of photonics [61, 62]. New approaches have been explored for enhancing the resonant optical processes in photonic devices by matching the periodic dimensional structures with the wavelength of incident light. The optical properties of light can also be manipulated and controlled by filling the micro or nanostructured materials with other materials such as polymers [63], semiconductors [64], dye molecules [65], molecular nanoparticle materials [66], etc. Among the various approaches adopted so far, an alternative has been demonstrated recently for controlling and localizing the

electromagnetic radiation by embedding lanthanide doped nanoparticles in patterned structures with micrometer dimensions [67]. Trivalent lanthanide ions present a rich optical spectra and a high quantum efficiency that allowed to demonstrate new functionalities for the materials in which they have been embedded in the fields of biological and medical applications. However, the optical properties of lanthanide ions doped nanoparticles embedded in patterned microstructures have been minimally explored [68]. For instance, embedding high refractive index optically active lanthanide ions doped nanoparticles in ordered microstructures inscribed on a lower index material would give an additional possibility to confine the emitted light that can provide brighter emissions [69]. Apart from this, the use of microstructured nonlinear optical materials to embedded luminescent nanoparticles in them, might also provide multifunctional devices capable to generate additional electromagnetic radiations through nonlinear optical processes.

The control and localization of the emission radiation generated by luminescent nanoparticles spatially at the micro-meter scale and embedding them in 2D micro-structured patterns inscribed on the surface of nonlinear optical materials would show interesting new possible applications such as RGBY laser phosphor display devices.

Display technology plays a crucial role in how information is conveyed. A picture is a worth of thousand words, so this technology simplifies information sharing. The cathode ray tube (CRT) was the first device which revolutionized display industry. However, a vast research on display technology has increased demand for displays that rival and surpass CRTs parameters such as picture quality, size, and power consumption. CRT displays use scanning electron beams in a vacuum tube to excite color phosphors in red, green and blue colors on the screen to emit colored light to produce color images. Although CRT displays can produce vivid colors and bright images with high resolution, the use of CRTs places severe technical limitations, such as difficult to set possible geometric configuration of electron gun axes and aperture positions in the CRT displays and leads to dramatic decline in demand for CRT displays. Later, liquid crystal displays (LCD) devices replaced CRTs due to their light weight, low operating power, and compact design. So, this technology allowed to design numerous devices such as digital watches, cell phones, laptops and small screened electronics. Display technology has extended to design

other display devices such as organic light emitting diodes (OLEDs), digital light processing technology, plasma displays, liquid crystal displays (LCDs), light emitting diodes (LEDs) displays, and field emission displays (FEDs).

The modern displays have direct configuration where the screen itself contains light emitting color pixels to directly form color images on the screen. However, these direct emitting displays avoid the optical lens systems for projecting images. In projection display systems, white light sources are used where beams are filtered and modulated to produce images in red, green and blue colors. Alternatively, three light sources in the red, green, and blue may be used to directly produce three beams in red, green and blue colors and the three beams are modulated to produce multi-color images.

Demand for high quality displays has driven to the evolution of a new approach made to innovate high quality RGB displays with laser phosphor display (LPD) technology. LPD is a new category of large format digital display technology, with a low power consumption, and long lasting performance and brilliant picture quality. LPDs consist in three main parts, such as the laser engine, the laser module, and the phosphor panel. The phosphor panel (display screen) comprises a substrate on which parallel phosphor stripes are made of different phosphors that emit RGB colors by absorbing light at a particular excitation wavelength in the UV, emitted by the laser engine. The laser module is used to project and scan the laser beam onto the screen producing color image generated by the phosphor stripes deposited on the substrate.

The main attractive feature of this LPD technology is that the phosphor pixels can be any shape, from small squares to long ribbons. In theory LPD can change images faster than LCD and LED technologies as well, making it an invaluable option for many areas such as space and weather stations, trading exchanges, broadcasting, airports and security settings.

In this thesis, we contributed to the development of LPD technology by embedding lanthanide doped nanoparticles which emit RGBY colors, inside patterned 2D microstructures inscribed on the surface of nonlinear optical materials. These RGBY colors can be produced simultaneously by using the single excitation wavelength with NIR laser source. Another important aspect of this approach is that it

can also be applicable for producing high resolution images through RGBY LPD technology due to the small size of the pixels we propose.

1.6. Generation of visible light by upconversion processes

The lanthanide ions are a series comprises the fifteen metallic chemical elements occupy special place in periodic table with atomic numbers 57 through 71, from lanthanum through lutetium.

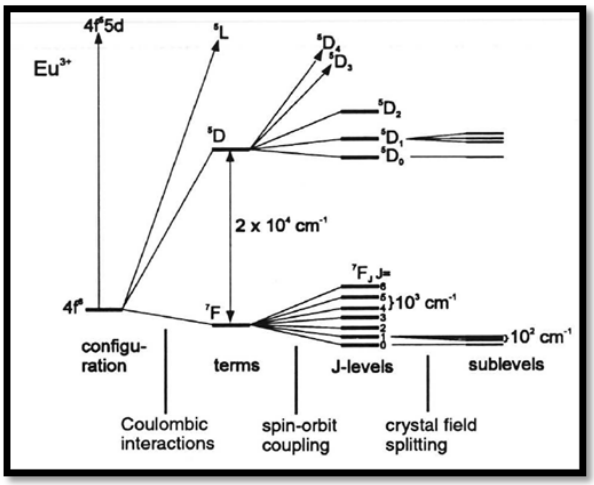

Figure 1.9*. Effect of the crystal field on energy level splitting of the* Eu^{3+} *ion*

The ground state electronic configuration of rare earth atoms consists of a core which is identical to xenon, plus additional electrons in higher orbits. In xenon, the shells with quantum numbers n=1, 2, 3 are completely filled. The shell n=4 has its s, p, and d subshells filled, where as the 4f subshell capable of accommodating 14 electrons is completely empty.

However, the n=5 shell has acquired its first 8 electrons, which fill the 5s and 5p orbits. Moving from La^{3+} to Lu^{3+} elements, the 4f-shell of lanthanides, which is situated inside the 5s and 5p orbitals, is being filled from 0 to 14 electrons.

The Russel-Saunders coupling allows the representation of the electronic states of Dieke diagrams for lanthanides, as a function of the total angular momentum (L), the spin multiplicity (2S+1), and the total angular quantum number (J) the following expression $^{(2S+1)}L_J$; where $L = \Sigma_i\, l_i$, $S = \Sigma_i s_i$ and J =L+S, L+S-1, L+S-2,…., $\left| S-L \right|$.

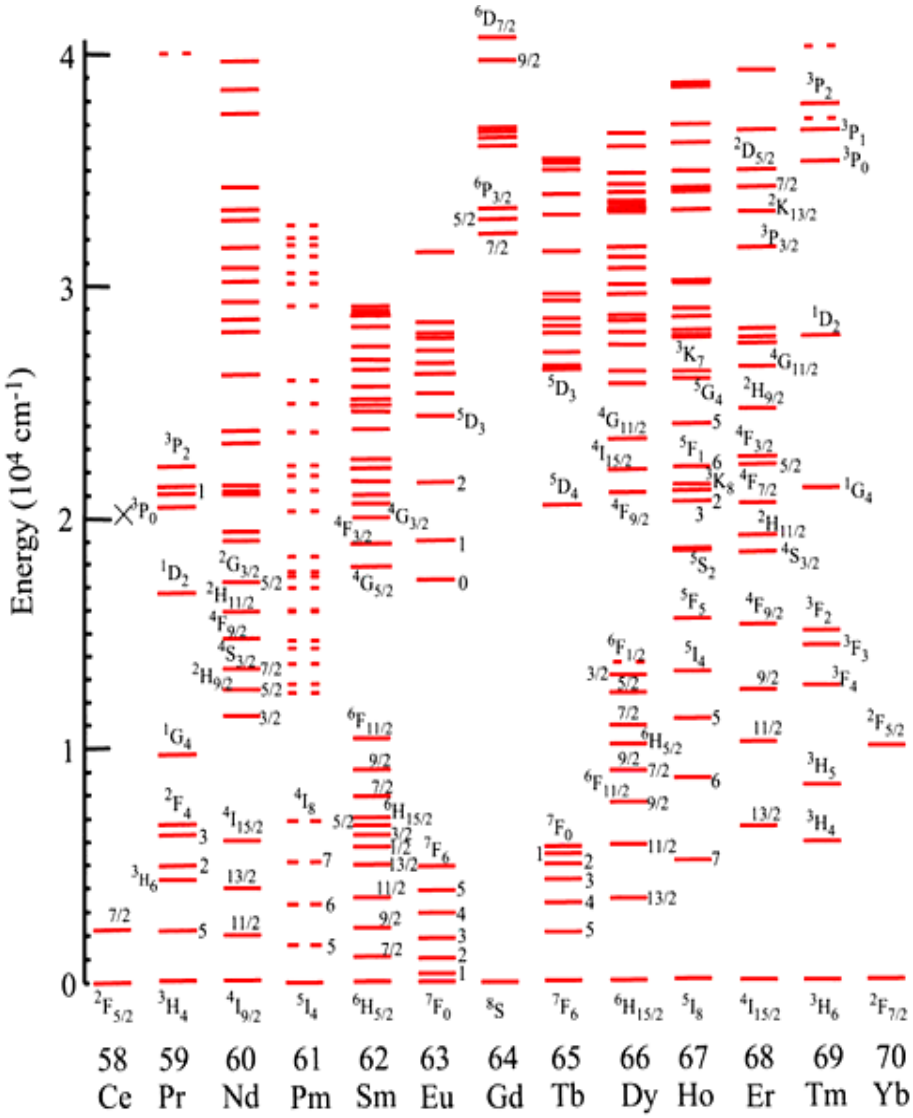

Figure 1.10. *Energy level diagram of lanthanide ions (Dieke diagram)*

Given L = 1,2,3,4… the spectroscopic terms are S(L=0), P(L=1), D(L=2), F(L=3)…respectively [70].

The electronic configuration of lanthanide ions is energetically split in spectroscopic terms, levels and states because of (i) electronic repulsion (ii) spin-orbit coupling (iii) ligand field splitting when they are bound to a solid (in a coordinating environment)

as showed in Figure 1.9, for Eu^{3+}, as a representative lanthanide ion, and in the Dieke energy level diagram of lanthanide ions, shown in Figure 1.10.

The selection rules state that electronic transitions must accomplish involve the promotion of electrons without a change in their spin ($\Delta S = 0$) and with a variation of either the total angular momentum and the total angular momentum quantum number of one unit at most ($\Delta L = \pm 1,0$; $\Delta J = \pm 1,0$). Relaxation of these rules can occur when the lanthanide ions are surrounded by other ions and ligands in molecules and solids that create an electric field around these ions (crystal field in crystalline solids) even though it must be remarked by their scarce efficiency to lessen the prohibition, as confirmed by weak Ln ions absorption coefficients and long luminescence lifetimes.

1.6.1. Upconversion processes in lanthanide ions

The concept of upconversion in ion-doped solids was first proposed by Bloembergen in 1959 [71] and demonstrated experimentally by Auzel in 1966 [72]. Auzel described a method to detect infrared radiation by converting it into visible light. With the invention of the laser, the upconverting processes could be more thoroughly studied [73]. Upconverting materials are fabricated by doping the materials with active lanthanide ions. Upconversion processes involving ions have been observed in many types of solid hosts, including crystals [74], and wave guides [75]. The upconversion processes involve energy transfer between lanthanide ions of the same kind as well as different kind of ions. The first ion being excited is called sensitizer, and the ion to which the energy is transferred to is called an activator.

A number of different mechanisms are involved in the upconversion process. These mechanisms can be described with the use of physically existing energy levels in Ln ions. The first mechanism is the excited state absorption (ESA), in which a photon with energy $h\upsilon_1$ (h is plank constant and ν is photon frequency) is absorbed by an ion embedded in a crystal matrix, promoting the electronic transition from the ground level (E_1) to a metastable intermediate level (E_2) as can be seen Figure 1.11. Then, it may absorb a second photon $h\upsilon_1$ and rise up to an even higher level (E_3) (see in Figure 1.11). There, when this superexcited electron drops back to the E_1 ground state, the energy may be relaxed in a radiative manner, yielding an emitted photon with energy $h\upsilon_3$, where υ_3 is larger than υ_1.

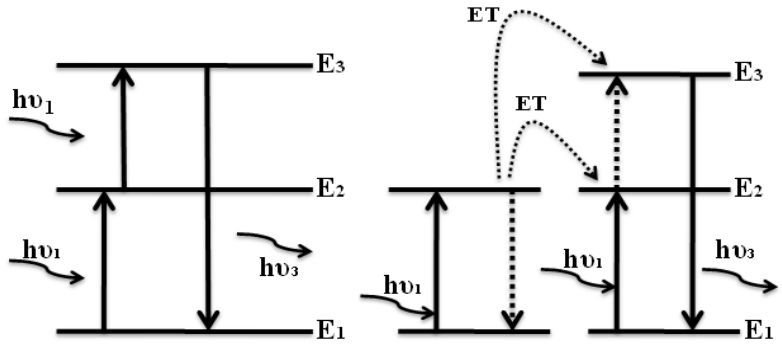

(a) (b)

Figure 1.11. *(a) Schematic representation of the ESA process, where upward arrows represent direct excitation of an electron to a higher energy level, downward arrows represent radiative relaxation (b) Schematic representation of the ETU process, where dotted downward arrows represent non-radiative relaxation, dotted curve arrows represent energy transfer, and dotted upward arrows represent indirect excitation of an electron*

The upconversion emission originating from ESA was not easily observed, mainly owing to the fact that the second photon must be captured by an electron at the intermediate level (E_2), and the population there is usually rather low. There are three factors determining the population at the metastable excited state: the power of the excitation source, the lifetime of the metastable state, and the absorption cross section of the ions. The ESA process is typical of upconversion processes involving only ions of the same kind.

The energy transfer upconversion (ETU) is another important upconversion mechanism besides ESA. The ETU mechanism involves energy transfer between two adjacent ions, namely a sensitizer and an activator. After the excitation of the sensitizer, the energy can be transferred to the activator, promoting an electronic transition from level E_1 to E_2 (when the activator is in the ground state), or from level E_2 to E_3 (when the activator is in the intermediate state), while the sensitizer is relaxed to its ground state. This process is typical of upconversion processes involving ions of different kinds. Introducing sensitizers can be used to enlarge the absorption cross-section of the activator, because the sensitizers help to capture photons and promote electrons of the activator to the super excited state (E_3). In this process, the energy transfer process is independent of the excitation power, and can be quite efficient

under optimized conditions. The schematic view of ETU process is shown in Figure 1.11 (b).

1.6.2. Active lanthanide ions used in this thesis

In this thesis, we analyzed the luminescence properties and the upconversion possibilities of different lanthanide ions such as ytterbium (Yb^{3+}), erbium (Er^{3+}), thulium (Tm^{3+}), holmium (Ho^{3+}) and europium (Eu^{3+}) in two different matrices, the monoclinic double tungstates and the Gd_2O_3, that we will present later.

Ytterbium is ideally well suited for diode pumping since it has a very simple energy level scheme consisting only of two manifolds: the ground $^2F_{7/2}$ state and an excited $^2F_{5/2}$ state, which are separated approximately by 10,000 cm^{-1}. It shows a broad emission bandwidth, which enables tunable laser emissions and allows to generate ultrashort pulses in mode locked lasers. Furthermore, the lifetime of its upper state is long which maximizes the electronic energy storage by pumping. Yb^{3+} ions are widely used as sensitizer ions for increasing the absorption of light from other ions such as Er^{3+}, Tm^{3+}, and Ho^{3+}. Since it poses a high absorption cross section in the 0.9 to 1.1 µm spectral range. On the other hand, Yb^{3+} exhibits a quasi three level laser mechanism, which tends to lead to a low laser threshold and it is the ion called to replace Nd^{3+} based lasers, since it does not suffer from reabsorption losses, and it has a low thermal load.

Erbium has a rich energy level structure, showing different sharp spectral lines depending on the host material in which it is embedded. Erbium ions have a characterstic emission at 1.5 µm wavelength from the $^4I_{13/2} \rightarrow {}^4I_{15/2}$ transition that is used for optical communication devices. Due to the low absorption cross section in the spectral range around 980 nm, it limits the pump efficiency of this ion. To increase this efficiency, Yb^{3+} can be used as a ion sensitizer ion due to the high energy overlap between the $^4I_{11/2}$ level of Er^{3+} and the $^2F_{5/2}$ level of Yb^{3+} as can be seen Figure 1.10 (Dieke diagram). The green wavelength emission through upconversion from Er^{3+} ion from the $^4S_{3/2} \rightarrow {}^4I_{15/2}$ transition is interesting for phosphor displays, high density optical storage, biomedical diagnostics, and sensors of applications [76, 77].

Thulium has also numerous energy levels. For Tm^{3+}, laser operation has been demonstrated in many host materials with high efficiency [78, 79]. Tm^{3+} can also be used as a sensitizer ion for other optically active lanthanide ions, because it has an extraordinary ability to transfer part of the energy to other neibouring lanthanide ions [80-82] such as Ho^{3+}, Gd^{3+}, and Pr^{3+} etc. The most characterstic emission of Tm^{3+} in the blue arises from the $^1G_4 \rightarrow {}^3H_6$ transition. The emission wavelength of Tm^{3+} ions in the near infrared region is at 1.5 μm from the $^3H_4 \rightarrow {}^3F_4$ transition, which is very interesting for telecommunication purposes and at around 1.8 μm from the $^3F_4 \rightarrow {}^3H_6$ transition, which is used in remote sensing of the atmosphere (LIDAR devices) and in developing medical laser technologies.

Holmium shows considerable potential as an active ion for laser generation and nearly fourteen stimulated emission channels have been discovered for the Ho^{3+} ion as activator in different hosts in the 0.55 to 3.99 μm range [83]. The emission near 2 μm from the $^5I_7 \rightarrow {}^5I_8$ transition is specially interesting because it belongs to the eye-safe spectral region [84-86]. On the other hand, its emission from the $^5S_2 + {}^5F_4 \rightarrow {}^5I_8$ transition around 0.5 μm is interesting due to the present requirement for short wavelength emitting solid state lasers. Using the holmium ion as an active laser ion, green, blue or red upconversion emission can be obtained in different host materials [87-89].

Europium has a simple energy level structure, where the ground state and the main emitting state are not degenerated which allows using this ion as a probe [90-92]. The emission lines typically occurs from the lowest excited state level ($^5D_0$) to the ground level ^7F_J (where J =0-6). There are transitions associated to the higher levels $^7F_5$ and $^7F_6$, but they are very difficult to detect due to their low intensity [93]. The strongest red emission at ~ 610-620 nm occurs from $^5D_0 \rightarrow {}^7F_2$ transition, which makes this ion interesting in the applications of fluorescent lamps and other optoelectronic devices [94].

1.7. Materials used in this work

In this thesis, we structured by different techniques the surface of crystals of the $KTiOPO_4$ (KTP) family and $LiNbO_3$ crystals. These crystals have received enormous attention in the last four decades, since they show high nonlinear optical behavior, and

have been extensively used for frequency doubling of Nd:YAG laser radiation at 1064 nm, high conversion efficiency, with negligible absorption both at 1064 nm and 532 nm [95,96].

1.7.1. $KTiOPO_4$

KTP crystals have attracted the particular attention of researchers owing to their excellent nonlinear optical properties along with its interesting features:

1. Large nonlinear optical coefficient [97]. (d_{33} ~17.4 pm/V)
2. High laser damage threshold [98]. (~1.5-2.2 GW/cm^2 @11 ns,1064 nm)
3. High electro-optic coefficient [99]. (r_{33} ~ 35 pm/V)
4. Large spectral wavelength range [100]. (0.35- 4.5 μm)
5. Nonhygroscopic, chemically and thermally stable

KTP crystal was first synthesized in 1890 [101] and later its crystal structure was determined by Torjdjman et al belonging to the orthorhombic system with the non-centrosymmetric space group $Pna2_1$ [102]. The unit cell has the following lattice constants $\boldsymbol{a}$ = 12.819 Å, $\boldsymbol{b}$ = 6.399 Å, $\boldsymbol{c}$ = 10.584 Å [103]. However, shortly afterwards large nonlinear susceptibility was discovered in KTP and since then it has been intensively employed for various nonlinear optical processes [104].

Apart from a material to double the frequency of Nd:YAG lasers, KTP is also used in optical parametric amplification systems with high output power, short pulse width, high repetition rate, and excellent operational stability for applications in ultrafast time-resolved spectroscopy [105], nonlinear pulse propagation in optical fibers, and carrier dynamic studies in semiconductors [106]. These crystals are also widely used in many laser applications such as electro-optic modulation [107] and deflection, acousto-optical modulation [108], optical wave guides [109], and integrated optical devices [110].

1.7.2. $RbTiOPO_4$

$RbTiOPO_4$ (RTP) is an isostructural compound to KTP. The lattice parameters of RTP measured by Thomas et al. are $\boldsymbol{a}$ = 12.974 Å, $\boldsymbol{b}$ = 6.494 Å, $\boldsymbol{c}$ = 10.564 Å. RTP was the first discovered isostructural to KTP [110].

RTP crystals present also interesting properties:

1. Large nonlinear optical coefficient [111]. (d_{33}~ 17.1 pm/V)
2. High laser damage threshold [112]. (0.9 GW/cm^2 @ 15 ns, 1064 nm)
3. High electro optic coefficient [111]. (r_{33}~ 36.3 pm/V)
4. Broad spectral width [113] (0.35 – 4.5 µm)
5. Non hygroscopic, chemically and thermally stable

RTP is a good candidate for optical parametric oscillator (OPO) pumped at 1064 nm because its efficiency is comparable to that of KTP. Moreover, RTP absorbs the generated idler wavelength less than KTP, this can be an advantage in the case of high average power operation. Compared with other crystals, RTP can be operated at low voltage in electro-optics applications due to its high electro-optic coefficients and without piezoelectric ringing at high repetition rates [114]. At low switching voltage RTP is important in applications where the power supply has to remain as small as possible like in space applications. The absence of piezoelectric ringing allows Q-switching at frequencies in the 100 kHz range while maintaining short pulse lengths. Finally, RTP proves to be also a good choice for electro-optic Q-switch applications at high repetition rate compared to other materials [115].

1.7.3. $LiNbO_3$

Lithium niobate ($LiNbO_3$) is one of the most used crystalline dielectric materials at the present days in the electronics and optoelectronics industry. It is also important for optical communications, as it is a key material for many types of electro-optic modulators [116].

The interesting properties of $LiNbO_3$ crystal are

1. High nonlinear optical coefficient [117]. (d_{33}~31.5 pm/V)
2. Large optical damage threshold [118]. (0.5-2 GW/cm^2 @ 10 ns, 1064 nm)
3. High electro-optic coefficient [119]. (r_{33} ~31 pm/V @ 633 nm)
4. Broad spectral width [120]. (0.32 – 5 µm)

The structure and properties of $LiNbO_3$ were reported by H. Megaw in 1954 [121]. Its crystalline form is a solid material chemically very stable at room

temperature, that crystallizes in the trigonal system with the non-centrosymmetric space group R3c. The unit cell has the following lattice constants ***a*** = 5.15 Å, ***c*** = 13.864 Å [122].

The broad spectral window of $LiNbO_3$ provides a wide spectral window for photonic applications. The nonlinear optical properties of $LiNbO_3$ have also made it an increasingly popular material for optical frequency conversion. The high second order χ^2 nonlinearities of $LiNbO_3$, have made it possible to demonstrate wave modulators [123], optical switch arrays [124], wavelength converters [125], and tunable mid-IR coherent light sources. The development of periodically poled $LiNbO_3$ and other ferroelectric optical crystals such as KTP or $LiTaO_3$, has enabled the production of visible laser sources, optical parametric oscillators and optical signal processing devices avoiding the light limitations of phase-matching.

1.7.4. Monoclinic potassium double tungstates; $KRE(WO_4)_2$

The choice of the host lattice for the active lanthanide ions determines the distance among the doping ions, their relative spatial position, their coordination numbers, and the type of anions surrounding the dopant. The properties of the host lattice and its interaction with the doping ions therefore have strong influence on the upconversion process.

Monoclinic potassium rare earth double tungstates ($KRE(WO_4)_2$ or KREW, (RE = Yb, Gd) crystallize in the monoclinic system with space group C2/c [126] with unit cell parameters ***a*** = 10.590/10.652 Å, ***b*** = 10.290/10.374 Å, ***c*** = 7.478 /7.582 Å, and β = 130.70/130.80 for KYbW [127] / KGdW [128]. KREW are widely known as hosts for active ions to constitute a solid-state laser material. The advantages of this family of materials is that they can be doped with optical active lanthanide ions even at high concentrations without concentration quenching effects, and that active lanthanide ions show high absorption and emission cross-sections in these matrices [129].

1.7.5. Gd_2O_3

Gadolinium oxide (Gd_2O_3) has two most common structures: monoclinic with space group C2/m and cubic with space group Ia3. We have worked with the last

cubic one, since it is the most stable one at room temperature. There are two types of gadolinium sites in the cubic structure, both with a coordination number of 6 but with different geometry of the surrounding oxygen atoms [130]. Gd_2O_3 is another promising host matrix for upconversion because of its good chemical durability, thermal stability, and low phonon energy (phonon cut off ~600 cm^{-1}). In addition, Gd_2O_3 can be easily doped with active lanthanide ions [131,132].

1.8. The aim of this doctoral thesis

The objectives of this doctoral thesis were divided into two parts. The first part mainly focused on the fabrication and characterization of diffraction gratings on the surface of nonlinear optical materials. The second part was focused on the localized emission of light from luminescent nanoparticles embedded inside the microstructures generated on the surface of the nonlinear optical materials.

Top Seeded Solution Growth-Slow Cooling (TSSG-SC) technique was chosen to grow single crystals of the KTP family (basically KTP and RTP), because these crystals melt incongruently. Ultrafast laser ablation was used to fabricate surface relief diffraction gratings on the surface of these crystals. To have a better understanding of the interaction between ultrafast lasers and matter, a detailed structural characterization of these fabricated diffraction gratings was carried out in this thesis. We also carried out a detailed study of the optical properties of these diffraction gratings.

On the other hand, we also used the selective chemical etching technique to fabricate diffraction gratings on the surface of a periodically poled $LiNbO_3$ crystal that we characterized in the same optical way than previous samples.

To explore the localization of emission of light from luminescent nanoparticles embedded inside microstructures generated on the surface of nonlinear optical materials, we used the sol-gel method to synthesize luminescent nanoparticles of $KYb(WO_4)_2$, $KGd(WO_4)_2$ and Gd_2O_3 doped with Yb^{3+}, Er^{3+}, Tm^{3+}, Ho^{3+} and Eu^{3+}, and we embedded them on the holes fabricated by ultrafast laser ablation on the surface of the KTP crystals. Then, we characterized their luminescent properties using upconversion mechanisms by pumping them at 980 nm to get visible emissions in the red, green, blue and yellow regions of the electromagnetic spectrum.

The structure of this manuscript is the following. The details of the experimental techniques used in this doctoral thesis are described in Chapter 2. In this chapter we summarized the fundamentals and experimental conditions of the techniques we used. The Top Seeded Solution Growth - Slow Cooling method (TSSG-SC) was used for growing RTP and KTP single crystals. The surface relief diffraction gratings were fabricated on the surface of these crystals by ultrafast laser ablation and by the selective chemical etching technique. The structural, characterization was carried out by using X-ray diffraction and by micro-Raman scattering.. The morphology of the samples was investigated by electron microscopy, optical microscopy, and confocal-interferometric microscopic techniques. The diffraction properties of the surface relief diffraction gratings were characterized by FT-IR Bragg diffraction measurements and by diffraction measurements after illuminating them with a laser source at different wavelengths. We also described the sol-gel technique used to synthesize the luminescent nanoparticles and the characterization of these nanoparticles in terms of optical emission through upconversion mechanisms.

In Chapter 3, the results obtained on the crystal growth of KTP and RTP bulk single crystals are described in detail, together with the morphological characterization of the as-grown crystals.

Chapter 4 deals with the fabrication and morphological characterization of the diffraction gratings. The structural changes that the single crystals suffer after ultrafast laser ablation and after thermal annealing are discussed in detail.

Chapter 5 deals with the optical characterization of diffraction gratings inscribed on the surface of the nonlinear optical materials. This chapter begins with the determination of the period of the diffraction gratings by optical means and an analysis of the diffraction of the incident beam as a function of wavelength and polarization. Later we discussed about the determination of shape of the fabricated channels from the diffraction properties of the sample, and we analyzed the diffraction of the second harmonic beam generated by the same samples. Finally, the last section was devoted to characterize the diffractions as 1D photonic crystals.

The synthesis and characterization of luminescent nanoparticles are discussed in chapter 6 together with the characterization of the composites that we formed with

them and the micro-structured nonlinear optical materials. In the first section we analyzed the synthesis of luminescent nanoparticles by the sol-gel process, and their structural characterization, and spectroscopic properties. In the next section, we discussed about the morphological characterization of the as-fabricated microstructured patterns and the preparation of the luminescent nanocomposites by embedding the luminescent nanoparticles in them. Finally, the spectroscopic characterization of these composites is analyzed.

All these chapters have been linked to the research papers we prepared during these four years and that we publish or submit to different international journals or conference proceedings. In these papers, parts of the results obtained are already presented, so we decided not to duplicate their contents in this thesis. For instance, the results of chapter 3 about the conditions of the growth of KTP and RTP bulk single crystals by the TSSG-SC technique have been reported in *papers I-VI*. The results obtained in chapter 4 about the structural and morphological characterization of the diffraction gratings were reported in *papers III, IV, V, VII*. The structural changes that the materials suffer due to the ablation process and annealing or chemical etching processes were reported in *paper VII*. The results presented in chapter 5, regarding the period of the diffraction gratings by optical means and the determination of the shape of the channels were reported in *papers I,II,V*. The diffraction of the second harmonic beam generated by 1D and 2D diffraction gratings were reported in *paper III*. The results represented in chapter 6, about the localization of emission light from embedded luminescent nanoparticles in microstructured KTP single crystals were reported *papers VI, IX*. Finally, the interparticle energy transfer among oxide luminescent nanocomposites through the energy migration upconversion mechanism was reported in *paper VIII*.

CHAPTER TWO

Experimental Techniques

In the present chapter, the experimental techniques used in this work are described. An overview of the basis and the description of the procedure involved in each experimental technique and equipments are presented. These can be classified in to two groups: (i) the techniques used for the fabrication of diffraction gratings and photonic composites and (ii) different techniques to characterize these diffraction gratings and photonic composites. In the first part of this chapter, the single crystal growth (Top Seeded Solution Growth, TSSG, from high temperature solutions), the cut and polishing of bulk single crystals, the ultrafast laser ablation, the selective chemical etching and the synthesis of nanoparticles are described. In the second part, the structure analysis (X-ray diffraction, micro-Raman scattering), morphology analysis (Confocal microscopy, Environmental Scanning Electron Microscopy, Transmission Electron Microscopy, Atomic Force Microscopy), spectroscopic characterization (optical absorption and transmission, Fourier Transform Infra Red spectroscopy), and diffraction analysis will be described.

2.1. Crystal Growth of bulk single crystals by the TSSG Method

2.1.1. Fundamentals

The Top-Seeded Solution Growth (TSSG) method is one of the methods included in the high temperature solution (HTS) techniques for the growth of bulk single crystals. The important advantage of crystal growth from high temperature solutions, or flux growth, that is another way to name this growth technique, is that it allows crystals to grow below their melting temperatures [133]. These methods have to be used when crystals melt incongruently or when there exists a phase transition below their melting temperature [134]. These methods can also be used when the crystals melt at very high temperatures [135]. The crystal growth process by high temperature TSSG – Slow Cooling (TSSG-SC) method is based on the concepts of solubility and supersaturation. At a given temperature, a limited amount of a substance dissolves in a particular solvent. The amount dissolved defines the solubility at that temperature. The supersaturation refers that the solution contains more dissolved solute than is predicted by the solubility limit without precipitation of the solute. The TSSG technique cannot be used at room temperature because the solvent solidifies at room temperature. So that, high temperature solution methods must be used when the materials suffer from polymorphic transitions below crystallization temperature or when they melt at high temperatures.

The key issues for growing bulk single crystals by the Top Seeded Solution Growth method are:

1. Selection of the correct flux composition for the single crystal to be grown: structural, thermal, and optical properties that have to be accomplished by the solvent
2. Effective homogenization of the solution should be achieved, ideally, by increasing temperature.
3. Optimized hydrodynamic conditions for mass transport and controlled growth of a crystal can be achieved, for instance by suitable seed rotation, which helps to keep the melt blended when the crystal is growing and to maintain the same temperature at the crystallization front, which will depend on the temperature gradient in the solution.

4. Temperature gradient inside the solution is an important parameter for the growth of the crystal. If the gradient is not high enough it may produce spurious crystallization in areas of the solution out of the crystal seed. Larger temperature gradients may lead to crystal redisolution or cracking.
5. Growth experiments have to be performed with the knowledge of the appropriate solubility data. The driving force for high temperature solution growth is supersaturation of the solution. This supersaturation can be created by slow cooling of the solution, by evaporation of the solvent or by increasing the solute concentration at constant temperature.

To obtain single crystals with large dimensions, and to improve the quality of the grown crystals, a rotation, and pulling of the growing crystals out of the solution can be applied, which enhance mass transport conditions in the solution and avoid supersaturation gradients. The TSSG-SC method has several advantages compared with other growth techniques such as the Czochralski, Bridgman, and hydrothermal methods, since crystals can be grown in a fluid with a lower viscosity than the melt, and most importantly, thermal strain is minimized due to the relatively low growth temperature, the much smaller thermal gradients used in these methods compared with classical methods based on growth from melts, and the free growth into a liquid. So that, these factors make this method proceed to grow crystals near thermodynamic equilibrium conditions, in a way that minimizes the superficial energy, developing facets.

The disadvantage of this method is that it uses of low growth rates, in general hundreds of times slower than the growth rates used in melt based growth methods. Along with this, the difference in linear growth rates among the different faces of the crystal, which lead to chemical and structural inhomogeneities in the crystal, hampers the industrial production of crystals grown from high temperature solution methods. However, this technique has a great deal of interest in the field of solid state technologies, mainly in microelectronics and optoelectronic device applications.

2.1.2. Experimental set-up

Figure 2.1 shows the schematic representation and the picture of the system used to grow KTP and RTP single crystals by using the TSSG-SC method. It includes

a single-thermal-zone vertical tubular furnace, the crystal seed attach, rotation, and pulling systems, the crucible and its support, and the temperature controller/programmer. The heat is produced by a Kanthal resistance heating wire which is rolled around an alumina tube. The whole system is thermally insulated from the environment by means of insulator refractory bricks of alumina and an external metallic steel cover that can also be seen in the cross section of the furnace provided in the schematic representation. The temperature in the furnace is measured with an S-type thermocouple Pt/Pt-Rh 10% (partially protected by covering it with an alumina tube) and placed near the resistances of the central zone of the furnace to guarantee a reliable and stable measurement. The temperature in the furnace is controlled by a Eurotherm 903 controller/programmer that allows to control the temperature with a precision of 0.01 K. It is connected to a thyristor that controls the power of the furnace.

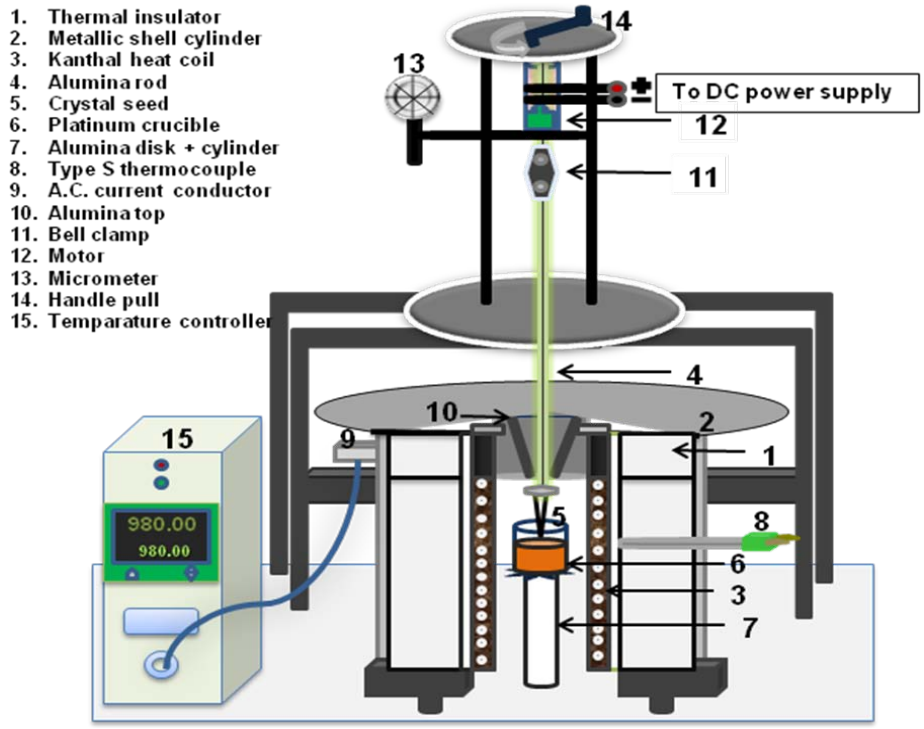

Figure 2.1. *Schematic view of the verticular tubular furnace used in the bulk single crystal growth experiments.*

The mechanical part of the growth device, which consists of a series of high-precision mechanisms attached to two different stepper motors and a bell clamp, are placed above the furnace, and supports, vertically displaces, and rotates the crystal seed during the crystal growth process. It comprises a vertical metal structure that is extremely rigid and stable from which an alumina rod is hung. The speed of rotation and the speed of pulling can be modified according to the voltage provided by the power source. The seed is attached to a platinum holder, which is also attached to an alumina rod, both which are laced with thin platinum wire. The attach system can be moved up and down to locate the crystal seed precisely in contact with the surface of the solution. This movement can be monitored with a micrometric comparer for better precision with an accuracy of 0.01 mm.

To identify the best location for the crucible filled with the solution inside the furnace, an alumina rod, which can be manually handled upwards and downwards, was used to place the crucible at the right position.

The temperature profile of the solution in the furnace is shown in Figure 2.2. When the platinum crucible filled with the solution is located inside the furnace, the thermal gradient of the solution must be measured and optimized to assure a suitable thermal gradient in the solution while keeping the surface of the solution colder than the bottom of the crucible. This can be achieved by adjusting the height of the crucible support to place it in the right thermal zone of the furnace.

The experimental procedure followed in this work for growing bulk single crystals by the TSSG-SC technique is the result of previous works carried out at the Physics and Crystallography of Materials and Nanomaterials, FiCMA-FiCNA, group of the Universitat Rovira i Virgili, URV, in Tarragona.

2.1.3. Experimental procedure

For the TSSG-SC growth process, it is very important to have an accurate knowledge of saturation temperature (T_s), that is the temperature below which the crystal starts to grow. The solution should be homogenized before starting to determine T_s. The saturation temperature can be defined as the highest temperature at which the seed crystal remains undissolved, and the lowest temperature at which no spontaneous nucleation occurs. To have an estimation of T_s, nucleation on a Pt wire can be analyzed. To obtain the desired orientation of the crystal, the crystal seed has

to be selected with the same structure of the material to be grown before introducing into the solution, so that the substance precipitating from the solution grows around the seed crystal to form a larger single crystal keeping the crystallographic orientation of the seed. The crystal seed should be placed at the coldest point of the solution on the surface of the solution just at the centre of the platinum crucible. The temperature profile of the solution inside the furnace is shown in Figure 2.2.

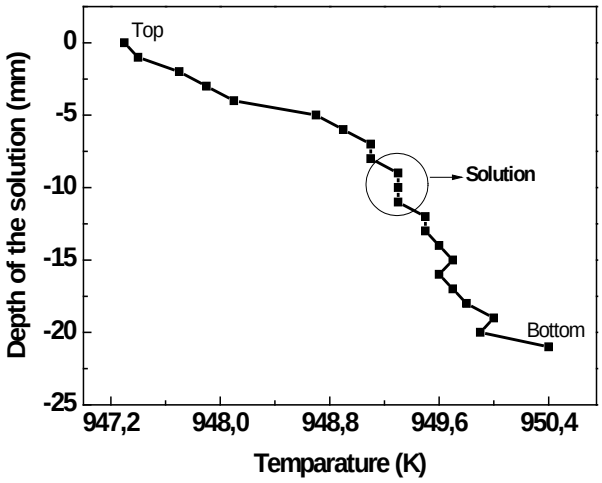

Figure 2.2. *Temperature profile of the solution inside the furnace*

If the growth process is started at $T>T_s$, The crystal seed will dissolve and will lose contact with the solution. If the growth process is started at $T<T_s$, the spontaneous nucleation and growth will prevail over the top-seeded growth, resulting in numerous small crystals visible on the surface of the molten system. The saturation temperature T_s, can be determined precisely by placing the seed in contact with the surface of the solution and controlling the temperature at which neither growth nor dissolution of the seed is observed. The best way to do that is, by using a starting temperature T above T_s and then decrease the temperature until T_s is reached, in other words, only dissolution of the crystal seed should be observed before reaching T_s. In this way, it allows to dissolve the outer layer of the crystal seed, thus the crystal growth process can proceed from a structure with less crystal defects. The growth/dissolution of the crystal seed is controlled with an accuracy of ~10 μm with a Mitutoyo micrometer comparer fixed at the mechanical structure of the furnace that allows vertical travelling of the rod, which supports the crystal seed (see in figure 2.1).

After determining the T_s, the seed is placed in contact with the surface of the solution and a rotation of the seed over its axis is applied. Later the slow cooling of the solution is applied to create supersaturation in the solution. From T_s, the temperature is decreased by 15 K typically at a rate of 0.1 $K \cdot h^{-1}$. To obtain single crystals with larger sizes the interval of cooling can be increased and a pulling rate can also be applied during the crystal growth process. In the case of our growth experiments the crystals were pulled up of 0.5 mm after every 12 h from the surface of the solution during the crystal growth. The mixing of the solution must be good in order to maintain a good homogenisation of the solution and to obtain macroscopic defect free crystal. When the slow cooling programme is finished, the grown crystal is extracted slowly from the solution, 1 mm every 5 min in our case, and placed slightly above the surface of the solution. Then, the furnace is cooled down to room temperature at 15 $K \cdot h^{-1}$.

As the typical growth period runs for a couple of weeks, the ability to observe the quality of the growing crystal can lead to substantial saving of system run time since it allows to decide to abort a growth run that has been spoiled by spontaneous nucleation.

2.2. Cutting and polishing of crystals

To prepare the samples for the fabrication and characterization of diffraction gratings, and laser phosphor displays, the KTP and RTP single crystals were crystallographically oriented, cut and polished.

Prior to cut the crystals, they should be free of defects and seed fragments. To do this, the crystal is fixed to a sample holder with wax. The lapping of the undesirable zone of the crystal was made with a polishing machine Logitech PM5. The face of the crystal with the seed was lapped with alumina powder of 9 µm (hardness~7 mohs), followed by a smooth polishing with 1 µm alumina powder. After removing the origin of the seed and surrounding defects, the crystal was placed on a goniometer and oriented with the desirable direction to cut the KTP and RTP substrates. This was done by using a Minitom Struers Accutom diamond disk saw. The diameter and thickness of the disk were 75 mm and 0.125 mm, respectively. As a reference to correctly orient the crystals, we used their morphology. The morphology of the crystals was discussed in detail in chapter 3. Finally, the samples were polished

in the Logitech PM5 polisher with an oscillatory arm. This enables accurately rotate and pressurise the samples depending on the hardness of the material to be polished. Figure 2.3 (a) and (b) show that the used diamond saw and Logitech PM5 polisher for cutting and polishing the crystals, respectively. As abrasive substances, alumina powders with grain size of 9, 3, 1 and 0.3 µm were used.

The final quality of the polishing was measured using parameters such as roughness, flatness and parallelism. The roughness (rms) ~ 50 nm and flatness ~ 14 m values of the samples were measured by confocal optical imaging profiler (see section 2.7.1) through an extended profile measurement.

(a) (b)

Figure 2.3. *Images of (a) the diamond disk saw and (b) the Logitech PM5 polisher used in this work*

The parallelism was measured by self-collimator, between opposite faces of the sample using the two reflections on the opposite faces of the sample. These equipments were available at Physics and Crystallography of Materials and Nanomaterials, FiCMA-FiCNA, group of the Universitat Rovira i Virgili, URV, in Tarragona.

2.3. Synthesis of the luminescent nanoparticles

2.3.1. Sol-Gel: the modified Pechini method

Sol gel technology is a typical nanotechnology process because all gel products may contain nanoparticles or nanocomposites [136]. In this sense it plays a principal role in the development of modern nanotechnology for the preparation of new materials. The modified Pechini method is used to synthesize potassium-rare earth tungstates ($KRE(WO_4)_2$ or KREW), and Gd_2O_3 nanoparticles. Stoichiometric amounts of the oxides of the elements contained in the nanoparticles were first converted to their nitrate forms by dissolution in concentrated HNO_3. Later the excess

of HNO_3 was evaporated to obtain nitrate precipitates by slow heating. In the next step, the tungstates, and an aqueous solution of ethylenediaminetetraacetic acid (EDTA), used as the chelating agent in a specific molar ratio (C_M) to prepare metal-EDTA complexes, were mixed and added to them to nitrate precipitates. The molar ratio C_M was defined as

$$C_M = \frac{[EDTA]}{[METAL]} \qquad \text{Eq. 2.1}$$

which describes the degree of the chelation process of the metal in the organic product. Afterwards, ethylene glycol (EG), the sterification agent was added in molar ratio (C_E), which describes the degree of sterification between the chelating agent and the ethylene glycol:

$$C_E = \frac{[EDTA]}{[EG]} \qquad \text{Eq. 2.2}$$

In this process, the molar ratios of C_M and C_E are used in the ratio of 2:1, respectively. The resulting solution was heated slowly to obtain the precursor resin, which is rigid polyster net that reduces any segregation of metals. The following stage is the two step calcinations procedure using furnace.

1. Calcination at 573 K for 3 hours, during which the precursor resin decomposes to provide the precursor powder.
2. The calcinations procedure depends on the nanocrystals. Each material was calcined at a certain temperature and for a particular length of time in accordance with the previous studies.

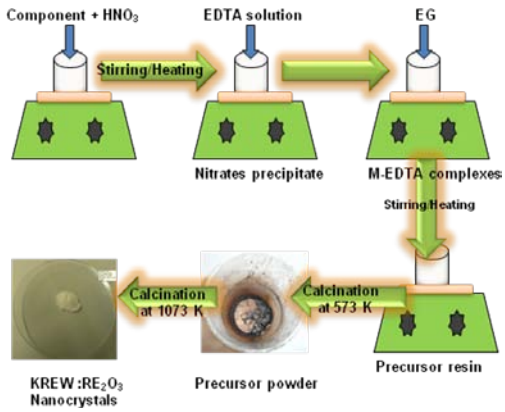

Figure 2.4. *Schematic diagram of the synthesis method used to obtain nanoparticles of luminescent by the sol-gel Pechini method*

The schematic view of the synthesis of nanoparticles by modified sol-ge pechini method is shown in Figure 2.4.

2.4. Deposition of metallic nanoparticles

The radio frequency (RF) sputtering technique was used to deposit the metallic nanoparticles on the surface of the diffraction gratings. RF sputtering involves running an energetic wave in the radio frequency range through an inert gas to create positive ions. The target material is stuck by these ions and broken up into a fine spray that covers the substrate. During RF sputtering process, the target material, substrate, and RF electrodes are located in a vaccum chamber. Then, the inert gas, which is usually argon gas depending on the size of the target material´s molecules, is directed into the chamber. The RF power source is then turned on, sending radio waves through the plasma to ionize the gas atoms. Once the ions begin to contact the target material, it is broken into small pieces that travel to the substrate and begin to form deposition. RF sputtering systems require higher powers and lower pressures when compared to other sputtering methods, such as DC sputtering. This allows for fewer collisions between the target material particles and the gas ions, creating a more direct pathway for the particles to travel to the substrate material. The combination of this decreased pressure, along with the method of using radio waves instead of direct current for the power source, makes RF sputtering ideal for target materials that have insulating qualities.

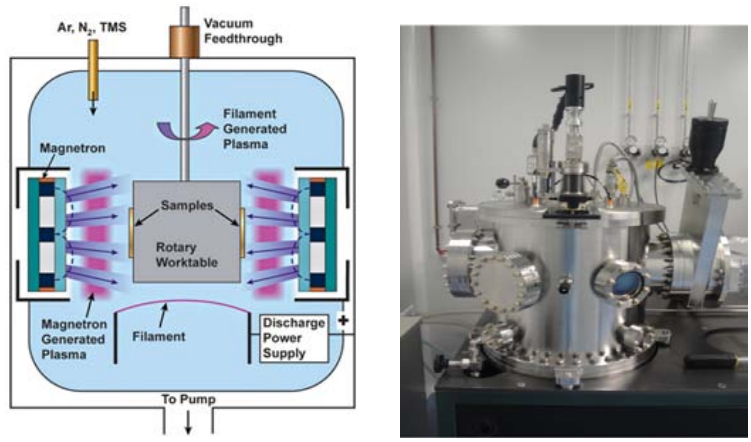

(a) (b)

Figure 2.5. *(a) Schematic view of the RF sputtering equipment and (b) image of the used equipment of RF sputtering*

In this work, we used RF sputtering system (AJA Intrnational, Inc. ORION-8-HV model) to deposit the metallic gold nanoparticles on the surface of the KTP microstructures at a pressure of 3 mTorr and a power of 75 W during 15 sec. The schematic view and the image of the used equipment are shown in Figure 2.5. This equipment is available at the Servei de Recursos Cientifico i Tecnics, Universitat Rovira i Virigili.

2.5. Techniques for the structuration of the surface of nonlinear optical materials

2.5.1. Ultrafast laser ablation

The rapid advances in the generation and amplification of ultrashort pulses have opened up many new possibilities in laser-matter interaction and materials processing [137]. The extreme short pulse width also makes it easy to achieve very high peak laser intensity with low pulse energies. Recently, micro-fabrication of materials, including metals, ceramics, glasses, plastics, and crystals has been achieved using focused ultrashort laser pulses [138-141]. This technique is a versatile tool for inducing microstructures and a possible way to perfect the laser micro-processing of ultra hard materials, that lead to a notable improvement in technological developments. The technological potential of ultrashort laser pulses is based primarily on localization of energy, minimizing the thermal damage to the materials.

Ultrafast laser ablation compared with traditional fabrication techniques such as lithographic techniques, or electron beam writing, has a number of advantages: (i) it uses simpler and less expensive device production equipment, avoiding photolithography and clean room facilities; (ii) it enables rapid prototyping, since the device pattern can be easily changed by simple software control, with sufficient cost reduction with respect to standard techniques using photolithographic steps and requiring the production of a mask; (iii) it is intrinsically a three-dimensional (3D) technique, since refractive index changes can be induced in any point in the bulk material within the given depth (10 μm – 10 mm) from the surface; this capability can be exploited to implement novel device functionalities which are impossible with standard fabrication techniques [142]. These features are extremely attractive for various applications, such as micro-fabrication of polymeric materials,

structuring of dielectric materials and metallic surfaces, and laser treatment of biological tissues.

The processing of dielectric materials by ultrashort pulses is a topic of intense investigations for at least two reasons. The first one is that short pulses excitation appears to be a valuable tool for efficient and well controlled material removal and modification of material properties such as the refractive index. Second, understanding the interaction of ultrashort pulses with high band gap materials requires a good description of physical mechanisms involved, such as strong field excitation, multiphoton ionization, and charge/heat diffusion in lattice. These mechanisms have been discussed in detail in chapter 1. The schematic view of the equipment we used for ultrafast laser ablation experiments is shown in Figure 2.6, together with a picture of it.

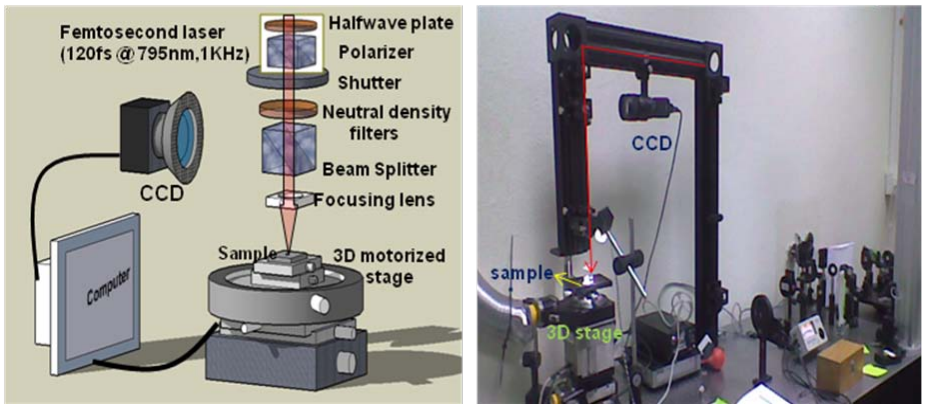

(a) (b)

Figure 2.6. *(a) Schematic view of the ultrafast laser ablation set-up used in our experiments and (b) a picture of the same equipment.*

The ultrafast laser ablation set-up we used comprises a halfwave plate, a polarizer, and neutral density filters to reduce the intensity of the laser pulses before the focusing lens. We used a commercial Ti:Sapphire oscillator (Tsunami, Spectra Physics) and a regenerative amplifier system (Spitfire, Spectra Physics) based on chirped pulse amplification (CPA) for the fabrication of 1D and 2D diffraction gratings on RTP and KTP crystals. This femtosecond laser system is available at the Centro de láseres pulsados, ultra cortos, ultra intensos (CLPU), Salamanca (Spain). The system delivers linearly polarized 120 femtosecond pulses at a wavelength of 795 nm with a repetition rate of 1 kHz. The sample was placed on a motorized 3D

translation stage in order to achieve optimal focussing on the surface of the target. One dimensional (1D) and two dimensional (2D) diffraction gratings were fabricated on the surface of KTP and RTP samples. The details of the experimental conditions were given in *paper I-V*.

2.5.2. Selective chemical etching

Chemical etching is a simple and widely used technique to reveal the domain structure in ferroelectric materials. Etching techniques are required for a reliable fabrication of deep (micro and sub-micrometer) structures or straight walled structures [143]. The existing etching methods can be classified into two categories: wet (chemical) etching and dry (ion) etching. In ferroelectric materials, such as LiNbO3, and in crystals of the KTP family ferroelectric domains can be visualized these micro-structures can be fabricated by wet chemical etching [144,145]. Ferroelectric domains of opposite spontaneous polarization present different etching speeds when dipped in some acid mixtures [146]. This property has been used to reveal the domain pattern at the surface of periodically poled crystals [147]. The selective chemical etching process provides further capabilities for versatile surface engineering of domain engineered crystals, allowing the production of deep, high aspect ratio structures, with side walls that can be extremely smooth [148].

Wet chemical etching of periodically poled LiNbO3 crystals at room temperature, is generally performed in a 1:2 ratio molar weight of hydrofluoric (HF) and nitric (HNO_3) acid [144]. The molten KOH: KNO_3 2:1 M ratio mixtures have been extensively studied for this purpose in crystals of the KTP family [145]. In both cases, the corresponding etchants selectively attacks the negative (001) face of the crystal at etch rates of around 1 $\mu m.h^{-1}$ while the positive (001) face is left relatively unetched and the used temparture around 363 K.

The chemical etching is a key technique to fabricate smooth patterning structures on the surface of ferroelectric materials compared with the structures fabricated from the laser assisted patterning methods. In this thesis, the ultrafast laser ablation was used to fabricate relief structures on the surface of KTP and RTP samples. In these relief patterned structures, a high roughness was observed. So that, we used chemical etching to reduce the roughness of these structures.

More recently, the fabrication of periodic 1D and 2D surface structures in congruent $LiNbO_3$ by periodic electric field poling and selective wet chemical etching under appropriate conditions have also been reported with feature sizes and periods down to submicron and nanoscale range [149-151]. The list of etchants and the experimental conditions used are shown in Table 2.1.

Table 2.1. *The list of etchants and experimental conditions*

Sample	**Etchant (2:1)(M)**	**Temperature (K)**
$LiNbO_3$	HNO_3:HF	368
RTP	KOH:KNO_3	353

2.6. Structural characterization

X-ray diffraction is a non-destructive analytical technique which provides detailed information about the structure of crystalline substances, including unit cell dimensions. An X-ray diffractometer consists of three basic elements such as the X-ray tube, the sample holder, and an X-ray detector. The schematic view of the X-ray diffractometer and the set-up used in this work are shown in Figure 2.7.

X-ray diffraction is based on constructive intererference of monochromatic X-rays and a crystalline sample. These X-rays are generated by a cathode ray tube, filtered to produce monochromatic radiation, collimated to concentrate it, and direct it towards the sample. The interaction of the incident rays with the sample produces constructive interference (and thus a diffracted ray) when conditions satisfy Bragg´s law

$$2d \sin\theta = n\lambda \qquad \text{Eq. 2.3}$$

This law correlates the wavelength of the X-rays (λ) to the diffraction angle (2θ) and the lattice spacing (d) in a crystalline sample. Diffracted waves from different atoms can interfere with each other and the resultant intensity distribution is strongly modulated by this interaction. The powder X-ray diffraction is most widely used X-ray diffraction technique for characterizing materials. The sample is usually in a powdery form, consisting of fine grains of single crystalline material. The term

powder means that the crystalline domains are randomly oriented in the sample. This technique can be used when the powder size is below1000 Å. The diffraction pattern consists concentric rings with different intensities corresponding to the diffraction of various d spacings in the crystal lattice. The positions and intensities of the peaks are used for identifying the underlying structure or phase of the material. The peaks in an X-ray diffraction pattern are directly related to the atomic distances.

Bruker-AXS D8-Discover diffractometer equipped with an open Euler ring working with Schulz geometry with parallel incident beam (Gobel mirror) and a vertical goniometer. The system was also equipped with a collimator for the X-ray beam of 500 µm and a General Area Detector Diffraction System (GADDS) detector. The GADDS detector was 30 × 30 cm^2 with a 1024 × 1024 pixel CCD detector. Cu (λ = 1.54056 Å) radiation was obtained from a copper X-ray tube operated at 40 kV and 5 mA. The X-ray diffraction pattern of the samples studied in this work were obtained using the K_α line of copper available at the Servei de Recursos Cientifics i Tecnics, Universitat Rovira i Virgili, Tarragona. This system works with the Bragg-Brentano parafocusing geometry and a θ-θ configuration. As represented in Figure 2.7 (a), the source and the detector move synchronously, always symmetrically, where as the sample is kept fixed. To obtain the pattern of reflection from all possible planes of the sample, the θ angle of the source and the detector is varied.

In this work, the first step after cutting and polishing the crystal substrates of KTP and RTP samples, was the verification of the orientation of the desired crystallographic plane by powder X-ray diffraction.

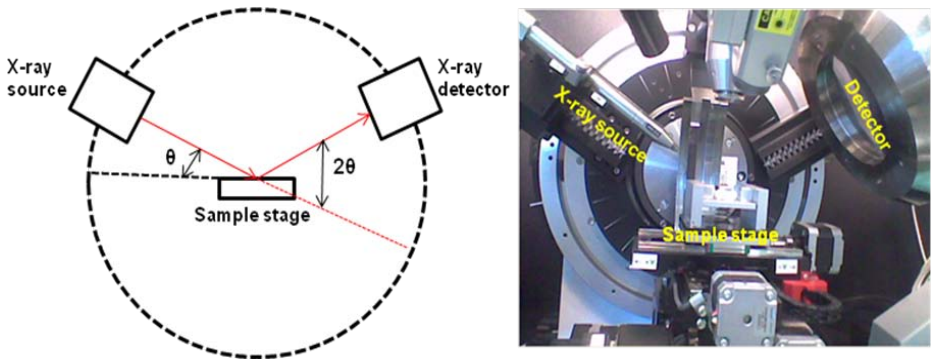

(a) (b)

Figure 2.7*. (a) schematic view of X-ray diffractometer (b) X-ray diffractometer*

First, a 2θ scan was recorded on the samples in order to check the orientation of the substrate. The orientation of the sample is defined by three angles with respect to the diffraction plane: the complementary incident angle (ω), the rotation angle between the intersection of the plane of the sample and the plane of the diffraction (χ), and the rotation angle around the normal axis to the plane of the sample (φ). Data were recorded in three different steps with the area detector by performing ω-scan with a frame width of 15º in the θ range in between 5-45º with an integration time of 60 s/frame.

2.7. Microscopic Characterization Techniques

2.7.1. Confocal profilometry

Confocal imaging profilers have been used in the non contact surface metrologyfield. They are both capable of accurately and reliably measuring surface topographies on the scale millimetres to nanometres. In a confocal microscope the light coming from the light source crosses a pinhole, where it is divided in many rays. This set of beams is reflected by a beam splitter towards the objective lens which is located upon the sample. Each light ray transmitted by the objective arrives at the surface of the sample in different points located at different heights (due to the topography of the sample´s surface). The plane that contains the surface of the sample, and that is simultaneously perpendicular to the beam, is called the focal plane, thus, many focal planes exist, as beams may that arrive to the sample. Every focal plane reflects the light, which again crosses the objective lens and the dichoric mirror until it reaches the detector pinhole.

The schematic view of a confocal microscope is shown in Figure 2.8. Those rays coming from the different focal planes that are focused just before the detector pinhole are called the in-focus light rays (i.e. confocal). Thus only the in-focus light rays can pass through the pinhole before reaching the detector. The sample is scanned vertically (z-direction) in steps so that the light rays arising from the different focal planes of the sample passes through the lens.

For the purposes of this work a Sensofar PLμ2300 optical imaging profiler that can also be used as microscope was employed mainly for:

1. Inspection of the surface quality, by means of optical images and topographies. by taking extended profiles of the as fabricated diffraction gratings

2. Groove depth and width measurements by either extended profiles or extended topographies.

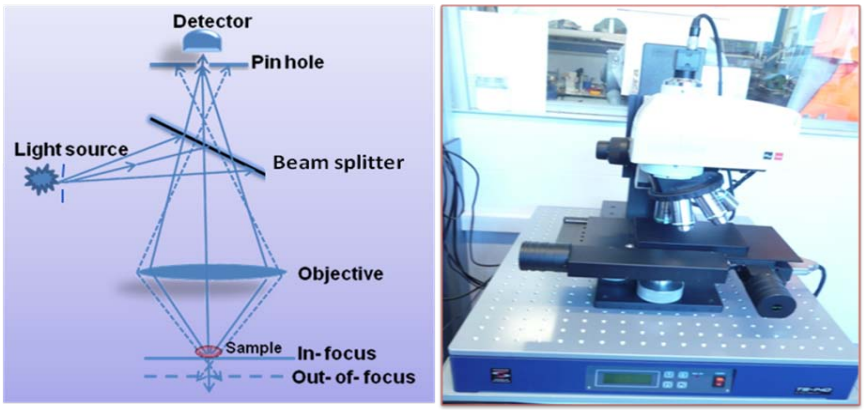

(a) (b)

Figure 2.8. *(a) Schematic view and (b) picture of the confocal microscope used in this work.*

This equipment is available at the Physics and Crystallography of Materials and Nanomaterials, (FiCMA-FiCNA) group of the Universitat Rovira i Virgili (URV), in Tarragona.

2.7.2. Environmental Scanning Electron Microscopy (ESEM)

The scanning electron microscope (SEM) uses a focussed beam of high-energy electrons to generate a variety of signals at the surface of solid specimens to reveal information about the sample including external morphology and chemical composition. These signals include secondary electrons, back-scattered electrons and X-rays. In this work we used secondary and back-scattered electrons for imaging samples depending on the requirement. The secondary electrons are sample atom electrons that they can can be ejected by interactions with the primary electrons of the beam.

Back-scattered electrons are primary beam electrons that have been scattered back out of the sample by elastic collisions with the nuclei of sample atoms and an

energetic electrons of the beam scatters an inner shell electron from the sample. The secondary electrons are most valuable due to their lower energy for showing high resolution images of morphology and topography on samples while back-scattered electrons are most valuable due to their higher energies for illustrating contrasts in composition in multiphase samples.

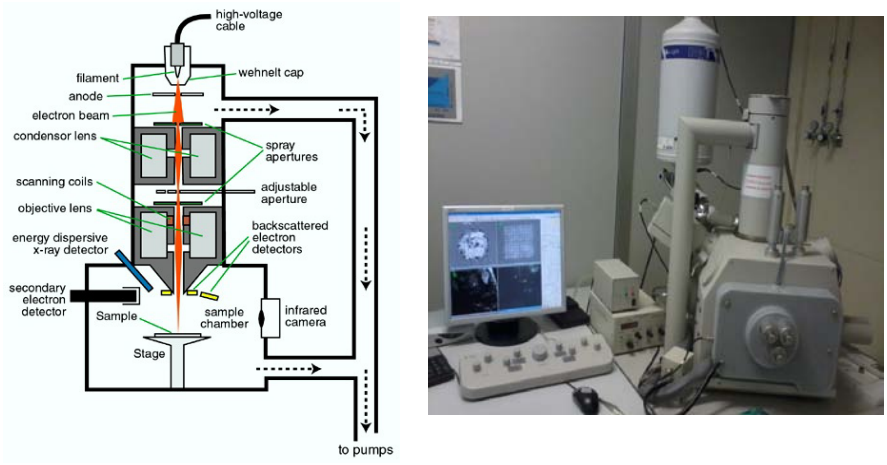

(a) (b)

***Figure 2.9**. Environmental Scanning electron microscope (a) Schematic view (b) the used equipment*

In this study we used an Environmental Scanning Electron Microscopy (ESEM) FEI QUANTA 600. The schematic view of the ESEM and image of the used equipment are shown in Figure 2.9. This technique is very similar to standard SEM but contains a low pressure of gas in the sample chamber, where the primary electrons travel across the gas phase and interact with the surface of the sample, which release secondary electrons that interact with the gas phase producing additional secondary electrons. The primary electrons interact with the gas molecules producing ions and additional electrons. In this way, the gas phase function as an amplifier of the electron signal from the sample. The ESEM retains all of the performance advantages of a conventional SEM. One main advantage of using ESEM is that it is not necessary to cover the nonconductive samples with a conductor medium, such as gold or silver, and their original characteristics can be observed for further manipulation. The ESEM can image wet, dirty and oily samples. The contaminants do not damage or degrade

the image quality. It eliminates the need of sample preparation, particularly the need for conductive coating, makes it possible to investigate specimen in dynamic processes, such as tension, compression, heating, cooling, melting and sublimation. We used 60 mTorr low pressure vacuum at 20 kV. This system is available at the Servei de Recursos Cientifics i Tecnics, Universitat Rovira i Virgili, Tarragona.

2.7.3. Transmission Electron Microscopy (TEM)

The transmission electron microscopy (TEM) is microscopy a technique where a beam of electrons is transmitted through an ultra thin specimen, interacting with the specimen as it passes through. An image is formed from the interaction of the electrons transmitted through the specimen; the image is magnified and focused onto an imaging device, such as a fluorescent screen, on a layer of photographic film, or to be detected by a sensor such as a CCD camera. The main use of this technique is to examine the specimen structure, composition or properties of sub-microscopic details so that this technique is significantly involved in numerous fields such as material science, chemistry, biological components etc.

Figure 2.10 shows the schematic view of the TEM set-up and a picture of the equipment we used in this work. The TEM utilizes a focused beam of electrons instead of light, which increases greatly the resolving capabilities. In this TEM system, there are essentially three types of lenses used to obtain the final image. These are condenser, objective, and projector lenses. The function of condenser lenses is to concentrate and focus the beam of electrons coming from the filament on to a sample to a uniformly illuminate it. The objective lens and its associated apertures are the heart of the TEM. These are used to form the initial enlarged image of the illuminated portion of the specimen in a plane that is suitable for further enlargement by the projector lens. When the electrons pass through the sample, some electrons are passed through the dense atoms in the sample and only some deflected. These scattered electrons generally make their way down in the column and contribute to the image. So, in order to eliminate these scattered electrons to form the image, an aperture is placed at the objective lens. Smaller apertures are used to deviate those electrons to form the image. Finally the projector lens is used to magnify the image on the phosphor screen. For higher magnifications the intermediate lenses can also be

used to obtain an image. TEM produces high resolution with two dimensional images at a maximum potential magnification of 1 nm resolution.

(a) (b)

Figure. 2.10. *Transmission electron microscope system (a) schematic view and (b) picture of the used TEM equipment*

TEMs offer the most powerful magnification with high quality images, and provide information on element and compound structure. These are able to yield information of surface features, shape, size and structure. However, TEM has some disadvantages compare with conventional microscopy techniques. TEMs are more expensive systems and require a laborious sample preparation. It needs high vacuum to operate and samples are limited to those that are transparent to electrons, able to tolerate the vacuum chamber and small enough to fit in the chamber. In our present study we used a JEOL model-1011 TEM equipment with a current accelerating voltage of 100kV. This equipment is available at the Servei de Recursos Cientifics i Tecnics, Universitat Rovira i Virgili, Tarragona.

2.7.4. Atomic Force Microscopy (AFM)

The Atomic Force Microscope (AFM) is one of about two dozen types of scanned-proximity probe microscopes. All of these microscopes work by measuring a

local property, such as height, optical absorption or magnetism, with a probe or tip placed very close to the sample. The concept of resolution in AFM is different from radiation-based microscopes because AFM imaging is three dimensional. AFM can achieve a resolution of 10 pm and, unlike electron microscopes, it can image samples in both air and in liquids.

The principle behind AFM is very simple. A sharp tip is scanned over a surface with feed back mechanisms that enable the piezo-electric scanners to maintain the tip at a constant force (to obtain height information) or height (to obtain force information) above the sample surface. AFM operates by measuring attractive or repulsive forces between the tip and the sample. In its repulsive mode the AFM measures the local sample height. In its attractive or non-contact mode the AFM derives topographic images from measurements of attractive forces although the tip does not touch the sample. The schematic view of an AFM system and a picture of the equipment we used are shown in Figure 2.11.

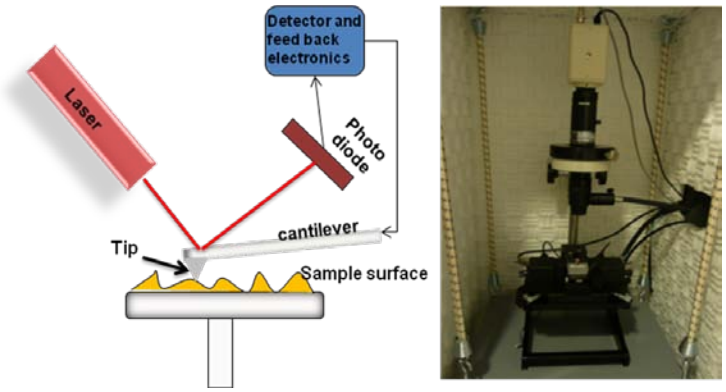

(a) (b)

Figure 2.11. *Atomic force microscope (a) schematic view of the system (b) image of the used AFM equipment*

The tapping mode overcomes problems caused by friction, adhesion, electrostatic forces and others of conventional AFM scanning methods by alternatively putting the tip contact with the surface to provide high resolution, and then lifting the tip off the surface to avoid dragging it across the surface. This mode allows high-resolution topographic imaging of sample surfaces that are easily damaged, loosely held to their substrate or difficult to image by other AFM techniques.

Unlike SEM, AFM provides extraordinary topographic contrast, direct height measurements and unobscured views of surface features. In this work, we used a Pico SPM II (Pico+) AFM equipment to characterize the topography and side walls height of the channels of the chemically etched $LiNbO_3$ sample, with the scanning speed of the tip at 0.5 µm/sec, 0 V sample bias, 20% gain and 1.376 V set point voltage. This is available at Servei de Recursos Cientifics i Tecnics, Universitat Rovira i Virgili. Tarragona.

2.8. Spectroscopic Techniques

2.8.1. Optical absorption and transmission measurements

Absorption is the energy extracted from the electromagnetic wave and transformed into another type of energy when the electromagnetic wave passes through the material. The information about the material properties, such as absorption and transmission, can be obtained when a material interacts with an electromagnetic radiation. When a beam of light (photons) is incident on a material, the intensity of light is expressed by the Lambort´s- Beer law [152, 153].

$$I = I_0 \exp(-\alpha t) \qquad \text{Eq. 2.4}$$

Where I_0 is the intensity of the incident light before passing through the material, t is the thickness of the material, I is the intensity of transmitted light through the material, and α is the absorption coefficient.

The optical density (OD) of the sample is measured by a double ray spectrophotometer as a function of wavelength λ. The OD is given by

$$OD = -\log(I/I_0) = \log(I_0/I) \qquad \text{Eq. 2.5}$$

Using the Equations (2.4) and (2.5), α can be expressed as

$$\alpha = OD\left(\frac{1}{d \log_e}\right) \qquad \text{Eq. 2.6}$$

Since α depends on the concentration of the absorbent centres, a more convenient parameter for describing the absorption process is the absorption cross-section (σ_{abs}). Then the absorption coefficient α can be correlated with the absorption corss-section by

$$\alpha = \sigma_{abs} \, N \qquad \text{Eq. 2.7}$$

where N is the density of absorbent centres. In this expression, α is given in cm^{-1}, N in atoms; cm^{-3} and σ_{abs} has units of atoms; cm^2 or simply cm^2.

Transmission is the property of a substance to permit the passage of light, with some or none of the incident light being absorbed in the process. If some light is absorbed by the substance, then the transmitted light will be a combination of the wavelengths of the light that were transmitted and not absorbed.

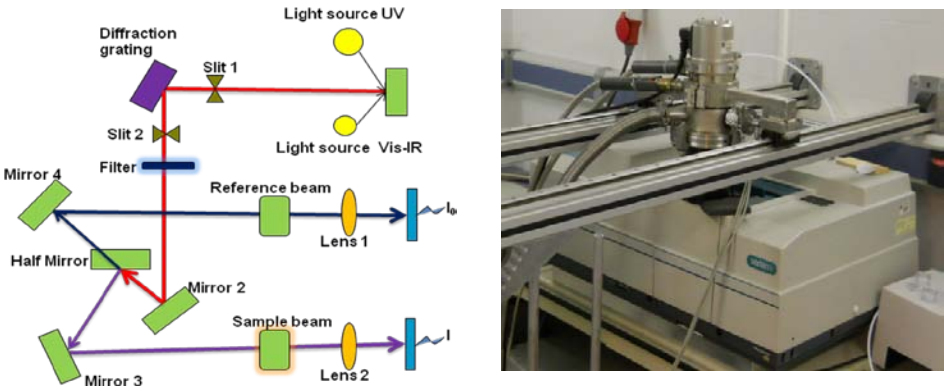

(a) (b)

Figure 2.12. *UV-Vis-NIR spectrophotometer: (a) Schematic view and (b) image of the used equipment.*

Absorption and transmission studies were carried out in a Varian Cary 500 Scan spectrophotometer, available at the Physics and Crystallography of Materials and Nanomaterials (FiCMA-FiCNA), group of the Universitat Rovira i Virgili, Tarragona. This is a double ray spectrophotometer with an effective spectral range from 0.25 to 3 μm and allows to measure optical densities from 0 to 10. This spectrophotometer has two monochromators that can separate 1200 lines/mm in the UV-visible region and 300 lines/mm in the IR region. The light sources of the spectrophotometer are a deuterium lamp in the UV region and a quartz halogen source in the visible-IR region. The light is detected by a photomultiplier (PMT) in the UV-

visible region and a lead sulphide (PbS) detector in the IR region. When we expected differences due to the polarisation of the incident beam, we used a Glan-Thompson quartz polarizer, located before the sample, to eliminate any polarisation induced by the optical components of the spectrophotometer and ensure that we were working only with a polarised component of the incident light. The schematic view and a picture of the system are shown in Figure 2.12. In all experiments we set an aperture to ensure that the measurement beam was absorbed or transmitted with no crystal-edge obscuration. A reference measurement was taken before the crystal sample was placed in the beam path. In this work we measured the absorption and transmission spectral properties of RTP samples and luminescent composites.

2.8.2. Photoluminescent measurements

Photoluminescence is the spontaneous emission of light from a material under optical exicitation. When light of sufficient energy is incident on a material, photons are absorbed and electronic excitations are created. Eventually, these excitations relax and the electrons return to the ground state. If radiative relaxation occurs, the emitted light is called photoluminescence. This emitted light can be collected and analyzed to yield a wealth of information about the photoexcited material. The photoluminescence spectrum provides the transition energies, which can be used to determine electronic energy levels. The luminescent intensity gives a measure of the relative rates of radiative and nonradiative recombination. A typical photoluminescence experimental set-up is shown in Figure 2.13.

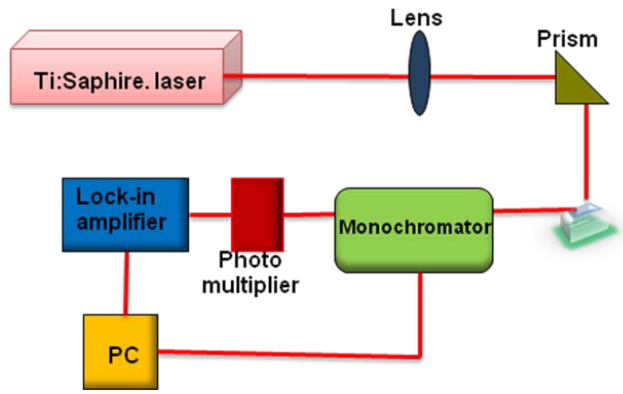

***Figure 2.13**. Schematic view of the photoluminescence experimental set-up we used in this work*

Unpolarized photoluminescence spectroscopic measurements were carried out on KTP diffraction gratings in which we embedded $KYb(WO_4)_2$ nanoparticles doped with Er^{+3}. These experiments were performed by using a Ti:Sapphire laser modulated at 30 Hz, and an InGaAs diode laser with a repetition rate of 10 Hz. In both laser excitation sources, the wavelength used was 980 nm. The fluorescence was recorded in a 90º configuration and was dispersed by a double monochromator (Jobin Yvon-Spex Hr 460), with a focal length of 46 cm, a spectral resolution of 0.05 nm and different grating elements (1800 g/mm, 600 g/mm, and 300 g/mm) depending on the wavelength range to be dispersed. In these experiments we used different kinds of detectors: for example, for visible emission wavelengths we used a Hamamatsu PMTR928 photomultiplier tube, and for detecting emission wavelengths between 800 nm and 1700 nm we used a Hamamatsu R5509-72 NIR photomultiplier tube. The lock-in technique was used to amplify the collected signal with a Perkin Elmer DSP-7265 lock-in amplifier, and a computer was used to process the data. This experimental set up is available at the Physics and Crystallography of Materials and Nanomaterials, (FiCMA-FiCNA), group of the Universitat Rovira i Virigili, Tarragona.

Micro-spectroscopy measurements of the luminescent nanocomposites were also carried to have a better resolution of the photoluminescence spectra and to record intensity maps of the luminescence generated by the sample. The schematic view of the experimental set-up we used is shown in Figure 2.14.

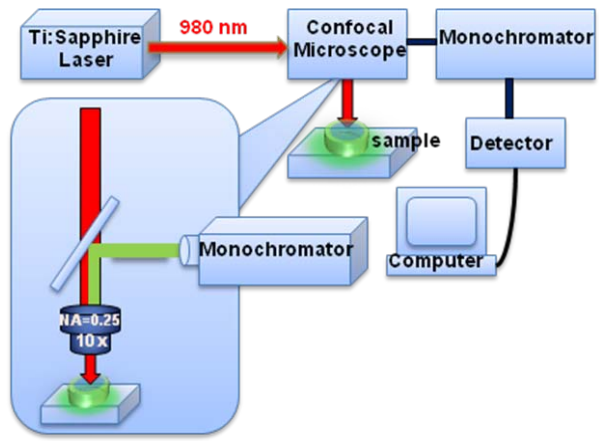

Figure 2.14. *Schematic view of the micro-spectroscopy experimental set-up used in this work*

A Ti:sapphire tunable laser (Tsunami, Spectra Physics) was used as the excitation source emitting at 980 nm. The NIR laser beam was focused into the sample by using a ×10 microscope objective with a numerical aperture (NA) of 0.25. The NIR excitation intensity was controlled by using variable neutral density filters and it was measured by placing a calibrated powermeter after the focusing objective. The same objective was used to collect the back-scattered visible fluorescence. After collection, this fluorescence was coupled into a fiber-coupled high-resolution spectrometer equipped with a calibrated diffraction grating and a CCD camera. This experimental set-up is available at the Departamento de Física de Materiales, Universidad Autónoma de Madrid, Cantoblanco, Madrid.

2.8.3. Fourier Transform Infrared Spectroscopy (FTIR)

Fourier transform infrared (FTIR) spectroscopy has been a workhorse technique for materials analysis in the laboratory since a couple of decades. In infrared spectroscopy, IR radiation is passed through a sample. Some of the infrared radiation is absorbed by the sample and some of it passes through (transmitted). The resulting spectrum represents the molecular absorption and transmission creating a molecular fingerprint of the sample. FTIR represents a fingerprint of a sample with absorption peaks which correspond to the frequencies of vibrations between the bonds of the atoms, that is different for each compound. Therefore, infrared spectroscopy can result in a positive identification (qualitative analysis) of every different kind of material. In addition, the size of the peaks in the spectrum is a direct indication of the amount of material present.

We recorded the transmission of RTP diffraction gratings in the range between 2500 cm^{-1} and 4500 cm^{-1} (λ = 2.2 μm to 4 μm) using with a FTIR, FT/IR-680 Plus Fourier Transform Infrared Spectrometer available at the Servei de Recursos Cientifics i Tecnics, Universitat Rovira i Virgili, Tarragona. The average measurement was 32 scans with a resolution equal to 2 cm^{-1}.

In addition to these transmission measurements on the RTP diffraction gratings, we also used a Bruker-Vertex 70 FT-IR equipment to determine the lattice properties of photonic structures based on the Bragg´s diffraction in the near- and mid-infrared spectral range. The generated incoming light from an halogen tungsten

lamp, illuminated perpendicularly the sample and we collected the diffraction spectra at a set of angles ranging from 24º to 60º in 2º steps. The diffracted light was collected by a reflective mirror fixed on the movable arm of the system and detected with a the liquid nitrogen cooled DLATGS detector in the spectral from 7500 cm^{-1} to 400 cm^{-1} (λ = 1.3 μm to 25 μm).The specular reflection at an incident angle of 12º was taken as a reference. This equipment is available at the Departament d'Enginyeria Electronica of the Universitat Rovira i Virgili and it is shown in Figure 2.15.

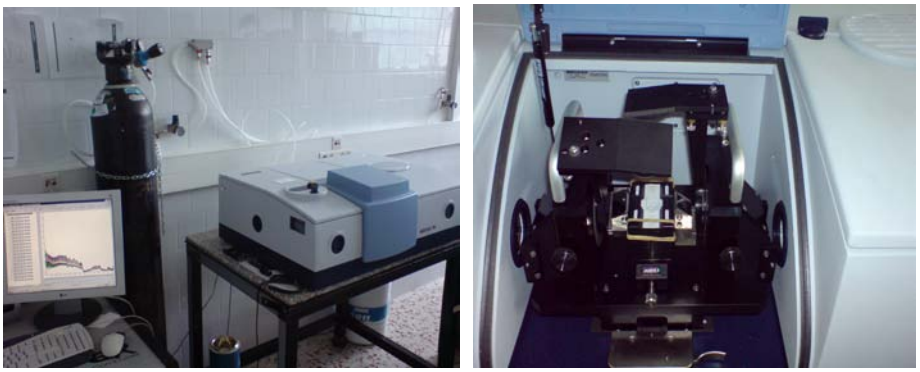

(a) (b)

Figure 2.15*. (a) FTIR-Spectrometer Bruker-Vertex 70 with (b) the reflectivity accessory.*

2.8.4. Raman scattering

Raman scattering is used as a tool in spectroscopic studies. It involves the inelastic scattering of light from a crystal. The Raman effect belongs to a class of nonlinear optical processes that can be called quasi-resonant. Although one of the fields is in resonance with the atomic or molecular transitions, the sum or difference between two optical frequencies equals the transition frequency. Raman scattering is one of the physical processes that can lead to spontaneous light scattering, means, light scattering under conditions such that the optical properties of the material system are unmodified by the presence of the incident light beam.

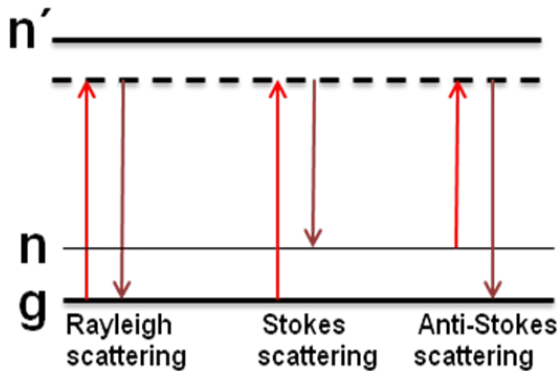

***Figure 2.16**. Energy level diagrams describing Rayleigh, Raman Stokes, and Anti-Stokes scattering*

Generally, there are three different scattering phenomenon such as Brillouin, Rayleigh and Raman scattering, that can be observed with the interaction of light with matter. The difference is that Rayleigh scattering considers only random and incoherent thermal fluctuations, in contrast with the correlated, periodic fluctuations (phonons) of Brilliouin scattering and Raman scattering phenomena, involving inelastic scattering processes of light with vibration and rotational properties of matter.

Spontaneous Raman scattering was discovered in 1928 by Raman [154]. To observe the effect, a beam of light illuminates a material sample and the scattered light is observed spectroscopically. The scattered light generally contains frequencies different from those of the excitation source, i.e., contains Stokes and anti-Stokes lines.

(a) A molecule with no Raman active modes absorbs a photon with the frequency ν_0. The excited molecule returns back to the same basic vibrational state and emits light with the same frequency ν_m as in excitation source. This is called an elastic Rayleigh scattering.

(b) A photon with frequency ν_0 is absorbed by a Raman-active molecule which at the time of interaction is in the basic vibrational state. Part of the photon energy is transferred to the Raman-active mode with frequency ν_m and the resulting frequency of scattered light is reduced to $\nu_0 - \nu_m$, what is called the Stokes frequency.

(c) A photon with frequency ν_0 is absorbed by a Raman-active molecule, which, at the time of interaction, is already in the excited vibrational state. The excessive energy of the excited Raman-active mode is released, the molecule returns to the basic vibrational state and the resulting frequency of scattered light goes up to $\nu_0 + \nu_m$. This Raman frequency is called anti-Stokes frequency.

These differences of Raman scattering can be understood through the use of the energy level diagrams as the one shown in Figure 2.16. Anti-Stokes lines are typically much weaker than the Stokes lines because, in thermal equilibrium, the electronic population in level n is smaller than the electronic population in level g by the Boltzmann factor $\exp(-h\omega/kT)$. Here g is the ground state and n´ is a virtual state. The ability of lasers to produce light of extremely high intensity makes them especially attractive sources for Raman spectroscopy of molecules by increasing the intensity of the anti-Stokes components in the Raman effect. Each resulting pair of lines equally displaced with respect to the laser line, reveals a characteristic vibrational frequency of the molecule.

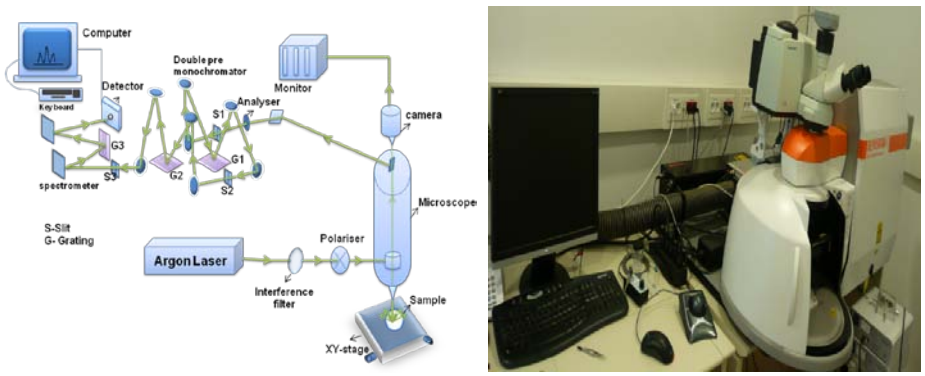

(a) (b)

Figure 2.17*. (a) Schematic view of the micro-Raman experimental set-up and (b) picture of the equipment used.*

Raman scattering measurements were carried out using a micro-Raman system Renishaw-InVia spectrometer equipped with a confocal microscope Leica 2500 and a CCD camera as detector. The schematic view and used equipment is shown in Figure 2.17. Micro-Raman spectroscopy is an ideal non destructive and accurate tool for materials characterization at the micrometer scale. Radiation of an Ar laser (λ = 514 nm and 25 mW) was focused by microscope objectives on the surface of the samples. A back-scattering scheme was used to collect the Raman

signal through a confocal hole, allowing the extraction of the light scattered from an extremely small region of the sample with a spatial resolution of about 1 μm using a long working distance microscopic objective ×100. In addition, polarized micro-Raman scattering investigations were also carried out to investigate the structural modifications on single crystals and a polycrystalline region of the samples This micro-Raman equipment is available at the Servei de Recursos Cientifics i Tecnics, Universitat Rovira i Virgili, Tarragona.

2.9. Optical Diffraction

The measurement of the diffraction patterns generated by the 1D and 2D diffraction gratings in transmission and reflection configurations was performed without polarization by using a He-Ne laser, that operates at 633 nm with a power of 3 mW. The spot size of the He-Ne laser was reduced to 1 mm using a circular aperture and localized with a lens with focal length of 13 cm. The diffraction patterns were observed on a screen. This set up is available at the Physics and Crystallography of Materials i Nanomaterials (FiCMA-FiCNA), Universitat Rovira i Virigili, Tarragona. We also recorded the intensity profiles of transmission diffraction orders generated by our samples using a CCD camera (DCU series, Thorlabs). In this experiment, density filters were used to reduce the energy of the incident laser beam because of high sensitivity of the CCD camera.

To understand the effect of polarization on 1D diffraction gratings, we also recorded the linear diffraction patterns in the reflection configuration using a He-Ne laser, and controlling the polarization with a half wave plate to reduce the power of the laser and two polarizers, located at before the sample, and the detector, respectively. The schematic view of the used experimental set-up is shown in Figure 2.18.

To record diffraction as a function of the wavelength, we also recorded the diffraction patterns of 1D diffraction gratings at wavelengths ranging from 400 to 700 nm using an optical parametric oscillator (Sure light-Continuum) with a repetition rate of 10 Hz, and a pulse width of 5 ns.

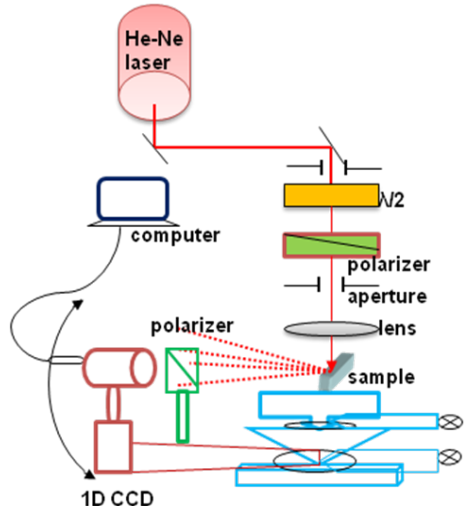

***Figure 2.18**. Schematic view of diffraction experimental set-up used for polarization configurations.*

The sample was mounted on an angule rotation stage controlled by a computer, with an angle resolution of 2º. The generated diffraction patterns were captured using a web camera and the intensity profiles of these diffraction patterns were recorded by using a conventional image-J software. A schematic view of the experimental set-up we used shown in Figure 2.19. This experimental set-up is available at the Neel institute, Grenoble (France).

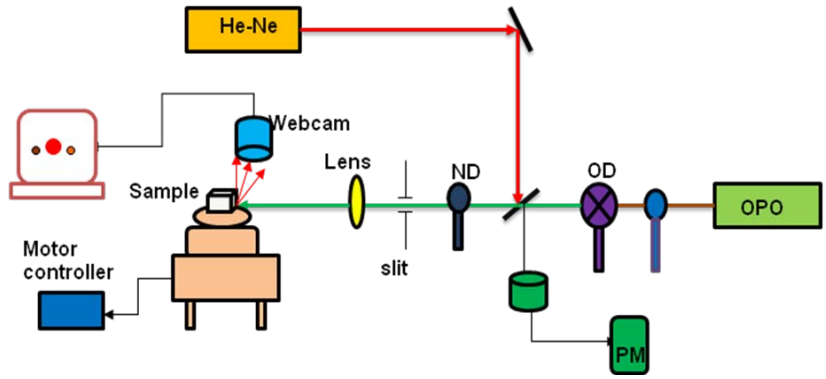

***Figure 2.19**. Schematic view of diffraction experimental set-up*

The diffraction patterns at the second harmonic wavelength (in the visible range), generated by the samples were obtained by illuminating the RTP and $LiNbO_3$ 1D gratings at 1064 nm with a pulsed Surelite Nd:YAG laser with 7 ns pulse width and 10 Hz repetition rate. The energy per pulse was around 50 mJ. The second

harmonic diffraction was measured in the reflection geometry. This configuration allows minimizing the SHG contribution coming from the (unpatterned) bulk of the crystal. We placed the sample on a XYZ positioning stage mounted on a rotating stage to set the desired angle of incidence of the fundamental light on the diffraction grating. The sample was placed close to the focal point of a 100 cm lens used to focus the infrared pulses. The beam was incident onto the diffraction grating at a fixed angle (between 42º and 60º) with respect to the surface normal. This angle was optimized for each sample to avoid components of internal reflections from the other faces of the crystals in the measured second-harmonic diffraction patterns.

The generated second-harmonic light was filtered from the diffracted and diffuse fundamental beam with the use of heat-absorbing filters and an interference filter centred at 532 nm and its intensity was measured using a photomultiplier tube (H5783) that was rotated around the same rotation axis of the rotating stage on which the sample was mounted. This experimental set up is available at the Institut de Ciències Fotòniques (ICFO), Barcelona.

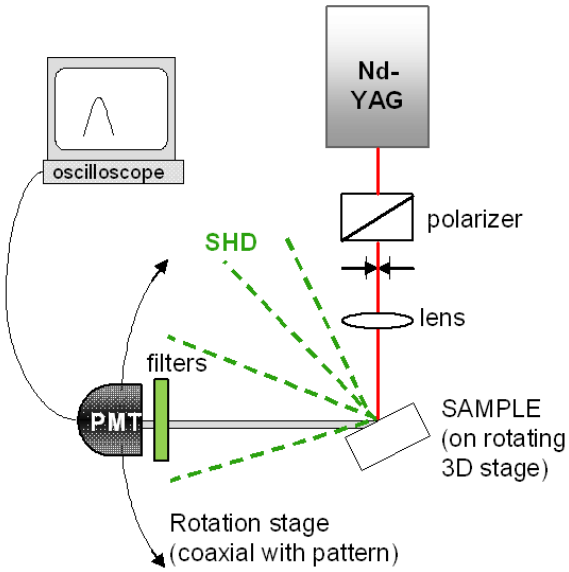

***Figure 2.20**. Scheme of the experimental set-up used for recording the second harmonic diffraction (SHD) patterns.*

In addition to these measurements, the same scheme of the set-up was used to record the intensity profiles of the generated nonlinear diffraction patterns using

web camera at the Neel institute, Grenoble (France). Figure 2.20 shows a scheme of the experimental set-up used for recording the nonlinear diffraction patterns.

To understand the effect of polarization on the generated second harmonic radiation from the surface of the diffraction gratings, we used different polarization configurations at the incident and diffraction beams. We recorded the nonlinear diffraction patterns generated from the surface of the 1D diffraction gratings illuminating them with a Nd: YAG laser at 1064 nm. We also recorded the intensity profiles of the generated nonlinear diffraction patterns. These measurements were done at the Neel Institute, Grenoble (France).

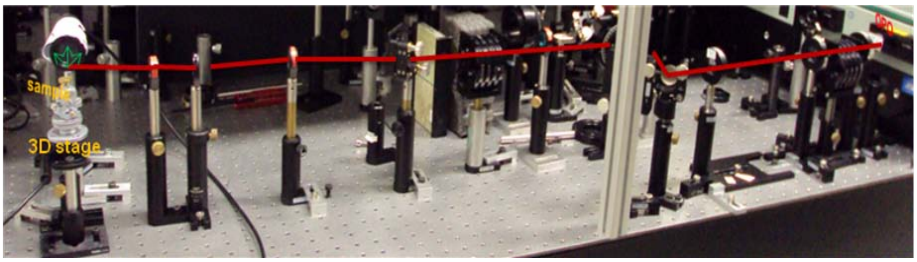

Figure 2.21. *The nonlinear diffraction experimental set-up*

We also analyzed the influence of the wavelength of the incident beam on the diffraction patterns obtained for the second harmonic by tuning the fundamental beam from 350 nm to 1250 nm using the OPO and recording the intensity of the diffracted SH with a silicon photo diode and an oscilloscope. The picture of the experimental set-up we used is shown in Figure 2.21. These experiments were perfomed at the Neel Institute, Grenoble (France).

UNIVERSITAT ROVIRA I VIRGILI
MICROSTRUCTURATION OF NONLINEAR OPTICAL MATERIALS:
METHODOLOGIES, CHARACTERIZATION, AND APPLICATIONS
Raj Kumar Golconda
Dipòsit Legal: T. 55-2013

CHAPTER THREE

Crystal growth of $KTiOPO_4$ and $RbTiOPO_4$ single crystals

Crystal growth is the part of crystallography that studies how to produce a crystalline structure. Crystals had developed along with technological development in the 20th century. There is an ongoing demand for crystals for their physical properties. In fact, it is hard to imagine the reinforcement of the electronics and optical industry, if large and defect free crystals could not be produced. The structural characterization of the crystals will play a promising role in determining their physical properties, in our case putting more stress in their optical and spectroscopic properties. Crystals have become prominent for their applications in many exciting fields, such as it is the photonic industry. These are still showing great promising interest for providing us in the near future with many breakthroughs that will change the direction of technological advances in a wide range of applications. In this chapter, the summary of the crystal growth experiments and the morphology obtained for the crystals will be discussed in detail.

3.1. Crystal Growth

We grew bulk $KTiOPO_4$ (KTP) and $RbTiOPO_4$ (RTP) single crystals in fluxes containing WO_3 by the Top-Seeded Solution Growth (TSSG) technique and slow-cooling method of the solution. The pros and cons and the description of the used TSSG-SC technique for the preparation of KTP and RTP crystals were discussed in chapter 2. A complete crystal growth experiment process would take quite a long time, between two to three weeks on average.

The growth of the KTP and RTP crystals in WO_3 containing fluxes is more advantageous than crystals growing in self fluxes:

1. The time of homogenization was shorter.

2. The cooling interval applied can be larger.

3. It allows us to obtain bigger size crystals.

4. The low viscosity of the solution enables to accelerate the growth process

The main advantage of the WO_3 containing fluxes is that those are less viscous than self fluxes. This allows to obtain a better homogenisation of the solution by only using the temperature gradient of the solution. Furthermore, this gradient can be smaller than those applied in self fluxes. The reduction of the viscosity also allows the structural units to be incorporated easily to the growing crystal, and minimizes the thickness of the boundary layer created by the concentration gradient around the crystal. A thinner boundary layer around the crystal is more advantageous, the incorporation of more structural units on the growing crystal can be increased and it is also possible to obtain large size crystals. This, together with the reduction of the metastable zone defined as the temperature difference between the supersaturation and a temperature at which the crystal starts to grow created by the supersaturation during the crystal growth process allows to extend the cooling interval in the solution. All these result in the growth of bulk single crystals with better quality than those that can be routinely obtained from self fluxes in this family of materials.

3.1.1. $KTiOPO_4$

The phase diagram for tungsten containing fluxes systems to grow KTP crystals was determined by Iliev et al. [155]. When WO_3 is present in the solution, the region of the crystallization of KTP [156] shifts to compositions richer in K_2O and the solution viscosity was found to decrease with increasing concentrations of WO_3.

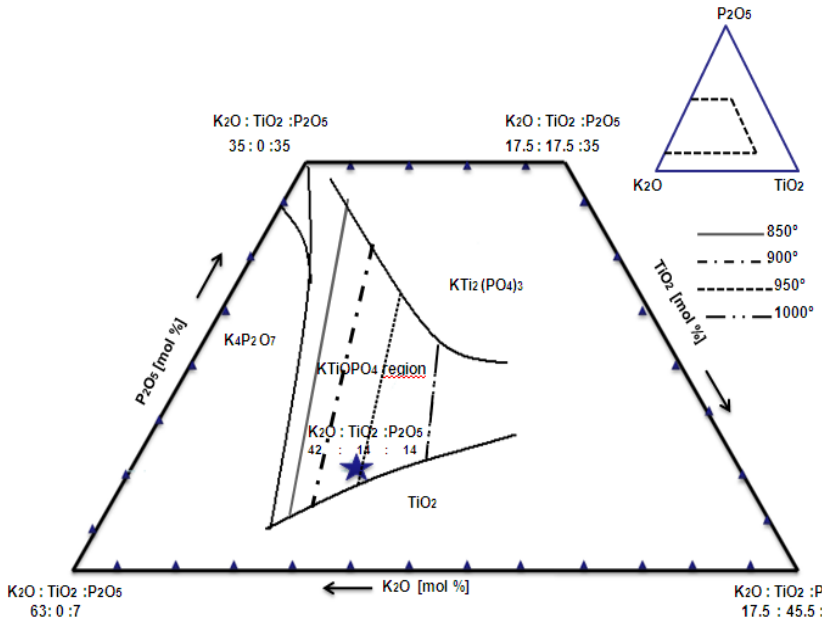

***Figure 3.1**. Concentration region and temperatures of spontaneous crystallization of KTP in solutions containing 30 mol % WO_3.*

Simultaneously, the increase of the concentration of WO_3 (>40 mol %) in the solution leads to a decrease in the solubility of $KTiOPO_4$. We decided to use a solution containing 30 mol% of WO_3 because it is a good compromise between a low viscosity for the solution and still a relatively high solubility for KTP. From Figure 3.1, it is observed that the concentration region of KTP is surrounded by regions of (a) $K_4P_2O_7$ phases crystallizing from solutions with low TiO_2 content, (b) the phase $KTi_2(PO_4)_3$ crystallizing from solutions rich in P_2O_5 and TiO_2, and (c) the phase TiO_2 crystallizing from solutions rich in K_2O and TiO_2.

To grow our desired bulk KTP single crystals, we prepared solutions by mixing the required amounts of K_2CO_3, $NH_4H_2PO_4$, TiO_2 and WO_3, used as initial reagents. The composition of the solution to prepare KTP crystals was the following

in mol % K_2CO_3 = 42, P_2O_5 = 14, TiO_2 = 14 and WO_3 = 30. This solution is marked in the blue color in Figure 3.1. We used Pt cylindrical crucible of 125 cm^3 to prepare the solutions with a weight of around 120 g.

In all our experiments, we used ***c***-oriented crystal seeds of KTP to grow KTP bulk single crystals. The crystal seeds were cut using a diamond disk saw and these crystal seeds were laced with the platinum wire at the end of an alumina rod and placed at the centre of the surface of the solution with the ***c***-direction, normal to the surface of the solution. The used crystal seed dimensions were typically 2 × 2 × 5 mm along the ***a***, ***b***, and ***c*** crystallographic directions, respectively. Before placing the crystal seed at the end of an alumina rod, we made small grooves on the (100) and (010) planes of the crystal seed that enabled us to lace the crystal seed to the alumina rod using thin Pt wires.

While growing the bulk single crystals, the most common problem that can be encountered is the formation of inclusions of the solution, which introduces undesirable strain in the grown crystal. Such inclusions are due to the high temperature gradients present because of poor thermal characteristics of the solution or its high viscosity. Avoidance of solution inclusions in advanced stages of growth requires a crystal orientation configuration and rotation pattern that does not gives rise to stable region of non-circulating growth solution. In all our crystal growth experiments, stirring was applied by rotating the seed and the growing crystal to avoid this problem at a constant angular speed of 45 rpm.

After determining the saturation temperature of the solution, we applied a cooling programme by decreasing the temperature of the solution by 10-20 K at a cooling rate of 0.1 $K \cdot h^{-1}$. Finally, the system was cooled down to room temperature at a rate of 15 $K \cdot h^{-1}$. Using these experimental conditions we successfully grew KTP single crystals in fluxes containing 30 mol % WO_3.

The experimental conditions of HTTSSG-SC technique were discussed in detail in some of the papers included in this thesis (*paper III, IV, V*). The results of the crystal growth experiments are summarized in this chapter to understand them in detail.

The most significant results obtained from the experiments with different intervals of temperature cooling as well as the crystal dimensions, saturation temperatures, weight of the obtained crystals, and their quality are listed in Table 3.1.

In the Table 3.1, we observe that crystals obtained in experiments from 9 to 14; grew at lower temperature as compared with the previous experimental results. In the case of these experiments, a new KTP solution was prepared due to the contamination of the previous solution.

Table 3.1. *Growth data associated with KTP single crystals*

A	***B***	***C***	***D***	***E***	***F***	***G***	***H***	***I***
1	1238.3	***c***	20	0.1	13.41 × 15.46 × 13.47	4.39	-	Inclustions
2	1238.5	***c***	20	0.1	13.22 × 13.26 × 14.25	3.94	-	Good
3	1240.5	***c***	20	0.1	14.32 × 18.50 × 18.46	8.36	-	Very good
4	1235.5	***c***	50	0.1	13.40 × 17.20 × 20.01	7.61	1	Very good
5	1229	***c***	20	0.1	6.32 × 8.52 × 9.94	1.10	-	Inclusions
6	1229	***c***	40	0.1	13.41 × 16.53 × 18.78	5.36	1	Very good
7	1229	***c***	50	0.1	13.55 × 15.87 × 23.30	9.55	1	Good
8	1232.1	***c***	50	0.1	13.77 × 18.47 × 20.30	8.06	1	Very good
9	1214.9	***c***	40	0.1	11.58 × 13.75 × 17.09	7.11	1	Very good
10	1219.3	***c***	24	0.1	10.63 × 14.89 × 15.28	4.17	1	Good
11	1214.3	***c***	30	0.1	13.47 × 18.87 × 12.68	6.13	1	Very good
12	1204	***c***	22	0.1	11.53 × 18.33 × 13.18	4.72	1	Very good
13	1204.7	***c***	30	0.1	13.47 × 18.87 × 12.68	6.03	1	Good
14	1196.7	***c***	40	0.1	9.54 × 13.56 × 21.48	7.94	1	Very good

A: Number of experiment. **B**: Saturation temperature (K). C: Seed crystallographic orientation. **D**: Cooling interval (K). **E**: cooling rate ($K \cdot h^{-1}$) **F**: Dimensions along the ***a***, ***b,*** and ***c*** crystallographic directions, respectively (mm). **G**: Crystal weight (g). **H**: pulling rate (mm/day). **I**: Quality of the crystal.

In all above crystal growth experiments, we found that the largest crystals can be obtained by increasing the cooling interval programme as well as slowly pulling (from 4, 6-14 crystals in Table 3.1) the crystal from the surface of the solution

simultaneously. The pulling process will be discussed later in this chapter. The larger the cooling interval applied to the crystal growth experiments, the bigger the size of the crystals obtained.

3.1.2. $RbTiOPO_4$

Along with bulk KTP single crystals we also grew RTP crystals in flux containing WO_3 by the TSSG technique. To prepare bulk RTP single crystals, the composition of the solution was made with (mol %) Rb_2O_3 = 44.24, P_2O_5 = 18.96, TiO_2 = 16.80 and WO_3 = 20. The weight of the prepared RTP solution was ~140 g. Figure 3.2 shows the crystallization region of RTP in a solution contained 20 mol % WO_3. The composition of the solution we prepared is marked with the star in this Figure. As neighbouring phases to RTP we found Rb_3Ti_3O (P_2O_7) $(PO_4)_3$ for solutions containing low concentration of TiO_2 and high concentration of P_2O_5.

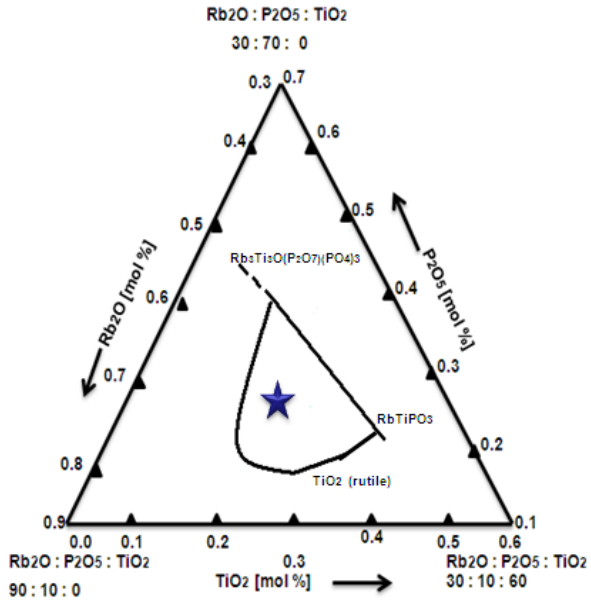

Figure 3.2. *Concentration region RTP in solutions containing 20 % WO_3.*

When the concentration of P_2O_5 is low, however, the $RbTiPO_3$ appears. Finally the TiO_2 phase crystallizes from solutions rich in Rb_2O and TiO_2 [148]. It has also been reported that the saturation temperature decreases slightly when the concentration of WO_3 increases especially to above 20%.

Similar experimental conditions were used to grow RTP crystals as like KTP single crystals. The results of RTP single crystal growth experiments are briefly summarized in this section.

The grown RTP crystals with containing WO_3 fluxes by TSSG-SC were listed in Table 3.2.

Table 3.2. *Data associated to the growth of RTP single crystals*

A	*B*	*C*	*D*	*E*	*F*	*G*	*H*
1	1160.7	***c***	20	0.1	11.10×14.05×26.30	7.99	Very good
2	1162.9	***c***	22	o.1	14.95×15.16×15.87	5.71	Very good
3	1187.4	***c***	30	0.1	17.29×18.74×20.45	9.36	Very good
4	1190	***c***	47	0.1	17.29×18.74×20.45	13.94	Good
5	1187.4	***c***	40	0.1	17.86×20.03×21.54	12.32	Good

A: Number of experiment. **B**: Saturation temperature (K). **C**: Seed crystallographic orientation. **D**: Cooling interval (K). **E**: Cooling rate (K). **F**: Dimensions along the ***a***, ***b*** and ***c*** crystallographic directions, respectively (mm). **G**: Crystal weight (g). **H**: Quality of the crystal

In all the above crystal growth experiments, we obtained larger crystals by increasing the cooling interval program.

3.2. Crystal structure of $KTiOPO_4$ and $RbTiOPO_4$

Crystals of the KTP family belong to the orthorhombic system with the space group $Pna2_1$. The crystal structure of KTP was firstly determined by Tordjman et al. in 1974 [157] .There are 64 atoms in a unit cell in the KTP lattice. This 64 atom group separates into four subgroups of 16 atoms each, and within each sub group there are two inequivalent K sites, two inequivalent titanium sites, two P sites, and ten inequivalent oxygen sites. Two of the latter oxygen sites represent bridging ions

located between titanium ions, while the other eight are contained in PO_4 groups where they link one Ti and one P ion.

The KTP structure is characterized by helical chains of distorted TiO_6 octahedra linked two corners. These chains bridged along the c crystallographic direction by PO_4 tetrahedra, forming an infinite PO_4-TiO_6-PO_4-TiO_6-lattice array. The K^+ lattice sites are in the channels of the framework. These channels are along the (001) direction, along which K^+ easily diffuses via the vacancy mechanism being responsible for the high ionic conductivity of KTP along this direction [158]. K+ ions are either 8 or 9 coordinated with oxygens, and they are denoted by K(1) and K(2), respectively. Each of the TiO_6 distorted octahedra contains a short Ti-O double bond and a long Ti-O bond which are commonly assumed as primarily responsible for the optical nonlinearity [159]. Those oxygens are denoted usually as OT(1) and OT(2). Stimulated Raman measurements show that, in KTP, the strongest vibrations occur in the direction collinear with the distortion of TiO_6 octahedra [160]. Table 3.3 shows the atomic coordinates of all the atoms of the KTP. The structure of these crystals is quite effective for the development of new nonlinear optical materials based on KTP and its isomorphs, that has contributed to a better understanding of the structural properties of this family of crystals.

Table 3.3. *Atomic coordinates and equivalent isotropic displacement parameters of $KTiOPO_4$ from X-ray single crystal diffraction [161].*

Atom	X	Y	Z	U_{iso} (Å²)
K(1)	0.37807(8)	0.7806(1)	0.6880(9)	0.0246(5)
K(2)	0.10526(7)	0.6990(1)	0.9332(1)	0.0142(5)
Ti(1)	0.37290(4)	0.5001(1)	-0.00040(8)	0.0075(3)
Ti(2)	0.24658(6)	0.2695(5)	0.74836(9)	0.0072(3)
P(1)	0.49808(8)	0.3363(1)	0.7397(1)	0.0061(4)
P(2)	0.18079(7)	0.5020(1)	0.4872(1)	0.0085(4)
O(1)	0.4859(2)	0.4867(5)	0.8497(2)	0.009(1)
O(2)	0.5103(2)	0.4657(5)	0.6170(2)	0.010(2)
O(3)	0.4004(2)	0.1986(4)	0.7208(2)	0.010(1)
O(4)	0.5934(2)	0.1930(4)	0.7589(2)	0.007(1)
O(5)	0.1126(2)	0.3106(4)	0.4585(2)	0.011(1)

O(6)	0.1113(2)	0.6918(4)	0.5117(3)	0.012(1)
O(7)	0.2525(2)	0.5402(5)	0.3718(2)	0.010(2)
O(8)	0.2528(2)	0.4619(5)	0.6008(2)	0.012(2)
OT(1)	0.2248(2)	0.9653(4)	0.3561(2)	0.008(1)
OT(2)	0.2232(2)	0.0413(5)	0.6097(2)	0.009(2)

Table 3.4. *Atomic coordinates and equivalent isotropic displacement parameters of $RbTiOPO_4$ from X-ray single crystal diffraction [110].*

Atom	**X**	**Y**	**Z**	**U_{iso} (Å²)**
T(1)	0.37284(6)	0.4998(1)	0.00081(9)	0.0066(3)
Ti(2)	0.24836(7)	0.2678(1)	0.74858(9)	0.0067(3)
P(1)	0.4997(1)	0.3332(2)	0.7422(1)	0.0070(4)
P(2)	0.18035(9)	0.5014(2)	0.4884(1)	0.0079(4)
Rb(1)	0.38504(4)	0.78347(8)	0.67465(7)	0.0205(2)
Rb(2)	0.10537(4)	0.69184(9)	0.92598(8)	0.0176(2)
O(1)	0.4862(3)	0.4786(7)	0.8535(4)	0.008(1)
O(2)	0.5141(3)	0.4604(7)	0.6199(3)	0.009(1)
O(3)	0.4024(2)	0.2026(5)	0.7207(3)	0.009(1)
O(4)	0.5949(3)	0.1943(6)	0.7616(4)	0.011(1)
O(5)	0.1141(3)	0.3109(6)	0.4583(3)	0.009(1)
O(6)	0.1128(3)	0.6894(6)	0.5174(4)	0.012(1)
O(7)	0.2505(3)	0.5423(6)	0.3729(3)	0.009(1)
O(8)	0.2522(3)	0.4576(6)	0.6010(4)	0.011(1)
OT(1)	0.2218(3)	0.9607(6)	0.3564(4)	0.008(1)
OT(2)	0.2226(3)	0.0437(7)	0.6097(3)	0.009(1)

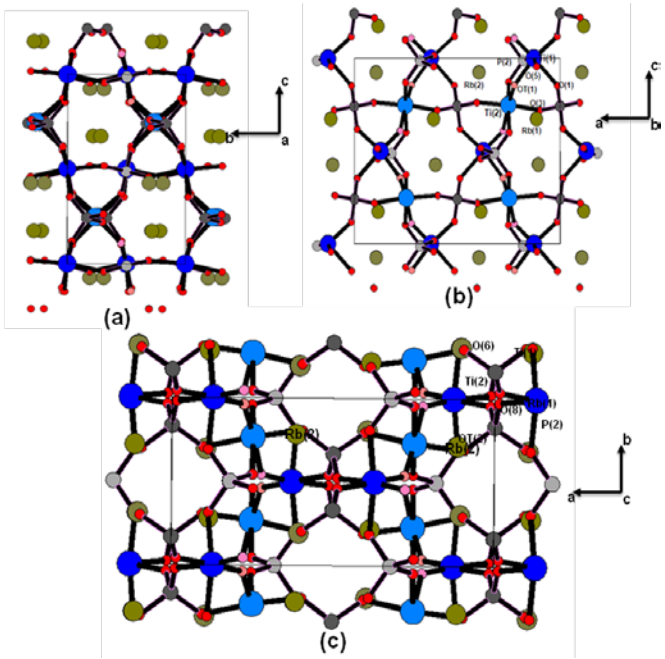

***Figure 3.3**. View of the structure of the RTP crystal with a projections parallel to (a) [100] (b) [010] and (c) [001] directions.*

RTP is an isomorphic material to KTP and it is viewed as a particularly useful member of the KTP family. The lattice parameters for the KTP and RTP crystals are very close, so that the PO_4 tetrahedra have much more influence on the lattice constants than the monovalent cations K^+ or Rb^+. Table 3.4 shows the atomic coordinates of all the atoms of the RTP. The crystal structure of RTP, which is equivalent to that of KTP, is shown in Figure 3.3 along the ***a***, ***b***, and ***c*** crystallographic directions.

3.3. Morphology of $KTiOPO_4$ and $RbTiOPO_4$ crystals

The external shape of the crystals depends on their internal structure. Therefore, the spatial group of symmetry, the cell parameters and atomic positions affect to the shape of the crystals. On the other hand, there are several other parameters that could affect the morphology of the crystals, such as the solution composition, the thermal profile of the furnace, the temperature gradient of the solution inside the crucible, etc. In the representation of the external morphology of a

crystal there can be seen a whole family of plane faces forming a polyhedron. Every one of the faces is associated to a family of Miller indexes (hkl). The orientation of crystal face is adequately described by three integers (hkl) which are prime in reference to each other. The importance of the face (hkl), is related with its growth rate, that can be correlated with the crystallographic spacing, d_{hkl} through the Wulff theorem [162] and the Donnay and Harker law [163]. The higher the d_{hkl}, the lower the growth rate of this face, and thus the larger the surface of this face in the final crystal.

The calculated d_{hkl} values for KTP crystals are summarized in Table 3.5 ordered from the higher to lower values. To calculate the spacing, the following expression can be used

$$d_{hkl} = 1/|r^*_{hkl}|$$

where $|r^*_{hkl}| = \sqrt{(ha^* + kb^* + lc^*) \cdot (ha^* + kb^* + lc^*)}$ for the orthorhombic system

The selected calculated d_{hkl} values for KTP are shown in Table 3.5

Table 3.5. *Selected d_{hkl} values of the KTP crystals*

{hkl}	KTP d_{hkl} (Å)
(200)	6.407
(110)	5.728
(011)	5.490
(201)	5.495
(002)	5.308

From the Donnay-Havker law and using strictly the Wueff theorem with the d_{hkl} calculated in Table 3.5, the resulting morphology of the crystal is that shown in Figure 3.4 (a). However, the external morphology of KTP crystals was studied

independently by Voronkova and Yanovski [164] and Pavlova et al. [165]. This morphology was significantly different that the one shown in Figure 3.4 (a), and it is shown in Figure 3.4 (b). The morphology of the KTP crystals grown in self fluxes varies and these crystals show 14 facets belonging to four families of crystallographic planes namely {110}, {100}, {011}, and {201} [164]. The {201} and {011} forms form sharp caps along the ***c*** axis, whereas the {011}, and {110} forms form less sharp caps along the ***b*** axis. The typical morphology of a KTP crystal is shown in Figure 3.4. The morphology is symmetrical. It resembles the *mmm* symmetry, which is higher than the internal structure (*mm2* symmetry) of KTP.

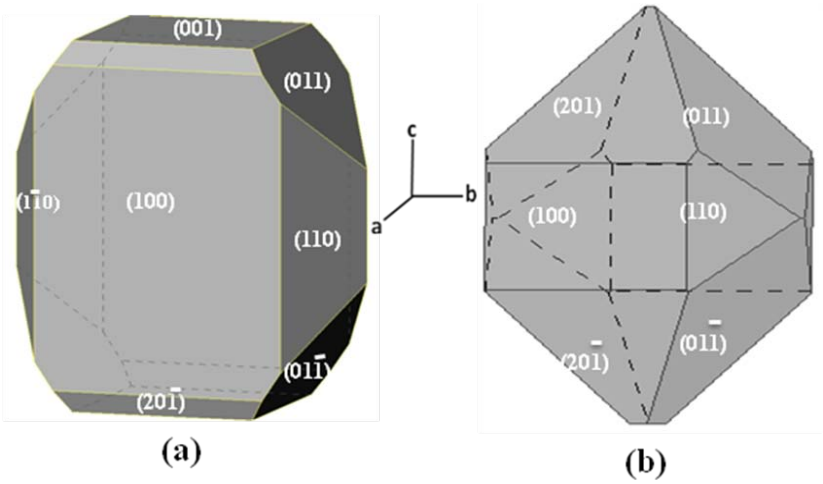

Figure 3.4*. The morphology of the* ***a****-oriented KTP single crystal*

The experimental conditions were not changed during all our crystal growth experiments but the morphology of the crystals changed, probably due to the different cooling program applied.

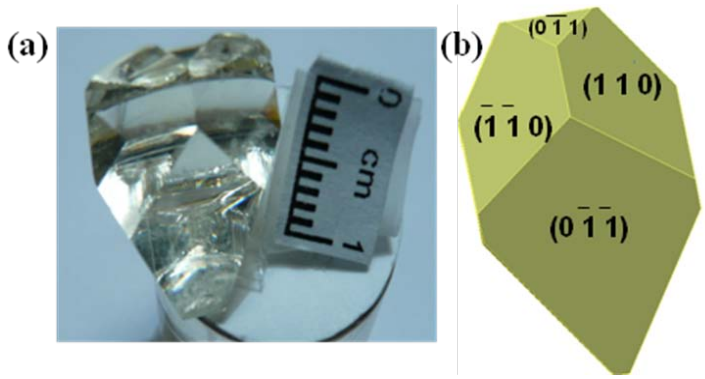

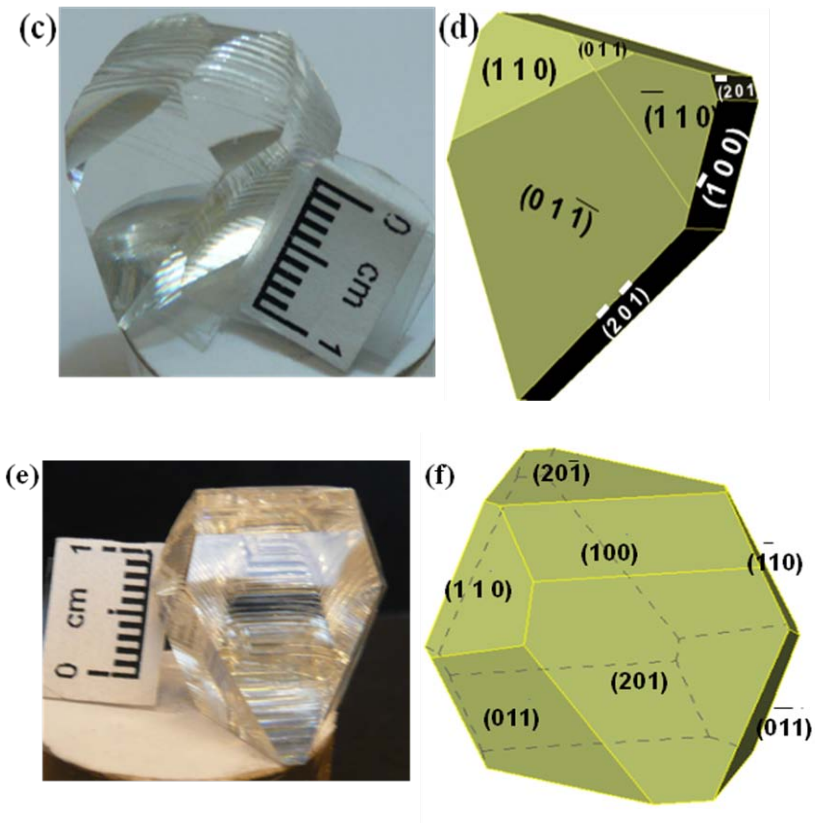

Figure 3.5. *Pictures and schematic drawings of the as-grown KTP bulk single crystals*

Figure 3.5 shows morphology of the grown crystals and the corresponding schematic drawings of the dominant faces of the KTP crystals. We see that the typical faces of the crystals appeared {100}, {110}, {011}, $\{0\bar{1}1\}$, {201}, $\{20\bar{1}\}$. It represents that there is no change in the morphology of the crystals grown in tungsten containing solutions when compared to those grown in self fluxes. Pictures of the as-grown KTP bulk crystal and the corresponding schematic drawings of the morphology are shown in Figure 3.5.

Figure 3.6 shows some pictures of the as-grown RTP bulk single crystals obtained from the TSSG-SC technique in this work and their corresponding schematic drawings showing their morphology. The morphology of RTP bulk single crystals is very similar to that of KTP crystals. Figure 3.6 shows the typical faces of these crystals corresponding to the {100}, {110}, {011}, $\{0\bar{1}1\}$, {201}, and $\{20\bar{1}\}$ forms.

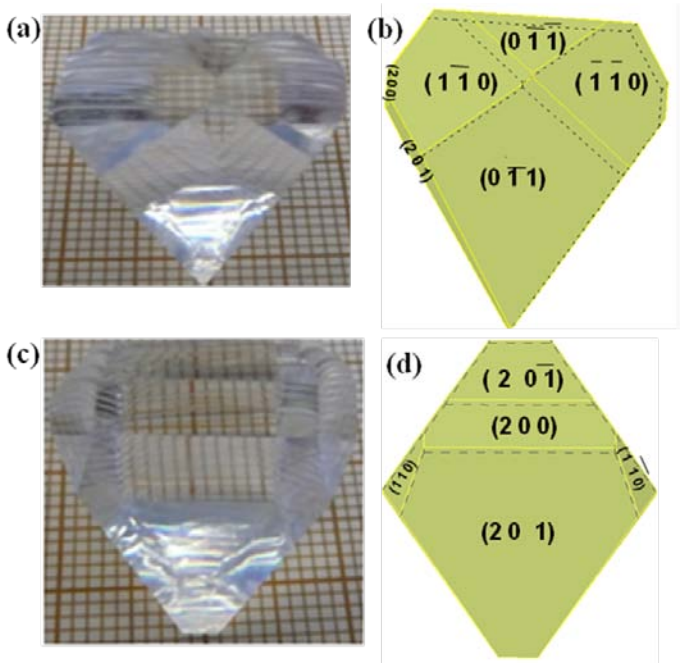

Figure 3.6*. Pictures and schematic drawings of the as-grown RTP bulk single crystals.*

However the crystals grow in larger size along the ***c***-direction compared with the sizes along the ***a*** and ***b*** directions. The similar morphological features were shown in RTP crystal when compared with KTP crystal morphology.

3.4. Pulling effect

Slow cooling rate is one of the key parameters which can be applied to obtain high quality crystals during the TSSG-SC crystal growth process and it has been extensively reported by several research groups [166-168]. In this procedure large size bulk single crystals with a prescribed orientation and shape can also be grown by slowly from pulling the crystal from the solution while it is growing. The KTP and RTP crystals were slowly pulled out of the solution at a rate of 1 mm per day. Figure 3.7 shows the images of the crystals obtained by applying the pulling process. The crystal pulling process is more advantageous economically for growing larger size crystals. The crystal pulling process can control the diameter of the crystal during the growth process by adjusting the speed of the growth temperature of the solution, and

the rate of pulling. The length of the crystal can also be increased in the growth direction by the pulling process.

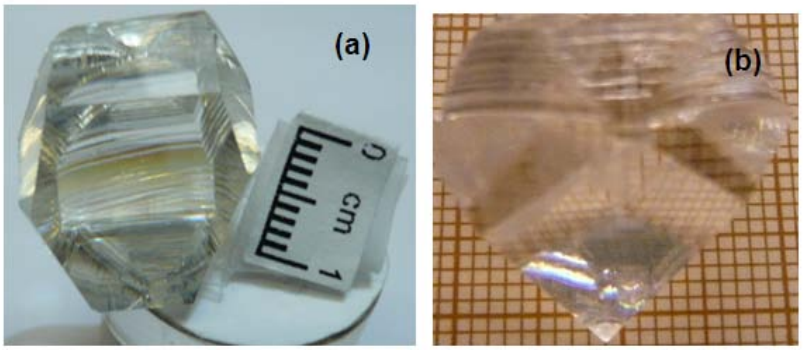

Figure 3.7*. Pulling effect on the morphology of bulk single crystals of (a) KTP (b) RTP*

The morphology of the crystal, obtained from the pulling process is slightly different than the morphology of the crystals obtained without pulling. In Figure 3.7, we can see that the surface of the crystal faces {100}and $\{\bar{1}10\}$show few steps after applying the pulling process. The faces {110}and $\{\bar{1}10\}$ were prolonged, while the {100}face of the crystal was slightly diminished. However, these issues are not a major problem for the use of these crystals for optical applications and will not effect the fabrication of diffraction gratings from these crystals and their optical characterization.

.

UNIVERSITAT ROVIRA I VIRGILI
MICROSTRUCTURATION OF NONLINEAR OPTICAL MATERIALS:
METHODOLOGIES, CHARACTERIZATION, AND APPLICATIONS
Raj Kumar Golconda
Dipòsit Legal: T. 55-2013

UNIVERSITAT ROVIRA I VIRGILI
MICROSTRUCTURATION OF NONLINEAR OPTICAL MATERIALS:
METHODOLOGIES, CHARACTERIZATION, AND APPLICATIONS
Raj Kumar Golconda
Dipòsit Legal: T. 55-2013

CHAPTER FOUR

Fabrication and morphological characterization of diffraction gratings on the surface of nonlinear optical materials

Surface relief diffraction gratings fabricated in connection with nonlinear optical media have been of interest in recent years because of their potential applications in photonics. In this chapter we discuss about the fabrication of surface relief diffraction gratings on nonlinear optical materials by ultrafast laser ablation and selective chemical etching methods, and their morphological characterization.

4.1. Fabrication of diffraction gratings by ultrafast laser ablation

We fabricated 1D and 2D diffraction gratings on the surface of RTP and KTP nonlinear optical materials. The experimental details of the fabrication process were discussed in Chapter 2. 1D and 2D micro-structural patterns were recorded on RTP and KTP substrates with different lattice spacing.

RTP-1 sample consisted of 1D channels in the area of 3 x 3 mm^2. To fabricate it we focused the laser beam by means of a 50 mm achromatic lens using pulse energy of 0.78 µJ, which provided a peak fluence of ~6.1 $J.cm^{-2}$. The 1D microstructure was fabricated on the (001) surface of RTP-1 sample, where the focused laser beam moved following straight lines parallel to the ***b*** crystallographic axis at all across the sample surface and with a constant scanning speed of 130 µm/s avoiding iterative passes along the same line. For this scanning speed, the number of pulses contributing to the ablation of a point within the sample surface was approximately 40. We have estimated the ablation threshold fluence following the procedure described on diamond and titanium nitride [169], giving 1.44 ± 0.18 $J.cm^{-2}$ for 40 pulses. For multishot conditions (> 100 pulses) the value for the threshold decreases to 1.18 ± 0.15 $J.cm^{-2}$ (incubation factor ξ =0.783) [170]. In RTP-1 sample lattice spacing between the grooves is 15 µm.

RTP-2 sample consisted of 1D channels with a spatial period of 20 µm in the area of 3 x 3 mm^2, For structuring it, the used focusing optics was a ×10 (0.22 NA) microscopic objective. A 6 mm diameter circular aperture was placed before the objective in order to slightly increase the spot size at focus. The pulse energy before the aperture was 0.27 µJ leading to a peak fluence at focus of ~3.2 $J.cm^{-2}$. The writing procedure was identical than for the RTP-1 sample and the scanning speed was set to 75 $\mu m.s^{-1}$ with a separation between lines of 10.5 µm and 9.5 µm, alternatively. Under these conditions, the number of pulses contributing to the ablation of a point within the sample surface was around 55. The total processing time took approximately 4h to fabricate the both RTP samples.

We followed a similar procedure for the fabrication of two different 2D micro-structures on the surface of KTP crystals. For KTP-1 sample that consisted of 2D square array of channels in the area of 3 x 3 mm^2. The 2D structure consisting of

two perpendicular arrays of grooves on (010) surface, parallel to the ***a*** and ***c*** crystallographic axes, respectively. The laser beam was focused by a ×10 objective lens with NA 0.30. It was achieved by moving the sample at a constant speed of 75 $\mu m.s^{-1}$ which means a number of pulses per spot (ø ~3 µm) of 40. A circular aperture 6 mm and some neutral filters were placed before the focusing lens in order to reduce the pulse energy to 0.48 µJ and produce a lattice pitch of 8.54 µm. The sample KTP-2 consisted of a square array of circular pores with a pitch of 8.85 µm. In this case, the sample was moved to the selected positions and then irradiated with 100 pulses. A circular aperture of 5.5 mm and some neutral filters were placed before the focusing lens in order to reduce the pulse energy to 0.39 µJ and achieve the desired pore diameter. The total processed area was 3 × 3 mm^2 and took approximately 8.5 h to fabricate the samples in both cases.

The experimental conditions used in the fabrication of 1D and 2D microstructures on the surface of RTP and KTP crystals are summarized in Table 4.1.

Table 4.1. *Fabrication conditions of 1D and 2D microstructures on RTP and KTP samples.*

Parameter	RTP-1 (1D)	RTP-2 (1D)	KTP-1 (2D)	KTP-2 (2D)
Pulse energy (µJ)	0.78	0.27	0.48	0.39
No. of pulses	40	55	40	100
Scanning speed (µm)	130	75	75	75
Beam diameter (mm)	6	6	6	5.5
Processed time (h)	4	4	8.5	8.5
Lattice spacing (µm)	15	20 (two sub periods 9.5, 10.5)	8.54	8.85

As we can see in this table, the 1D and 2D diffraction gratings have been fabricated using different experimental conditions. This conditioned their

morphology. The depth of the fabricated channels depends on the energy of the beam, pulse duration, no. of pulses, and the used wavelength. In Table 4.1, we showed the key parameters which influence the ablation of the material. The pulse width is used to obtain large peak power and to minimize thermal conduction to the surrounding material. In the case of our samples, the beam diameter was controlled efficiently to avoid the excessive ablated regions on the surface of the samples. Thus, for instance in the RTP-2 sample, we observed that the depth of the channel was larger than that obtained in the channels inscribed in the RTP-1 sample. This is due to the slow scanning speed and the use of a larger number of laser pulses.

4.2. Morphology of the fabricated 1D and 2D diffraction gratings

The morphological characterization of the fabricated diffraction gratings was done by using the optical imaging profiler PLμ 2300. The 3D confocal images of the fabricated diffraction gratings of the RTP and KTP samples are shown in Figure 4.1

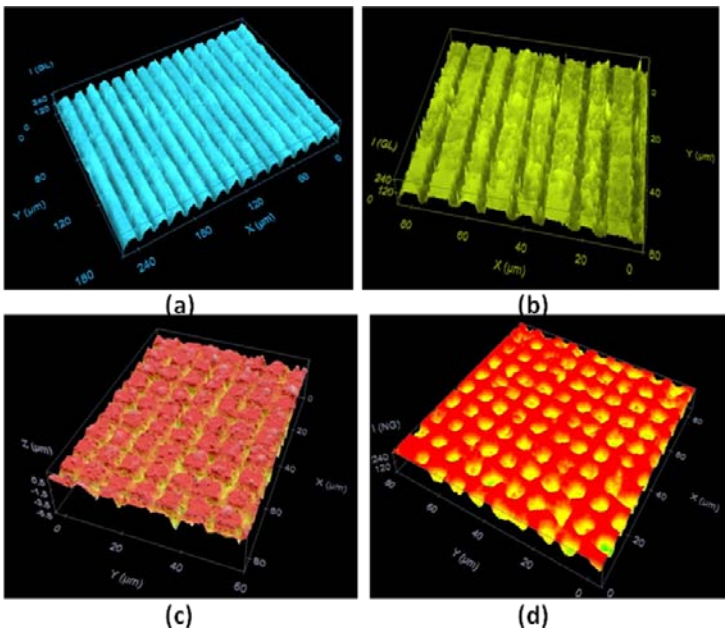

Figure 4.1. *Confocal images of the diffraction gratings fabricated by ultrafast laser ablation (a) RTP-1 (b) RTP-2 (c) KTP-1 (d) KTP-2*

The confocal images of the diffraction gratings of all the samples were recorded with a ×20 microscopic objective in the long range order where we can see a

higher number of channels. In Figure 4.1, we can see the long range ordering and the high degree of periodicity of the diffraction gratings fabricated by ultrafast laser ablation. Looking carefully at the Figure 4.1 (b), the image of the RTP-2 sample, the two different periods of the diffraction grating can be observed. In Figure 4.1 (c) the orthogonal array of channels of the KTP-1 sample is not showing a high degree of periodicity due to the difficulty of laser writing procedure. The 2D confocal images and their corresponding surface profiles of these diffraction gratings are reported in Figure 1 in *paper IV*.

The fabricated 1D and 2D diffraction gratings of RTP and KTP samples were also observed by optical microscopy analysis. The optical microscopy images of 1D RTP-1 and RTP-2 samples are shown in Figure 2 in *paper V*. From this analysis, the long range order was observed indicating a high degree of periodicity of the 1D RTP-1 and RTP-2, and KTP-2 2D diffraction gratings. From these images, it can be appreciated that while the periodicity was constant in the RTP-1 sample with an estimated lattice parameter of 14.92 μm in average, determined from the high magnification images of the sample, the periodicity of the RTP-2 sample was sub-modulated into two different sub-periods of 9.5 μm and 10.5 μm approximately of a spatial period of 20 μm imposed by alternative grooves of the diffraction grating. Similarly, in the case of KTP-1 and KTP-2 samples, we observed that the periodicity of the diffraction gratings estimated using high magnification images of optical microscopy are 8.91 μm and 9.02 μm, respectively. In this case, the KTP-2 sample shows a higher degree of periodicity.

Apart from this optical microscopy image analysis, a technique with higher spatial resolution is needed in order to investigate the structure morphology of the diffraction gratings at a local level. In this sense SEM has been the ideal tool for a more in detail morphological characterization of the diffraction gratings at the micrometer scale. Thus, the morphological characterization of the as-fabricated RTP and KTP diffraction gratings has also been done using by SEM. The recorded SEM images of the 1D and 2D diffraction gratings are reported in Figure 2 in *paper IV*. This Figure shows top views of the 1D and 2D diffraction gratings fabricated on the surface RTP and KTP crystals, respectively, by ultrafast laser ablation. The insets in Figure 2 in *paper IV*, show high magnification images of the corresponding samples. From these micrographs, we can still appreciate the high periodicity of the fabricated

structures. However, in this analysis we observed that the width of the grooves is not the same for all the samples. This is due to the result of the tight focusing conditions. If the focal plane does not match the surface of the sample, even slightly, the pulse energy distribution is modified at the area where the fluence is above the ablation threshold. In the case of the RTP-1 sample, the region where the fluence exceeded the ablation threshold fluence (multishot conditions) has a diameter of approximately 5 µm. However, in the case of the RTP-2 sample, the diameter of the groove was around 3.3 µm. Even though, the beam diameter was controlled efficiently in both of the samples, due to the focusing conditions and difference in the peak fluence at the focused area. It results that an excessive region was ablated in the case of the RTP-1 sample compared to the ablated area in the RTP-2 sample.

In the KTP-1 sample (see Figure 2 (c) in *paper IV*), the roughness of the grooves is very high, and the squares that should be formed between the grooves are much distorted as a result of the laser writing procedure. So, this difficults the determination of the exact width of the channels as well as the lattice period in this orthogonal array microstructure. The higher magnification image of the KTP-1 diffraction grating shows the distorted squares formed on the sample between channels. Figure 2 (d) in *paper IV* shows the top view of the fabricated conical pores on the surface of the KTP-2 sample. The higher magnification image of the KTP-2 sample shows that the fabricated conical pores are slightly distorted.

Figure 3 (a) in *paper IV* shows cross-section image of the channels inscribed on the RTP-1 diffraction grating. The roughness of the lateral walls of the RTP diffraction gratings was estimated to be around 0.4 µm. The depth of the channels inscribed on the RTP-1 diffraction grating is $t = 5 \pm 0.4$ µm and the maximum width is 5 – 5.5 µm. The cross-section images of the channels inscribed on the RTP-2 diffraction grating is shown in Figure 3 (b) in *paper IV*. From these images, the depth of the RTP-2 sample is $t = 7 \pm 0.4$ µm and the maximum width is 3.3 – 3.5 µm. Due to the low peak fluence used in the processing of these samples, we did not observe the formation of deposition of material at the edge of the grooves, neither splattered material, as it happened with moderate peak fluencies in $LiNbO_3$. From these images we also observed that the shape of these fabricated grooves inscribed on the surface of the RTP samples is a V-shape.

Similarly, we also recorded the cross sectional images of the KTP-1 sample. Figure 3 (c), (d) in *paper IV* revealed that the widths of the channels in square pattern of the 2D diffraction grating is different along the ***a*** and ***c*** crystallographic directions. The width of the channels along the ***a*** direction is larger than along the ***c*** direction due to the anisotropy of the material that leads to different ablation thresholds depending on the crystallographic directions in the crystal, since the laser fluence did not change during processing. The widths of the channel in the KTP-1 sample, along the ***a*** and ***c*** directions are 5.60 µm and 3.51 µm, respectively. The fact that the damage threshold is different in different directions is not surprising in crystals of the KTP family. In this family of materials it has been found that some physical properties are quite similar when measured along the ***a*** and ***b*** crystallographic direction, and significatively different from those measured along the ***c*** crystallographic direction [171]. In the KTP-1 2D square pattern, the depths of the channels inscribed along perpendicular directions are also different, due to the material anisotropy. We observed here that the depth of the ablated channel along the ***a*** direction is 6.1 µm, while the depth of the channel along the ***c*** direction is 3.5 µm. These images revealed that the shape of the channels is V-shape. Figure 3 (e) in *paper IV* shows the recorded lateral views of the inscribed conical pores on the KTP-2 sample and the depth of the conical pores was 4.3 µm. From these images we observed that the shape of the conical pores inscribed on the surface of the KTP-2 sample is conical. We also found here that the different laser pulse energy used for KTP-1 and KTP-2 samples resulted in a different diameter for the pores of the KTP-2 sample when compared to the width of the channels of the KTP-1 sample.

We also recorded 2D conical pores on the surface of the KTP-3 sample. Nine different sets of circular pores each in a square array were inscribed at 1 sec, 5 sec and 10 sec irradiation time with a pulse duration of 120 fs, and an output pulse energy was 300 µJ with a central wavelength of 799 nm, by femtosecond laser ablation process on the (001) surface of the KTP sample. The morphological characterization of the inscribed conical pores on the surface of KTP-3 sample by ultrafast laser ablation was carried by using ESEM analysis and revealed a high degree of periodicity. Figure 1 in *paper IX* shows a ESEM image of the inscribed 9 sets of 2D conical pores on the surface of the KTP-3 sample. The higher magnification images are shown to the corresponding set of the images irradiated with

1sec (1st row), 5 sec (2nd row), and 10 sec (3rd row), respectively. In this analysis we observed that the diameter of the conical pore was different in different set of images, due to the change of different laser irradiation times at different set of images while processing the sample. These images show that the diameter of the conical pores is around 28 µm, the period is around 50 µm, and the roughness at the edges of the conical pores is very small when compared for instance with the other microstructures fabricated by ultrafast laser ablation on the surface of crystals of the KTP family and described in chapter 4. A composition of different ESEM micrographs showing these conical pores is shown in Figure 1 in *paper IX*.

4.3. Fabrication and morphological characterization of diffraction gratings by selective chemical etching

Selective chemical etching is a technique which has the effect of distinguishing the presence of optically invisible ferroelectric domains in periodically poled $LiNbO_3$ because of their significantly different etching rates. The technique of etching ferroelectric domains predefined by the technique of electric field induced poling of $LiNbO_3$, can be used to effectively structurate a range of very smooth, well defined micrometer scale spatial structures. The description of this method was discussed in *Paper I*. We used the same technique to fabricate diffraction grating on the surface of $LiNbO_3$ sample. The most common wet selective etchant reported for ferroelectric domains of the $LiNbO_3$ has been a mixture of hydrofluoric acid (HF) and nitric acid (HNO_3), which attacks the negative -Z face of the $LiNbO_3$ at a rate that is appreciably higher than the positive +Z face [172]. At room temperature, in a 1:2 mixture ratio of HF and HNO_3 acids, the –Z face experiences etch rates of ~1 $\mu m.h^{-1}$, whereas the +Z face remains unetched [173]. Even at temperatures up to 368 K, where the –z etch rate increases to ~30 $\mu m.h^{-1}$, the +z face appears not to be etched at all, apart from at isolated sites where defects or dislocations may occur [174]. Furthermore, independent of the mixture composition, the etch depth increased linearly with respect to the etching time [175].

We used a commercially available periodically poled $LiNbO_3$ crystal sample from INO, 0.5 mm thick, with a period of 5.4 µm. The sample was etched in a $HF:HNO_3 = 1:2$ ratio acid mixture for 30 min at room temperature. After etching, the surface was observed by optical and electronic microscopy.

Optical microscope images were recorded after finishing the chemical etching process to visualize the ferroelectric domains pattern on the surface of the $LiNbO_3$ sample. Figure 4.2 shows the optical microscope images of the diffraction grating fabricated by selective chemical etching on the surface of the $LiNbO_3$ sample. Figure 4.2 (a) shows the image taken with a 5× objective while Figure 4.2 (b) shows a higher magnification of the same diffraction grating taken with a 50× objective.

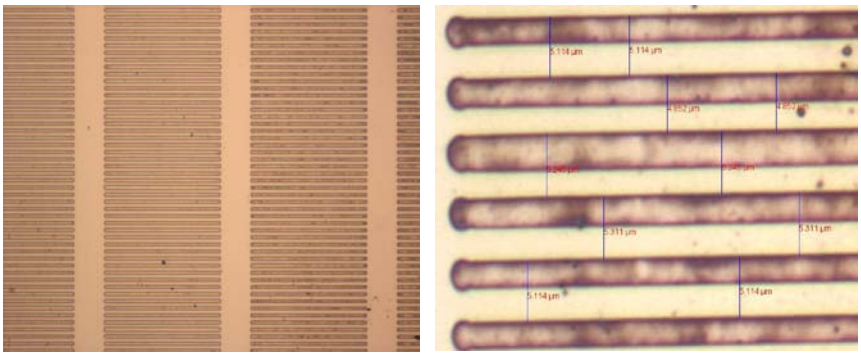

(a) (b)

Figure 4.2. *Optical microscope images of the $LiNbO_3$ sample: (a) image taken with a ×5 objective, and (b)image taken with a ×50 objective, with the lattice constants dimensions measured.*

We see two different types of periodicities in Figure 4.2 (a). One pattern with a large period consisting in the distance between the different columns that can be observed in Figure 4.2 (a) was generated by the mask used in the periodic poling process. The other pattern is the one revealed by the selective chemical etching process applied and consist on the different ferrelectric domains that can be observed in detail in Figure 4.2 (b). This pattern appears as very smooth walled. We estimated the lattice constant using these optical microscope images. The estimated lattice constant of the diffraction grating taken from these images was 5.13 µm.

The SEM micrographs showing the diffraction grating revealed by the selective chemical etching process on the surface $LiNbO_3$ sample can be seen in Figure 3 in *paper I*. If we compare the grooves with those generated by other techniques, we observe that the walls of the grooves are smooth on the surface of the $LiNbO_3$ sample. The high quality of the diffraction grating recorded on the surface of $LiNbO_3$ sample is also evident in this SEM images. The roughness of the lateral walls

and the bottom of the grooves is also very small when compared with the results obtained by using the ultrafast laser ablation technique.

The lateral view of the diffraction grating recorded on the surface of the $LiNbO_3$ sample is shown in Figure 4.3. The lattice constant of the grooves separated by removing one of the ferroelectric domains is observed to be roughly 5.2 μm, consistent with the data previously estimated from the optical microscope images. The depth of groove is around 239.5 nm. These SEM images revealed that the selective chemical etching technique can produce very smooth and high quality diffraction gratings with a uniform structure. But if the important parameter is the depth of the grooves, then the ultrafast laser ablation could be a better choice for fabricating the diffraction gratings

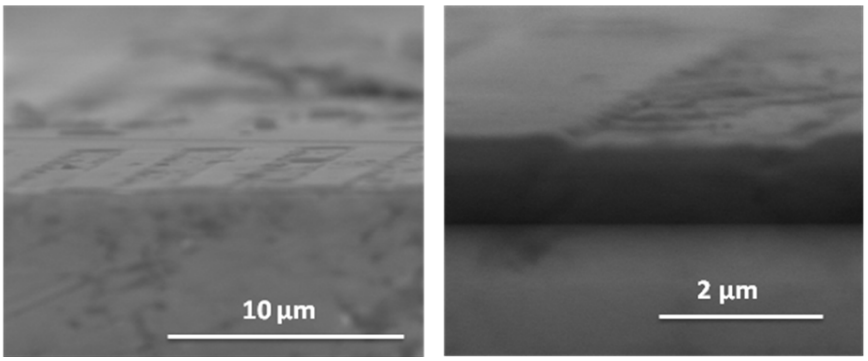

Figure 4.3. *Cross sectional SEM images of the channels inscribed on the surface of a periodically poled $LiNbO_3$ crystal by selective chemical etching (a)low magnification image, and (b) high magnification image.*

AFM images of the diffraction grating on the surface of $LiNbO_3$ sample were also recorded and shown in Figure 4.4. These images confirm that the walls of the grooves are smooth, and high degree of periodicity in the diffraction grating, indicating a high quality.

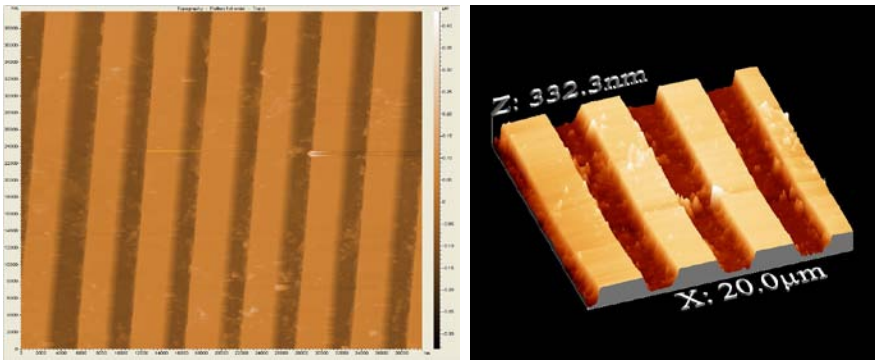

Figure 4.4. *AFM images of the $LiNbO_3$ sample (a) 2D image (b) 3D image*

The selective chemical etching technique has also been used to improve the quality of the inscribed diffraction gratings in crystals of the KTP family. A molten mixture of KOH:KNO_3 has been studied for this purpose. Here, we used this chemical etchant to smoothen the lateral walls of the diffraction gratings fabricated by the ultrafast laser ablation process. We performed the chemical etching process by dissolving the mixture of KOH:KNO_3 = 2:1 M ratio in distilled water at 353 K, and immersed the RTP-2 diffraction grating from 5 min to 1 h in this mixture.

To check the morphology of the etched RTP-2 diffraction grating, we recorded SEM images at each etching time from 5 min to 1 h. We observed that the edge of the groove is better defined with the chemical etching and the roughness of the lateral walls of the channels is reduced. The best results were obtained for an etching time of 15 min. The obtained results are shown in Figure 4 in *paper V*. Beyond this etching time, the groove is becoming wider, and the different ferroelectric domains start to be revealed on the surface of the sample, affecting the groove structure after 1 h of exposure to the etchant. This indicates that the sample was not constituted by a single ferroelectric domain, and that for long exposure times we start to reveal the distribution of the ferroelectric domains on the surface of the sample. By this analysis, it is clear that chemical etching with KOH:KNO_3 can be used to improve the quality of the features fabricated on the (001) surface of the RTP-2 crystal by using the ultrafast laser ablation.

4.4. Analysis of structural modifications on the diffraction gratings

Micro-Raman spectroscopy is the only technique capable of mapping the distribution of stresses in different materials with a good spatial resolution of around 1 µm. Micro-Raman scattering was used to analyze the structural modifications of the RTP and KTP samples by the effects of the ultrafast laser ablation process while processing the surface of the samples. The experimental details of the micro-Raman scatting technique were discussed in detail in Chapter 2.

4.4.1. $RbTiOPO_4$ (RTP)

We investigated the possible structural modifications in the ablated and unablated areas of the RTP-1 and RTP-2 samples by recording the micro-Raman spectra. Figure 5 in *paper IV*, and Figure 2 in *paper VII*, show the recorded micro-Raman spectra along the surface covering with an ablated and unablated areas of the samples. In Figure 5 in paper IV, we found two different spectra for ablated and unablated regions, respectively. In the unablated region the recorded spectrum coincides with the spectrum reported for a polarized $z(yy)\bar{z}$ geometry the RTP single crystal [176]. These results are shown in Figure 3 (b) in *paper VII*.

The Raman spectrum recorded at the ablated areas coincided with that of polycrystalline RTP, recorded for powdered RTP with sizes between 5 to 20 µm. These results are shown in Figure 3(c) in *paper VII*. These results indicate that there exists a polycrystalline layer deposited on the ablated region of the RTP diffraction gratings. This polycrystalline layer of RTP could possibly be formed by sublimation of the material and later condensation on the surface of the single crystal during the ultrafast ablation process. This layer is strongly attached to the surface of the grooves and could not be removed by mechanical means. In fact we observed the ejection of high quantities of material during the ablation process, and pent of it can be rediposited as polycrystalline RTP. The corresponding images of the ejection of the material during the ultrafast laser ablation are shown in Figure 4.5. This phenomenon has not been reported for other nonlinear optical materials.

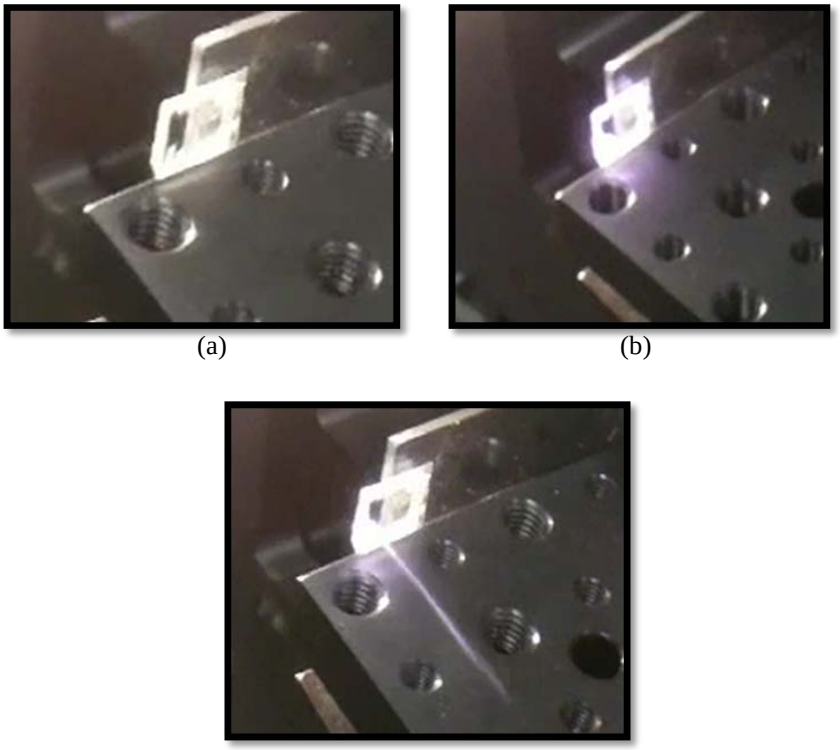

(a) (b)

(c)

Figure 4.5. *Processing of the material during ultrafast laser ablation process (a) before the ablation process, (b) during the ablation process, and (c) ejection of the material from the sample.*

These two different spectra show two peaks with maximum intensity located at 758 cm^{-1} and at 693 cm^{-1} for the spectra recorded in the unablated and ablated regions, respectively. We focused our attention on the peak located at 758 cm^{-1}, and we established the volume of the material affected by the ablation process by plotting the variation for the intensity of this peak along the surface and depth of the sample. These results are shown in Figure 4 in *paper VII*. We compared the profile establish with the Raman results, with that observed in SEM images of the same area. From these results, we observed that the area affected by the ablation process is wider than the ablated area. In the case of the RTP-1 sample, the profile established by Raman scattering is 1.05 μm wider at each side of the channel (see Figure 4 (a) in *paper VIII*) while it is thinner in the case of the RTP-2 sample (see Figure 4 (b) in *paper VIII*). This would indicate that it exist a layer of polycrystalline RTP at around the channel.

Since the Raman spctra were collected every 0.5 µm, this would coincide with the roughness determined from the SEM images recorded for this sample. In depth, we observed that it exists an area of a thickness of 2.75 µm for the RTP-1 sample, around the channel that was affected also by the ultrafast laser ablation process, as it can be seen in Figure 4 (c) in *paper VII*. This area also thinner in the case of the RTP-2 sample, as can be seen in Figure 4 (d) in *paper VII*. The schematic views of the affected ablated areas along the surface and depth of the channels are shown in Figure 5 in *paper VII*, for the RTP-1 and RTP-2 samples, respectively.

Further, we extended our investigation to explore the possibility of removing the polycrystalline layer of RTP and reveal the possible internal stresses generated during the ultrafast laser ablation process on the RTP samples. To investigate this, the RTP-1 sample was annealed for 5 h at 1173 K. Micro-Raman spectra were recorded at the ablated and unablated regions of the annealed RTP-1 sample and these results were shown in Figure 6, in *paper VII*. From these results, we observed that the peak located at 693 cm^{-1} in the ablated region is still present but it is not the most intense peak of the spectrum, after the annealing process. The most intense peak is observed at 142 cm^{-1}, also several new peaks with medium intensity appear at 638, 515, 394, 272 and 211 cm^{-1}. This spectrum corresponds to TiO_2 in its anatase form. To confirm these results, we recorded X-ray diffraction patterns on the ablated area of the RTP-1 sample. The X-ray diffraction pattern was recorded under specific conditions to avoid the diffraction of the (001) plane of the substrate, and maximizing in this way the contributions from the polycrystalline layer on the ablated channels. The recorded X-ray diffraction pattern was shown in Figure 7 in *paper VII*. The obtained X-ray diffraction shows that there exists a mixture of TiO_2 in their forms of anatase and rutile, and a minority phase corresponding to polycrystalline RTP. The most intense peak corresponds to anatase, indicating that this is the majority phase in the mixture. The phase transition in TiO_2 from anatase to rutile usually happens at around 1073 K [177]. However, in small particles, the surface free energy and the surface stress play a crucial role in rendering the phase stability of anatase, that depending on the conditions can be stable up to 1173 K, coexisting then with rutile [178]. This would coincide with the situation that we observed in our case. Then, it seems possible that due to the lower temperature at which it happens the decomposition of RTP in this case, we can stabilize the anatase phase, while from the previous studies in our group

[179], we could only observe the formation of rutile, since the RTP decomposed at much higher temperatures.

Again, we plotted profiles of t he channels by monitoring the intensity of the peak at 142 cm^{-1} from the Raman spectra along the surface of the unablated and ablated areas, and along the depth of ablated areas of the annealed sample. The corresponding profile is shown in Figure 8 in *paper VII* using a SEM image of the channel as background. These results show the thickness of the layer TiO_2 around the ablated channels that was found to be 0.5 µm at each side of the channel and 2 µm along the the depth of the channel. This profile is shown in Figure 9 in *paper VII*.

Since, we have not succeeded in removing the polycrystalline layer of RTP on the ablated region by using an annealing process, we extended our investigation to explore the possibility of removing this polycrystalline layer by selective chemical etching channels in the RTP-2 sample. Figure 10 in *paper VII*, shows the recorded SEM images of the selectively etched channels of the RTP-2 sample, with the times going from 5 min to 1 h. These images revealed the widening of the grooves with the etching time, and reduction of the roughness of the grooves with etching times going from 5 min to 15 min. Later, we did not see any reduction of the roughness of the lateral walls of the ablated channels, instead we observed the appearance of the ferroelectric domain that constitute this sample structures after etching time larger than 30 min (see Figure 10 (f) in *paper VII*). Micro-Raman spectra were recorded on the ablated and unablated regions of the chemically etched RTP-2 sample. In that case, the spectra use the same for the ablated and unablated areas (see Figure 11 (a)). In that case we plotted the profile of the channels by monitoring the intensity of the peak located at 758 cm^{-1} along the surface and depth of the channels after the etching process. We found that the channels are widened 1.65 µm at each side and 0.3 µm in depth by the Raman signal. This difference between the profile obtained by Raman scattering and that observed in the SEM images can only be explained in terms of structural stress of the sample [180].

4.4.2. $KTiOPO_4$ (KTP)

We recorded also the Raman spectra of the KTP-1 2D diffraction grating. The corresponding spectra are shown in Figure 4.6.

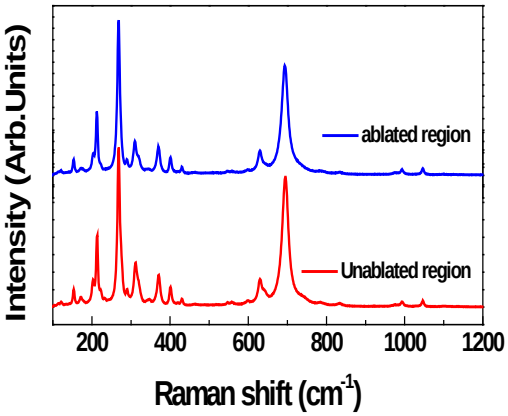

Figure 4.6*. Raman spectra recorded at ablated and unablated regions of the KTP-1 sample.*

We observed no significant changes between the spectra recorded in the ablated and unablated regions on the surface of the sample.

Instead, for the KTP-2 sample, we observed similar results than those obtained in RTP-2 samples, as can be seen in Figure 5 (b) in *paper IV*. We observed that all the peaks appearing at the ablated region are more intense than the peaks observed at unprocessed region. The differences in the Raman spectra between the KTP-1 and KTP-2 samples might be related with the face on which the diffraction grating were inscribed, the (010) face in the case of the KTP-1 sample and the (001) face in the case of the KTP-2 sample.

CHAPTER
FIVE

Optical characterization of the diffraction gratings inscribed on the surface of the nonlinear optical materials

Diffraction gratings, which are an integral part of many modern optical systems, have been widely investigated and found to be applicable in lasers, telecommunications, diffraction optics, optical switches, etc. Therefore, understanding the properties of the diffraction gratings. We fabricated on the surface of nonlinear optical materials will be useful to evaluate their performance. With this characterization of the diffraction grating we will be able to evaluate the conversion efficiency of frequency doubling when illuminating them with intense laser radiation, to characterize the potential fundamental and frequency doubled beams after the diffraction grating, and to develop potential applications for these devices such as any kind of beam manipulation or demultiplexing, particularly useful in telecommunications.

This chapter is organized as follows, in the two following sections we will walk through the determination of the period of the RTP, KTP and $LiNbO_3$ diffraction gratings by FT-IR Bragg´s diffraction (Sec. 1), and the qualitatively determination of the quality of the diffraction by recording the linear diffraction patterns (Sec. 2). In the next sections, we extend our investigation to determine the shape of the channels by optical means (Sec. 3), and we also discuss about the generation of second harmonic radiation from 1D and 2D diffraction gratings inscribed on the surface of nonlinear optical materials (Sec. 4). Finally, in Sec. 5, we discuss about the modeling and characterization of the as-fabricated diffraction gratings as potential 1D photonic crystals.

5.1. Determination of the period of the diffraction gratings by optical means

As we discussed in chapter 4, the SEM images revealed that the roughness of the as-fabricated RTP and KTP diffraction gratings is very high. Due to the existence of the roughness in the fabricated channels or grooves, it was very difficult to measure the precise lattice constants of these diffraction gratings using only the SEM images.

Here we proposed to use a long range order technique to evaluate this parameter. For this purpose Bragg-diffraction spectra of these samples have been recorded by using a FT-IR spectrometer (Bruker-Vertex 70) equipped with a special attachment that allows us to record the spectra by reflectivity. The details of this experiment were given in *Paper III.* In all these measurements, the specular reflection at an incidence angle of 12º was taken as reference. The incident light was pointed perpendicular to the 1D and 2D samples surface and several diffraction spectra were measured perpendicularly to the channels or grooves at collection angles ranging from 24º to 60º in 2º steps.

To evaluate the period from the recorded Bragg-diffraction spectra, the collected data were post-processed in several steps. Unwanted intensity maxima in these spectra corresponded to a noise coming from the resolution limit of the detector we used in the defined spectral range. To reduce this noise, the first step of the post processing procedure consisted in calculating an average on the spectra. For all

wavelengths, the dependence of the intensity with the diffraction angle shows the same tendency in all the samples. To remove this tendency we followed another step that is a flattening procedure. The flattening procedure consisted of fitting the intensity to a straight line for each wavelength and subtracting the resulting straight line from the data. The flattening procedure could improve the spectra to recognize clearly the different diffraction orders. The final step was used to evaluate the period of the diffraction grating flattened data with a function where, at least, one adjustable parameter was related to the period.

To evaluate the lattice constant, the Bragg-diffraction spectra were fitted to the 2-variable function

$$I(\lambda, \sin\theta) = -\sum_{n=1}^{3} \exp\left[\left(\sin\theta - \left(m\lambda/\Lambda\right)\right)/w_n\right]^2 \qquad \text{Eq. 5.1}$$

where Λ is the lattice constant of the diffraction grating, m is the diffraction order, and w_n is the parameter that takes into account the width of the diffraction peaks [181]. By fitting this function to the experimental data, we obtained a robust estimation of the lattice constant of the diffraction gratings, since all measurements were taken into account simultaneously.

Figure 5 in *paper V* shows the 2D intensity plots as a function of the wavelength and the diffraction angle of the measured data for the 1D diffraction grating recorded on the surface of the RTP-1 sample. In the same figure it is also shown the corresponding calculated data by the fitted function, for the same sample.

Experimentally we observed three diffraction orders in RTP-1. The most intense peak was referred as the zero order peak and appeared in the range between 4 and 8 μm for low values of sin θ with a lower slope.

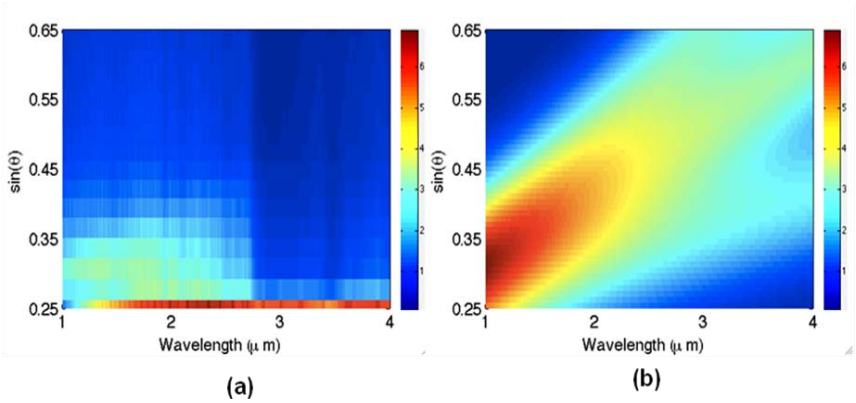

Figure 5.1. *(a) 2D intensity plot as a function of the wavelength and the diffraction angle corresponding to the 1D diffraction grating inscribed on the surface of the RTP-2 sample with a spatial period of 20 μm by ultrafast laser ablation, and (b) 2D calculated plot of the fitted function to the experimental data after considering one diffraction order.*

The first and second diffraction orders are observed at higher values of sin θ with higher slopes. These results fitted perfectly with the calculation from Bragg's law using Eq. 5.1. The period for the RTP-1 sample was estimated to be 14.98 µm, in good agreement with the results obtained from optical and electronic microscope images.

Instead, experimentally we observed only one diffraction order for the RTP-2 sample, as shown in Figure 5.1 (a). We believe that this might be due to the existence of two sub-periods on the surface of RTP-2 sample that created interference patterns that difficult the observation of higher diffraction orders by this method. Figure 5.1 (b) shows the 2D plot of the calculated data by the fitted function shown in Equation 5.1 for this sample.

With these results we estimated a period of 19.85 µm for the RTP-2 sample, indicating that this technique could not resolve the two sub-periods observed in this sample by the optical and SEM images.

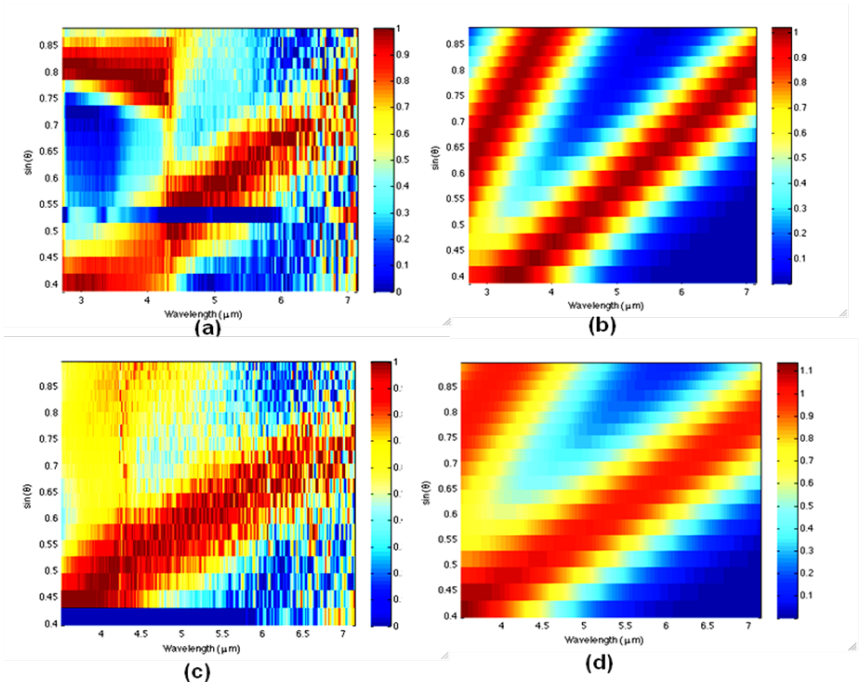

Figure 5.2. *(a) 2D intensity plot as a function of the wavelength and the diffraction angle of the diffraction grating with a period of 8.9 μm inscribed by ultra fast laser ablation on the surface of the KTP-1 sample. (b) 2D calculated plot of the fitted function to the experimental data after considering two diffraction orders. (c) 2D intensity plot as a function of the wavelength and the diffraction angle of the diffraction grating with a period of 9 μm inscribed by ultrafast laser ablation on the surface of the KTP-2 sample, and (d) 2D calculated plot of the fitted function to the experimental data after considering two diffraction orders.*

Similar measurements were performed on the KTP-1 diffraction grating fabricated by ultrafast laser ablation. Figure 5.2 (a) and (b) show the experimental and calculated data by the fitted function shown in Equation 5.1 for the KTP-1 sample, respectively. From Figure 5.2 (a), we observed that only two diffraction orders were obtained. The intensity of the diffraction orders decreases as the collection angle of Bragg-diffracted light increases. For all wavelengths, this dependence of the intensity with the angle θ shows the same tendency. The estimation of zero order from 3 to 7 μm by calculation from Bragg´s law coincided with our experimental results. From the fitted function data, the evaluated period for the KTP-1 sample was 9.1 μm, in

good agreement with the values of the period for this sample estimated by optical and electronic microscope images although this technique could not distinguish between the values for the periods evaluated along different directions by the microscopy techniques.

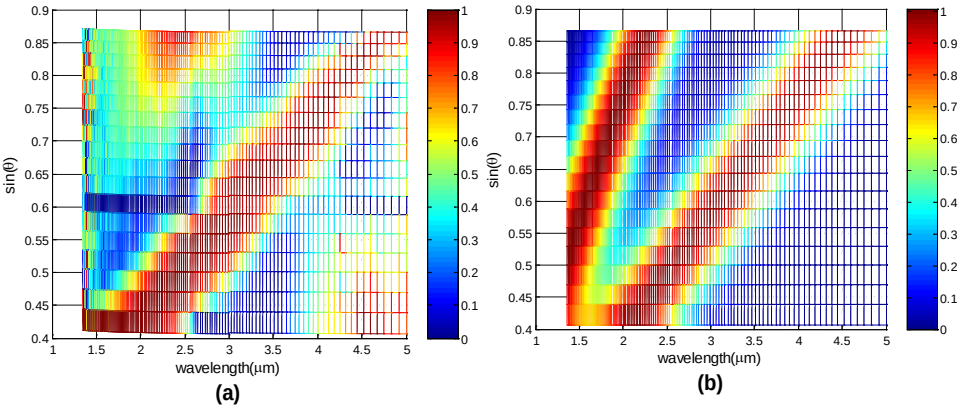

Figure 5.3. *(a) 2D intensity plot as a function of the wavelength and the diffraction angle of the diffraction grating with a period of 5 μm chemically etched on the surface of the PPLN sample (b) 2D calculated plot of the fitted function to the experimental data after considering two diffraction orders.*

We also performed similar measurements on the KTP-2 sample for the precise evaluation of the period of the diffraction grating. Similar results were obtained as like in the KTP-1 sample. We observed only two diffraction peaks in the experimental data. Figure 5.2 (c) and (d) show the measured and calculated data obtained for the KTP-2 sample, respectively. The evaluated period from the fitted function data for the KTP-2 sample was 9 μm. These results are in good agreement with the estimated lattice constant from optical and electronic microscopy. Again, however, this technique gives an average value of the period, and it does not distinguish the different periods observed along the different directions.

Finally, the same procedure has been applied to the diffraction grating fabricated by selective chemical etching in the periodically poled $LiNbO_3$ (PPLN) sample. The corresponding experimental and calculated data are shown in Figure 5.3.

The zero order peak was observed from 1 to 5 μm, as expected from the calculation from Bragg´s law. In this case, only two diffraction orders could be

considered to estimate the period of the diffraction grating. The estimated period was 5.23 μm and this value was in good agreement with the period measured by optical and electronic microscope analysis.

The values of the estimated periods from FT-IR Bragg diffraction of the different diffraction gratings fabricated by ultrafast laser ablation on RTP, and KTP samples, and the diffraction grating fabricated by selective etching on the PPLN sample are summarized in Table 5.1.

Table 5.1. *Periods observed by optical microscopy and estimated by Equation 5.1 on the different diffraction gratings fabricated in this work*

Sample	**Lattice parameters estimated from optical microscope images (μm)**	**Lattice parameters calculated from Bragg´s diffraction law (μm)**
RTP-1	14.92	14.98
RTP-2	9.4 and 10.48 (sub-periods)	19.85
KTP-1	8.95 //***a***, 8.91//***b***	9.1
KTP-2	9.04 //***a***, 9.02 //***b***	9
$LiNbO_3$	5.13	5.23

5.2. Diffraction of the fundamental beam

We also analyzed the characteristics of the diffraction pattern of a fundamental beam in the visible, which will provide information about the quality of the diffraction gratings we fabricated. The experimental details on how these diffraction patterns were recorded were discussed in Sec. 2.7.1, Chapter 2.

The recorded linear diffraction patterns on the RTP and KTP samples in the transmission configuration are shown in Figure 4 in *paper III*. On the screen, up to 11 diffraction orders, from +5 to -5 diffraction orders were generated by the RTP-1 sample (see Figure 4 (a) in *paper III*). The RTP-2 sample generated up to 15 diffraction orders from +7 to -7 diffraction orders (see Figure 4 (b) in *paper III*). Also in this sample, due to the sub-period existing in the diffraction grating, we observed a modulation on the intensity of the diffraction spots. Even orders show a larger intensity than odd ones.

Similarly in the case of the KTP-1 sample, we observed a large number of diffraction spots. In this case the diffraction pattern is defined in two dimensions, representing the square pattern of the diffraction grating inscribed on the (010) surface of the sample formed by two orthogonal arrays of grooves. The corresponding diffraction pattern was reported in Figure 4(c) in *paper III*. Finally, the KTP-2 sample had a pattern formed by conical pores forming a square grid on the (001) face of the sample. The diffraction pattern for this diffraction grating was reported in Figure 4(d) in *paper III*.

In all the samples, the large number of diffraction orders that were observed indicate a good quality for the diffraction gratings fabricated, regardless the roughness of the lateral walls of the grooves that we observed by SEM and the variation of the width of the grooves with depth induced by the V-shape of the grooves.

Similarly, we proceeded to record the linear diffraction patterns of the diffraction gratings in a reflection configuration using the same experimental set-up described in Sec. 2.7.1 in chapter 2. The corresponding diffraction pattern of the RTP-1 diffraction grating in the reflection configuration was reported in Figure 6(b) in *paper V*. On the screen, we observed up to 9 diffraction orders, from -4 to +4 diffraction orders. To obtain a clear picture of the diffraction pattern in this reflection configuration, the incident angle of the laser beam was set at 48º to respect the perpendicular to the surface of the sample to avoid internal reflections from the sample. In the RTP-2 sample, up to 11 diffraction orders were visible, from -5 to +5 diffraction orders. In that case the incident angle of the laser beam was set at 52º with

respect to the perpendicular to the surface of the sample. Furthermore, the sub-modulation of the period of the diffraction grating was again reflected in an alternation of high intensity and low intensity diffraction spots in the pattern, as can be seen in Figure 6 (d) in *paper V*. Finally, we also recorded the diffraction patterns generated by the KTP-1 and KTP-2 samples in the reflection configuration and these patterns are shown in Figure 5.4.

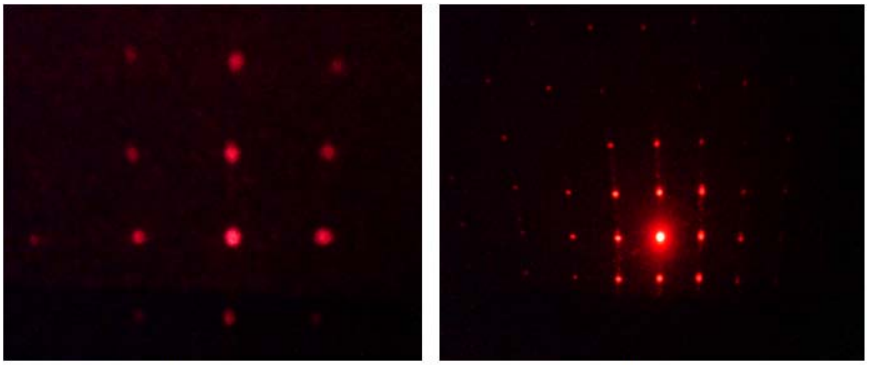

Figure 5.4*. Linear diffraction patterns of the different diffraction gratings recorded in a reflection configuration after illuminating the sample with a He-Ne laser. (a) Diffraction grating on the KTP-1 sample (period 9.1 μm) formed by two orthogonal arrays of grooves on the surface of the (010) face and (b) KTP-2 sample (period 9 μm) formed by circular pores forming a square grid on the surface of the (001) face.*

Figure 5.4 (a) shows the diffraction pattern generated by the KTP-1 diffraction grating recorded in a reflection configuration where the incidence angle of the laser beam was set at 54º. It consist again on a 2D array of diffraction spots with a square disposition. Similarly, we obtained a square grid pattern for the KTP-2 sample. In that case the angle of the incident laser beam was set at 42º. The corresponding diffraction pattern is shown in Figure 5.4 (b). In these pictures we observed a reduced number of spots when compared to the diffraction patterns collected in a transmission configuration due to the lower intensity of the reflected spots.

Finally, we recorded the linear diffraction pattern generated by the diffraction grating inscribed on a periodically poled $LiNbO_3$ crystal by chemical

etching. The recorded diffraction patterns are shown in Figure 5.5 in transmission and reflection configurations.

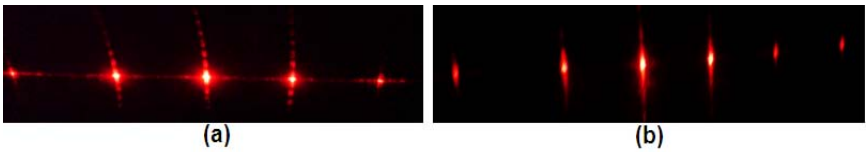

***Figure 5.5**. Diffraction patterns obtained in the $LiNbO_3$ sample in (a) transmission configuration and (b) reflection configuration.*

In the $LiNbO_3$ sample, the periodic ferroelectric domains were generated by using an electrical poling process. In this method, a mask was used to generate the desired grating pattern on the surface of the sample. Later, to reveal the ferroelectric domains fabricated, the sample was selectively chemically etched. This fabrication method produced two different diffraction patterns that are perpendicular to each other as can be seen in Figure 5.5 (a). One with a short period (5.13 µm) due to the ferroelectric domains of the sample revealed by selective chemical etching, that generates more brilliant and highly spaced diffraction spots. The second one, perpendicular to it, is due to the patterned and unpatterned regions in the sample due to the mask used during the electrical poling process. In this case the period is much larger (25 µm), which generates less brilliant and closely spaced diffraction spots. On the screen, we observed only up to 5 diffraction orders generated by the short period of the sample, from -2 to +2 diffraction orders. It was difficult to capture all the lower intensity diffraction orders due to their larger diffraction angles, although the quality of the sample was better. Figure 5.5 (b) shows the diffraction pattern from the same sample recorded in a reflection configuration. The incident angle of the laser beam on the sample was set at 40º to avoid internal reflection. In that case, only the diffraction pattern due to the diffraction grating generated by the selective chemical etching of the ferroelectric domains of the sample was observed. On the screen from -3 to +2 diffraction orders were seen.

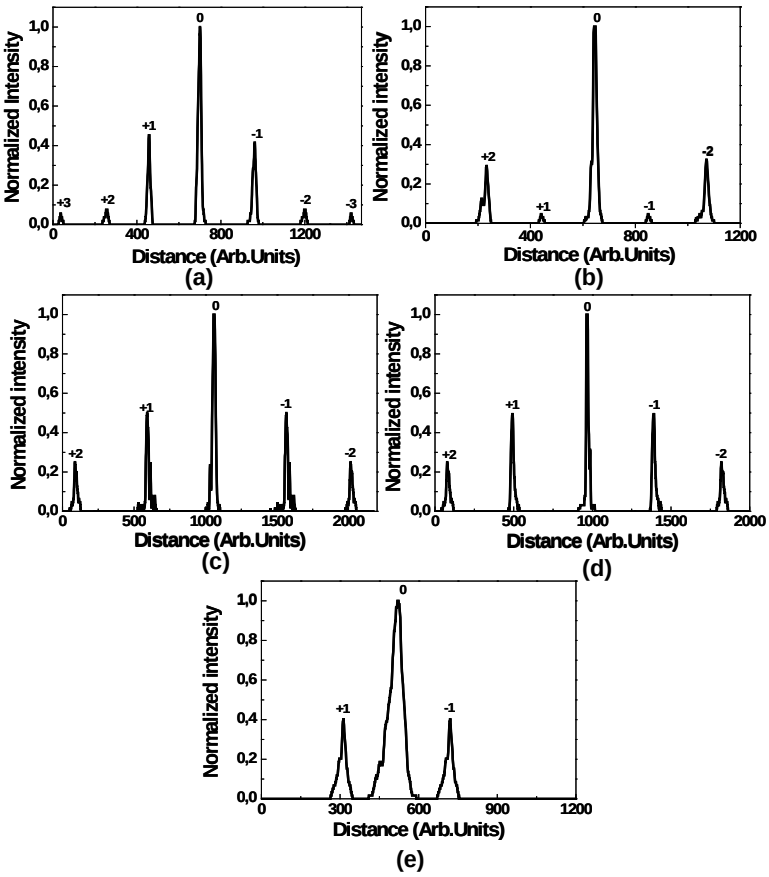

***Figure 5.6**. Intensity profiles of the transmitted diffraction patterns recorded on the (a) RTP-1, (b) RTP-2, (c) KTP-1, (d) KTP-2, and (e) $LiNbO_3$ samples, using the transmission configuration set-up.*

We also recorded the intensity profiles of the generated diffraction patterns from the diffraction gratings measuring them in a transmission configuration. The limited number of diffraction peaks observed was due to the low dynamic range of the CCD camera we used to record these diffraction patterns. These intensity profiles are shown in Figure 5.6. Figure 5.6 (a) shows the intensity profile of the transmission diffraction pattern of the RTP-1 sample. Figure 5.6 (b) shows the corresponding intensity profile for the RTP-2 sample. We see a clear difference on the intensity of the peaks corresponding to the ±1 diffraction orders compared with those

corresponding to the ±2 diffraction orders, due to the sub-modulation of the periodicity of the diffraction grating fabricated on the surface of the RTP-2 sample.

Similar results were obtained in the case of the two orthogonal arrays of channels fabricated on the surface of the KTP-1 sample and the corresponding recorded intensity profile of the KTP-1 sample parallel to the ***a*** direction is shown in Figure 5.6 (c). Similar results were obtained in the case of the diffraction grating fabricated with a square array of conical pores on the surface of the KTP-2 sample. The intensity profile of the generated diffraction from the KTP-2 sample parallel to ***a*** direction is shown in Figure 5.6 (d). Similarly we also recorded the intensity profiles of the diffraction orders generated by the different lines of squares or holes in the KTP-1 and KTP-2 samples, respectively. These intensity profiles are shown in Figure 5.7.

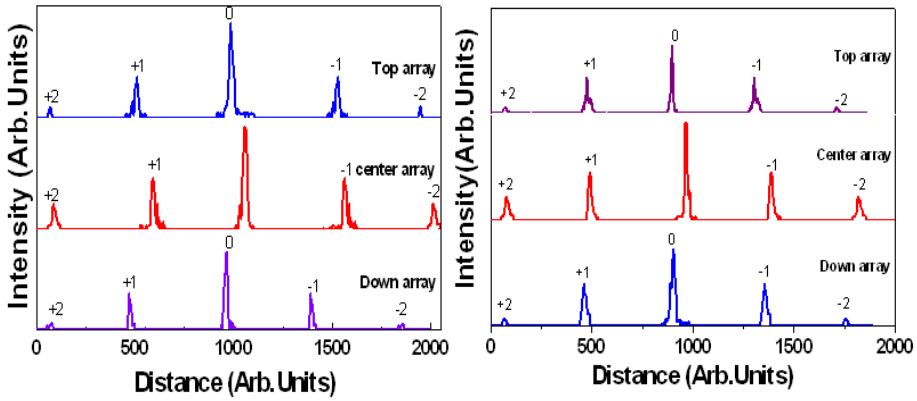

Figure 5.7*. Intensity profiles of the transmitted diffraction patterns recorded on the (a) KTP-1 and (b) KTP-2 samples.*

In this Figure it can be seen that the position of the different diffraction orders changes a little depending on the line at which we record the patterns, showing the slight variation on the period of these 2D diffraction gratings.

In the case of the $LiNbO_3$ sample, only three diffraction orders were observed and the recorded intensity profile of the diffraction pattern is shown in Figure 5.6 (e). We used the intensity profiles to determine the shape of the channels in RTP-1 and RTP-2 samples by optical means, as it has been detailed in section 5.3.

5.2.1. Effect of the wavelength on the diffraction of the fundamental beam

The diffraction patterns produced by the RTP-1 sample were recorded at different wavelengths using as the illumination source an optical parametric oscillator (OPO) (Continuum –Sure light) with a repetition rate of 10 Hz by tuning the wavelengths from 400 nm to 700 nm.

These measurements were performed in a reflection configuration. The details of the experimental set-up used were discussed in Chapter 2. We recorded the generated diffraction patterns and their intensity profiles. In each diffraction pattern, only three diffraction orders were captured due to the limited active area of the CCD camera we used as sensor. The recorded diffraction patterns and their intensity profiles are shown in Figure 5.8 with the corresponding wavelength of the incident beam.

In Figure 5.8, the diffraction images show that by increasing the wavelength of the fundamental beam, the intensity of the ±1 diffraction orders was decreasing and their location was moving out of the range of the camera at higher wavelengths because the diffraction orders are shifting to higher diffraction angles, as expected. At all different wavelengths, the intensity of the zero order is higher than that of the other two diffraction orders and the intensity of the -1 order is smaller than that of the +1 order.

The normalized intensity profiles of these diffraction patterns are over lapped to check the variation of the intensity of the diffraction orders generated from the RTP-1 sample, as a function of the wavelength and these profiles are shown in Figure 5.9. At longer wavelengths, the position of the higher diffraction orders (±1) is shifting and as well as the intensity of these diffraction orders is also changing as a function of wavelength.

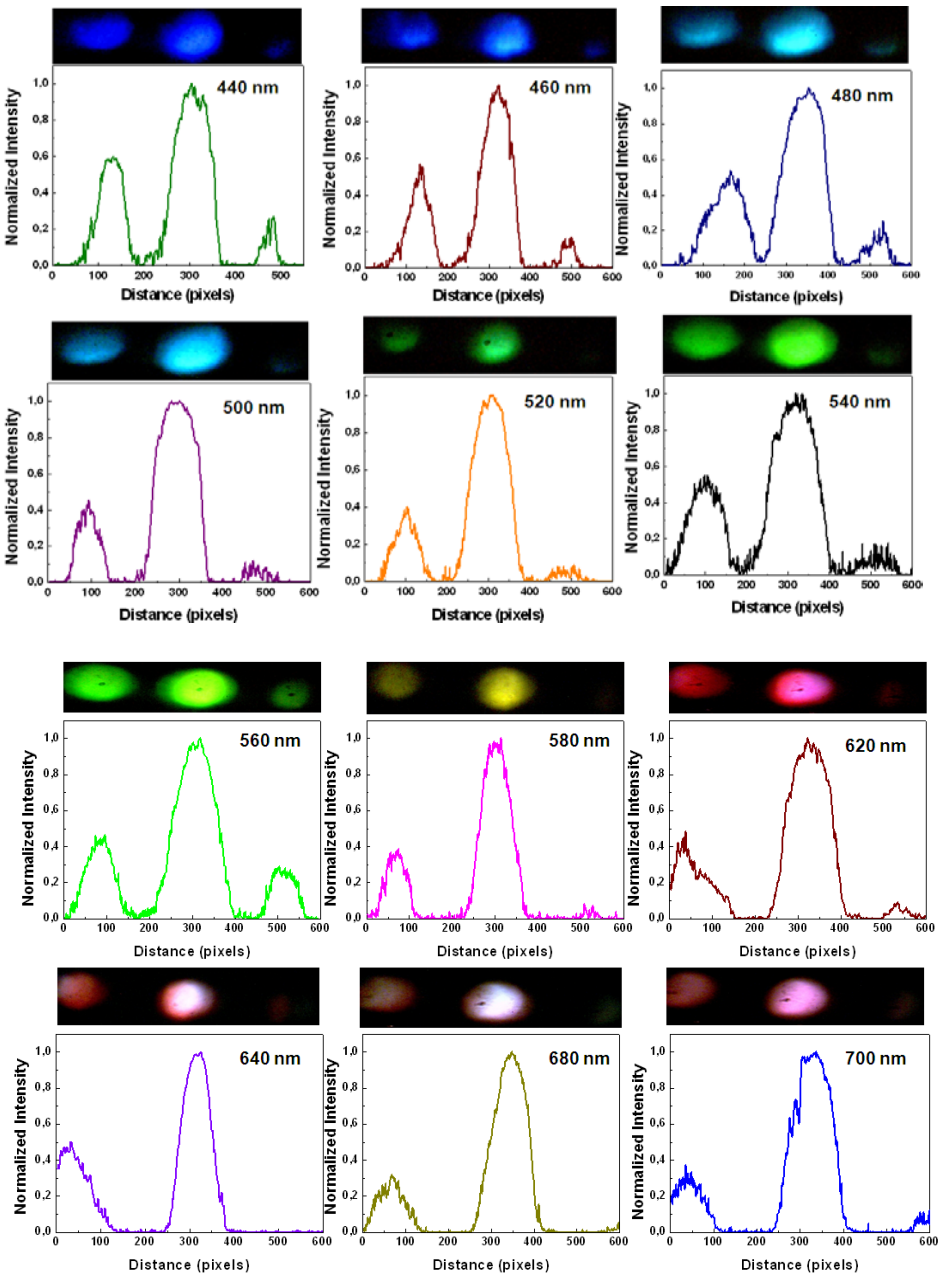

Figure 5.8*. Diffraction patterns and their corresponding intensity profiles generated by the RTP-1 diffraction grating as a function of wavelength.*

The position of the zero order is the same at all wavelengths. The most intense ±1 diffraction orders are observed in the diffraction pattern generated at 480 nm.

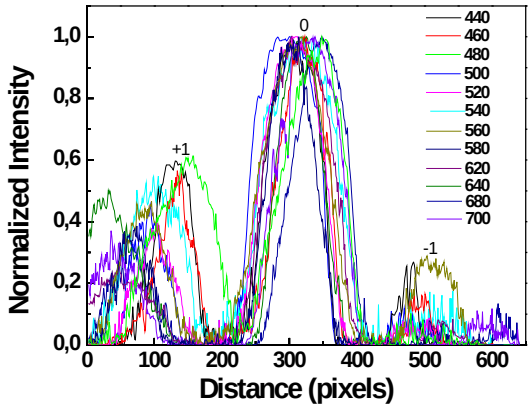

***Figure 5.9**. Normalized intensity profiles of the diffraction patterns generated by the RTP-1 sample as a function of wavelength.*

We also recorded the linear diffraction patterns and their intensity profiles at different wavelengths on the KTP-1 sample.

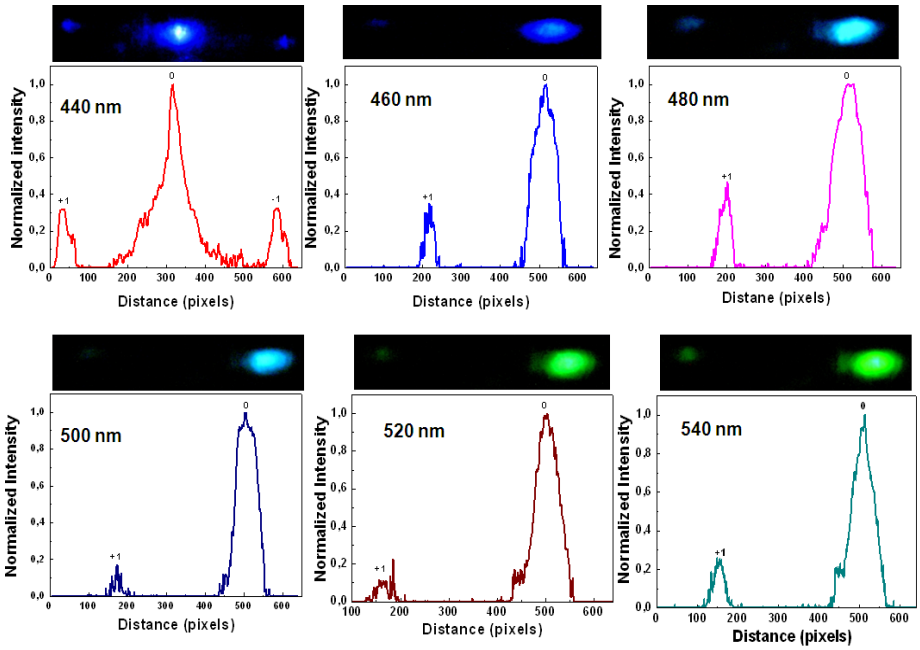

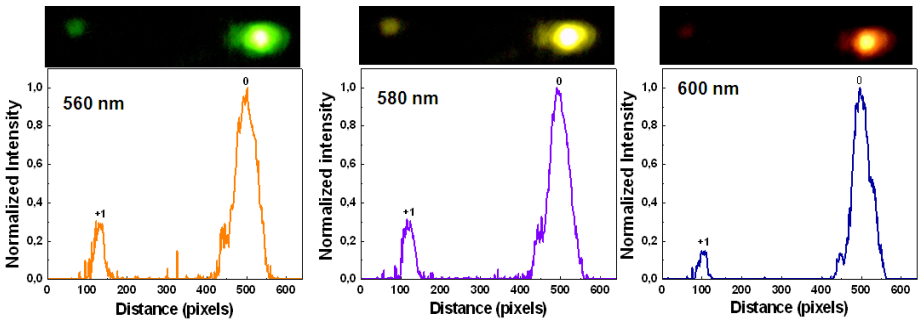

***Figure 5.10**. Diffraction patterns and their corresponding intensity profiles generated by the KTP-1 sample as a function of wavelength.*

In these measurements we observed only three diffraction orders at short wavelengths and two diffraction orders at long wavelengths, due to the limited area of the detector. The diffraction patterns and their corresponding intensity profiles are shown in Figure 5.10.

In Figure 5.10, similar spectral features are observed as like in the RTP-1 sample. The position of the order +1 was shifting with wavelength region to the long wavelength region, as expected.

Similarly, the normalized intensity profiles of the diffraction orders are plotted together and similar results were observed as like in the case of the RTP-1 sample. The corresponding intensity profiles are shown in Figure 5.11. The most effective diffraction patterns were observed at 480 and 580 nm.

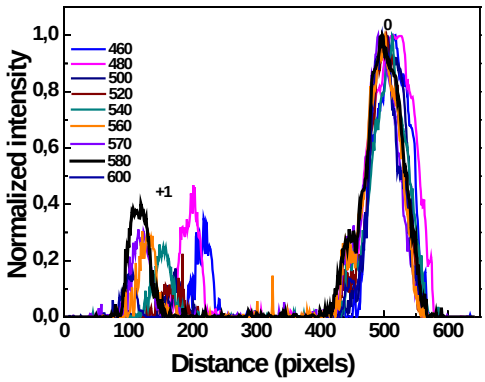

***Figure 5.11**. Normalized intensity profiles generated by the KTP-1 sample as a function of wavelength*

Finally, we also recorded the linear diffraction patterns generated by the KTP-2 sample at different wavelengths. We observed the same spectral features as like in previous measurements. The recorded diffraction patterns and their intensity profiles are shown in Figure 5.12.

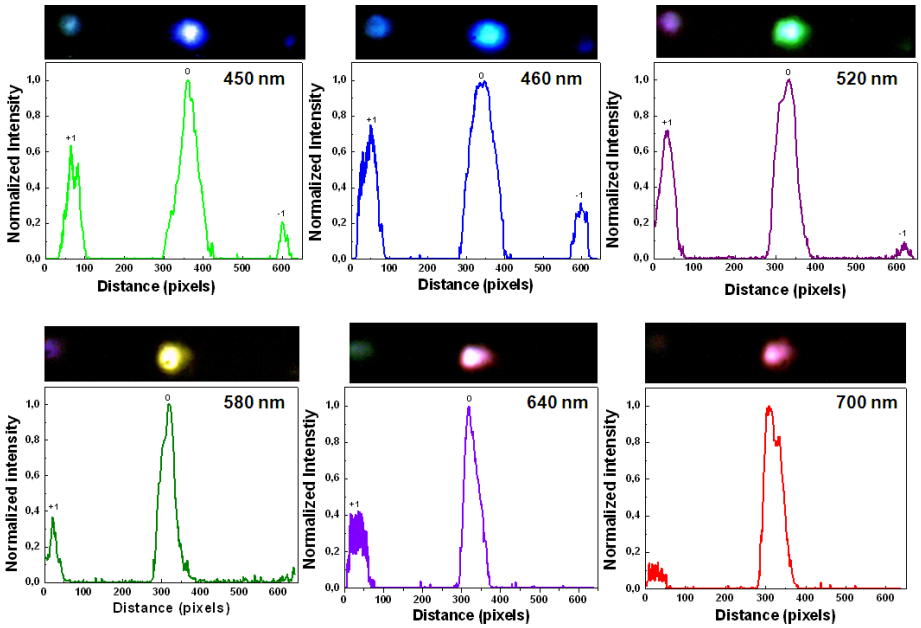

***Figure 5.12**. Diffraction patterns and their corresponding intensity profiles generated by the KTP-2 sample as a function of wavelength.*

The position of the ± 1 orders is shifting to longer wavelengths, as expected, when the wavelength of the incident beam increases. Similarly the normalized intensity profiles of the diffraction orders were plotted and shown in Figure 5.13.

From Figure 5.13, similar results were obtained as like in KTP-1 sample. The most effective diffraction pattern was observed in the short wavelength region at 460 nm, at which the intensity of the ±1 diffraction orders are higher than that of the ±1 diffraction orders observed at other wavelengths.

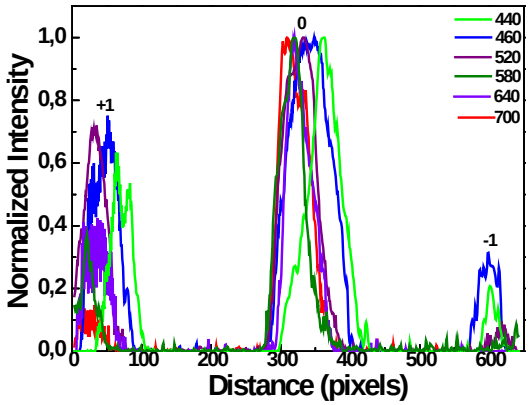

Figure 5.13*. Normalized intensity profiles generated by the KTP-2 sample as a function of wavelength.*

5.2.2. Effect of the polarization on the diffraction of the fundamental beam

The intensity of diffracted light can vary significantly with the polarization of the incident light. Diffraction measurements of the fundamental beam were performed on the surface of the RTP-1 sample with polarized light to investigate the effects of this parameter using a He-Ne laser at 633 nm with a power of 5 mW. In this experiment, a half wave plate located before the sample to depolarize the laser beam and two polarisers, one located before the sample and another in front of the detector, were used to record the intensity profiles of the diffraction patterns generated by the RTP-1 diffraction grating as a function of the polarization of the incident beam and the diffracted beam, in a reflection configuration. The intensity of the incident beam had to be reduced by rotating the half wave plate due to the high sensitivity of the CCD camera.

Four different polarization geometries were used to record the generated diffraction patterns from the RTP-1 sample. The plane of incidence is the plane formed by the incident and exiting beams, and is perpendicular to the surface of the sample. P-polarization refers to light that is polarized perpendicular to the surface of the sample. S-polarization refers to light that is polarized parallel to the surface of the sample. We also used light polarized at 45º of these directions. The four different polarization geometries we recorded are P-P, S-S, 45-P, and 45-S where the first

symbol indicates the polarization of the incident beam, and the second symbol indicates the polarization of the collected diffraction beams. P-S or S-P geometries did not provide any signal. The recorded diffraction patterns and their corresponding intensity profiles are shown in Figure 5.14 with the different polarization configurations used.

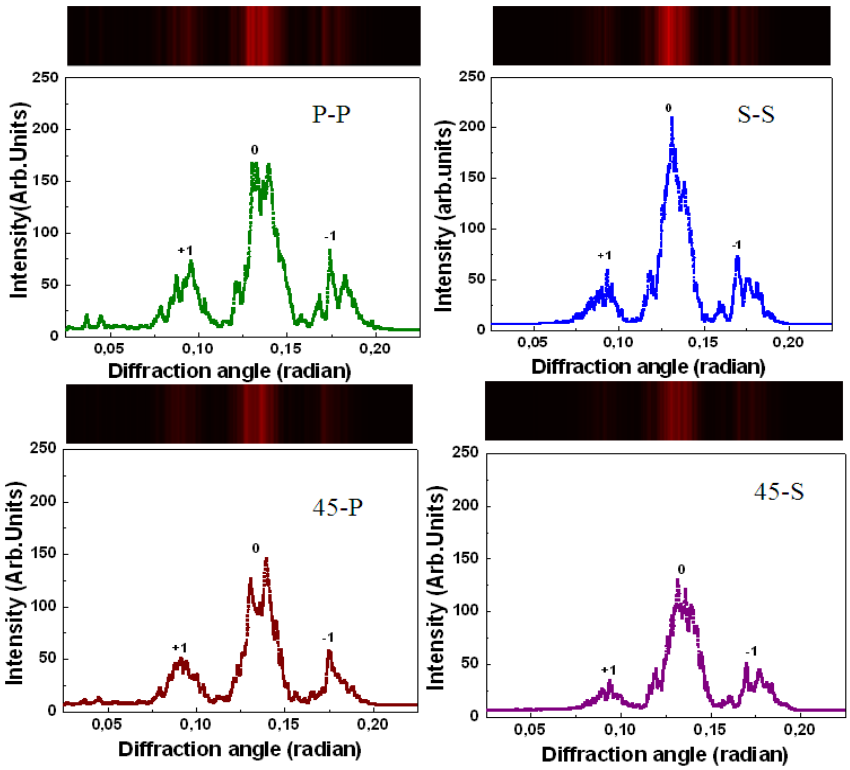

***Figure 5.14**. Diffraction patterns and their corresponding intensity profiles generated by the RTP-1 sample as a function of the polarization of the incident and diffracted beams.*

In Figure 5.14, we observed only three diffraction orders for all the different polarization configurations due to low dynamic range of the 1D array CCD camera. Bright and dark fringes are observed due to the constructive and destructive inference of the light waves. We observed that the intensity of the recorded diffraction pattern for S-S polarization configuration is showing higher intensity for the zero order when compared with the other diffraction patterns obtained. We observed that the P-P polarization configuration can be an efficient configuration because the value of the

intensity ratio between zero order and 1 order was larger when compared with the other polarization configurations.

5.2.3. Estimation of the diffraction efficiency

The diffraction efficiency for these samples was estimated by comparing the intensity recorded at the zero order with that of the incident beam. In both cases, this diffraction efficiency was found to be at around 0.1%. This value is not surprising since the measurements were not performed at the optimum wavelength for these diffraction gratings. However, comparing the quality of these RTP diffraction gratings with those patterns inscribed in $LiNbO_3$ for which up to a 30% diffraction efficiency has been reported and those inscribed in $BaBO_3$ with diffraction efficiencies between 50 to 60 %, one would expect to get similar results when using the optimum wavelength.

5.3. Determination of the shape of the channels by optical means

Diffraction patterns are sensitive to changes in the periodicity of the grating or filling fraction. The filling fraction *f* is referred to as the fraction of the grating period that is filled with the grating material. The value of the filling fraction must be less than 1, since a value of 1 would mean that no diffraction grating exist on the surface of sample. The filling fraction value can be determined from the intensity profiles of the diffraction patterns we recorded. Furthermore, analysing in detail these intensity profiles, we can also determine the shape of the grooves inscribed by ultrafast laser ablation.

In order to model the shape of the grooves and to fit adequately the results, the grating has been considered as a phase only grating, where the grooves introduce a lower phase shift with respect to the parts of the grating without grooves.

We used two different geometries to model the shape of the grooves by this method. Initially, we simplified the phase profile for a square shape with a height *t* (*t* is also referred as depth of the groove), since we considered that a triangular shape would not introduce much changes in the results.

According to this model, Equation 5.2 defines the envelope profile for the different diffraction orders observed in the case of the RTP-1 diffraction grating considering a pure phase grating with a filling fraction *f* and a period Λ.

$$I(K)\alpha\begin{cases}\left|1+f\cdot\left[\exp\left(i\frac{2\pi}{\lambda}(n-1)t\right)-1\right]\right|^2 & K=0\\ \left|\sin(\pi K)/(\pi K)+f\cdot\left[\exp\left(i\frac{2\pi}{\lambda}(n-1)t\right)-1\right]\cdot\sin(\pi fK)/(\pi fK)\right|^2 & K\neq 0\end{cases} \qquad \text{Eq. 5.2}$$

In Equation 5.2, *n* is the refractive index of the grating material, *K* are the different diffraction orders, and λ is the laser wavelength.

We could estimate a filling fraction *f* = 0.57 by fitting to the experimental data obtained for the RTP-1 diffraction grating. This filling fraction indicates that more than half of the diffraction grating inscribed in the RTP-1 sample is filled with RTP, while the rest is filled by air.

To calculate the envelope profile in the case of the RTP-2 diffraction grating, we defined the unit cell of the grating, considering it again as a phase grating, as:

$$P_{unit\_cell}(x)=\begin{cases}\exp(i\varphi)\ \text{for}\left(-\frac{g}{2}-\frac{f}{2}\right)\Lambda<x<\left(-\frac{g}{2}+\frac{f}{2}\right)\Lambda\\ \exp(i\varphi)\ \text{for}\left(\frac{g}{2}-\frac{f}{2}\right)\Lambda<x<\left(\frac{g}{2}+\frac{f}{2}\right)\Lambda\\ 1\,\text{otherwise between}-\Lambda<x<\Lambda\end{cases} \qquad \text{Eq. 5.3}$$

where $\varphi=2\pi(n\text{-}1)t/\lambda$. The parameters *f* and *g* are better defined in the Figure 5.15. This unit cell is periodically repeated every 2Λ.

The envelope of the diffracted intensity in this case is defined as:

$$I(K) \propto \begin{cases} \left|1+\left(\exp(i\varphi)-1\right)\cdot f\right|^2 \quad for\ K=0 \\ \left|\frac{\sin(\pi K)}{\pi K}+\left(\exp(i\varphi)-1\right)\cdot f\cdot\cos(\pi g K/2)\cdot\frac{\sin(\pi f K/2)}{\pi f K/2}\right|^2 \quad for\ K\neq 0 \end{cases} \qquad \text{Eq.5.4}$$

Using Equation 5.4, we estimated a filling fraction f = 0.815 for this sample. This filling fraction indicates that more than three quarter parts of the diffraction grating is filled by RTP in the RTP-2 sample, and only less than a quarter is filled by air.

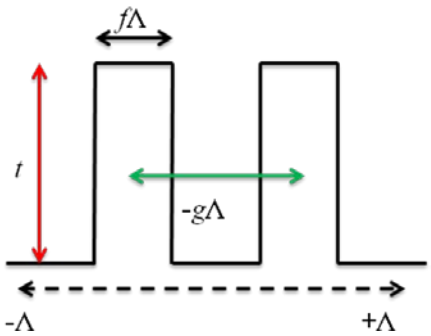

Figure 5.15. *Representation of parameters in the periodic structure of RTP-2 sample.*

Further, we introduced to a more realistic vision of the channels according to the images obtained by ESEM microscopy. We modelled the grooves by considering a triangular shape. This modelling has been reported in *paper V*. In this case, an analytic expression of the envelope of the diffraction order maxima would be very complex, and we avoided it. With this new model and the corresponding fitting envelope profile, the estimated filling fraction was f = 0.43 with a depth of the grooves t = 0.45λ for the RTP-1 sample. This filling fraction indicates that less than half of the diffraction grating inscribed in the RTP-1 sample is filled with RTP, and more than half is filled by air. In the case of the RTP-2 sample, we estimated a filling fraction f = 0.75, and a depth t = 0.35λ. We could also determine the fraction of each sub-period in this structure (g, in Equation 5.3 and 5.4) that corresponded to a value of 0.92. The exact value for g should be 0.95, according to the sub-periodicities observed in the sample. However, no reasonable fit could be obtained with this value of g, indicating also that these sub-periodicities are not exact.

Since we observed significative differences in the determination of *f* and *t* from the modelling of the shapes of the grooves according to a square or triangular shape, we extended this study to clarify which should be the real shape of the grooves according to these optical models in the case of the RTP-1 sample. For this we extended the calculations to different wavelengths and plotted the intensity of the different diffraction orders. The results are shown in Figure 5.16.

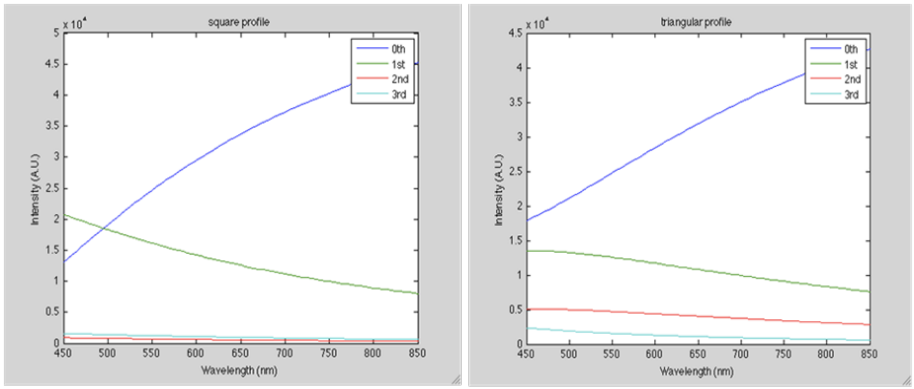

Figure 5.16*. Calculated intensity of the different diffraction orders at different wavelengths for a (a) a square profile and (b) a triangular profile of the grooves of the diffraction grating inscribed on the surface of the RTP-1 sample.*

According to Figure 5.16, if the grooves had a square profile, the intensities of the zero and first orders should cross at wavelengths below 500 nm. Instead, if the grooves have a triangular profile, the intensities of the zero and first orders should not cross in the range of wavelengths between 450-850 nm.

By plotting the intensities of the zero and first diffraction orders as a function of the wavelength, using the data presented in Figure 5.8, we can see that the intensities of these two diffraction orders did not cross at any wavelength (see Figure 5.17) indicating that the correct shape of the grooves is triangular, in agreement with the images obtained by ESEM.

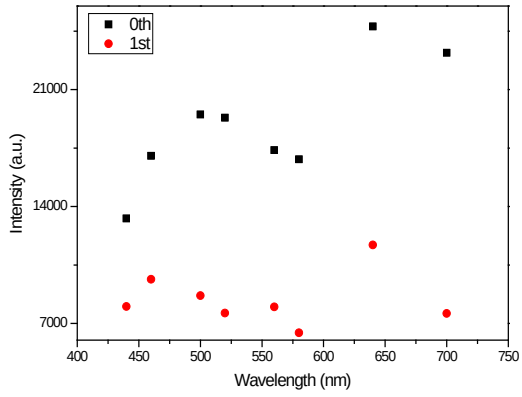

***Figure 5.17**. Experimental intensity of the 0th and 1st diffraction orders at different wavelengths for the RTP-1 sample.*

5.4. Diffraction of the second harmonic generated by the sample (nonlinear diffraction)

5.4.1. Analysis of the RTP-1 sample

Nonlinear diffraction patterns can be generated when a diffraction grating inscribed on a nonlinear optical material generates the second harmonic of the fundamental beam with which the sample has been illuminated. We recorded the nonlinear diffraction patterns generated by the different sample we prepared. For the RTP1 sample, three peaks were observed in the nonlinear diffraction pattern corresponding to the zero and ±1 orders. The generated second harmonic nonlinear diffraction pattern was compared with the diffraction pattern originating from the fundamental beam. The zero order of the fundamental and second harmonic diffraction patterns are located at the same diffraction angle and these patterns are shown in Figure 5 in *paper III*.

However, the most interesting feature of this diffraction pattern is that the intensity of the -1 diffraction order peak is larger than the intensity of the zero order peak, while the peak showing the smallest intensity is that corresponding to the +1 diffraction order, resulting in an asymmetric second harmonic diffraction pattern.

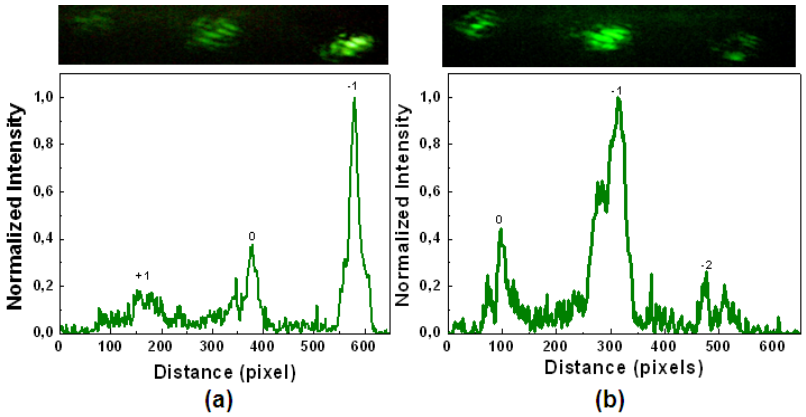

***Figure 5.18**. SHG diffraction pattern and its corresponding intensity profile obtained from the RTP-1 sample.*

A more detailed study of the SHG diffraction pattern in a reflection configuration is shown in Figure 5.18, confirming that the most intense peak in these diffraction patterns is that corresponding to the -1 order.

We then, extended this study by illuminating the sample at different fundamental wavelengths from 910 nm to 1250 nm by using an OPO and recording the second harmonic generated diffraction patterns by the RTP-1 sample in a transmission configuration. The corresponding diffraction patterns and their intensity profiles are shown in Figure 5.19. In all the recorded nonlinear diffraction patterns, three diffraction orders, zero and ±1 were observed. We observed that the intensity of the -1 order is higher than that of the other diffraction orders in all cases. We also observed that the intensity of the +1 diffraction order decreases as we are increase the wavelength.

UNIVERSITAT ROVIRA I VIRGILI
MICROSTRUCTURATION OF NONLINEAR OPTICAL MATERIALS:
METHODOLOGIES, CHARACTERIZATION, AND APPLICATIONS
Raj Kumar Golconda
Dipòsit Legal: T. 55-2013

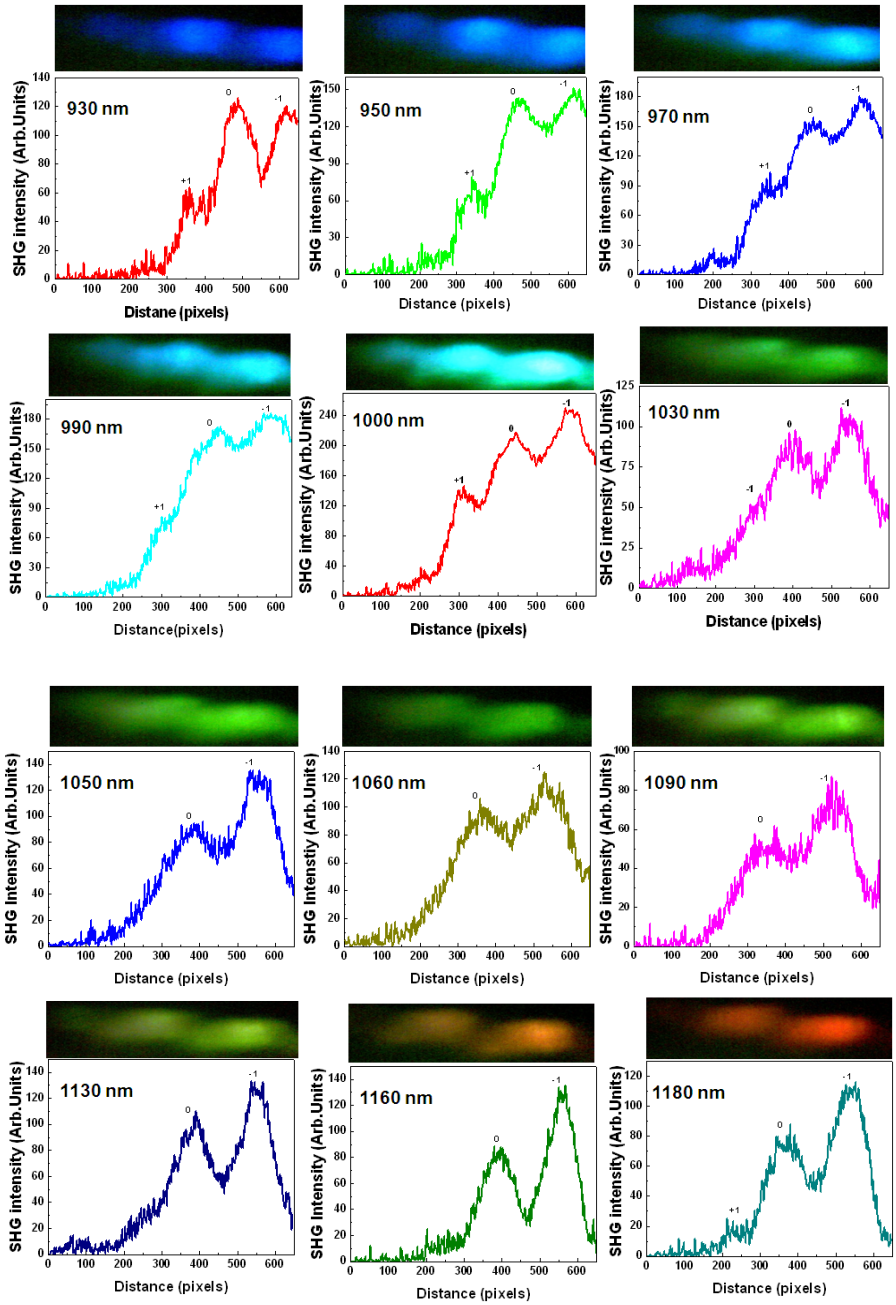

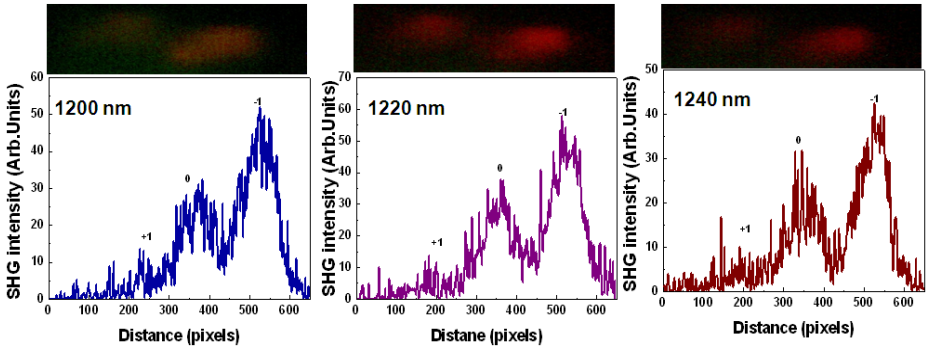

***Figure 5.19**. SHG diffraction patterns and their corresponding intensity profiles obtained from the RTP-1 sample at different wavelengths. The wavelength indicated in the figure corresponds to the fundamental wavelength.*

The results presented in Figure 5.19 indicates that second harmonic generation can be achieved in the RTP-1 sample at fundamental wavelengths ranging from 930 nm to 1240 nm, allowing a broad tuning range. The SHG in such a broad tuning band might be related to the existence of the polycrystalline layer of RTP redeposited after the ultrafast laser ablation process and discovered in the Raman characterization of the sample. From the data presented in Figure 5.19, it seems that the diffraction grating is more efficient in the conversion towards second harmonic at ~1000 nm of the fundamental beam. However, we should also take into account the variation of the power of the incident beam, that unfortunately was not recorded in these experiments excluding the possibility of extracting a definitive conclusion about the efficiency of the diffraction grating..

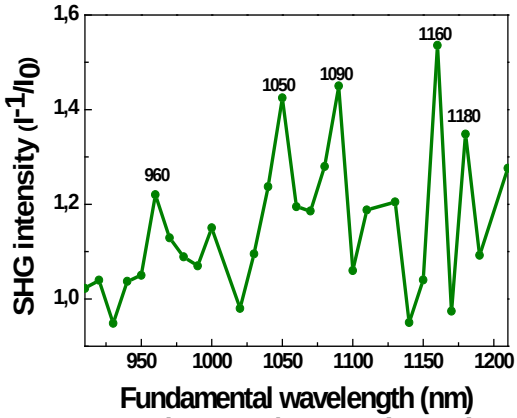

Figure 5.20. *Intensity ratio between the -1 and 0 orders as a function of the wavelength of the fundamental beam in the nonlinear diffraction pattern generated by the RTP-1 sample.*

The ratio between the intensities of the zero order (I_0) and the -1 diffraction order (I^{-1}) can also give as an idea about the efficiency of the diffraction grating as a function wavelength. The ratio I^{-1}/I_0 vs wavelength is shown in Figure 5.20. In this figure, we observe that the I^{-1}/I_0 ratio is in most of the cases higher than 1, showing that the -1 diffraction order is more intense than the zero order, generating then an asymmetric diffraction pattern for the second harmonic light generated by the sample. However, we also observed different wavelengths for which this ratio is maximum, and that are indicated in the figure although we still do not have any explanation for this phenomenon.

The highest I^{-1}/I_0 was obtained at a wavelength of 1160 nm of the fundamental beam. At this wavelength we analyzed the dependence of the I^{-1}/I_0 ratio as a function of the angle of incidence of the fundamental beam. These results are show in Figure 5.21.

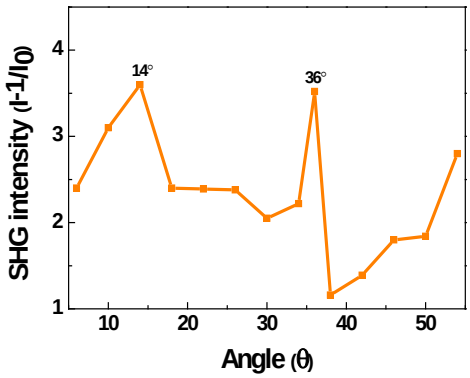

Figure 5.21. *Intensity profile of the ratio between the -1 and zero orders of the second harmonic beam generated by the RTP-1 sample as a function the of angle of incidence of the fundamental beam at 1160 nm.*

In Figure 5.21, the maximum intensity ratio value between -1 and zero diffraction orders at 1160 was observed at 14º and 36º, indicating that the intensity of the -1 order is maximum at these angles. These results also show that by optimizing the angle of incidence, intensities for the -1 diffraction order wave 3.5 times higher than the intensity of the zero order can be obtained. We extended the analysis of the influence of the incident angle of the fundamental beam on the SHG diffraction pattern by tuning the fundamental wavelength from 910 nm to 1080 nm in the RTP-1 diffraction grating. The results are shown in Figure 5.22. In these measurements, we only took into account the intensity of the -1 diffraction order since it was the most intense in all cases.

In Figure 5.22, we observed that the maximum intensity for the second harmonic generated by the sample was obtained between 480 to 500 nm. The optimum incident angle would be 48º.

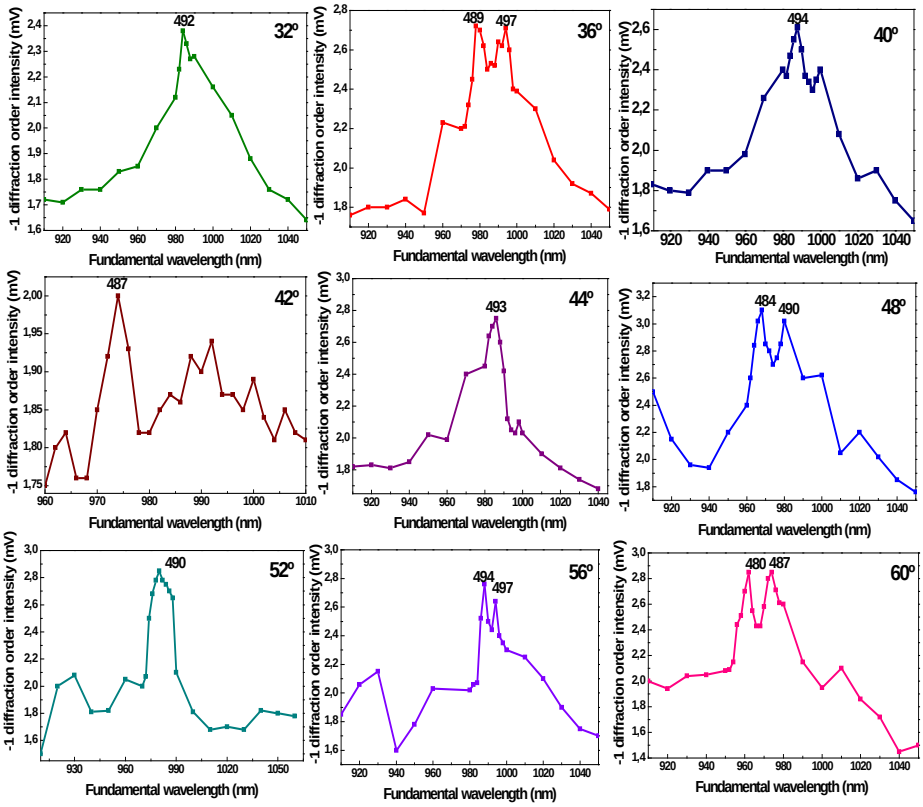

Figure 5.22. *Intensity of the -1 diffraction order as a function of the angle of incidence of the fundamental beam in the range between 910-1080 nm in the nonlinear diffraction pattern generated by the RTP-1 sample. The values shown in the figures indicate the SHG light exhibiting maximum intensities.*

In order to understand the asymmetric behaviour in the nonlinear diffraction pattern of the RTP-1 sample, we collected nonlinear diffraction patterns at different polarization configurations for the fundamental beam and the green light generated in a reflection configuration. The details of the experimental set-up were discussed in Sec. 2.9.2 in Chapter 2. In this set-up we used a CW Nd:YAG laser emitting at 1064 nm.

Four different polarization geometries were used to check the nonlinear diffraction patterns generated from the RTP-1 sample. These diffraction patterns are shown in Figure 5.23.

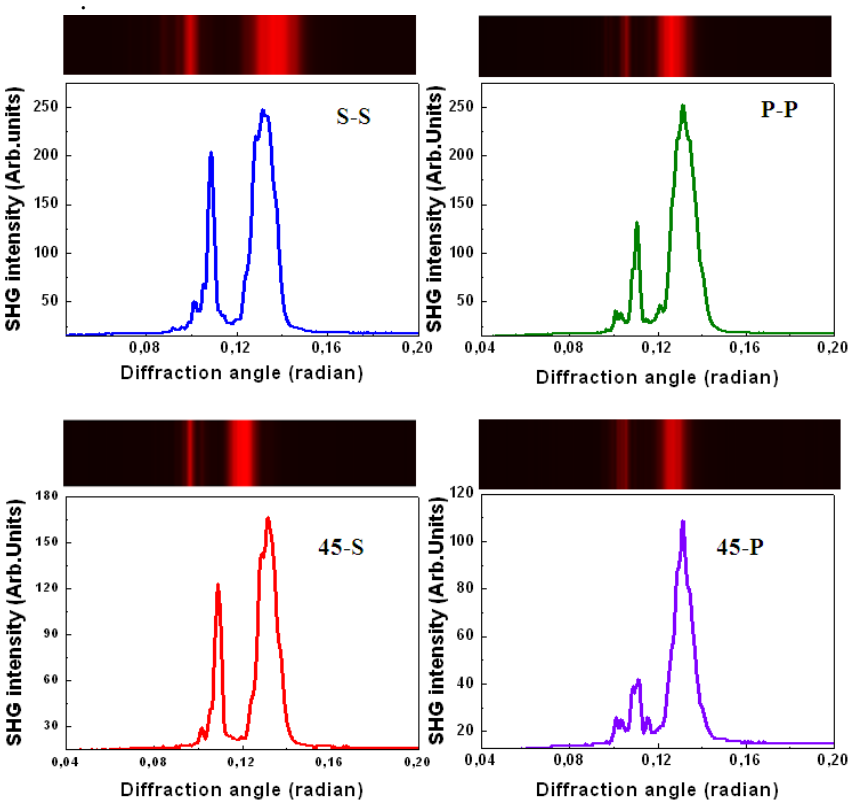

***Figure 5.23**. Second harmonic generated diffraction generated by the RTP1 sample at different polarization configurations.*

In Figure 5.23, we observed small interference lines at all diffraction patterns. We could be able to see only two diffraction orders for the second harmonic generated by the diffraction grating due to the small intensity of the generated green light in the reflection configuration, where the high intensity peak corresponds to the -1 diffraction order and the low intensity peak corresponds to the zero order peak. Among all polarization geometries the maximum intensity of the diffraction peaks was observed at the S-S polarization configuration. However, the intensity ratio between the -1 and zero orders peaks was higher at 45-P polarization configuration.

These measurements show that by changing the polarization of the fundamental light between S and P-polarizations does not imply any change in the shape of the diffraction pattern, and that the diffraction order that shows the

maximum intensity is always the -1 diffraction order. This seems to rule out any explanation for the generation of second harmonic by a conventional phase-matching mechanism in terms of the particular values of the elements of the hyperpolarizability tensor for the (001) RTP surface, since the involved matrix elements are different for different fundamental polarizations.

5.4.2. Analysis of the RTP-2 sample

We extended this analysis to the RTP-2 sample. The recorded nonlinear diffraction pattern generated by this sample is shown in Figure 5.24.

In Figure 5.24, we observe again an asymmetric diffraction pattern for the second harmonic generated by the sample when using a fundamental beam at 1064 nm. In this case the angle of incidence of the fundamental beam was 55º. The generated second harmonic light diffraction order maxima were calculated by using the Bragg´s law. Although in this case the signal to noise ratio is higher than in the RTP-1 sample, we could still indentify that the maximum of intensity occurs for the -4 diffraction order.

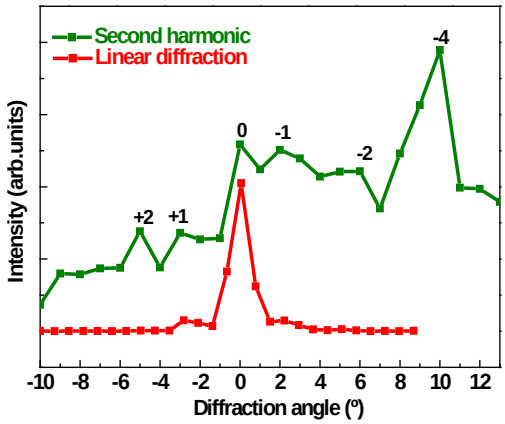

Figure 5.24*. Intensity of the diffraction patterns of the green light generated by the one-dimensional surface relief diffraction grating versus the diffraction angle on the RTP-2 sample. The diffraction pattern of the fundamental beam is also included for means of comparison.*

In this case, a tendency was observed for even order peaks to present higher intensity than odd order peaks, similar to what was observed when analyzing the

diffraction pattern of the fundamental beam in transmission and reflection configurations. This behaviour was attributed to the sub-modulation introduced in the period of this diffraction grating. The linear diffraction pattern of the fundamental beam is also shown in Figure 5.24 for comparison and for an easy identification of the zero order in the nonlinear diffraction pattern.

5.4.3. Analysis of the $LiNbO_3$ sample

Finally, we also extended this analysis of the nonlinear diffraction patterns to the $LiNbO_3$ sample. The surface of the $LiNbO_3$ diffraction grating was illuminated with a wavelength at 1064 nm at a fixed angle of 42º to avoid contributions from internal reflections in the sample.

The recorded second harmonic nonlinear diffraction pattern and the linear diffraction pattern of the fundamental beam are shown in Figure 5.25. Similar spectral features to the RTP samples are observed, generating again an asymmetric diffraction pattern. In this figure we can see that the zero order peak of the nonlinear diffraction pattern coincides with the zero order of the linear diffraction pattern of fundamental beam. The other peaks observed in the pattern of the generated second harmonic correspond to the -1 and -2 orders according to Bragg´s diffraction law. These peaks show more intensity than that observed for the zero order. Instead, in the linear diffraction pattern, only the zero order peak and -1 order showed intensity enough to be recorded here. However in this case the signal to noise ratio is higher than in the previous cases, showing clearly the different diffraction orders.

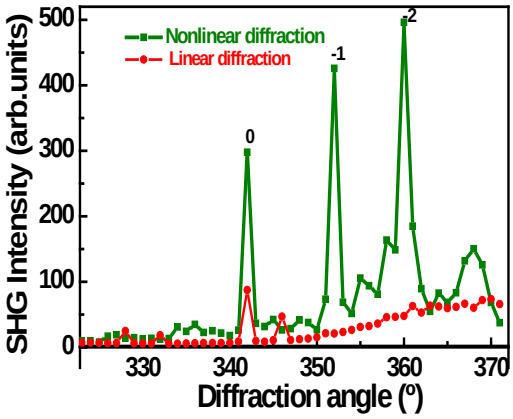

Figure 5.25. *Intensity of the diffraction patterns of the green light generated by the one-dimensional diffraction grating versus the diffraction angle on the surface of $LiNbO_3$. The diffraction pattern of the fundamental beam is also included for means of comparison.*

We also recorded the nonlinear diffraction patterns generated by the $LiNbO_3$ sample as a function of the incident angle of the fundamental beam after tuning the fundamental wavelength from 910 to 1250 nm. We followed the same procedure to record the intensity of the -1 diffraction order by isolating it from the diffraction pattern as we did with the RTP-1 sample. The recorded nonlinear diffraction spectra is shown in Figure 5.26.

In Figure 5.20, we see that the intensity of the -1 order of the second harmonic diffraction pattern depends on the fundamental wavelength and the incident angle

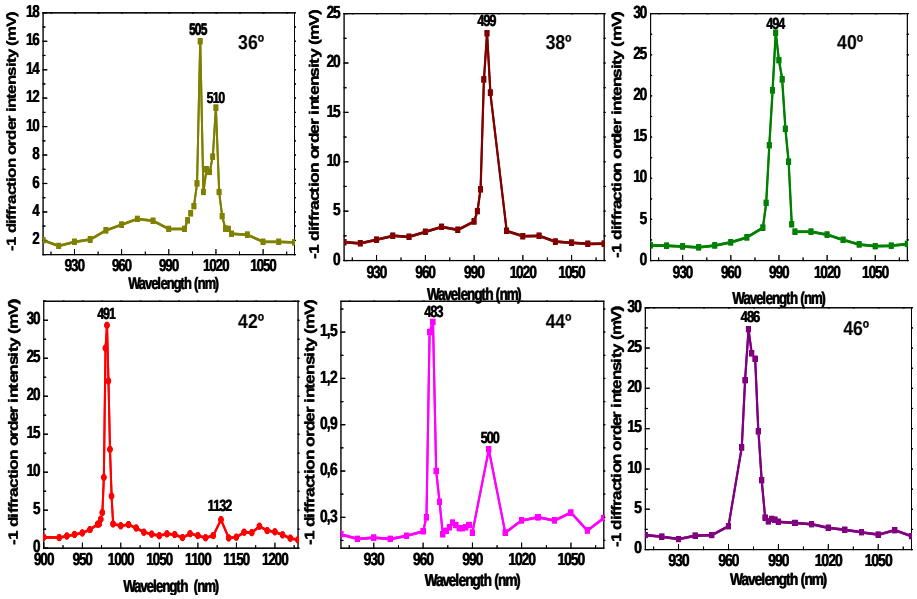

Figure 5.26*. Intensity of the -1 diffraction order as a function of the angle of incidence of the fundamental beam in the range between 910 to 1250 nm in the nonlinear diffraction pattern generated by the $LiNbO_3$ sample. The values shown in the figures indicate the SHG light exhibiting maximum intensities*

In that case, in most of the cases we observed only a maximum, probably related with the higher quality of this diffraction grating. The wavelength for which the SHG is more efficient is decreasing when the incident angle is increasing up to 44º, after which it increases again. The optimum incident angle would be 42º.

5.4.4. Analysis of the KTP-1 sample

We also performed nonlinear diffraction measurements on the KTP-1 sample and we observed that there are four circular rings for SHG light when projected onto a screen. The corresponding recorded diffraction pattern is shown in Figure 6 in *paper III*. Bright spots were observed on the intersections of these rings, and again, asymmetry in the intensity distribution of the diffraction orders was observed.

5.4.5. General analysis of the results obtained on the nonlinear diffraction

We estimated an efficiency of conversion to the second harmonic of ~0.1 % in the diffraction gratings we analyzed by comparing the area enclosed by the diffraction pattern of the fundamental wavelength with that of the second harmonic generated. This was done in this way since we observed a broadening of the peaks of the second harmonic generated diffraction pattern that would rule out the comparison just of the maximum intensity. This low conversion efficiency is not surprising taking into account that in the reflection configuration we took into account only the generation of second harmonic produced by the surface or a thin layer of the material. In all those measurements of nonlinear diffraction patterns, the most interesting feature was that the intensity of the -1 diffraction order peak is higher than the intensity of the zero order peak, resulting in an asymmetric second harmonic generated diffraction pattern.

The reason why the diffraction patterns at the second harmonic wavelength are asymmetric and the maximum intensity was found for other orders different to the zero order is not clear at present. It is worth recalling that Reinisch and Néviere developed in 1983 an electromagnetic theory of diffraction in nonlinear optics that accounted for nonlinear optical effects produced in diffraction gratings inscribed on the surface of thin films of nonlinear optical materials [182]. Among these, one was the possibility of observing asymmetric diffraction patterns for the SHG light, which was verified experimentally on metallic gratings [183]. Related effects in the visible or near IR range have been reported in dielectric and semiconducting resonant grating-waveguide structures [184]. However, in all these cases surface optical modes (such as surface plasmon polaritons or waveguide modes) are present at the surface of the material where the grating is inscribed which allows confinement of the generated light into surface waves, a precondition for the observation of asymmetric second harmonic diffraction patterns [182].

In the present case, there are in principle no surface modes in our structures to which light could resonantly couple to in the near infrared or the green portion of the spectrum, although ultrafast laser ablation is responsible for an amorphization of

the material that may change its refractive index in a thin layer of the material around the ablated area [185], as we have seen in chapter 4 resulting in a possible confinement effect. Another possibility is that the relatively large depth and width of the grooves may rise to a cavity effect for the infrared or green light, which could result in a stronger coupling of the incident light to the structure.

Finally, another configuration that could lead to confinement is that of the Rayleigh anomaly, in which one of the diffracted orders comes out at a grazing angle with respect to the grating plane and interacts with the periodic modulation of the surface. Although in the case of the RTP-1 sample the grating period is very close to a multiple of the fundamental wavelength, which is a necessary condition for the occurrence of this type of anomaly, this is not the case for the other gratings, so that the explanation in terms of a Rayleigh anomaly does not appear to be possible for our results.

5.5. Characterization of the diffraction gratings as a 1D photonic crystal

A photonic crystal (PC) is a structure in which the refractive index is modulated periodically over length scales of the order of the wavelength of light. It is said to be a ´crystal´ because it is formed by a periodic arrangement of basic building blocks. The term ´photonic´ is added since photonic crystals are designed to affect the propagation properties of photons. A diffraction grating can be considered as a one-dimensional (1D) photonic crystal. Thus, we investigated the possibilities of developing a 1D photonic crystal based on the RTP-1 sample. Ultrafast laser ablation affected the sample in the way analyzed in the previous chapter by Raman scattering. Thus, it exists a layer of the material affected by the ablation process that still remains in the sample and that could confine the light and yield the periodic refractive index change introduced by the diffraction grating as a photonic crystal.

Since the advent of the Bloch wave theory, the wave behaviour in periodic structures has generated a great deal of interest for developing new functional devices in the photonics industry. The wave propagation in periodic structures resembles the destructive and constructive propagation of electromagnetic waves caused by periodic

scattering that leads from the dispersion diagram to the generation of frequency gaps. This phenomenon is different from the study of the transmission in an homogenous medium. Generally these frequency gaps, termed as photonic band gaps (PBG), imply a certain frequency range in which no mode light can propagate through the structure.

Using the concept of this PBG, the photonic crystals have been the focus of intensive and extensive research interests to develop functional structural devices. The photonic band gap formation due to the interaction between an electromagnetic wave and the 1D periodic structure takes place in the vicinity of the Bragg resonance defined as, $\vec{\delta} = \vec{k} - \vec{k_1} + \vec{k_2}$ where $\vec{k}_{i,s}$ are the wave vectors of the incident and scattered waves defined as $|\vec{k}_{i,s}| = 2\pi\omega/c$,with c is the speed of light and ω as the wave frequency, $\vec{k}$ is the lattice eigen vector defined as $|\vec{k}| = 2\pi/\Lambda$, where Λ is the lattice period. The existence of band gaps makes the 1D photonic structures perfect reflectors for light at the corresponding frequencies with potential applications in optical communications, filters, etc.

We recorded optical transmission measurements in the RTP-1 sample to characterize it as a 1D photonic crystal in the wavelength range between 300 to 3300 nm. The transmission spectrum was recorded with light propagation in the upper part of the sample and travelling perpendicular to the grooves, i.e., propagation along the ***a*** crystallographic direction and polarized along the ***b*** crystallographic direction (see the scheme shown in Figure 5.27 (a)). The obtained spectrum is shown in Figure 5.27 (b). In this figure we observed that there are two deeps in the transmission curve of the RTP-1 sample at 2180 nm and 2.770 nm that could be related with high orders of a possible photonic band gap.

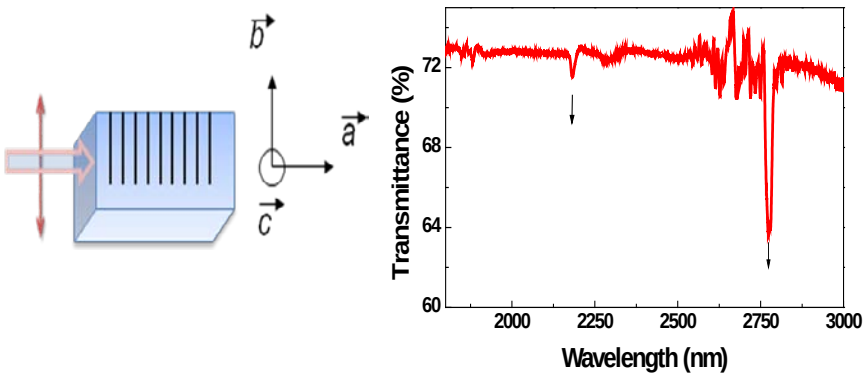

(a) (b)

Figure 5.27*. RTP-1 diffraction grating with wave propagation perpendicular to grooves and polarization parallel to grooves (a) Scheme of the recorded spectrum and (b) transmission spectrum.*

To verify the existence of the peak observed at 2770 nm, we recorded the absorption spectrum of the RTP-1 sample using the same measurement geometry, that is shown in Figure 5.28.

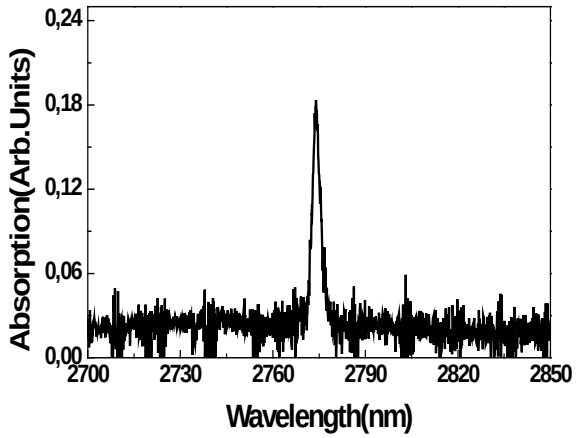

Figure 5.28*. Absorption spectrum of the RTP-1 sample with wave propagation perpendicular to the grooves and polarization parallel to the grooves.*

In this figure, we can see clearly the peak lying at 2770 nm, confirming the existence of the peak observed in the transmission spectrum.

5.6. Theoretical modelling of the 1D photonic crystal

To verify these results, we performed some modelling calculations. There are several capable techniques developed for this purpose such as the transverse matrix method [186], the scattering matrix method [187], the finite difference time domain (FDTD) method [188], and the finite element method [189], among others. One of the most studied and reliable methods are the plane wave expansion method [190-195]. It was used in some of the earliest studies of photonic crystals and is simple enough to be easily implemented. The plane wave expansion method consists in expanding the periodic functions in appropriate Fourier series and inserting the expansions into the wave equation. The result is an infinite matrix eigenvalue problem, which has to be truncated for numerical calculations. Through solving the eigenproblem, one obtains the spectrum of eigenfrequencies (i.e. band structure) and expansion coefficients for Bloch eigenmodes. The prerequisite of this method is indeed the assumption that the crystal is infinite along all directions of space. However, this method is being employed, and still plays a vital role for the calculation of photonic band gaps.

Two kind of polarizations are used to distinguish the dispersion curves, transverse electric (TE) and transverse magnetic (TM) polarizations. TE polarization is defined when the magnetic field of the incident radiation is parallel to the propagation direction. TM polarization is defined when the electric field of the incident radiation is parallel to the propagation direction. In our sample, we considered the TE polarization when the light propagates perpendicular to the grooves along the ***a*** crystallographic direction and is polarized along the ***b*** crystallographic direction. Then, the TM polarization is considered when the light propagates again perpendicular to the grooves along the ***a*** crystallographic direction and is polarized along the ***c*** crystallographic direction.

The 1D photonic crystal we investigated had the same lattice period, groove width and dielectric constants than the RTP-1 sample, i.e., period Λ = 15 µm, width of the grooves s = 5 µm, dielectric constant ε = 13. These parameters are represented in Figure 5.29. We considered that the profile of the grooves is squared.

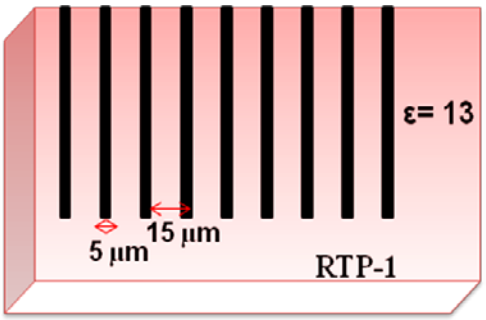

***Figure 5.29**. Schematic view of the 1D photonic crystal constituted by the RTP-1 sample*

In the calculation of photonic band diagrams, the frequency and wave vector are plotted in dimensionless units $\omega\Lambda/2\pi c$ where ω is the frequency, Λ is the lattice period and the c is the speed of light. The dimensionless frequency is equivalent to Λ/λ, where λ is the vacuum wavelength (given by $\lambda=2\pi c/\omega$). Figure 5.30 shows the photonic band structure calculated for the TE polarization for a 1D photonic crystal with a period Λ = 15 µm, groove width *s* = 5 µm, and a square profile for the grooves, similar to the parameters of the RTP-1 sample.

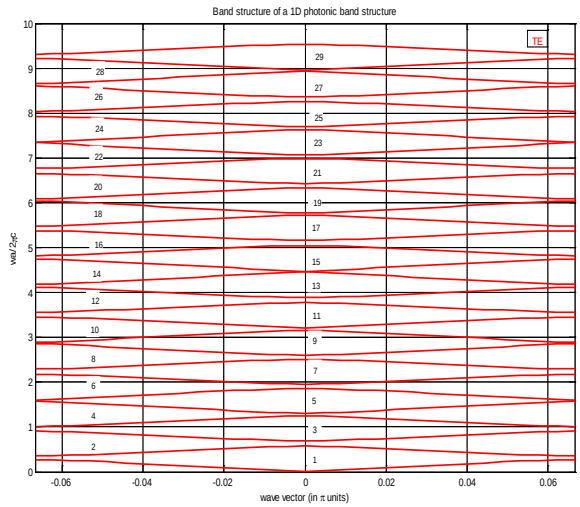

***Figure 5.30**. Photonic band structure calculation for a 1D PC with a period of 15 µm, a groove width of 5µm and a square profile for the grooves in terms of frequency vs wave vector for the TE polarization.*

The alternating layers of the periodic structure gives rise to several band gaps in the one dimensional photonic crystal. Here we considered that the material (RTP) has a high dielectric constant and the air has a low dielectric constant nearly equal to 1. The numbers in the graph indicate the index of the band gaps. Up to 29 band gaps were obtained for this structure in our calculations.

If we represent the same band structure in terms of wavelength (λ) we obtain the plot shown in Figure 5.31 for the spectral region of interest analyzed in the transmission measurements performed in the RTP-1 sample. This regions contains the high order optical gaps orders from 13 to 25.

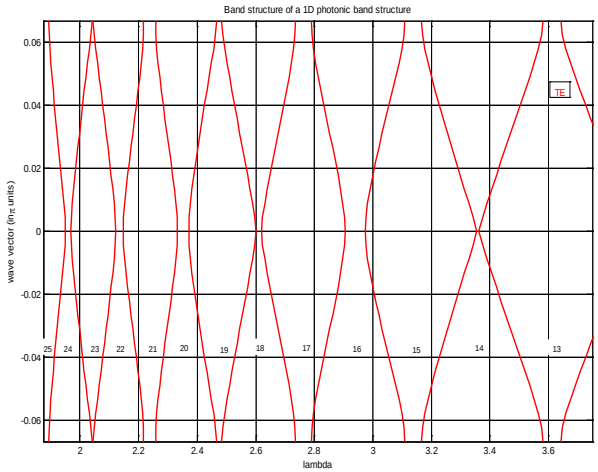

Figure 5.31. *Photonic band structure diagram for a 1D PC with a period of 15 μm, a groove width of 5 μm and a square profile for the grooves in terms of wavelength (μm) vs wave vector for the TE polarization*

The transmission window of this 1D photonic structure for the TE polarization has been calculated from these results within the range of wavelengths between 2 to 3.6 μm, and it is shown in Figure 5.32. The obtained results show the existence of several high order photonic band gaps at this interval of wavelengths (from gap orders 13 to 25) with different widths. The photonic band gaps were indicated with numerical numbers.

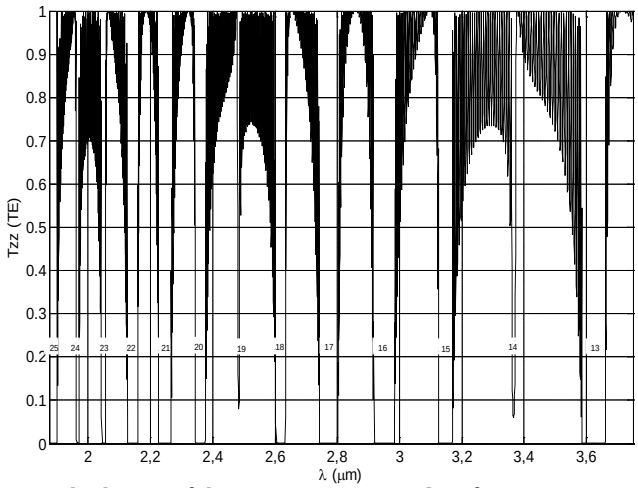

Figure 5.32. *Calculation of the transmission window for a 1D PC with a period of 15 μm, groove width of 5 μm and a square profile for the grooves for the TE polarization.*

If we compare the results of this modelling with the experimental data obtained in the transmission measurements, we observe that the most intense peak observed in this spectrum, and located at 2.77 μm coincides with the 17th order of the photonic band gap calculated for a 1D photonic crystal with the same parameters than our sample. The less intense peak observed at 2.18 μm would coincide with the 22nd order of the photonic band gap calculated for this structure.

After these positive results, we extended these calculations to the TM polarization. The corresponding band structure is shown in Figure 5.33 in terms of wave vector vs frequency and in Figure 5.34 in terms of wavelength vs wave vector in the region of interest according to the measurements performed by transmission for the TE polarization. The numbers in these figures indicate again the index of the band gap calculated.

.

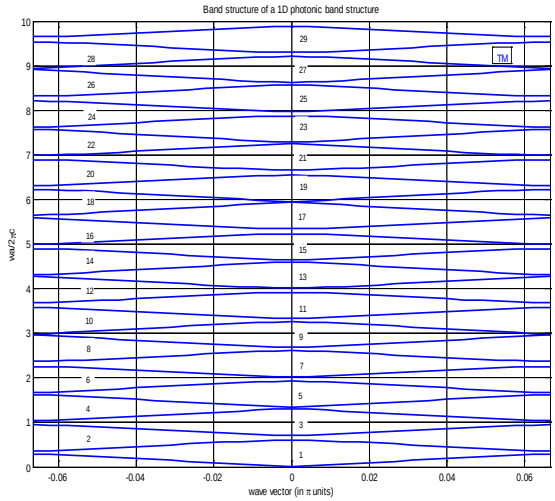

Figure 5.33. *Photonic band structure calculation for a 1D PC with a period of 15 μm, a groove width of 5 μm and a square profile for the grooves in terms of , wave vector vs frequency for the TM polarization*

Again, up to 29 band gaps were obtained for this polarization. In the region of interest we observed the gaps orders between 12 and 24. The calculated transmission window for this polarization is shown in Figure 5.35.

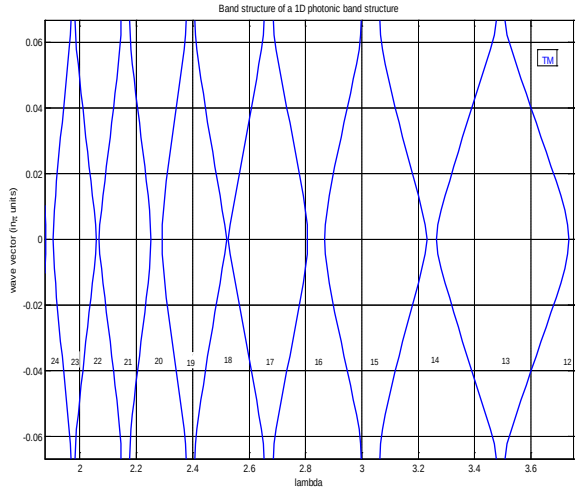

Figure 5.34. *Photonic band structure calculation for a 1D PC with a period of 15 μm, a groove width of 5 μm and a square profile for the grooves in terms of wavelength (μm) vs wave vector for the TM polarization.*

The obtained results show the existence of several high order photonic band gaps in this interval of wavelengths (from gap orders 12 to 24) with different widths. The photonic band gaps are indicated with numerical numbers.

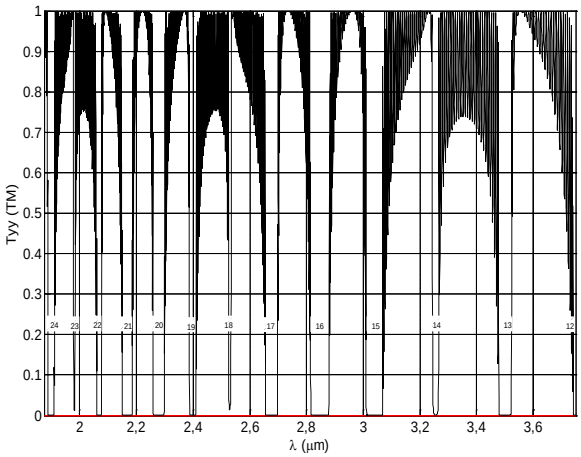

Figure 5.35*. Calculation of the transmission window for a 1D PC with a period of 15 μm, a groove width of 5 μm, and a square profile for the grooves for the TM polarization.*

Then, to confirm if our sample could behave as a 1D photonic crystal, we recorded the transmission spectrum of the RTP-1 sample with light propagating along the ***a*** crystallographic direction, polarized along the ***c*** crystallographic direction, equivalent to the TM polarization of our calculations.

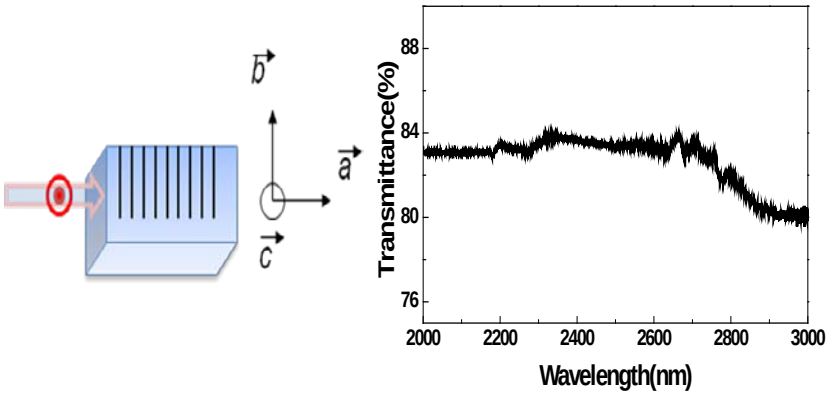

(a) (b)

Figure 5.36*. RTP-1 diffraction grating with wave propagation and polarization perpendicular to the grooves (a) scheme of the recorded spectrum and (b) transmission spectrum.*

The results are shown in Figure 5.36, together with a scheme of the polarization geometry used in these measurements.

For this TM polarization geometry, no evident peaks were observed in the transmission spectrum recorded for the RTP-1 sample. Again, we confirmed these results by absorption measurements under the same conditions of propagation and polarization. The recorded absorption spectrum for the RTP-1 sample for the TM polarization configuration is shown in Figure 5.37.

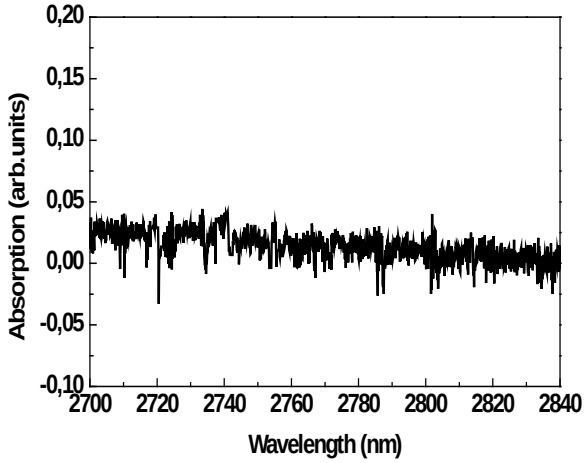

Figure 5.37. *Absorption spectrum of the RTP-1 sample with wave propagation and polarization perpendicular to the grooves*

These results do not reflect the calculations performed for the TM polarization. Since it has been reported in the literature the existence of absorption bands related to the hydroxyl group around 2800 nm for the crystals of the KTP family grown by the hydrothermal method [196], we performed a more detailed study of the transmission window in this region for our sample using a Fourier Transformed (FT) IR spectrometer in the wavelength range between 2000 to 5000 nm with wave propagation along the ***a***, ***b***, and ***c*** crystallographic directions, respectively. The obtained transmission spectra are shown in Figure 5.38.

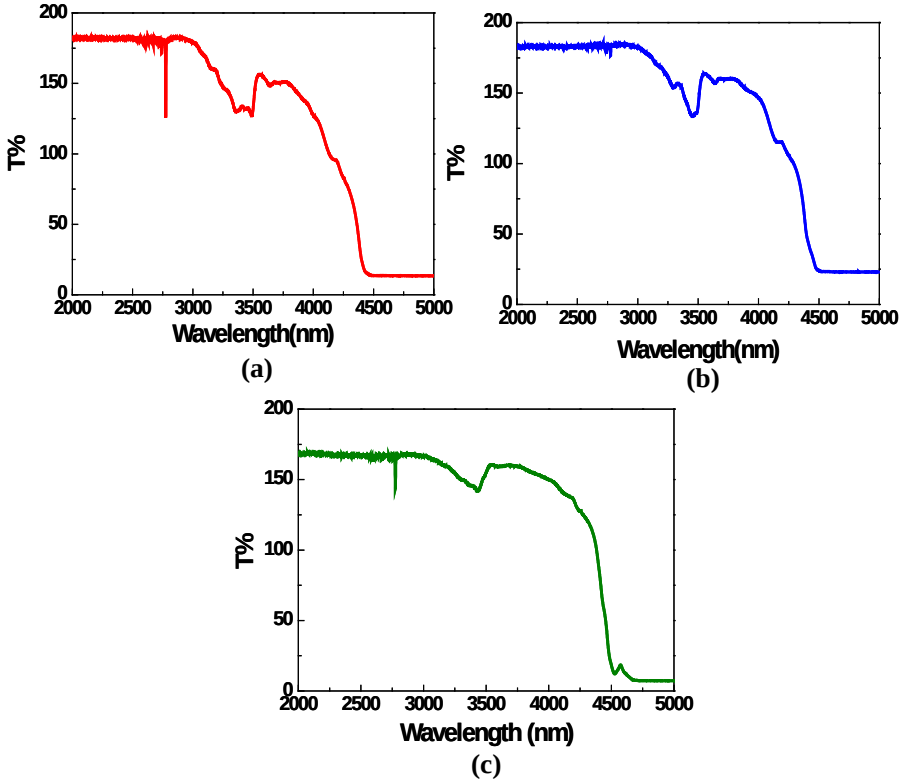

***Figure 5.38**. Transmission spectra of the RTP-1 sample with light propagation along (a) **a**, (b) **b**, and (c) **c** crystallographic directions.*

In this figure, it is clear that the peak at 2770 nm is present in all the spectra, thus indicating that it is related with the adsorption of water on the surface of the sample, and not with the existence of possible photonic band gaps, rulling out the possibility of using this kind of samples as photonic crystals.

UNIVERSITAT ROVIRA I VIRGILI
MICROSTRUCTURATION OF NONLINEAR OPTICAL MATERIALS:
METHODOLOGIES, CHARACTERIZATION, AND APPLICATIONS
Raj Kumar Golconda
Dipòsit Legal: T. 55-2013

CHAPTER
SIX

Preparation and characterization of luminescent composites

The field of nanotechnology utilizes the materials, devices, and systems through the control of matter on the nanometer length scale. In this context, lanthanide elements play a fundamental role due to their singular chemical and physical properties. They are the fundamental materials in a large range of areas such as new materials applied to sensor, electronics [197], probes for biological membranes [198] etc. On the other hand, the prospects of potential applications have stimulated further research which deepened the knowledge on lanthanide ions. In this chapter, we discuss the preparation of luminescent composites based on embedding lanthanide doped luminescent nanopartilces on microstructured nonlinear optical substrates fabricated by ultrafast laser ablation. The spectroscopic studies of the

lanthanide doped nanoparticles are discussed in detail as well as the spectroscopic characterization of the luminescent composites, producing multicolor RGBY emission for possible laser phosphor display applications. Apart from this, we also discuss the different upconversion mechanisms involved in the emission of light from these nanoparticles as well as the interparticle energy migration between luminescent nanocomposites. The synthesis, spectroscopic and optical measurements of luminescent nano composites were performed at the laboratories of the research group Física i Cristal·lografia de Materials i Nanomaterials (FiCMA-FiCNA), of the Universitat Rovira i Virgili, Tarragona and at the Laser Processing Group, Instituto de Optica, CSIC, Serrano**,** Madrid**.**

6.1. Synthesis of lanthanide doped luminescent nanoparticles

Sol gel technology plays a principal role in the development of modern nanotechnology for the preparation of new materials. We used the modified sol-gel Pechini method to synthesize monoclinic potassium-rare earth double tungstates ($KRE(WO_4)_2$ or KREW (RE = Yb, Gd,)) and Gd_2O_3 nanoparticles doped with active lanthanide ions. The experimental details were discussed in Chapter 2, and the raw materials used in this synthesis are summarized in Table 6.1.

Table 6.1. *Summary of reagents used in each nanoparticles synthesis*

	A	*B*	*C*	*D*	*E*	*F*	*G*	*H*	*I*	*J*	*K*	*L*
Nanoparticles	Er_2O_3	Tm_2O_3	Ho_2O_3	Eu_2O_3	Yb_2O_3	Gd_2O_3	K_2CO_3	$(NH_4)_2WO_4$	*EDTA*	*EG*	*C.T*	*Time*
50% Er:KYbW	0.417				0.419		0.294	2.416	4.975	476	973	3
5% Tm:KYbW		0.049			0.793		0.292	2.407	4.956	474	1073	2
2.5% Er, 5% Tm:KYbW	0.020	0.040			0.772		0.293	2.407	4.957	474	1073	2
5% Tm, 10% Yb:KGdW		0.041			0.085	0.665	0.298	2.453	5.052	483	1073	2
1% Tm, 45% Yb:KGdW	0.008				0.380	0.419	0.296	2.435	5.015	479	1073	2
5% Eu:KGdW				0.038		0.746	0.299	2.461	5.067	484	1073	2
5% Eu:Gd_2O_3				0.128		2.520			4.277	409	1073	2
1% Tm, 45% Yb:Gd_2O_3		0.027			1.252	1.382			4.126	394	1073	2
10% Er, 10% Yb:Gd_2O_3	0.161				0.161	2.70			4.833	462	1073	2
1.5% Ho, 5% Yb:KGdW			0.012		0.042	0.733	0.291	2.4581	5.061	484	1073	2

Note: All the quantities of reagents from A-I in grams, J in microliters, K in Kelvin (C.T- calcination temperature), and L in hours

The mole ratio between the concentration of metals and EDTA was 1:1, while the mole ratio between EDTA and EG was 1:2 in all cases. The SEM and TEM images of the synthesized luminescent nanoparticles are shown in Figure 1 in *paper VIII*. These particles show a more facetted morphology with smaller sizes of the order of 30-40 nm.

6.2. Structural characterization of luminescent nanoparticles

The structural characterization of the as-synthesized luminescent nanoparticles was carried out by the X-ray powder diffraction method. Figure 6.2 (a) shows the X-ray powder diffraction patterns of the as-synthesized KREW nanoparticles with different doping ions at room temperature.

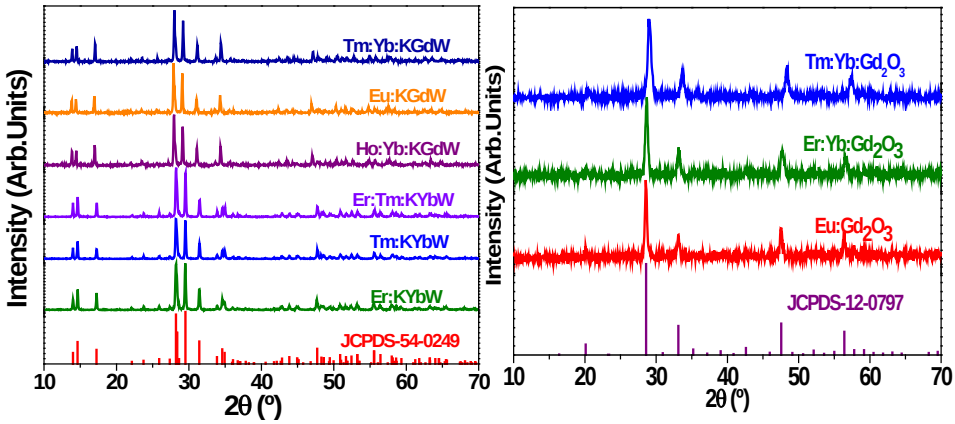

(a) (b)

Figure 6.2. *X-ray powder diffraction patterns of (a) monoclinic KREW (RE=Yb,Gd) nanoparticle and (b) Gd_2O_3 nanoparticles.*

The powder diffraction patterns of the KREW nanoparticles are compared with that of KYbW according to the JCPDS file no. 54-0249, also included in the figure. Similarly, the expected powder diffraction patterns of Gd_2O_3 nanoparticles show the expected diffraction peaks according to the JCPDS file no. 12-0747. These patterns are represented in Figure 6.2 (b).

6.3. Spectroscopic characterization of luminescent nanoparticles

The different colored light emissions from the lanthanide ions are utilized mostly in television screens and display panels. For the new developments in the field of light and display devices, a detailed knowledge of the luminescent properties of the luminescent nanopartcles is essential. The detailed information on the positions of energy levels of these lanthanide ions is essential for developing new phosphors. Essentially, visible and IR regions in the electromagnetic spectrum from the lanthanide ions through the excitation of near-IR laser wavelengths is of increasing interest in recent years.

6.3.1. Er $^{3+}$ doped KYbW luminescent nanoparticles

KYbW is a promising laser crystal and laser host material [199,200]. The low temperature phase of KYbW is a monoclinic biaxial crystal with inversion centre. Here we doped the KYbW host matrix with Er^{3+} to obtain emission in the green. The most important features of the KYbW host are, the high quantity of Yb^{3+} ions with a large absorption cross section that can efficiently transfer the pump energy to Er^{3+}, thus increasing the emission intensity in the visible region, and due to the similar nature of the Er^{3+} and Yb^{3+} ions concerning charge and size, it makes possible an easy substitution of Yb^{3+} by Er^{3+} in the host material.

In the Er-Yb system the green emission obtained after infrared pumping can be attributed to an up-conversion mechanism involving a two photon energy transfer process to erbium ions from ytterbium ions. Because of the energy overlap between Yb^{3+}, Er^{3+} energy levels $^2F_{5/2}$ and $^4I_{11/2,}$ there is a resonant energy transfer via two step cross transfers. The excited electrons of Yb^{3+} in the $^2F_{5/2}$ level decay non-radiatively to the $^2F_{7/2}$ ground state and transfer part of their energy to the Er^{3+} electrons of in the $^4I_{15/2}$ state promoting them to the $^4I_{11/2}$ energy level. A second photon can be absorbed by the electrons of Er^{3+} in the $^4I_{11/2}$ level consistently increasing their energy to the $^4F_{7/2}$ level. After that, a very fast nonradiative relaxation takes place to the $^4S_{3/2}$ and $^2H_{11/2}$ levels of Er^{3+}, where the transitions $^2H_{11/2} \rightarrow {}^4I_{15/2}$ and $^4S_{3/2} \rightarrow {}^4I_{15/2}$ takes place, with emissions at around 520 and 550 nm, respectively.

From the $^4S_{3/2}$ level it is possible also to find a non-radiative relaxation to the $^4F_{9/2}$ level, from which an emission at around 669 nm can be generated, attributed to the $^4F_{9/2} \rightarrow {}^4I_{15/2}$ transition. Finally, the $^4S_{3/2} \rightarrow {}^4I_{13/2}$ transition can generate light at 848 nm. We observed these transitions in the Er: KYbW nanoparticles we synthesized. And they are shown in Figure 6.3 (a) and (b).

Figure 6.3. *Optical emission spectra of Er:KYbW nanoparticles corresponding to the (a)* $^2H_{11/2} \rightarrow {}^4I_{15/2}$ and $^4S_{3/2} \rightarrow {}^4I_{15/2}$ *(b)* $^5S_{3/2} \rightarrow {}^4I_{13/2}$ *(c)* $^4I_{13/2} \rightarrow {}^4I_{15/2}$ *transition (d) Energy level diagram of Er:Yb system.*

One more interesting infrared emission is the one related to the Er^{3+} $^4I_{13/2} \rightarrow {}^4I_{15/2}$ transition, located in the range of 1.55 μm. The corresponding emission spectrum is shown in Figure 6.3 (c). The nergy levels diagram of Er^{3+} and Yb^{3+}, together with the transitions involved in the emissions we observed for the Er: KYbW nanopartilces.

6.3.2. Tm^{3+} doped KYbW luminescent nanoparticles

The absorbed energy from the excited radiation at 980 nm wavelength delivered by the Ti:Sapphire laser is absorbed by the Yb^{3+} ion that transfers then its energy to the Tm^{3+} ion which emits the radiation back in the visible. The mechanism involved in the upconversion observed for this system is called a phonon assisted non-radiative energy transfer.

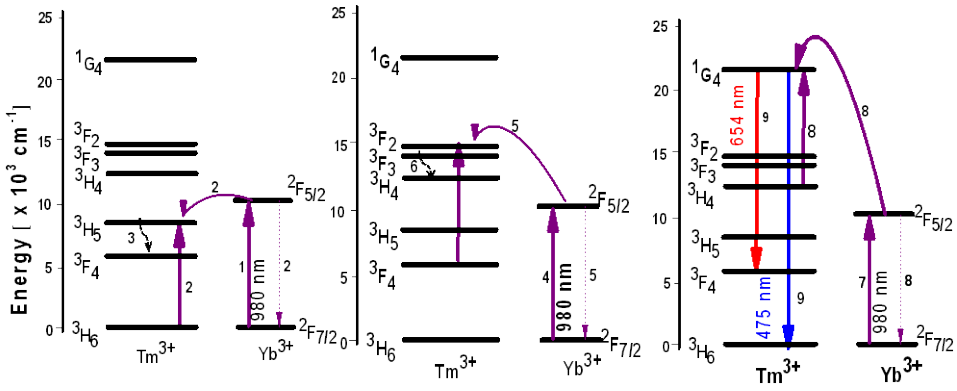

(a)

(b)

Figure 6.4. *(a) Upconversion mechanism occurring in the Yb^{3+}, Tm^{3+}:KYbW nanopartilces to produce emission at 475 nm. The numbers represent the sequence of events. (b) Emission spectrum of Tm:KYbW nanoparticles and image of the pellet fabricated with the nanoparticles showing the color of the emission.*

The energy level diagram corresponding to the transitions involved in the Yb^{3+} -Tm^{3+} energy transfer mechanism are shown in Figure 6.4 (a). Yb^{3+} absorbs radiation at 980 nm (step 1), transfers its energy to the Tm^{3+} ion (step 2) through the $^3H_5$ energy level. The Tm^{3+} then relaxes down through a non-radiative process to the $^3F_4$ energy level (step 3) that has a relatively long lifetime, and allows to absorb nearby another photon of the Yb^{3+} ion (step 4), and promote the electron to the $^3F_2$ energy level (step 5). After internal relaxation to the $^3H_4$ level (step 6), the Tm^{+3} ion receives another photon from Yb^{3+} (step 7) to reach the higher level $^1G_4$ (step 8), from which it can emit at 475 nm by the transition $^1G_4 \rightarrow {}^3H_6$ and at 655 nm by the transition $^1G_4 \rightarrow {}^3F_4$ (step 9). The corresponding emission spectra of Tm^{3+} doped KYbW nanoparticles is shown in Figure 6.4 (b). The inset of this Figure shows an image of the visible emission obtained from the nanoparticles.

6.3.3. Ho^{3+}, Yb^{3+} co-doped KGdW luminescent nanoparticles

The photoluminescent measurements of Ho,Yb:KGdW nanoparticles WAS carried out also by optical excitation at 980 nm using the Ti:Sapphire laser.

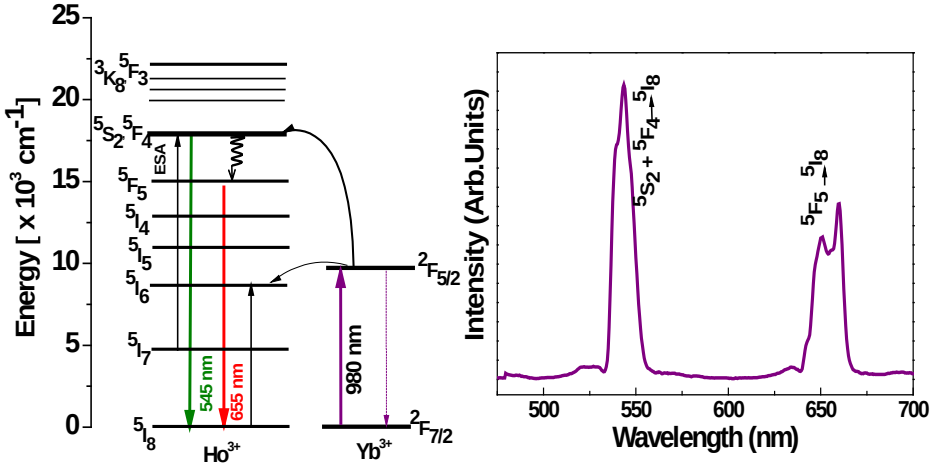

(a) (b)

Figure 6.5. *(a) Energy level diagram of Ho:Yb.KGdW nanoparticles (b) corresponding emission spectrum of nanoparticles and an inset figure shows an image obtained from nanoparticles.*

The photoluminescence generated from the Ho:Yb:KGdW nanoparticles after Yb^{3+} excitation occurred by the energy transfer from the $^2F_{5/2}$ energy level of Yb^{3+} to the $^5I_6$ level of Ho. Then, after transferring a second photon from Yb3+, it

experiences excited state absorption to the $^5S_2$ + $^5F_4$ energy levels, that are close in energy. At these levels, the most intense emission is generated around 545 nm. However, a nonradiative relaxation can take places from the $^5S_2$ energy level to the $^5F_5$ level, where the radiative process associated to the $^5F_5 \rightarrow {}^5I_8$ transition occurs, emitting red light at around 655 nm. The corresponding energy level diagram of Ho:Yb:KGdW nanoparticles and its emissions spectra are shown in Figure 6.5, together with a picture showing the color of this emission.

6.3.4. Er^{3+} and Yb^{3+} co-doped Gd_2O_3 luminescent nanoparticles

Similarly, Er:Yb:Gd_2O_3 nanoparticles generated low green emission from the $^4H_{11/2} \rightarrow {}^4I_{15/2}$ and $^4S_{3/2} \rightarrow {}^4I_{15/2}$ transitions (see Figure 3 (e) in *paper VI*) and the most strong red emission was generated through the transition $^4F_{9/2} \rightarrow {}^4I_{15/2}$, at around 660 nm. The corresponding emission spectrum and the image of the visible emission obtained from the nanoparticles are shown in Figure 6.6. In that case the mechanisms involved in the generation of these emissions are the same described in section 6.3.1 for the Er^{3+} doped KYbW luminescent nanoparticles. .

Figure 6.6. *Emission spectrum of Er:Yb:Gd_2O_3 nanop articles*

We calculated the chromaticity color coordinates x and y of all luminescent nanoparticles by integrating the area of the photoluminescence spectra of each color at different wavelengths with the help of the CIE 1931 XYZ color matching functions [201]. The calculated x and y color coordinates are listed in Table 6.2.

Table 6.2. *Chromaticity x and y coordinates of the emission generated by our nanoparticles.*

Nanoparticles	Chromaticity coordinates (x, y)	Name of the color
Er:Yb: Gd_2O_3	(0.4141, 0.5214)	Red
Er: KYbW	(0.2838, 0.6983)	Green
Tm: KYbW	(02772, 0.1590)	Blue
Ho:Yb: KGdW	(0.3351, 0.6271)	Yellow

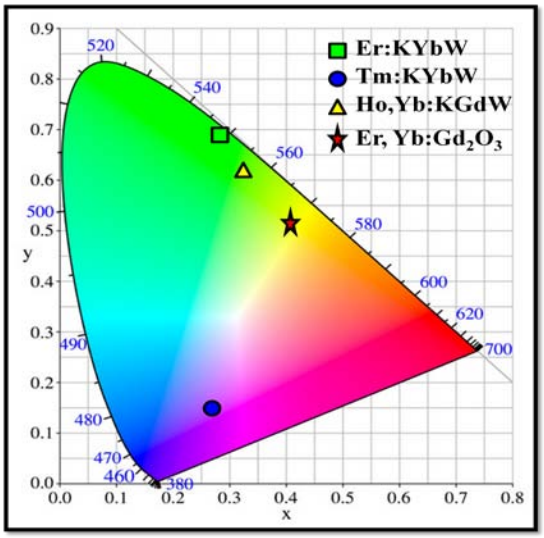

Figure 6.7. *CIE (x,y) chromaticity diagram indicating the color coordinates*

We plot these coordinates in the CIE chromaticity diagram for each of the nanoparticles emission colors as it is shown in Figure 6.7. The coordinates of the red color emission are located in yellow color region due to the combination of green and red color emission wavelengths emitted by the Er:Yb:Gd_2O_3 nanoparticles. In the figure we will need to develop a more pure red emission generated by upconversion. The chromaticity coordinates of the Ho:Yb:KGdW nanoparticles are located at the greenish yellow color region. Again we will need to develop new strategies to obtain more pure yellow emission by upconversion mechanisms.

6.4. Fabrication of photoluminescent nanocomposites for laser phosphor display applications

Paper VI describe the process of fabrication of photoluminescent nanocomposites for laser phosphor displays (LPDs) that consisted in introducing Er:KYbW nanoparticles in the conical pores fabricated by ultrafast laser ablation on the surface of the KTP-2 sample by mechanical means, and then annealing the sample at 1173 K for 5 h to consolidate the structure. Figures 1 (c) and (d) in *paper VI* show ESEM micrographs of the Er:KYbW nanoparticles inside the conical pores after the annealing process.

We also confirmed that the structure of the KTP substrate and the embedded nanoparticles in the KTP conical pores is maintained after the annealing process by recording the Raman scattering spectra. Figure 2(a) in *paper VI* shows that in the micro-Raman spectra, the regions from 200 – 400 cm^{-1} and 600 – 850 cm^{-1} are associated with the TiO_6 octahedral tortional and stretching modes of KTP, respectively. The Raman bands in the 900 – 1200 cm^{-1} region are due to the PO_4 tetrahedra of KTP. At the low band region, it appears a Raman mode at 138 cm^{-1} related to the Er:KYbW nanoparticles embedded inside the KTP conical pores. The corresponding 2D Raman intensity maps showing the distribution of the nanoparticles in the KTP substrate are shown in Figure 2 (c) and (d) in *paper VI*. These results indicate that both KTP and Er:KYbW nanoparticles have not changed their crystallographic structure during the thermal annealing process applied to the sample to consolidate the structure of the composite. Also, no new compounds were formed by the interaction between the KTP sample and the Er:KYbW nanoparticles at the edges of the pores.

The spectroscopic characterization of the luminescent composites was carried out by pumping at 980 nm with a Ti:Sapphire laser. The obtained Er^{3+} green and red emissions from the luminescent nanocomposites generated by a process of upconversion after energy transfer from Yb^{3+}, are shown in Figure 3 (b) and (c) in *paper VI.*

A similar procedure was followed to fabricate RGBY multicolor emission from different luminescent nanoparticles embedded inside the conical pores of the KTP-3 sample. Nine sets of conical pores were inscribed at different irradiation times.

The morphological characterization of inscribed circular pores on the surface of KTP-3 sample was discussed in detail in chapter 4. These sets of conical pores were used to fabricate the multicolor emission of luminescent composites as an initial step, embedding a particular kind of nanoparticles emitting red, green, blue, and yellow light, respectively, in each set.

Er:Yb:Gd_2O_3 nanopartilces for red light, Er:KYbW nanopartilces for generation of green light, Tm:KYbW nanopartilces for generation of blue light, and Ho:Yb:KGdW for generation of yellow light were introduced inside the conical pores of the KTP-3 sample by mechanical means at different sets of conical pores forming RGBY multicolour emission. After filling the conical pores with the nanoparticles, the sample was annealed at 1173 K for 3 h at each time. ESEM images were recorded after annealing the composites, as shown in Figure 3 in *paper IX*.

To fill a set of conical pores with a different kind of luminescent nanopartilces the rest of the sets were protected by covering them with a colloidon film to avoid the mixing of the luminescent nanoparticles. This colloidon layer was removed prior to the process of annealing of the newly filled nanoparticles.

The structure of the substrate was verified by X-ray diffraction after the different annealing processes and it revealed that the crystallinity of the KTP substrate was maintained in the whole process. The recorded X-ray diffraction pattern is shown in Figure 6.8.

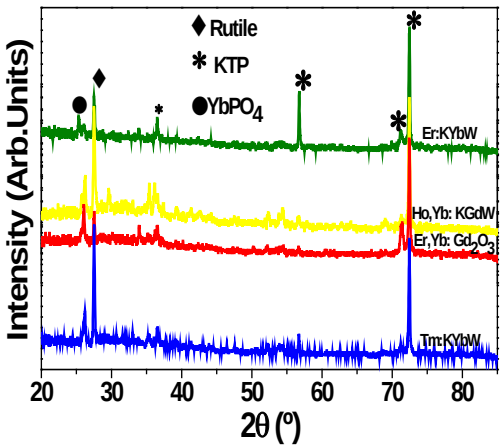

Figure 6.8. *X-ray diffraction pattern of the luminescent composites after the successive annealing processes.*

In this analysis, we also found a peak related to the generation of TiO_2 in its rutile phase during the cannealing process. This result is not surprising because it can be formed by the decomposition of KTP with temperature.

The photoluminescence measurements were performed on the surface of each set of nanoparticles embedded into the conical pores of the KTP sample by pumping at 980 nm. The sample was placed on a 2D stage, perpendicular to the direction of the incident laser radiation. The sample was moved slowly to the position of the desired emission wavelength generated by the luminescent nanoparticles with the help of a moving stage. Images showing the colored emission of each set of embedded luminescent nanoparticles were recorded with a CCD camera with the help of a telescope, and are shown in Figure 5 (b) in *paper IX*. The emission spectra of embedded luminescent nanoparticles are shown in Figure 4 in *paper IX* and discussed in detail in the previous sections.

UV laser has been used traditionally as pumping sources in laser phosphor displays. However, those lasers are expensive. Using luminescent nanoparticles that can be excited with chip NIR lasers could be an interesting alternative for the development of laser phosphor displays. Moreover, multicolor emission with sharp emission bands from new luminescent nanoparticles through upconversion mechanisms could be helpful for the development of RGBY laser phosphor display devices.

6.5. Enhancement of specific emission from luminescent nanoparticles by Au nanoparticles

Metallic Plasmonic effects have been intensively investigated to enhance luminescence and absorption properties of optical systems [202] among other interesting properties. The enhancement of local field intensity that can be caused by the plasmon resonance positively influences the upconversion efficiency because of the nonlinear nature of this process. The metallic nanoparticles can also influence the transition probabilities of the luminescent nanoparticles if these transitions are resonant with the plasmon resonances [203]. Lanthanide doped materials with Au nanoparticles deposited on the surfaces have recently received a lot of attention because of the possibility to modify the emission spectra by systematic amplification of certain transitions by the plasmonic resonances [204]. In this work, the Au metallic

nanoparticles were used for the enhancement of the red emission of the Er:KYbW nanoparticles embedded inside the conical pores of the KTP-2 sample.

Prior to deposit the Au metallic nanoparticles on the surface of embedded nanoparticles inside the conical pores of KTP substrate, the deposition rate of Au nanoparticles were optimized by recording the absorption spectra of nanoparticles at different deposition rates. In the first step, Au nanoparticles were deposited on the surface of borosilicate glass at different deposition rates and recorded the absorption spectra at each different deposition rates. Table 6.3 shows list of deposition rates which we used to optimize the deposition rate of Au nanoparticles for the enhancement of specific wavelength.

***Table 6.3**. Summary of deposition rates of Au nanoparticles*

Glass			***$KLu(WO_4)_2$***		
Power (W)	**Pressure (mTorr)**	**Time (sec)**	**Power (W)**	**Pressure (mTorr)**	**Time (sec)**
50	3	5	75	3	10
50	3	10	75	3	15
50	3	15	75	3	20
50	3	20	75	3	30
50	3	25	-	-	-
50	3	30	-	-	-
75	3	10	-	-	-
75	3	20	-	-	-
75	3	30	-	-	-

Figure 6.9 shows TEM images of Au sputtered nanoparticles on the surface of the glass. At higher deposition rate the size distribution of nanopraticles is increasing.

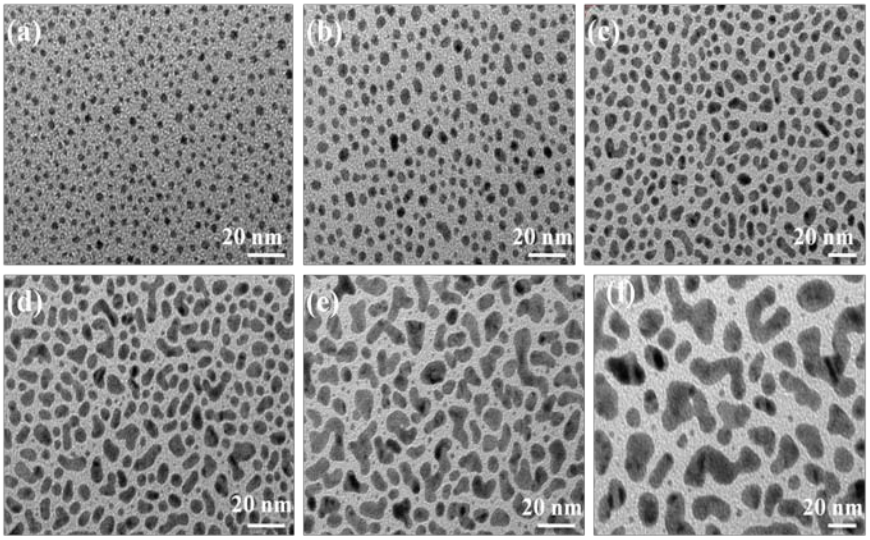

***Figure 6.9**. TEM images of the deposited Au nanoparticles on the surface of glass substrate with a power of 50 W and pressure at a 3 mTorr (a) 5 sec, (b) 10 sec, (c) 15 sec, (d) 20 sec, (e) 25 sec, and (d) 30 sec.*

To optimize the deposition rate of Au nanoparticles, the absorption spectra were recorded at each different deposition rate and the recorded absorption spectra are shown in Figure 6.10.

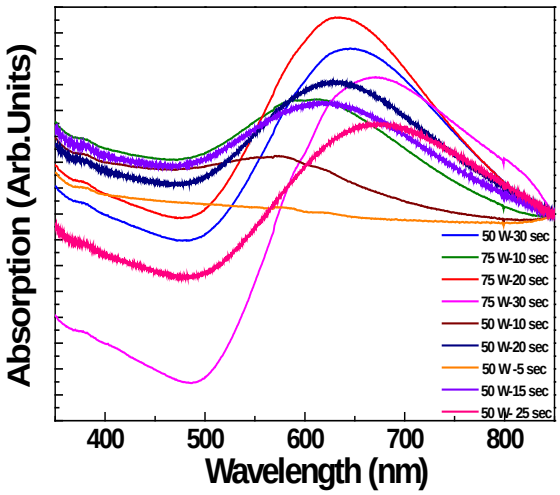

***Figure 6.10**. Absorption spectra of Au nanoparticles deposited on the surface of the glass*

From Figure 6.10, we found that the suitable absorption spectrum at a deposition rate 75 W- 30 sec where our desired wavelength absorption was maximum at 660 nm.

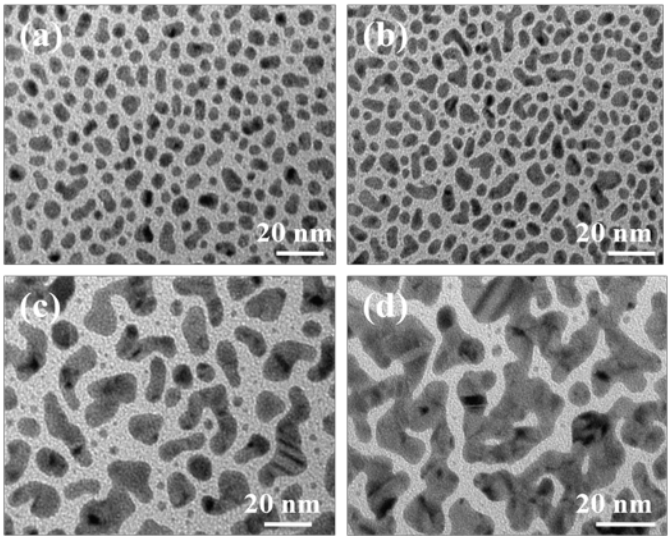

Figure 6.11. *TEM images of sputtered Au nanoparticles on the surface of KLuW substrate with a power of 75 W and pressure at 3 mTorr (a) 10 sec, (b) 15 sec, (c) 20 sec, and (d) 30 sec.*

Later, we extended our investigation to reproduce this absorption spectra by depositing Au nanoparticles on the surface of $KLu(WO_4)_2$ (KLuW) substrates, because its properties such as refractive indices, etc. are more suitable for our KTP substrate. The recorded TEM images of the deposited Au nanoparticles are shown in Figure 6.11. The size distribution of nanoparticles was increased as we are increasing the deposition rate. The recorded absorption spectra of deposited Au nanoparticles on the surface of KLuW substrate are shown in Figure 6.12. The deposition rate of Au nanoparticles was optimized at 15 sec at the power of 75W. This deposition rate was chosen, where the absorption spectrum of these nanoparticles was suitable for our desired wavelength to couple the plasmonic resonance with our embedded luminescent nanoparticles around 660 nm.

The optimized rate Au nanoparticles were deposited on the surface of the KTP substrate filled with nanoparticles inside the conical pores by using RF Magnetron sputtering. The details of the deposition of the Au nanoparticles were given in Chapter 2.

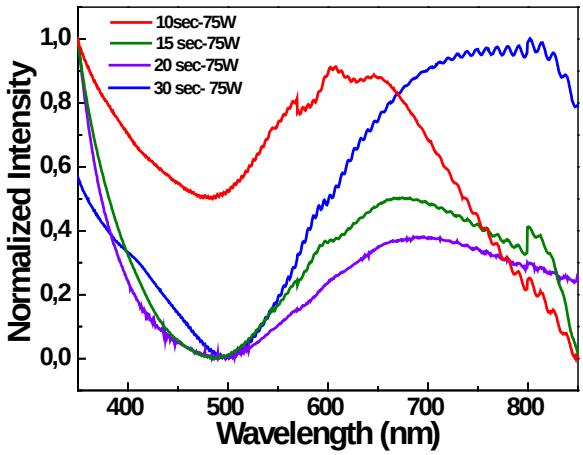

Figure 6.12. *Absorption spectra of Au nanoparticles deposited on the surface of the KLuW substrate.*

In order to check the effect of the plasmons coupled to the embedded luminescent nanoparticles for the enhancement of the red emission, half part of the surface of the KTP susbstrate embedded luminescent nanoparticles inside the conical pores was covered with the colloidon film to protect the nanoparticles while depositing the Au sputtered nanoparticles and the remaining part of the surface of the KTP substrate embedded nanoparticles was deposited by Au nanoparticles.

Photoluminescence measurements were carried out on the surface of the KTP substrate embedded with luminescent Er^{3+}: KYbW nanoparticles, at uncovered and covered regions with the Au nanoprticles by pumping with 980 nm wavelength. The obtained photoluminescent spectra is show in Figure 6.13.

From Figure 6.13, we observed that the there is no any significant photoluminescence was enhanced due to the coupling of Er:KYbW nanoparticles embedded inside the conical pores of the KTP substrate with the Au plasmons at $^4F_{9/2} \rightarrow {}^4I_{15/2}$ transition around 660 nm when compared with the spectra obtained at the uncovered region of the Au nanoparticles. There is no any effect of the gold nanoparticles on the transition from $^4F_{9/2}$ to the ground state $^4I_{15/2}$, enhanced light emission from the upconversion due to the plasmon resonances in our sample.

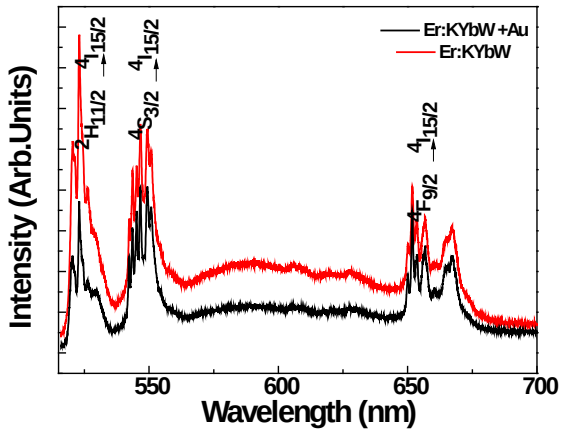

***Figure 6.13**. Photoluminscence spectra of Er:KYbW nanoparticles embedded inside the conical pores of the KTP-2 sample with the covered and uncovered Au plasmons.*

However, this could be the another alternative way to enhance the particular low intensity wavelengths from the lanthanide ions, and this enhancement of the smaller wavelengths could be possible for the development of phosphor displays at particular single Near IR wavelength excitation source.

6.6. Interparticle energy migration between oxide luminescent nanoparticles

As has been shown in the previous section, the red light we obtained from the luminescent nanoparticles we synthesized was of a dark red color, since it is obtained at a wavelength of ~ 700 nm. To obtain a lighter red light, that can be perceived as more brilliant by the human eye, we pursued another approach, using the interparticle energy migration upconversion (EMUC) process [205]. The results obtained in this approach are presented in *paper VIII*. In this process we doped the nanoparticles with four different types of lanthanide ions. The ion being excited directly by the pump source is called the sensitizer (type I) (Yb^{3+} in our case), the ion to which energy is transferred and which raises to an excited state is called the accumulator (type II) (Tm^{3+} in our case). The migrator (type III) ion Gd^{3+} receives energy from the high-lying energy states of the accumulator ion and then energy hopping can be produced from migrator ion to the activator ion (type IV) (Eu^{3+} in our case). The required emission wavelengths can be obtained by choosing the right activator by this process. The only requirement to use this approach is that the

sensitizer and the accumulator have to be spatially apart from the activator, while the migrator ion has to be present in the two parts. We used two different kinds of nanoparticles to confine the sensitizer/accumulator and the activator, such as Yb,Tm:KGdW and Yb,Tm:Gd_2O_3, from one side, and Eu:KGdW and Eu:Gd_2O_3 nanoparticles, from the other. As can be seen, the sensitizer and the accumulator are present in one type of nanoparticles the activator is present in the other type of nanoparticles, while the migrator is present in the two types of nanoparticles.

Then, we mixed the nanoparticles of the same kind containing the sensitizer/accumulator with the nanoparticles containing the activator, inducing the interparticle energy migration upconversion process. For mixing the nanoparticles, we added a small amount of ethanol and mixed them properly in an ultrasonic bath for 10 min. Finally we obtained two different set of nanocomposites: Yb:Tm:KGdW + Eu:KGdW (here after M1) and Yb:Tm:Gd_2O_3 + Eu:Gd_2O_3 (here after M2). In M1 the concentration of doping ions was 10 mol % of Yb^{3+} and 5 mol % Tm^{3+}, as sensitizer and accumulator, respectively, and 5 mol % of Eu as an activator in the host matrix of KGdW. In M2 the concentration of doping ions was 45 mol % of Yb^{3+} and 1 mol % of Tm^{3+}, and 5 mol % of Eu in the Gd_2O_3 host matrix.

To investigate the size distribution and morphology of the nanoparticles we used SEM and TEM analysis, prior and after mixing them. Figure 1 in *paper VIII* shows the recorded SEM and TEM images of the as-prepared nanocomposites before and after mixing them. From the TEM analysis, we estimated the particle size of around 30 – 40 nm. This analysis revealed an agglomeration of the nanoparticles after mixing. However, from the SEM and TEM image analysis, we did not see any significant differences on the morphology in the nanoparticles prior and after mixing.

Photoluminescence measurements were performed on the different nanocomposites prepared after pumping at 980 nm. The EMUC process between the accumulator and the migrator ions was influenced by the doping concentrations in the nanoparticles. By increasing the doping concentration we could also induce a cross relaxation process that quenched the emission of light. So that the dopants, specially the accumulator and the activator have been added to the host lattice in relatively low concentrations to obtain efficient up-conversion emissions.

The ratios at which we mixed the nanoparticles also influenced their luminescent properties. We optimized the M1 and M2 ratios to obtain maximum intensity for the emission arising from Eu^{3+} in both cases. In Figure 3 and Figure 4 in *paper VIII*, we observe the emission from the Eu^{3+} activator ion in these particles. We could obtain efficient red emission from Eu:Gd_2O_3 nanoparticles after interparticle energy migration from Tm, Yb:Gd_2O_3 nanoparticles, suppressing the blue emission generated by Tm^{3+} for a ratio Tm,Yb,Gd_2O_3/Eu:Gd_2O_3 = 1/3. However, in the case of Eu:KGdW, although we obtained red emission, it was with a small intensity when compared to the blue and red emissions generated by Tm^{3+} in the Tm,Yb:KGdW nanoparticles. The proposed energy transfer mechanism is shown in Figure 5 in *paper VIII*. We are still investigating those two systems to find an explanation for their different behaviors.

UNIVERSITAT ROVIRA I VIRGILI
MICROSTRUCTURATION OF NONLINEAR OPTICAL MATERIALS:
METHODOLOGIES, CHARACTERIZATION, AND APPLICATIONS
Raj Kumar Golconda
Dipòsit Legal: T. 55-2013

Conclusions

The potential of microstructured nonlinear optical materials, specially by ultrafast laser ablation, has been demonstrated successfully by characterizing the optical behavior of these materials in the linear and nonlinear diffraction phenomenon. We also demonstrated a possible application for these microstructured nonlinear optical materials in the controlled and localized emission properties of luminescent nanoparticles for the possible applications in the field of laser phosphor display technology.

KTP and RTP single crystals were grown by using the Top Seeded Solution growth technique. 1D and 2D periodically ordered microstructures were fabricated on the surface of these nonlinear optical materials by using ultrafast laser ablation. Selective chemical etching was performed on a periodically poled single crystal $LiNbO_3$ to reveal the ferroelectric domains on the surface of this material. A surface relief diffraction grating with smooth lateral and bottom walls was fabricated using this technique.

The detailed morphological and structural characterization of microstructured nonlinear optical materials was carried out. The optical properties of the KTP, RTP and $LiNbO_3$ diffraction gratings were analyzed in linear and nonlinear regimes. For instance, the generation of second harmonic light from these diffraction gratings was analyzed as a function of wavelength, polarization, and angle of incidence of the fundamental beam. Asymmetric diffraction patterns were observed in all these samples, although a clear explanation of the phenomena that produce such diffraction patterns was not found.

A complete micro-Raman scattering analysis was performed on the 1D and 2D microstructures fabricated on these materials. The structural properties of these

microstructured materials can change during the processing of their surfaces by ultrafast laser ablation. We observed the formation of polycrystalline RTP and TiO_2 on the surface of the ablated channels during femtosecond laser processing.

Apart from this, a theoretical modeling was also proposed to determine the shape of the fabricated channels and these periodically ordered microstructures patterns were characterized as 1D photonic crystals through experimental and theoretical modeling.

$KYb(WO_4)_2$, $KGd(WO_4)_2$, and Gd_2O_3 nanoparticles doped with different lanthanide ions were synthesized by the sol-gel Pechini method. The morphological and structural characterization was analyzed prior to the photoluminescence measurements of these nanoparticles that emitted red, green, blue, and yellow light after excitation at 980 nm. We embedded the luminescent nanoparticles inside the conical pores of KTP substrates microstructured by ultrafast laser ablation and achieved localized and spatially controlled light emissions from the luminescent nanoparticles. We successfully demonstrated that multicolor emission is possible paving the way towards the development of RGBY laser phosphor display technology.

References

[1]. P. Simon, J. Ihlemann, Appl. Phys. B **63**, 505, 1995.

[2]. G. Herbst, M. Steiner, G. Marowsky, and E. Matthias, Mater. Res. Soc. Sym. Proc. **397**, 69, 1996.

[3]. K. Kawamura, T. Ogawa, N. Sarukura, M. Hiramo, and H. Hosono, Appl. Phys. B **71**, 119, 2000.

[4]. S. Kuper, M. Stuke, Appl. Phys. Lett. **54**, 4, 1989.

[5]. S. Bauddach, J. Bonse, and W. Kautek, Appl. Phys. A, **69**, S395, 1999.

[6]. H. Loesel, J.P. Fischer, M.H. Gotz, C. Horvath, T. Juhasz, F. Noack, N. Suhm, and J.F. Bille, Appl. Phys. B, **66**, 121, 1998.

[7]. J. Flwman, Sensors & Actuators A, **56**, 151, 1996.

[8]. Y.F. Lu, Y. Zhang, W. Song, Appl. Surf. Sci. **139**, 140, 1999.

[9]. J. Kruger, W. Kautek, Laser Phys. **9**, 30, 2000.

[10]. S.S. Li, Semi cond. Phys. Elec. Plenum, NewYork, 1993.

[11]. P.P. Pronko, P. Vanrampay, A. Horvath, C.F. Loesel, T. Juhasz, X. Liu, and G. Mourou, Phys. Rev. B, **58**, 2387, 1998.

[12]. K. Wong, S. Vongehr, and V.V. Kresin, Phys. Rev. B, **67**, 035406, 2003.

[13]. A. Kaiser, B. Rethfeld, M. Vicanek, and G. Simon, Phys. Rev. B, **61**, 11437, 2000

[14]. B.C. Stuart, M.D. Feit, S. Herman, A.M. Rubenchik, B.W. Shore, and M.D. Perry, Phys. Rev. B, **53**, 1749, 1996.

[15]. X. Liu, D. Du, and G. Mourou, IEEE J. Quant. Elect. **33**, 1706, 1997.

[16]. B. C. Stuart, M. D. Feit, S. Herman, A. M. Rubenchik, B.W. Shore, and M. D. Perry, Phys. Rev. B, **53**, 1749, 1996.

[17]. B.C. Stuart, M.D. Feit, A.M. Rubenchik, B.W.Shore, and M.D. Perry, Phys. Rev. Lett. **74**, 2248, 1994.

[18]. M.D. Perry, B.C. Stuart, P.S. Banks, M.D. Feit, V. Yanovsky, and A.M. Rubenchik, J. Appl. Phys. **85**, 6803, 1999.

[19]. E.N. Glezer, Y. Siegal, L. Huang, and E. Mazur, Phys. Rev. B, **51**, 9589, 1999.

[20]. H.P. Cheng and J.D. Gillaspy, Phys. Rev. B, **55**, 2628, 1997.

[21]. H.O. Jeschke, M.E. Garcia, and K.H. Bennemann, Phys. Rev. Lett. **87**, 015003, 2001.

[22]. M. Lenzner, J. Krüger, S. Sartania, Z. Cheng, C. Spielmann, G. Mourou, and W. Kautek, Phys. Rev. Lett. **80**, 4076, 1998.

[23]. B.C. Stuart, M.D. Feit, S. Herman, A.M. Rubenchik, B.W. Shore, and M.D. Perry, Phys. Rev. B, **53**, 1749,1996.

[24]. Francesco Maria Grimaldi, Physico mathesis de lumine, coloribus, et iride, aliisque annexis libri duo (Bologna ("Bonomia"), Italy: Vittorio Bonati, pp.1-11, 1665.

[25]. D. Rittenhouse, American Philosophical Society, 1785.

[26]. M.A. Sutton, Y.J. Chao, and C.E. Taylor, Experimental mechanics, **23**, 370, 1983.

[27]. W. Lee, S. Long Yeh, Chich-Chao chang, and C. Chich-Lee, Opt. Express. **9**, 791, 2001.

[28]. D.W. Vahey, C.M. Verber, and R.P. Kenan, Proc. SPIE, **139**, 151, 1978.

[29]. C.S. Tsai, and S.K. Yao, J. Appl. Phys. **43**, 5081, 1972.

[30]. W.J. Tomlinson, Appl. Opt. **16**, 2180, 1977.

[31]. Y. Fuji, and J. Minowg, Appl. Opt. **22**, 974, 1983.

[32]. E. Treacy, IEEE. J. Quant. Electron, **QE-5**, 454, 1969.

[33]. J. Agostinelli, G. Harvey, T. Stone, and C. Gabel, Appl. Opt. **18**, 2500, 1979.

[34]. M.B. Schulz, M.G. Holland, and L. Davis, Appl. Phys. Lett. **11**, 237, 1967.

[35]. E.M. Philipp-Rutz, R. Linaree, and M. Fakuda, Appl. Opt, **21**, 2189, 1982.

[36]. P. Franken, A. Hill, C. Peters, and G. Weinreich, Phys. Rev. Lett. **7**, 118, 1961.

[37]. J.A. Giordmaine, Phys. Rev. Lett. **8**, 9, 1962.

[38]. P.D. Maker, R.W. Terhune, M. Nisenoff and C.M. Savage, Phys. Rev. Lett. **8**, 21, 1962

[39]. J.A. Armstrong, N. Bloembergen, J. Ducuing, and P.S. Pershan, Phys. Rev. **127**, 1918, 1962.

[40]. P.A. Franken, and J.F. Ward, Rev. Mod. Phys. **35**, 23, 1963.

[41]. J. A. Giordmaine, Phys. Rev. Lett. **8**, 19,1962

[42]. S.M. Salitiel, D.N. Neshav, R. Fischeer, W. Krolisowski, A. Arie, and Y.S. Kivshar, Phys. Rev. Lett. **100**, 103902, 2008

[43]. H.E. Bates, J. Opt. Soc. Am. **61**, 904, 1971.

[44]. Issac. Freund, Phys. Rev. Lett. **19**, 1404, 1968.

[45]. G. Dolino, Phys. Rev. B, **6**, 4025. 1972.

[46]. D. Rouede, C. Odin, R. aubry, and S. Mattauch, Opt. Comm. **200**, 249, 2001.

[47]. A.L. Aleksandrovskii, and V.V. Volkov, Quantum Electron, **26**, 542, 1996.

[48]. A. Apostoluk, D. Chapron, G. Gadret, B. Sahraoui, J. Nunzi, C. Fiorini-Debuisschert, and P. Raimond, Opt. Lett. **27**, 2028, 2002.

[49]. S. Moscovich, A. Arie, R. Urneski, A. Agronin, G. Rosenman, and Y. Rosenwaks, Optics. Express, **12**, 2236, 2004.

[50]. S. Saltiel, D. Neshev, W. Krolikowski, R. Fischer, A. Arie, and Yu. Kivshar, Phys. Rev. Lett. **100**, 103902, 2008

[51]. S. Saltiel, D. Neshev, W. Krolikowski, R. Fischer, A. Arie, and Yu. Kivshar, Jap. J. Appl. Phys. **47**, 6777, 2008.

[52]. T. Schneider, and J. Reif, Phys. Rev. A, **65**, 23801, 2002.

[53]. A.A. Fedyanin, O.A. Aktipetrov, D.A. Kurdyukov, V.G. Golubev, and M. Inoue, Appl. Phys. Lett. **87**, 151111, 2005.

[54]. S.M. Saltiel, D.N. Neshev, Robert Fischer, W. Krolikowski, Ady Arie, and Y.S. Kivishar, Phys. Rev. Lett. **100**, 103902, 2008.

[55]. S.M. Saltiel, D.N. Neshev, W. Krolikowski, Ady Arie, O. Bang, and Y.S. Kivishar, Opt. Lett. **34**, 848, 2009.

[56]. S.M. Saltiel, D.N. Neshev, W. Krolikowski, Ady Arie, O. Bang, and Y.S. Kivishar, Phys. Rev. Lett. **104**, 83102, 2010.

[57]. A.S. Aleksandrovsky, A.M. Vyunishev, A.I. Zaitsev, A.A. Ikonnikov, and G.I. Pospelov, Appl. Phys. Lett. **98**, 61104, 2011.

[58]. C. Méndez, J.R. Vázques de Aldana, G.A. Torchia, and L. Roso, Opt. Lett. **30**, 2763, 2005.

[59]. Y. Li. P. Lu, N. Dai, X. Wang, B. Yu, and H. Long, Appl. Phys. B, **88**, 227, 2007.

[60]. G.A. Torchia, C. Mendez, I. Arias, L. Roso, A. Rodenas, and D. Jaque, Appl. Phys. B, **83**, 559, 2006.

[61]. G. Fleming, S.Y. Lin, I. Ei-Kady, R. Biswas, and K.M. Ho, Nature, **417**, 52-55, 2002.

[62]. T.W. Ebbesen, H.J. Lezec, H.F. Ghami, T. Thio, and P.A. wolf, Nature, **391**, 667, 1998.

[63]. K. Sasaki, S. Inoue, K. Nishio, H. Masuda, A. Otomo and S. Yokovama, Opt. Mater. **32**, 543, 2010.

[64]. J.A. Sazio, A.A. Correa, C.E. Finlayson, J.R. Hayes, T.J. Schieidemantel, N.F. Baril, B.R. Jakson, D.J. Won, F. Zhang, E.R. Margine, V. Gopalan, V.H. Crespi, and J.V. Badding, Science, **311**, 1583, 2006.

[65]. W. Hu, N. Lu, H. Zhang, Y. Wang, N. Kehagias, V. Reboud, C.M. Sotomayor Torres, J. Hao, W. Li, H. Fuchs, and L. Chi, Adv. Mater, **19**, 2119, 2007.

[66]. N. Gaponik, I.L. radtchenko, M.R. Gerstenberger, Y.A. Feduitik, G.B. sukhorukov, and A.L. Rogach, Nano Lett. **3**, 369, 2003.

[67]. J.V. García-Santizo, P. Molina, M.O. Ramírez, K. Lemanski, W. Strek, P.J. Deren, and L.E. Bausa, Opt. Express. **18**, 18269, 2010.

[68]. A.R. Zanatta, and C.T. M.Riberio, J. Appl. Phys. **96**, 5977, 2004.

[69]. P. Molina, M.O. Ramirez, J.V.Garcia-santizo, S.Alvarez-Garcia, R.Pazik, W. Strek, P.J. Deren, and L.E. Bausa, Appl. Phys. Lett. **95**, 051103, 2009.

[70]. G.H. Dieke, Spectra and energy levels of rare earth ions in crystals, Interscience Publishers, 1968.

[71]. N. Bloembergen, Phys. Rev. Lett. **127**, 1918, 1962.

[72]. F. Auzel, C.R. Acad. Sci. (paris), **262**, 1016, 1966.

[73]. F. Auzel, Chem. Rev. **104**, 139, 2004**.**

[74]. I. Iparraguirre, J. Azkargorta, R. Balda, and J. Fernandez, Opt. Mater. **27**, 1697, 2004.

[75]. L. Zang, P.D. Townsend, P.J. Chanler, and A.J. Silversmith, Elect. Lett. **30**, 1063, 1994.

[76]. P.F. Wysocki, M.J. Digonnet, B.Y. Kim, and H.J. Shaw, J. Light wave Tech. **12**, 550, 1994.

[77]. Y. Kuei Hsu, C.W. Chen, J.Y. Huang, and C.L. Pan, Opt. Express, **14**, 5484, 2006.

[78]. E.C. Honea, R.J. Beach, S.B. Sutton, J.A. Speth, S.C. Mitchell, J.A. Skidmore, M.A. Emanuel and S.A. Payne, IEEE J. Quant. Electron. **33**, 592-1600, 1997.

[79]. M. Schellhorn, Appl. Phys. B, **91**, 71, 2008.

[80]. L.J. Li, B.Q. Yao, C.W. Song, X.M. Duan, and T.H. Wang, Laser Physics **18**, 1512, 2008.

[81]. D. Howse, M. Logie, A. Bluiett, S.O. Connor, N.J. Condon, J. Ganem, and S.R. Bowman, J. Opt. Soc. Am. B, **27**, 2384, 2010.

[82]. F. Cornacchia, A. Di Lieto, P. Maroni, P. Minguzzi, A. Toncelli, and E. Sorokin, Appl. Phys. B, **73**, 191, 2001.

[83]. A.A. Kaminski, Laser & Photon. Rev. **1**, 93, 2007.

[84]. D.Y. Shen, A. Andolvand, L.J. Cooper, and W.A. Clarkson, Appl. Phys. B, **79**, 559, 2004.

[85]. B.Q. Yao, X.T. Yang, X.M. Duan, T.H. Wang, Y.L. Ju, and Y.Z. Wang, Laser Phys. Lett. **6**, 509, 2009.

[86]. X . Zhang, X.G. Liu, J. P. Jouart, and G. Mary, J. Lumin. **78**, 289, 1998.

[87]. X. Zhang, X. Liu, J.P. Jouart, and G. Mary, Chem. Phys. Lett. **287**, 659, 1998.

[88]. D.N. Patel, B.R. Reddy, and S.K. Nashstevenson, Opt. Mater. **19**, 225, 1998.

[89]. G. Blasse, and B. Grabmeier, Lumin. Mater., Springer-Verlag, New York, 1994.

[90]. T. Monteiro, C. Boemare, M.J. Soares, R.A. Sa Ferreira, L.D. Carlos, K. Lorenz, R. Viander, and E. Alves, Physica B, **308-310**, 22-25, 2001.

[91]. E. EiNyein, U. Hommarich, J. Heikendfield, D. Lee, A.J. Steckl, and J.M. Zavada, Appl. Phys. Lett. **82**, 1655, 2003.

[92]. H. Homonerich, E.E. Nyein, D.S. Lee, J. Heikenfeld, A.J. Steckl, and J.M. Zavada, Mater. Sci. Eng. **B105**, 91, 2003.

[93]. M. Hail Nazarov, and D. Young Noh, Journal of rare earths, **28**, 1, Special Issue, 2010.

[94]. M.V. Nazarov, D.Y. Jeon, J.H. Kang, E.J. Popovici, L.E. Luresan, M.V. Zamoryanskaya, and B.S. Tsukerblat, Solid State Comm. **131**, 307, 2004.

[95]. J.D. Bierlein and H. Vanherzeele, J. Opt. Soc. Am. B, **6,** 622, 1989.

[96]. P.E. Perkins, and T.S. Fahlen, J. Opt. Soc. Am. B, **4**, 1066, 1987.

[97]. A. Anema, and T. Rasing, Appl. Opt. **36,** 5902, 1997.

[98]. P. Yankov, D. Schumov, A. Nenov, and A. Monev, Opt. Lett. **18,** 1771, 1993.

[99]. L.K. Cheng, and J.D. Bierlein, Ferroelectrics, **142**, 209, 2003.

[100]. A.L. Aleksandrovskii, S.A. Akhmanov, V.A. Dyakov, N.I. Zheludev, and V.I. Pryalkin, Kvant.Elektron, **12**, 1333, 1985.

[101]. L. Ouvrad, and M. Troost, Compt. Rend, **11**, 117, 1890.

[102]. I. Tordjman, R. Masse, and J.C. Guitel, Zeitschrift fur Kristallographie, **139**, 103, 1974.

[103]. P.A. Thomas, A.M. Glazer, and B.E. Watts, Acta Cryst. **B46**, 333, 1990.

[104]. F.C. Zumsteg, J.D. Bierlein, and T.E. Gier, J. Appl. Phys. **47**, 4980, 1976.

[105]. M. Gong, Z. Li, J. Wang, Y. Liu, G. Zhai, S. Shi, F. Jin, S. Wang, N. Ma, and J. Li, Appl. Opt. **38**, 7402, 1999.

[106]. J.D. Bierlein, Appl. Phys. Lett. **49**, 917, 1986.

[107]. K. Yang, S. Zhao, G. Li, and H. Zhao, IEEE. J. Quant. Elect. **40**, 1252, 2004.

[108]. J. Bierlein, Appl. Phys. Lett. **50**, 1216, 1987.

[109]. M. Tottschalk, B. Zeitner, V. Grober, and A. Rasch, Elect. Lett, **34**, 363, 1998.

[110]. P.A. Thomas, S.C. Mayo, and B.E. Watts, Acta Crystallophica, **B48**, 401, 1992.

[111]. L.K. Cheng, L.T. Cheng, J. Galperin, P.A. M.Hotsenpiller and J.D. Bierlein, J. Cryst. Growth, **137**, 107, 1994.

[112]. Y.S. Oseledchik, A.I. Pisarevsky, A.L. Prosvirnin, V.V. Starshenko, and N.V. Svitanko, Opt. Mater. **3**, 237, 1994.

[113]. Y. Guillien, B. Menaert, J.P. Feve, P. Segonds, J. Douady, B. Boulanger, and O. Pacud, Opt. Mater. **22**, 155, 2003.

[114]. H. Albrecht, C. Bonnin, Y. Gromfeld, and M.A. Hermann, Solid state lasers XV, H.J. Hoffman, and R.K. Shori, eds, Proc. SPIE, **6100**, 61001F, 2006.

[115]. M. Roth, M. Tseitlin, and N. Angert, Glass Phys. & Chem **31**, 86, 2005.

[116]. J.Y. Wang, Y.G. Liu, J.Q. Wei, L.P. Shi, and M. Wang, Z. Krist. **191**, 231, 1990.

[117]. J.A. Yariv, and P. Yeh, John Wiley & Sons, New York, 1984.

[118]. R.M. Wood, R.T. Taylor, and R.L. Rouse, Opt. Laser Tech. **7**, 105, 1975.

[119]. I.P. Kaminow. CRC Handbook of laser science and Technology, vol. III, Opt. Mater: Part 2 ed. by M.J. Wber CRC press, Boca Raton, 253-278, 1986.

[120]. G.D. Boyd, R.C. Miller, K. Nassau, W.L. Bond, and A. Savage, Appl. Phys. Lett. **5**, 234, 1964.

[121]. M.E. Kubesm, and A.M. Glass, Principles and applications of ferroelectric and related materials, Clareon press oxford, 1977.

[122]. Y.S. Kim, and R.T. Smith, J. Appl. Phys. **40**, 4637, 1969.

[123]. E.L. Wooten, K.M. Kissa, A. Yi-Yan, E.J. Murphy, D.A. Lafaw, P.F. Hallemeier, D. Maack, D.V. Attanasio, D.J. Fritz, G.J. McBrien, and D.E. Bossi, IEEE. J. Selec. Top. Quant. Elect. **6**, 69, 2000.

[124]. E.J. Murphy, T.O. Murphy, A. Ambrose, R. Irvin, B. Lee, P. Peng, G. Richards, A. Yorinks, J. Light wave Tech. **14**, 352, 1996.

[125]. A. Chowdhury, S.C. Hagness, and L. McCaughan, Opt. Lett, **25**, 832, 2000.

[126]. M.C. Pujol, M. Aguilo, F. Diaz, and C. Zaldo, Opt. Mater. **13**, 33, 1999.

[127]. M.C. Pujol, X. Mateos, R. Solé, J. Massons, J. Gavaldà, X. Solans, F. Díaz, and M. Aguiló, J. Appl. Crystallogr. **35**, 108, 2002.

[128]. M.C. Pujol, R. Solé, J. Massons, J. Gavaldà, X. Solans, C. Zaldo, F. Díaz, and M. Aguiló, J. Appl. Crystallogr. **34**, 1, 2001.

[129]. P. Klopp, U. Griebner, V. Petrov, X. Mateos, M. A. Bursukova, M.C. Pujol, R. Solé, Jna. Gavaldà, M. Aguiló, F. Güell, J. Massons, T. Kirilov, and F. Díaz, Appl. Phys. B, **74**, 185, 2002.

[130]. A.F. Wells, Structural Inorganic Chemistry 5th edition Oxford Science publications, 1984.

[131]. T. Hirai, and T. Orikoshi, J. Colloid Interface Sci. **269**, 103, 2004.

[132]. H. Guo, Y. Li, D. Wang, W. Zhang, M. Yin, L. Lou, and S. Xia, J. Alloys Compd. **23**, 376, 2004.

[133]. Dhanaraj, Byrappa, Prasad, and Dudley, Chapter 21, Springer Handbook of Crystal Growth, Springer-Verlag Berlin Heidelberg, 2010.

[134]. D. Elwell, and H.J. Scheel, Crystal growth from High temperature solutions Academic press, London 1975.

[135]. D.P. Shumov, V.S. Nikolov, K.N. LLiev, and A.L .Aleksandrovskii, Cryst. Reserch & Tech. **25**, 1245, 1990.

[136]. S. Sakka, J. Sol-Gel Sci. and Tech. **26**, 29, 2003.

[137]. Dieter Bauerle, Laser processing and chemistry, Springer-Verlag, Berlin, 2000.

[138]. B.C. Stuart, M.D. Feit, S. Herman, A.M. Rubenchik, B.W. Shore, M.D. Perry J. Opt. Soc. Am. B, **13**, 459, 1996.

[139]. E.N. Glezer, M. Milosavljevic, L. Huang, R.J. Finlay, T.H. Her, J.P. Callan, and E. Mazur, Opt. Lett. **21**, 2023, 1996.

[140]. K. Miura, J. Qiu, H. Inouye, T. Mitsuyu, and K. Hirao: Appl. Phys. Lett. **71**, 3329, 1997.

[141]. S. Bruneau, J. Hermann, M. Sentis, G. Dumitru, V. Romano, H.P. Weber, A. Semerock, and W. Marine, Proc. SPIE, **5147**, 199, 2003.

[142]. W.M. Steen (ed.) Laser material processing, New York, Springer Verlage, 1991.

[143]. E. Barry, G.W. Ross, P.G.R. Smith, R.W. Eason, and G. Cook, Mater. Lett. **37**, 246, 1998.

[144]. F. Laurell, J. Webjörn, G. Arvidsson, and J. Holmberg, J. Light. Tech. **10**, 1606, 1992.

[145]. F. Laurell, M.G. Roelofs, W. Bindloss, H. Hsiung, A. Suna, and J.D. Bierlein, J. Appl. Phys., **71**, 4664, 1992.

[146]. J. Capmany, C.R. Fernandez-Pousa, E. Dieguez and V. Bermu´dez, Appl. Phys. Lett. **83**, 5146, 2003.

[147]. Simonetta Grilli, Pietro Ferraro, and Paolo De Natale, Bruno Tiribilli and Massimo Vassalli, Appl. Phys. Lett. **87**, 233106, 2005.

[148]. I.E. Barry, G.W. Ross, P.G.R. Smith, R.W. Eason, and G. Cook, Mater. Lett. **37**, 246, 1998.

[149]. S. Grilli, P. Ferraro, P. De Natale, B. Tiribilli, and M. Vassalli, Appl. Phys. Lett. **87,** 233106, 2005.

[150]. K. Terabe, X.Y. Liu, X.J. Li, and K. Kitamura, Ferroelectrics, **340**, 121, 2005.

[151]. K. Mizuuchi, K. Yamamoto, and T. Taniuchi, Electron, Lett. **26**, 1992, 1990.

[152]. S.M. Physics of semiconductor devices, Wiley, Newyork, 2nd ed., 1981.

[153]. K.L. Chopra, R.C. Kainthla, D.K. Pandya, and A.P. Thankoor, Physics of Thinfilms, Academic press: New York **12**, 169, 1982.

[154]. D.J. Gardiner, Practical Raman Spectrocopy, Springer-Verlag, ISBW 978-0387502540, 1989.

[155]. K. Iliev, P. Peshev, V. Nikolov, and I. Koseva, J. Cryst. Growth, **100**, 225, 1990.

[156]. G.M. Loiacono, T.F. McGe, and G. Kostecky, J. Cryst. Growth, **104**, 389, 1990.

[157]. I. Tordjman, R. Masse, and J.C. Guitel, Crystalline Z. Krist, **139**, 103, 1974.

[158]. L. K. Cheng, and J.D. Bierlein, Ferroelectrics **142,** 209, 1993.

[159]. M. Munowitz, R.H. Jarman, and J.F. Harrison, Chem. Mater. **5**, 1257, 1993.

[160]. V. Pasiskevicius, C. Canalias, and F. Laurel, Appl. Phys. Lett. **88**, 041110, 2006.

[161]. P.A. Thomas, A.M. Glazer, and B.E. Watts, Acta Cryst. **B46**, 333, 1990.

[162]. G. Wulff, Zeitschrift der Kristallographie, **34**, 449, 1901.

[163]. J.D.H. Donnay, and D. Harker, Am. Mineral, **22**, 446, 1937.

[164]. V.I. Voronkova, and Y.K. Yanovskii, Sov. Phys. Crystallogr., **31**, 123, 1986.

[165]. Pavlova, V.M. Garmash, G.B. Silnitskaya, N.P. Stekolshchikova and V. A. Gerken, Sov. Phys. Crystallogr., **31**, 87, 1986.

[166]. A. Angert, M. T. Seitlin, E. Yashchin, M. Roth, Appl. Phys. Lett, **67**, 1941, 1995

[167]. R.J. Bolt, P. Bennema, J. Crystal Growth, 102, 329, 1990.

[168]. Cheng Gan Chao, Qian Zhi Qiang, Tang Guang Kui, Song Wen Bao, and Tang Hang Gao, J. Cryst. Growth, **112**, 294, 1991.

[169]. J.G. Dumitru, V. Romano, H.P. Weber, M. Sentis, and W. Marine, Appl. Phys. A, **74**, 729, 2002.

[170]. S. Baudach, J. Bonse, and J. Kruger, App. Surf. Sci. **154**, 555, 2000.

[171]. F.R. Wagner, A. hildenbrand, J.Y. Natoli, M. Commandre, F. Theodore, and H. Albrecht, Opt. Express. **15**, 13849, 2007.

[172]. I.E. Barry, G.W. Ross, P.G.R. Smith, R.W. Eason, and G. Cook, Mater. Let, **37**, 246, 1998.

[173]. D. Xue, and K. kitamura, Ferroelectrics Letters, **29**, 89, 2002.

[174]. C.L. Sones, S. Mailis, W.S. Brocklesby, R.W. Eason, and J.R. Owen, J. Mater. Chem. **12**, 295, 2002.

[175]. K. Terabe, X.Y. Liu, X.J. Li, and K. Kitamura, Ferroelectrics, **340**, 121, 2005.

[176]. J.J. Carvajal, P. Seconds, A. Peña, J. Zaccaro, B. Boulanger, F. Díaz, and M Aguiló, J. Phys. Cond. Mater. **19**, 116214, 2007.

[177]. P.S. Ha, H.J. Youn, H.S. Jung, K.S. Hong, Y.H. Park, K.H. Ko, J. Colloid Interf. Sci. **16**, 223, 2000.

[178]. Y. Djaoued, S. Badilescu, P.V. Ashrit, D. Bersani, P.P. Lottici, and J. Robichaud, J. Sol-gel Sci. Technol. **24,** 255, 2002 .

[179]. J.J. Carvajal, R. Solé, Jna. Gavaldà, J. Massons, F. Díaz, and M. Aguiló, Chem. Mater. **15**, 2730, 2003.

[180]. J. Cugat, R. Sole, J.J. Carvajal, X. Mateos, J. Massons, A. Ruiz de la Cruz, J. Solis, G. Lifante, F. Diaz, and M. Aguiló, Fs- laser microstructuring of ribs on active (Yb,Nb): RTP/RTP planar waveguides, (submitted to J. Light wave Tech.)

[181]. Z. Kraal, J. Ferré-Borrull, L.F. Marsal, J. Pallares, T. Trifonov, A. Rodriguez, and R. Alcubilla, IEEE, Electronic devices, 293-295, 2007.

[182]. R. Reinisch, and M. Neviere, Phys. Rev. B, **28**, 1870, 1983.

[183]. J.L. Coutaz, M. Neviere, E. Pic, and R. Reinisch, Phys. Rev. B, **32**, 2227, 1985.

[184]. A. Sharon, D. Rosenblatt, and A.A. Friesem, J. Opt. Soc. Am. A, **14**, 2985, 1997.

[185]. J.J. Carvajal, A. Peña, R. Kumar, M.C. Pujol, X. Mateos, M. Aguiló, F. Díaz, J. R. Vázquez de Aldana, C. Méndez, P. Moreno, L. Roso, T. Trifonov, A. Rodríguez, R. Alcubilla, Z. Král, J. Ferré-Borrull, J. Pallarès, L.F. Marsal, S. Di Finizio, R. Macovez, and J. Martorell, J. Lumin. **129**, 1441, 2009.

[186]. J.B. Pendry and A. MacKinnon, Phys. Rev. Lett. **69**, 2772, 1992

[187]. D. Felbacq, J. Opt. Soc. Am. A, **11**, 2526, 1994.

[188]. V. Kuzmiak, A.A. Maradudin, and F. Pinsemin, Phys. Rev. B, **50**, 16835, 1994.

[189]. A. Taflove and S. Hagness, Computational Electrodynamics. The finite-difference time-domain method, Artech House, Boston, 2005.

[190]. M. Plihal and A.A. Maradudin, Phys. Rev. B, **44**, 8565, 1991.

[191]. P. R. Villeneuve and M. Piché, Phys. Rev. B, **46**, 4969, 1992.

[192]. R.D. Meade, K. D. Brommer, A.M. Rappe, and J.D. Joannopoulos, Appl. Phys. Lett. **61**, 495, 1992.

[193]. K.M. Ho, C.T. Chan, and C.M. Soukoulis, Phys. Rev. Lett. **65**, 3152, 1990.

[194]. K. M. Leung, and M. Liu, Phys. Rev. B. **41**, 10188, 1990.

[195]. P.A. Morris, M. K. Crawford, and B. Jones, J. Appl. Phys. **72**, 5371, 1992.

[196]. G. Hansson, H. Karisson, S. Wang, F. Laurell, Appl. Opt. **39**, 5050, 2000.

[197]. David Parker, coordination chemistry reviews, **105**, 109, 2000.

[198]. S.V. Beltyukova, E.I. Tslik, A.V. Egorova, J. Pharmaceutical and Biomedical analysis, **18**, 261, 1998.

[199]. M.C. Pujol, M.A. Bursukova, F. Guiell, X. Mateos, R. Sole, Jna, Gavalda, M. Aguilo, J. Massons, F. Diaz, P. Klopp, U. Griebner, and V. Petrov, Phys. Rev. B, **65**, 165121, 2002.

[200]. P. Klopp. U.Griebner, V. Petrov, X. Mateos, M. Bursukova, M.C.Pujol, R.Solé, Jna, Gavalda, M. Aguiló, F. Guell, J. Massons, T. Kirilov, and F. Díaz, Appl. Phys. B: Lasers Opt. **74**, 185, 2002.

[201]. Smith Thomas, Guild John, The CIE colorimetric standards and their use, Transactions of the optical society, 33, 73, 1931.

[202]. O.L. Malta, P.A. Santa-Cruz, G.F. de Sa, and F. Auzel, J. Solid State Chem. **68**, 314, 1987.

[203]. G. Sun, J.B. Khurgin and R.A. Soref, Appl. Phys. Lett. **90**, 111107, 2007.

[204]. H. Mertens, and A. Polman, Appl. Phys. Lett. **89**, 211107, 2006.

[205]. F. Wang, R. Deng, J. Wang, Q.Wang, Y. Han, H. Zhu, X. Chen, and X. Liu, Nature Materials, **10**, 968, 2011.

UNIVERSITAT ROVIRA I VIRGILI
MICROSTRUCTURATION OF NONLINEAR OPTICAL MATERIALS:
METHODOLOGIES, CHARACTERIZATION, AND APPLICATIONS
Raj Kumar Golconda
Dipòsit Legal: T. 55-2013

UNIVERSITAT ROVIRA I VIRGILI
MICROSTRUCTURATION OF NONLINEAR OPTICAL MATERIALS:
METHODOLOGIES, CHARACTERIZATION, AND APPLICATIONS
Raj Kumar Golconda
Dipòsit Legal: T. 55-2013

Paper I

New approaches for the fabrication of photonic structures of nonlinear optical materials

J.J. Carvajal, A. Peña, R. Kumar, M.C. Pujol, X. Mateos, M. Aguiló, F. Díaz, J.R. Vázquez de Aldana, C. Méndez, P. Moreno, L. Roso, T. Trifonov, A. Rodríguez, R. Alcubilla, Z. Král, J. Ferré-Borrull, J. Pallarès, L.F. Marsal, S. Di Finizio, R. Macovez, J. Martorell

Journal of Luminescence, **129**, 1441-1447 (2009)

UNIVERSITAT ROVIRA I VIRGILI
MICROSTRUCTURATION OF NONLINEAR OPTICAL MATERIALS:
METHODOLOGIES, CHARACTERIZATION, AND APPLICATIONS
Raj Kumar Golconda
Dipòsit Legal: T. 55-2013

Journal of Luminescence 129 (2009) 1441–1447

Contents lists available at ScienceDirect

Journal of Luminescence

journal homepage: www.elsevier.com/locate/jlumin

New approaches for the fabrication of photonic structures of nonlinear optical materials

J.J. Carvajal [a], A. Peña [a], R. Kumar [a], M.C. Pujol [a], X. Mateos [a], M. Aguiló [a], F. Díaz [a,*], J.R. Vázquez de Aldana [b], C. Méndez [b], P. Moreno [b], L. Roso [b], T. Trifonov [c], A. Rodríguez [c], R. Alcubilla [c], Z. Král [d], J. Ferré-Borrull [d], J. Pallarès [d], L.F. Marsal [d], S. Di Finizio [e], R. Macovez [e], J. Martorell [e]

[a] Física i Cristal lografia de Materials i Nanomaterials (FiCMA–FiCNA), Univ. Rovira i Virgili (URV), Campus Sescelades, Marcel lí Domingo, s/n, E-43007 Tarragona, Spain
[b] Servicio Láser, Univ. Salamanca, E-37008 Salamanca, Spain
[c] Dept. Enginyeria Electrònica, Univ. Politècnica de Catalunya, E-08034 Barcelona, Spain
[d] Dept. d'Enginyeria Electrònica, Univ. Rovira i Virgili (URV), E-43007 Tarragona, Spain
[e] ICFO—Institut de Ciències Fotòniques, E-08860 Castelldefels, Spain

ARTICLE INFO

Available online 9 April 2009

PACS:
42.65.−k
42.70.Mp
42.70.Qs
42.79.Dj
42.82.Ds
42.82.Fv

Keywords:
Photonic crystals
Nonlinear optics
$LiNbO_3$
$KTiOPO_4$
Template growth
Liquid phase epitaxy

ABSTRACT

We revisited two different strategies to fabricate 1D photonic crystals of nonlinear optical dielectric materials based on ultrafast laser ablation of the surface of an $RbTiOPO_4$ crystal, and selective etching of ferroelectric domains of the surface of a periodically poled $LiNbO_4$ crystal. We evaluated their behaviour as Bragg diffraction gratings. We also presented the recent advances we developed in a new procedure of fabrication of 2D and 3D photonic crystals of $KTiOPO_4$ (KTP) grown on the surface of a KTP substrate by liquid phase epitaxial means within the pores of a silicon macroporous template. Optical, structural, morphological, and compositional characterization for the photonic crystals produced through this technique are presented.

1. Introduction

Since 1987, when the first work about photonic crystals (PCs) was published [1,2], many interesting properties have been studied in one, two, and three dimensions. Besides their peculiar linear optical properties [3], photonic crystals present many interesting features for controlling the nonlinear optical interactions. They provide the possibility to enhance [4–6] a second-order nonlinear optical interaction and an alternative phase-matching mechanism [7,8]. It has been shown that even in a centrosymmetric material it is possible to hold an efficient second-order interaction employing the photonic crystal properties [9]. Furthermore, the periodic modulation of both refractive index and second-order nonlinear susceptibility might allow backward parametric oscillation [10], a nonlinear effect predicted many years ago but not yet observed experimentally.

To obtain a very efficient and durable nonlinear interaction in a PC it would be adequate to use a material with high second-order nonlinear optical properties, such as $LiNbO_3$ (LN), $KTiOPO_4$ (KTP), and its isostructural $RbTiOPO_4$ (RTP). Lithium niobate, LN, is a ferroelectric material of considerable interest to the optical, laser, and communications industry, due to its large values of nonlinear optical, electro-optic, piezoelectric, and acousto-optical coefficients [11]. Potassium titanyl phosphate, KTP, has been recognized as the material of choice for second-harmonic generation of Nd:YAG light, due to its extremely low onset power threshold, high-power conversion efficiency, and high threshold to laser-induced damage [12]. It has also been the focus of considerable attention for optical parametric oscillation, sum and difference frequency mixing [13], and electro-optic switching [14]. Among the isostructural materials to KTP, RTP presents a high surface damage threshold ($9.0\times10^6\,MW\,m^{-2}$) and large temperature matching bandwidth ($50\,K\,cm^{-1}$), double than that of KTP [15].

In this paper, we propose two different strategies to fabricate 1D photonic crystals based on these nonlinear optical materials. These strategies are based on previous methodologies used for the microstructuration of the surface of materials to fabricate

* Corresponding author.
E-mail addresses: joanjosep.carvajal@urv.cat (J.J. Carvajal), f.diaz@urv.cat (F. Díaz).

0022-2313/$ - see front matter © 2009 Elsevier B.V. All rights reserved.
doi:10.1016/j.jlumin.2009.03.035

diffraction gratings, such as the ultrafast laser ablation, and the selective etching of ferroelectric domains. We fabricated diffraction grating on the surface of an RTP and the periodically poled $LiNbO_3$ crystals, and evaluated their behaviour as Bragg diffraction gratings.

One of the challenges for fabricating higher dimensional (2D and 3D) photonic crystals is the production of these structures with sufficient precision to prevent scattering losses blurring the crystal properties. We present here the advances we developed recently in a completely new procedure that combines top-down and bottom-up approaches to fabricate 2D and 3D PCs of nonlinear dielectric materials, and that for the moment has been tested on KTP [16]. These crystals are grown on the surface of a KTP substrate, which gives to the photonic structure the requested crystallographic orientation, within the pores of a silicon macroporous template that gives the final shape to the photonic structure.

2. Strategies to fabricate diffraction gratings: towards the fabrication of 1D photonic crystals

Optical diffraction gratings constitute a fundamental optical component used to periodically modulate the phase or amplitude of incident waves, and are expected to be useful devices for wavelength division multiplexing systems in optical communications and optical sensors. Moreover, in integrated optoelectronics they have applications as optical wave couplers and filters.

2.1. Ultrafast laser ablation

A 1D relief grating was recorded on the surface of an RTP sample by ultrafast laser ablation. This technique uses very short (some tens picoseconds is the limit for the process, depending on the materials) and intense laser pulses to remove thin layers from the surface of a bulk target by means of physical mechanisms different from those taking place in conventional laser ablation. The collateral thermal and mechanical effects around the ablated area are diminished to such an extent that precision and quality of the microstructures higher than those obtained with other techniques can be achieved. Nonlinear absorption and ionization processes are on the basis of this technique. Focusing on dielectrics, within the duration of a pulse and for moderate intensities, a thin layer on the surface of the material is almost fully ionized by multiphoton and collisional mechanisms so that the number of free electrons rapidly amounts to the solid-state density. As a consequence of the poor electric transport properties of the material, surface charging takes place and the ultraintense "quasielectrostatic" field generated overcomes the binding energy of the ions and drag them out of the solid. This mechanism is known as Coulomb explosion and since thermal coupling with the lattice is negligible during this short period of time, the process is a purely non-thermal process.

For larger intensities, total ionization of the surface is achieved for the leading edge of the laser pulse. Therefore, free electrons can absorb energy from the laser pulse in the presence of the lattice atoms and ions by means of inverse bremsstrahlung mechanism. This absorbed energy contributes to raise the temperature of a deeper surface layer by electron heat diffusion to a value close to the thermodynamic critical temperature giving rise to a phase explosion process, resulting in violent expulsion of both vapor and equilibrium liquid droplets [17]. The depth of the ablated layer is determined by the electron heat diffusion length and the laser fluence. Although the process is still very fast, some thermal damage must be expected on the areas surrounding the microstructured region.

We have used a commercial Ti:Sapphire oscillator (Tsunami, Spectra Physics) and a regenerative amplifier system (Spitfire, Spectra Physics) based on chirped pulse amplification (CPA). The system delivers linearly polarized 120-fs pulses with central wavelength 795 nm with a repetition rate of 1 kHz. The maximum available pulse energy is 1 mJ but for the purpose of microstructuring the grating it was reduced to 0.78 μJ using a half-wave plate and a linear polarizer. The transverse mode is gaussian and the beam width is 9 mm ($1/e^2$ criterion). The beam was then focused by a 50 mm achromatic lens resulting in a peak fluence of $\sim 7\,J\,cm^{-2}$ at focus.

The sample was placed on a motorized XYZ translation stage in order to achieve optimal focusing on the target surface. The focused beam moved in straight lines across the sample surface at a constant scanning speed of $130\,\mu m\,s^{-1}$ avoiding iterative passes along the same line. The pitch between successive grooves was set to 15 μm. For this scanning speed, the number of pulses contributing to the ablation of a point within the sample surface was approximately 40. We have estimated the ablation threshold fluence following the procedure described in Ref. [18], giving $1.44 \pm 0.18\,J\,cm^{-2}$ for 40 pulses. For multishot conditions (>100 pulses) the value for the threshold decreases to $1.18 \pm 0.15\,J\,cm^{-2}$ (incubation factor $\xi = 0.783$ [19]).

Fig. 1 shows two pictures, taken with a scanning electron microscope (SEM) FEI QUANTA 600, of the sample after the ultrafast laser ablation process where it can be seen the diffraction grating generated on the surface of the sample. The sample was also observed under a Carl Zeiss Axio Imager A1 optical microscope. The lattice constant estimated from this microscope is approximately 15 μm. However, the roughness achieved on the lateral walls of the channels is still excessive for optical purposes.

We have recorded Bragg-diffraction spectra of this sample by using a FT-IR spectrometer (Bruker-Vertex 70) equipped with a special reflectivity attachment. The light source was a halogen tungsten lamp, and we collected the intensity of the diffracted light with a DLATGS detector in the spectral range from 7500 to $400\,cm^{-1}$. The incoming light was pointed perpendicular to the plane of the sample and the diffraction spectra were measured in a direction perpendicular to the grooves and at collection angles ranging from 24° to 60° in 2° steps. Two repeated measurements were collected for the sample. The measured data are represented in Fig. 2 with an intensity plot as a function of the wavelength and the diffraction angle.

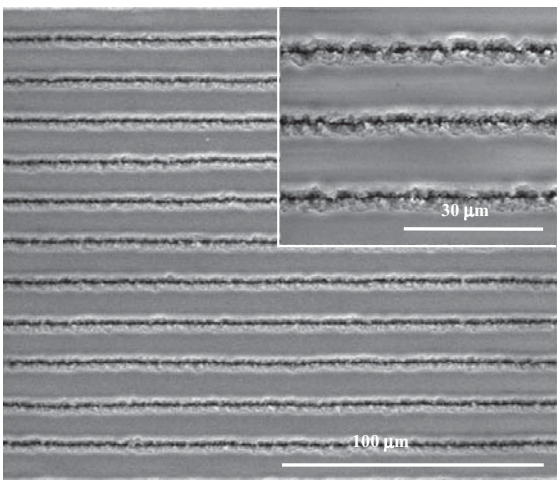

Fig. 1. SEM images of the diffraction grating generated on the surface of an RTP crystal by ultrafast laser ablation.

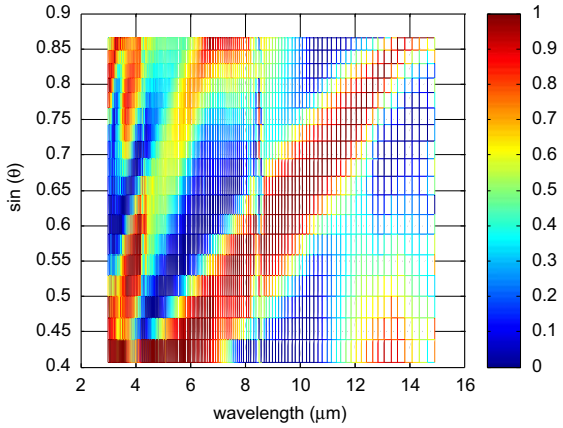

Fig. 2. A 2D intensity plot as a function of the wavelength and the diffraction angle for the diffraction grating generated on the surface of an RTP crystal by ultrafast laser ablation. Dark zones represent the diffraction orders.

To evaluate the lattice constant, the Bragg-diffraction spectra were fitted to the following two-variable function:

$$I(\lambda, \sin\theta) = \sum_{n=1}^{3} \exp\left[\left(\frac{\sin\theta - (n\lambda/a)}{w_n}\right)^2\right] \quad (1)$$

where w_n takes into account the width of the diffraction peaks, a is the lattice constant, and n is an integer (the number of the diffraction order). The fitting of this function to the experimental data gives a robust estimation of the lattice constant from the data, since all the measurements are taken into account simultaneously. The value of the lattice constant measured by this procedure was 14.92 μm, which was in good agreement with the value estimated by optical microscopy.

2.2. Selective chemical etching of ferroelectric domains in periodically poled crystals

Ferroelectric domains of opposite spontaneous polarization present different etching speeds when dipped in some acid mixtures. This property has been used to reveal the domain pattern at the surface of periodically poled crystals. However, the selective etching process provides further capabilities for versatile surface engineering of domain-engineered crystals, allowing the production of deep, high aspect ratio structures, with side-walls that can be extremely smooth [20]. These structures can find applications in the fields of optics and optoelectronics for waveguides, Bragg reflectors, and photonic band-gap devices. More recently, the fabrication of periodic 1D and 2D surface structures in congruent LN by periodic electric-field poling at the overpoling regime and selective wet chemical etching under appropriate conditions have also been reported [21–23], with feature sizes and periods down to submicron and nanoscale range.

The most common wet selective etchant reported for the ferroelectric domains of LN has been a mixture of hydrofluoric (HF) and nitric (HNO_3) acids, which attacks the negative z face ($-z$) of LN at a rate that is appreciably higher than the positive z face ($+z$) [20,22,24]. At room temperature, in a 1:2 mixture of HF and HNO_3 acids, the $-z$ face experiences etch rates of $\sim 1\,\mu m\,h^{-1}$, whereas the $+z$ face remains unetched. Even at temperatures up to 368 K, where the $-z$ etch rate increases to $\sim 30\,\mu m\,h^{-1}$, the $+z$ face appears not to etch at all, apart from at isolated sites where defects or dislocations may occur. Furthermore, independent of the mixture composition, the etch depth increased linearly with respect to etch time.

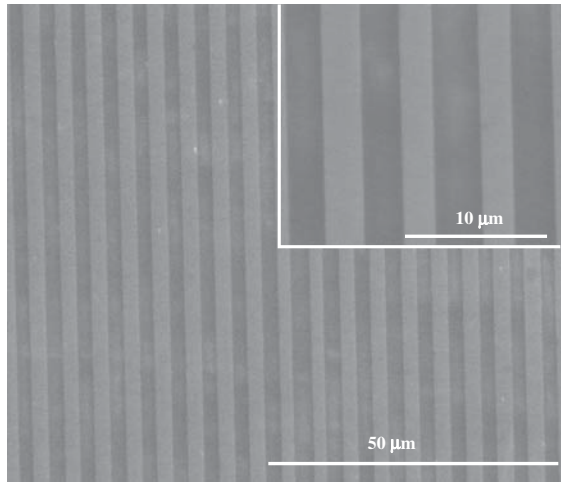

Fig. 3. SEM images of the diffraction grating generated on the surface of a periodically poled LN crystal by selective chemical etching of one of the ferroelectric domains.

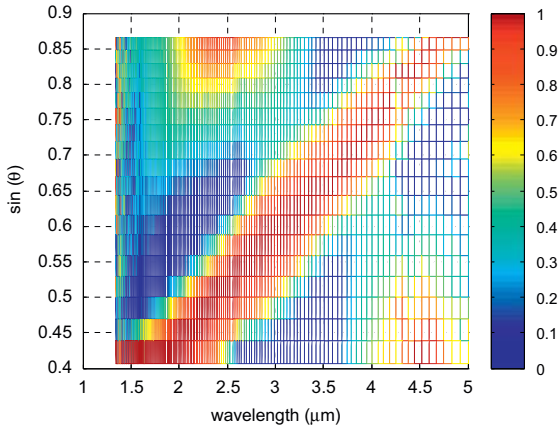

Fig. 4. A 2D intensity plot as a function of the wavelength and the diffraction angle for the diffraction grating generated on the surface of a periodically poled LN crystal by selective chemical etching of one of the ferroelectric domains.

We used a commercially available periodically poled LN crystal sample from INO, 0.5 mm thick, with a period of 5.4 μm. The sample was etched in a $HF:HNO_3 = 1:2$ acid mixture for 30 min at room temperature. After etching, the surface was monitored by optical and electronic microscopy. The surface of the sample after etching is shown in Fig. 3.

The lattice constant estimated from the optical microscope images is 5.13 μm. The characterization of the Bragg-diffraction spectra (see Fig. 4) resulted in a lattice constant of 5.25 μm.

3. A new strategy to fabricate 2d and 3d photonic crystals

One of the main challenges for the production of photonic structures with higher dimensionality is the fabrication of these structures with sufficient precision to prevent scattering losses

blurring the crystal properties. For this reason, new fabrication techniques can be proposed to avoid or reduce these problems.

The procedure for fabricating 2D and 3D photonic crystals we developed combines two well-known techniques: the fabrication of 2D and 3D macroporous silicon membranes and the epitaxial growth of KTP within the pores of these membranes. This procedure, in addition to its simplicity, results in KTP and silicon integrated in a single structure that would eventually be used to generate or modulate light.

We fabricated these 2D and 3D PCs in four different steps which involved the preparation of high-quality ordered macroporous silicon templates, the growth of the KTP epitaxial layer within the pores of the silicon template, the polishing of the top or bottom surface of the KTP epitaxial layer, and finally, a selective etching of the silicon matrix.

Silicon membranes were prepared by light-assisted electrochemical etching and post-processing. The starting material was n-type $\langle 1\,0\,0 \rangle$ silicon with resistivity of 2–6 Ωcm. The front side of the wafers was patterned with inverted pyramidal shaped pits arranged in a square or triangular periodic lattice with periods ranging from 4.5 to 10 μm by oxidation, photolithography and subsequent etching with tetramethyl ammonium hydroxide (TMAH) that act as nucleation sites for the ordered pore growth along the $\langle 1\,0\,0 \rangle$ direction. A low-resistance transparent ohmic contact was formed by n^+-ion implantation on the back side of the silicon wafer. The wafers were incorporated in an electrochemical etching cell containing a 5 wt% aqueous solution of hydrofluoric acid. The chemical dissolution of silicon requires the generation of positive carriers (holes), which was achieved by using an LED matrix (880 nm peak emission wavelength) for back side illumination and the size and the quality of the pores was controlled by means of a computerized feedback mechanism that regulates the generation of holes by continuously adjusting the back side illumination. Periodicity in the third dimension was introduced by modulating the light intensity during etching which leaded to a modulation of pore diameter in depth. Macroporous arrays with sine-wave modulated pores were produced in this way. In order to fabricate a fully 3D structure, adjacent pores had to be also connected laterally, i.e. in $\langle 1\,1\,0 \rangle$ directions. To do that the samples were subjected to multiple oxidation/oxide-removal cycles after etching. In each cycle, pores became widened because of the dissolution of the silicon consumed during the thermal oxidation. After several cycles, pore walls were dissolved first at the position of diameter maxima of the pores and adjacent pores become then connected sideways. To obtain a free-standing macroporous membrane, the back side of the samples was polished down until the opening of the pores. Fig. 5 shows some SEM images of the silicon templates produced, with thicknesses over 100 μm.

In a second step, the silicon template was closely bound to a KTP single-crystal substrate with typical dimensions 5 mm long, 3 mm wide, and 1 mm thick. The crystal was oriented in such a way that the largest surface was perpendicular to the ***c*** crystallographic direction with the edges parallel to ***a*** and ***b*** crystallographic directions. The template/substrate set was immersed into a solution formed by mixing of K_2O, P_2O, TiO_2, and WO_3 with a molar % composition K_2O–P_2O–TiO_2–$WO_3 = 42$–14–14–30 for a period of time between 5 and 10 min. WO_3 was used for decreasing the viscosity of the solution and allowing a faster growth process. A special vertical furnace was used for the epitaxial growth experiments of KTP that provided a wide region with practically no axial gradient. The temperature was controlled by a Eurotherm 903 P controller–programmer. We determined accurately the saturation temperature (T_s) and the epitaxial growth of the KTP photonic structure started two degrees below T_s, which provided a supersaturation degree in the solution of about 2%. After the epitaxial growth experiment, the template/substrate/epitaxy composite was removed from the solution, but

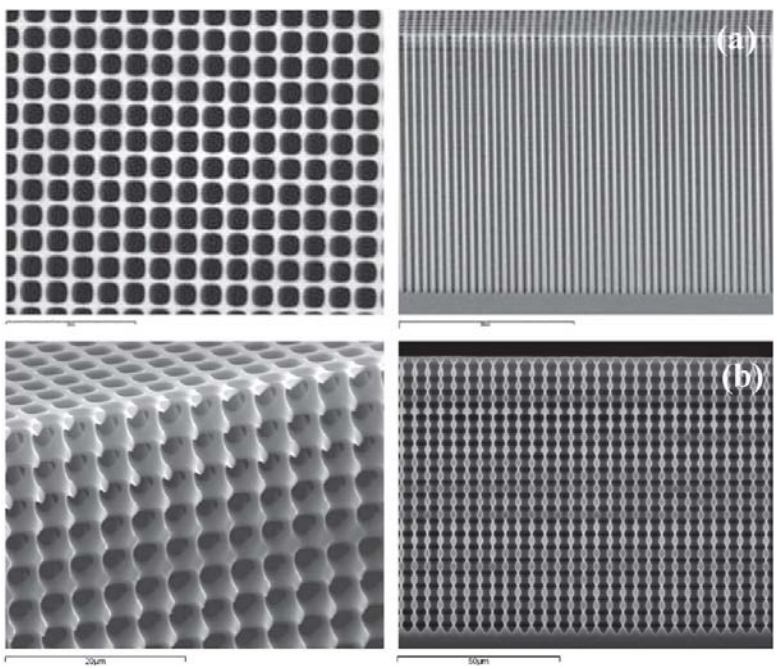

Fig. 5. SEM pictures of a (a) 2D and a (b) 3D macroporous silicon template.

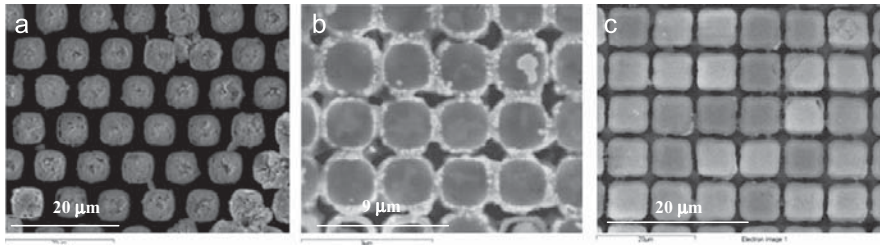

Fig. 6. SEM figures of the top surface of a 2D KTP photonic structure after polishing and partial removing of the silicon template. (a) Sample polished with 0.3 μm-size Al_2O_3 powders. (b) Sample polished using colloidal silicon (Logitech SF1). (c) Sample polished with 0.1 μm-size diamond powders.

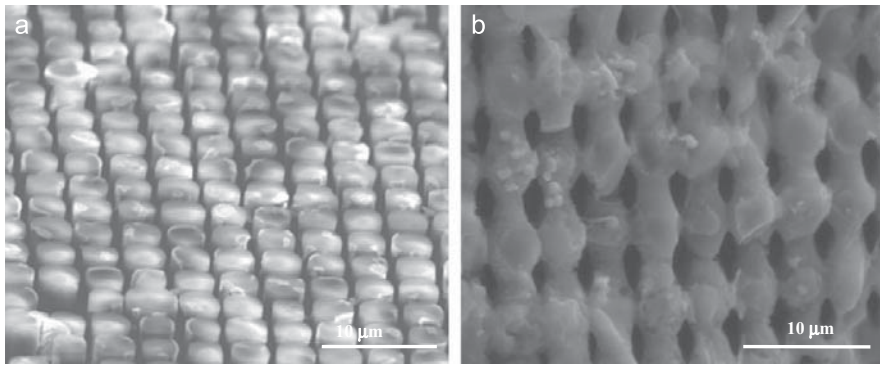

Fig. 7. SEM pictures of a (a) 2D and a (b) 3D KTP photonic crystal after polishing of the top surface and selective etching of the silicon template.

kept inside of the furnace above the surface of the solution while the furnace was cooled down to room temperature at a cooling rate of 15 K/h in order to avoid thermal stresses that could result into cracks in the photonic structures or in the substrate.

After growth, the top part of the KTP photonic structure was polished. The different hardness between silicon and KTP made the polishing process of the two materials simultaneously not easy. We used different procedures for this purpose, including alumina powders, colloidal silicon, and diamond powders. In Fig. 6 several SEM pictures show the top surface of a 2D KTP photonic structure polished following these procedures. The best results were obtained when polishing with diamond powders $\phi = 0.1\,\mu m$.

Once an optical-quality surface for the KTP photonic structure was obtained, the last step in our approach was to remove the silicon template by selective chemical etching with TMAH diluted in distilled water (5 vol%) at 354 K. The effect of the selective etching is clearly visible in Fig. 7, where a side-view image of the KTP photonic structure taken with the SEM is shown.

By using the aforesaid procedure we fabricated different KTP PCs with triangular and square lattices and lattice parameters ranging from 4.5 to 10 μm.

The crystallographic orientation of the substrate is transferred to the KTP photonic structure. To prove this we performed an X-ray texture analysis of the final photonic structure after removing the KTP substrate to ensure that the measured signal comes only from the photonic structure. Part of the silicon membrane was still maintained on the lower part of the photonic structure to give the 2D PCs the necessary mechanical rigidity for further characterization. The texture characterization was performed with a Siemens D5000 diffractometer equipped with an

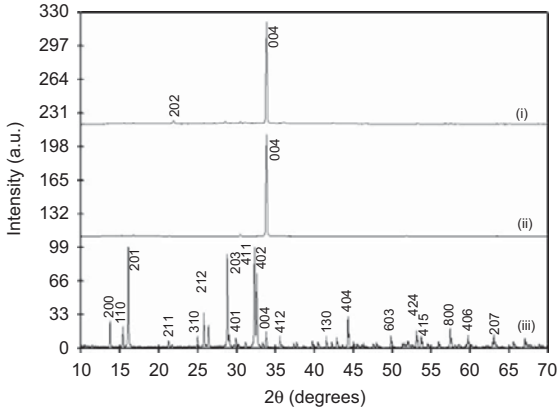

Fig. 8. X-ray powder diffraction patterns of (i) the photonic structure, (ii) KTP substrate, and (iii) KTP crystalline powders.

Euler goniometer and we obtained a 2θ scan from 10° to 70°, with a step size (ss) of 0.05° and a step time (st) of 3 s. This procedure also provided an estimation of the degree of crystallinity of the photonic structure. Fig. 8 shows the 2θ scan for a 2D KTP PC (pattern i), the substrate (pattern ii), and for a KTP crystalline powder sample, milled from a single crystal (pattern iii). The reflections were indexed according to the powder diffraction pattern of KTP, entry 80–0893 of the database maintained by the Joint Committee for Powder Diffraction Studies (JCPDS). As can be seen, the peak with the highest intensity in patterns (i) and (ii) is

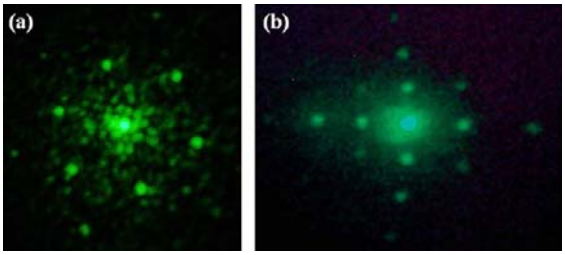

Fig. 9. Pictures of the linear diffraction pattern from a 2D KTP PC with (a) triangular lattice and (b) square lattice.

the (0 0 4) peak. However, this is not the dominant peak in the powder diffraction pattern (iii), which indicates the high degree of texturization and orientation of the KTP columns grown from the KTP substrate. The full-width at half-maximum (FWHM) for the (0 0 4) peak in the photonic structure was found to be 0.4°, very similar to that of the initial substrate, indicating the high degree of crystallinity of the photonic structure. The transference of the crystallographic orientation of the substrate to the KTP PC is advantageous for second-order nonlinear applications since it may allow the use of the most appropriate nonlinear or electro-optic coefficient for a specific application in combination with a phase-matching condition, which would be provided by the photonic structure. This is not possible with bulk KTP where phase-matching relies on the birefringence and the coefficients with the largest nonlinearity cannot be used for efficient SH generation.

A more detailed optical characterization of a 2D KTP PC can be found in Ref. [13]. Here we present the results of some basic light diffraction measurements performed on these structures. The surface of the photonic crystal will act as a diffraction grating and one would expect to see a diffraction pattern in accordance to the KTP photonic structure distribution in a square or triangular lattice. When measuring the linear diffraction in reflection we placed the sample on a XYZ positioning stage mounted on a rotating stage to be able to change the angle of incidence. Once mounted, the sample was illuminated with light at 527 nm. Some pictures of the observed diffraction patterns from samples with triangular and square lattices can be seen in Fig. 9. In those pictures one can see the presence of an intense central spot corresponding to the specular reflection and some other spots that reflect the lattice of the sample.

The PC properties of a 2D KTP structure were demonstrated by performing a measurement of the specular reflection as a function of the wavelength of the incident field. We used a 2D KTP PC of KTP columns in air and periodicity of 4.5 μm. The sample was shined with p-polarized laser pulses, spectrally tuned in the range 940–1220 nm, at an angle of incidence of 25° with respect to the axis of the photonic structure. The specular reflectance spectrum, as shown in Fig. 10, presents a dip at 1100 nm, which corresponds to the spectral position of the third-order Bragg reflection band, which was determined from a numerical calculation using the transfer matrix method.

4. Conclusions

We have used two techniques for the fabrication of 1D photonic crystals: the fabrication of periodically poled ferroelectric materials, such as $LiNbO_3$, and partial removing of one of the ferroelectric domains by selective wet chemical etching; and the microstructuration of the surface of nonlinear optical crystals,

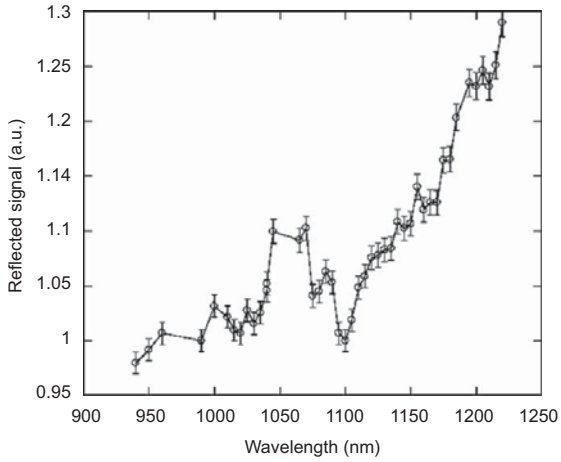

Fig. 10. Measurement of the specular reflection as a function of the wavelength of the incident light.

such as monoclinic double tungstates and $RbTiOPO_4$, by ultrafast laser ablation.

We have also fabricated 2D and 3D KTP photonic crystals by the templated growth of KTP by liquid phase epitaxy within the pores of a Si template. In this way, the single-crystal substrate provided the desired crystallographic orientation, while the silicon template gave the desired final form to the thin layer.

In the data we collected from the growth procedure we followed there is no indication that KTP PCs with smaller periods could not be grown, as macroporous silicon templates or templates of other kind, with a smaller diameter pore become readily available. Additionally, this approach to fabricate 2D and 3D photonic structures can be extended to other nonlinear and optical materials that can be grown by liquid phase epitaxy.

With these photonic structures, in the future, we pretend to study different effects, such as the generation of light at different frequencies, parametric oscillation, and guiding and bending of light in previously designed line defects.

Acknowledgements

This work was supported by the Spanish government under projects TEC2006-06531, MAT2008-C02-02/NAN, and CONSOLIDER HOPE porject CSD 2007-00007. J.J. Carvajal and M.C. Pujol are supported by the Education and Science Ministry of Spain and European Social Fund under the Ramón y Cajal program, RYC2006-858 and RYC2004-1453, respectively.

References

[1] E. Yablonovitch, Phys. Rev. Lett. 58 (1987) 2059.
[2] S. John, Phys. Rev. Lett. 58 (1987) 2486.
[3] E. Ozbay, I. Bulu, K. Aydin, H. Caglayan, K. Guven, Photon. Nanostruct. 2 (2004) 87.
[4] J. Trull, R. Vilaseca, J. Martorell, R. Corbalan, Opt. Lett. 20 (1995) 1746.
[5] P.P. Markowicz, H. Tiryaki, H. Pudavar, P.N. Prasad, N.N. Lepeshkin, R.W. Boyd, Phys. Rev. Lett. 92 (2004) 083903.
[6] J. Torres, M. Le Vassoi d'Yerville, D. Coquillat, E. Centeno, J.P. Albert, Phys. Rev. B 71 (2005) 195326.
[7] J. Martorell, R. Vilaseca, R. Corbalan, Appl. Phys. Lett. 70 (1997) 702.
[8] M. Centini, C. Sibilia, M. Scalora, G. D'Aguanno, M. Bertolotti, M.J. Bloemer, C.M. Bowden, I. Nefedov, Phys. Rev. E 60 (1999) 4891.
[9] J. Martorell, R. Vilaseca, R. Corbalan, Phys. Rev. A 55 (1997) 4520.
[10] J. Martorell, Appl. Phys. Lett. 86 (2005) 241113.

[11] A.M. Prokhorov, YUS Kuz'miniv, Physics and Chemistry of Crystalline Lithium Niobate, Adam Hilger, Bristol, 1990.
[12] G.D. Stucky, M.L.F. Phillips, T.E. Gier, Chem. Mater. 1 (1989) 492.
[13] H. Vanherzeele, J.D. Bierlein, F.C. Zumsteg, Appl. Opt. 27 (1988) 3314.
[14] J.D. Bierlein, A. Ferretti, L. Brixner, Y. Hsu, Appl. Phys. Lett. 50 (1987) 1216.
[15] Y.S. Oseledchik, S.P. Belokrys, V.V. Osadchuk, A.L. Prosvirnin, A.F. Selevich, V.V. Starshenko, K.V. Kuzemchenko, J. Cryst. Growth 125 (1992) 639.
[16] A. Peña, S. Di Finizio, T. Trifonov, J.J. Carvajal, M. Aguiló, J. Pallarès, A. Rodríguez, R. Alcubilla, L.F. Marsal, F. Díaz, J. Martorell, Adv. Mater. 18 (2006) 2220.
[17] R. Kelly, A. Miotello, Appl. Surf. Sci. 96–98 (1996) 205.
[18] G. Dumitru, V. Romano, H.P. Weber, M. Sentis, W. Marine, Appl. Phys. A 74 (2002) 729.
[19] S. Baudach, J. Bonse, J. Krüger, W. Kautek, Appl. Surf. Sci. 154–155 (2000) 555.
[20] I.E. Barry, G.W. Ross, P.G.R. Smith, R.W. Eason, G. Cook, Mater. Lett. 37 (1998) 246.
[21] S. Grilli, P. Ferraro, P. De Natale, B. Tiribilli, M. Vassalli, Appl. Phys. Lett. 87 (2005) 233106.
[22] K. Terabe, X.Y. Liu, X.J. Li, K. Kitamura, Ferroelectrics 340 (2005) 121.
[23] A. Gruverman, O. Auciello, H. Tokumoto, Appl. Phys. Lett. 69 (1996) 3191.
[24] C.L. Sones, S. Mailis, W.S. Brocklesby, R.W. Eason, J.R. Owen, J. Mater. Chem. 12 (2002) 295.

UNIVERSITAT ROVIRA I VIRGILI
MICROSTRUCTURATION OF NONLINEAR OPTICAL MATERIALS:
METHODOLOGIES, CHARACTERIZATION, AND APPLICATIONS
Raj Kumar Golconda
Dipòsit Legal: T. 55-2013

Paper II

Fabrication and characterization of photonic structures in crystals of the $KTiOPO_4$ family

G. Raj Kumar, J.J. Carvajal, M.C. Pujol, X. Mateos, M. Aguiló, F. Díaz, J.R. Vázquez de Aldana, C. Méndez, P. Moreno, L. Roso, T. Trifonov, A. Rodríguez, R. Alcubilla, Z. Král, J. Ferré-Borrull, J. Pallarès, L.F. Marsal, S. Di Finizio, R. Macovez, J. Martorell

Óptica Pura y Aplicada, **42,** 147-152 (2009)

UNIVERSITAT ROVIRA I VIRGILI
MICROSTRUCTURATION OF NONLINEAR OPTICAL MATERIALS:
METHODOLOGIES, CHARACTERIZATION, AND APPLICATIONS
Raj Kumar Golconda
Dipòsit Legal: T. 55-2013

ÓPTICA PURA Y APLICADA. www.sedoptica.es

Sección Especial: VI Reunión Española de Optoelectrónica – Optoel'09

Fabrication and characterization of photonic structures in crystals of the $KTiOPO_4$ family

Fabricación y caracterización de estructuras fotónicas en cristales de la familia $KTiOPO_4$

G. Raj Kumar[1], J. J. Carvajal[1,*], M. C. Pujol[1], X. Mateos[1], M. Aguiló[1], F. Díaz[1], J. R. Vázquez de Aldana[2], C. Méndez[2], P. Moreno[2], L. Roso[2], T. Trifonov[3], A. Rodríguez[3], R. Alcubilla[3], Z. Král[4], J. Ferré-Borrull[4], J. Pallarès[4], L. F. Marsal[4], S. Di Finizio[5], R. Macovez[5], J. Martorell[5]

1. Física i Cristal·lografia de Materials (FICMA), Univ. Rovira i Virgili (URV), Campus Sescelades, Marcel·lí Domingo, s/n, E-43007 Tarragona (Spain).
2. Servicio Láser, Facultad de Ciencias, Univ. Salamanca, E-37008 Salamanca (Spain)
3. Dept. Enginyeria Electrònica, Univ. Politècnica de Catalunya, E-08034 Barcelona (Spain)
4. Dept. d'Enginyeria Electrònica, Univ. Rovira i Virgili (URV), E-43007 Tarragona (Spain)
5. ICFO-Institut de Ciències Fotòniques, E-08860 Castelldefels (Spain)

[*] Email: joanjosep.carvajal@urv.cat

Recibido / Received: 10/07/2009. Versión revisada / Revised version: 07/09/2009. Aceptado / Accepted: 08/09/2009

ABSTRACT:

Two different procedures have been used for the fabrication of photonic structures in crystals of the $KTiOPO_4$ family. We used ultrafast laser ablation to fabricate a 1D photonic crystal on the surface of an $RbTiOPO_4$ crystal, and we evaluated its properties as diffraction grating. We also present the recent advances we developed in a new procedure of fabrication of 2D and 3D photonic crystals of $KTiOPO_4$ grown on the surface of a KTP substrate by liquid phase epitaxial means within the pores of a silicon macroporous template, and their morphological, structural and optical characterization.

Key words: Diffraction Gratings, Photonic Crystals, Nonlinear Optical Materials, Nonlinear Optics, Laser Ablation, $KTiOPO_4$, Template Growth, Liquid Phase Epitaxy.

RESUMEN:

Se presentan dos procedimientos diferentes para fabricar estructuras fotónicas en cristales de la familia $KTiOPO_4$. En primer lugar hemos usado ablación mediante láser ultrarápido para fabricar un cristal fotónico 1D en la superficie de un cristal de $RbTiOPO_4$, y hemos evaluado sus propiedades como red de difracción. También presentamos recientes avances obtenidos mediante un nuevo procedimiento de fabricación de cristales fotónicos 2D y 3D de $KTiOPO_4$, crecidos epitaxialmente en la superficie de un substrato de KTP mediante fase líquida dentro de los macroporos de un molde de silicio. Se presentan resultados de su caracterización morfológica, estructural y óptica.

Palabras clave: Redes de Difarcción, Cristales Fotónicos, Materiales Ópticos No Lineales, Óptica No Lineal, Ablación Láser, $KTiOPO_4$, Crecimiento con Molde, Epitaxia de Fase Líquida.

ÓPTICA PURA Y APLICADA. www.sedoptica.es.

REFERENCES AND LINKS

[1] E. Yablonovitch, "Inhibited spontaneous emission in solid-state physics and electronics", *Phys. Rev. Lett.* **58**, 2059-2062 (1987).

[2] S. John, "Strong localization of photons in certain disordered dielectric superlattices", *Phys. Rev. Lett.* **58**, 2486-2489 (1987).

[3] J. Trull, R. Vilaseca, J. Martorell, R. Corbalán, "Second-harmonic generation in local modes of a truncated periodic structure", *Opt. Lett.* **20**, 1746-1748 (1995).

[4] J. Martorell, R. Vilaseca, R. Corbalán, "Second harmonic generation in a photonic crystal", *Appl. Phys. Lett*. **70**, 702-704 (1997).

[5] J. Martorell, "Broadband efficient nonlinear difference generation in a counterpropagating configuration", *Appl. Phys. Lett.* **86**, 241113 (2005).

[6] G. D. Stucky, M. L. F. Phillips, T. E. Gier, "The potassium titanyl phosphate structure field: a model for new nonlinear optical materials", *Chem. Mater.* **1**, 492-509 (1989).

[7] Y. S. Oseledchik, S. P. Belokrys, V. V. Osadchuck, A. L. Prosvirnin, A. F. Selevich, V. V. Starshenko, K. V. Kuzemchenko, "Growth of $RbTiOPO_4$ single crystals from phosphate systems", *J. Crystal Growth* **125**, 639-643 (1992).

[8] A. Peña, S. Di Finizio, T. Trifonov, J. J. Carvajal, M. Aguiló, J. Pallarès, A. Rodríguez, R. Alcubilla, L. F. Marsal, F. Díaz, J. Martorell, "A two-dimensional $KTiOPO_4$ photonic crystal grown using a macroporous silicon template", *Adv. Mater.* **18**, 2220-2225 (2006).

[9] R. Kelly, A. Miotello, "Comments on explosive mechanisms of laser sputtering", *Appl. Surf. Sci.* **96-98**, 205-215 (1996).

[10] T. Trifonov, A. Rodríguez, L. F. Marsal, J. Pallarès, R. Alcubilla, "Macroporous silicon: A versatile material for 3D structure fabrication", *Sensor. Actuat. A-Phys.* **141**, 662-669 (2008).

1. Introduction

Since 1987, when the first work about photonic crystals (PCs) was published [1,2], many interesting properties have been studied in one-, two- and three dimensions. Besides their peculiar linear optical properties, photonic crystals present many interesting features for controlling the nonlinear optical interactions. They provide the possibility to enhance [3] a second order nonlinear optical interaction and an alternative phase-matching mechanism [4]. The periodic modulation of both refractive index and second order nonlinear susceptibility might allow backward parametric oscillation [5], a nonlinear effect predicted many years ago but not yet observed experimentally.

To obtain a very efficient and durable nonlinear interaction in a PC it would be adequate to use a material with high second order nonlinear optical properties, such as $KTiOPO_4$ (KTP) and its isostructural $RbTiOPO_4$ (RTP). KTP has been recognized as one of the materials of choice for second harmonic generation of Nd:YAG light, due to its extremely low onset power threshold, high power conversion efficiency, and high threshold to laser-induced damage [6]. Among the isostructural materials to KTP, RTP presents a high surface damage threshold (9.0×10^6 MW m^{-2}) and large temperature matching bandwidth (50 K cm^{-1}), double than that of KTP [7].

In this paper we propose two different strategies to fabricate photonic crystals based on these non-linear optical materials. We fabricated diffraction gratings on the surface of an RTP crystal by ultrafast laser ablation, and evaluated its behaviour as a Bragg diffraction grating. One of the challenges for fabricating higher dimensional (2D and 3D) photonic crystals is the production of these structures with sufficient precision to prevent scattering losses blurring the crystal properties. We present here the advances we developed recently in a completely new procedure that combines top-down and bottom-up approaches to fabricate 2D and 3D PCs of non-linear dielectric materials [8]. These crystals are grown on the surface of a KTP substrate within the pores of a silicon macroporous template.

2. Fabrication of diffraction gratings

A 1D relief grating was recorded on the surface of a RTP sample by ultrafast laser ablation. This technique uses very short and intense laser pulses to

remove thin layers from the surface of a bulk target by means of physical mechanisms different from those taking place in conventional laser ablation. The collateral thermal and mechanical effects around the ablated area are diminished in such an extent, that precision and quality of the microstructures higher than those obtained with other techniques can be achieved. Non-linear absorption and ionization processes are on the basis of this technique. Focusing on dielectrics, within the duration of a pulse and for moderate intensities, a thin layer on the surface of the material is almost fully ionized by multiphoton and collisional mechanisms so that the number of free electrons rapidly amounts to the solid-state density. As a consequence of the poor electric transport properties of the material, surface charging takes place and the ultraintense "quasielectrostatic" field generated overcomes the binding energy of the ions and drags them out of the solid. This mechanism is known as Coulomb explosion and since thermal coupling with the lattice is negligible during this short period of time, the process is a purely non-thermal process.

For larger intensities, total ionization of the surface is achieved for the leading edge of the laser pulse. Therefore, free electrons can absorb energy from the laser pulse in the presence of the lattice atoms and ions by means of inverse bremsstrahlung mechanism. This absorbed energy contributes to raise the temperature of a deeper surface layer by electron heat diffusion to a value close to the thermodynamic critical temperature giving rise to a phase explosion process, resulting in violent expulsion of both vapor and equilibrium liquid droplets [9]. The depth of the ablated layer is determined by the electron heat diffusion length and the laser fluence. Although the process is still very fast, some thermal damage must be expected on the areas surrounding the microstructured region.

We have used a commercial Ti:Sapphire oscillator (Tsunami, Spectra Physics) and a regenerative amplifier system (Spitfire, Spectra Physics) based on chirped pulse amplification (CPA). The system delivers linearly polarized 120-fs pulses with central wavelength 795 nm with a repetition rate of 1 kHz. The maximum available pulse energy is 1 mJ but for the purpose of microstructuring the grating it was reduced to 0.78 μJ using a half-wave plate and a linear polarizer. The transverse mode is gaussian and the beam width is 9 mm ($1/e^2$ criterion). The beam was then focused by a 50 mm achromatic lens resulting in a peak fluence of ~7 J cm^{-2} at focus.

The sample was placed on a motorized XYZ translation stage in order to achieve optimal focusing on the target surface. The focused beam moved in straight lines across the sample surface at a constant scanning speed of 130 μm s^{-1} avoiding iterative passes along the same line. The pitch between successive grooves was set to 15 μm. For this scanning speed, the number of pulses contributing to the ablation of a point within the sample surface was approximately 40. We have estimated the ablation threshold fluence to be 1.44±0.18 J cm^{-2} for 40 pulses. For multishot conditions (>100 pulses) the value for the threshold decreases to 1.18±0.15 J cm^{-2}.

Figure 1 shows a picture of the RTP sample taken with a Carl Zeiss Axio Imager A1 optical microscope after the ultrafast laser ablation process where it can be seen the diffraction grating generated on the surface of the sample. The lattice constant estimated from this microscope is approximately 15 μm.

We have recorded Bragg-diffraction spectra of this sample by using a FT-IR spectrometer (Bruker-Vertex 70) equipped with a special reflectivity attachment. The light source was a halogen tungsten lamp, and we collected the intensity of the diffracted light with a DLATGS detector in the spectral range from 7500 to 400 cm^{-1}. The incoming light was pointed perpendicular to the plane of the sample and the diffraction spectra were measured in a direction perpendicular to the grooves and at collection angles ranging from 24 to 60º in 2º steps. The measured data are represented in Fig. 2 with an intensity plot as a function of the wavelength and the diffraction angle.

To evaluate the lattice constant, the Bragg-diffraction spectra were fitted to the following 2-variable function:

$$I(\lambda, \sin\theta) = \sum_{n=1}^{3} \exp\left[\left(\frac{\sin\theta - \frac{1}{a}n\lambda}{w_n}\right)^2\right], \qquad (1)$$

where w_n takes into account the width of the diffraction peaks, a is the lattice constant and n is an integer (the number of the diffraction order). The fitting of this function to the experimental data gives a robust estimation of the lattice constant

from the data, since all the measurements are taken into account simultaneously. The value of the lattice constant measured by this procedure was 14.92 μm, which was in good agreement with the value estimated by optical microscopy.

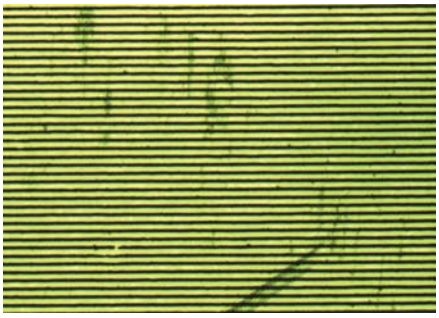

Fig. 1. Optical microscopy image of the diffraction grating generated on the surface of an RTP crystal by ultrafast laser ablation.

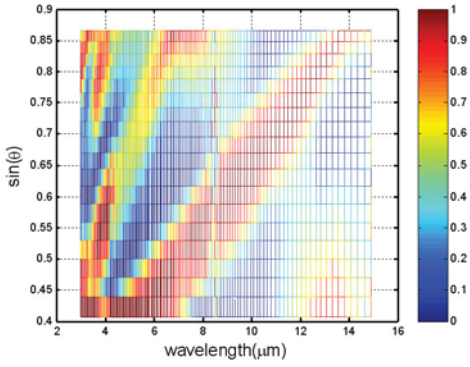

Fig. 2. 2D intensity plot as a function of the wavelength and the diffraction angle for the diffraction grating generated on the surface of an RTP crystal. Dark zones represent the diffraction orders.

3. Crystal growth of 2D and 3D photonic crystals by liquid phase epitaxy

The procedure for fabricating 2D and 3D photonic crystals we developed combines two well known techniques: the fabrication of 2D and 3D macroporous silicon membranes and the epitaxial growth of KTP within the pores of these membranes. This procedure, in addition to its simplicity, results in KTP and silicon integrated in a single structure that would eventually be used to generate or modulate light.

We fabricated these 2D and 3D PCs in four different steps which involved the preparation of high quality ordered macroporous silicon templates by light assisted electrochemical etching [10], the growth of the KTP epitaxial layer within the pores of the silicon template by liquid phase epitaxy, the polishing of the top or bottom surface of the KTP epitaxial layer, and finally, a selective etching of the silicon matrix.

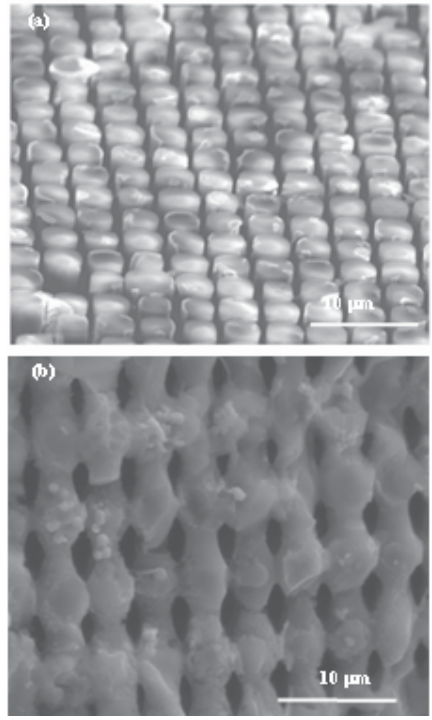

Fig. 3. SEM pictures of a (2D) and (b) 3D KTP photonic crystal.

The 2D or 3D silicon template was closely bound to a KTP single crystal substrate with typical dimensions 5 mm long, 3 mm wide and 1 mm thick. The crystal was oriented in such a way that the largest surface was perpendicular to the ***c*** crystallographic direction. The template/substrate set was immersed into a solution formed by mixing of K_2O, P_2O, TiO_2 and WO_3 with a molar % composition K_2O-P_2O-TiO_2-WO_3 = 42-14-14-30 for a period of time between 5 and 10 min at a supersaturation degree of about 2%. After growth, the top part of the KTP photonic structure was polished by using diamond powders ϕ = 0.1 μm. Once an optical-quality surface for the KTP

photonic structure was obtained, the last step in our approach was to remove the silicon template by selective chemical etching with TMAH diluted in distilled water (5 vol%) at 354 K. The effect of the selective etching is clearly visible in Figure 3, where a side-view image of the KTP photonic structure taken with the SEM is shown.

By using the aforesaid procedure we fabricated different KTP PCs with triangular and square lattices and lattice parameters ranging from 4.5 to 10 μm.

The crystallographic orientation of the substrate is transferred to the KTP photonic structure which we confirmed by X-ray texture analysis. The transference of the crystallographic orientation of the substrate to the KTP PC is advantageous for second order nonlinear applications since it may allow the use of the most appropriate nonlinear or electrooptic coefficient for a specific application in combination with a phase-matching condition, which would be provided by the photonic structure. This is not possible with bulk KTP where phase-matching relies on the birefringence and the coefficients with the largest nonlinearity cannot be used for efficient SH generation.

A more detailed optical characterization of a 2D KTP PC can be found in ref. [13]. Here we present the results of some basic light diffraction measurements performed on these structures. We placed the sample on a XYZ positioning stage mounted on a rotating stage to be able to change the angle of incidence to record the linear diffraction of the sample. Once mounted, the sample was illuminated with light at 527 nm. Some pictures of the observed diffraction patterns from samples with triangular and square lattices can be seen in Fig. 4 (a) and (b). In those pictures one can see the presence of an intense central spot corresponding to the specular reflection and some other spots that reflect the lattice of the sample.

The PC properties of a 2D KTP structure were demonstrated by performing a measurement of the specular reflection as a function of the wavelength of the incident field. We used a 2D KTP PC of KTP columns in air and periodicity of 4.5 μm. The sample was shined with p-polarized laser pulses, spectrally tuned in the range 940-1220 nm, at an angle of incidence of 25º with respect to the axis of the photonic structure. The specular reflectance spectrum, as shown in Fig. 4 (c), presents a dip at 1100 nm, which corresponds to the spectral position of the third-order Bragg reflection band, which was determined from a numerical calculation using the transfer matrix method.

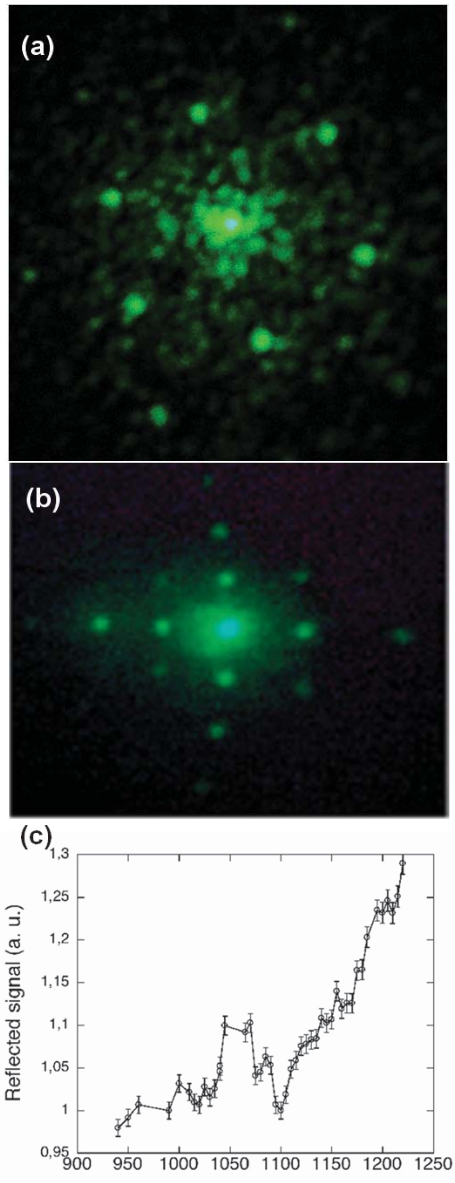

Fig. 4. Pictures of the linear diffraction pattern from a 2D KTP PC with (a) triangular lattice, and (b) square lattice. (c) Measurement of the specular reflection as a function of the wavelength of the incident light.

4. Conclusions

We have microstructured the surface of non-linear optical crystals, such as $RbTiOPO_4$, by ultrafast laser ablation for the fabrication of 1D photonic crystals.

We have also fabricated 2D and 3D KTP photonic crystals by the templated growth of KTP by liquid phase epitaxy within the pores of a Si template. In this way, the single-crystal substrate provided the desired crystallographic orientation, while the silicon template gave the desired final form to the thin layer.

In the data we collected from the growth procedure we followed there is no indication that KTP PCs with smaller periods could not be grown, as macroporous silicon templates or templates of other kind, with a smaller diameter pore become readily available. Additionally, this approach to fabricate 2D and 3D photonic structures can be extended to other nonlinear and optical materials that can be grown by liquid phase epitaxy.

With these photonic structures, in the future, we pretend to study different effects, such as the generation of light at different frequencies, parametric oscillation, and guiding and bending of light in previously designed line defects.

Acknowledgments

This work was supported by the Spanish Government under projects MAT2008-06729-C02-02/NAN, TEC2006-06531 and HOPE CSD2007-00007, and by the Catalan Authority under project 2005SGR658. J. J. Carvajal and M. C. Pujol are supported by the Education and Science Ministry of Spain and European Social Fund under the Ramon y Cajal program, RYC2006 – 858 and RYC2004 – 1453, respectively.

This work was presented at the VI Reunión Española de Optoelectrónica (OPTOEL'09), held in Málaga (Spain), 15-17 July 2009.

UNIVERSITAT ROVIRA I VIRGILI
MICROSTRUCTURATION OF NONLINEAR OPTICAL MATERIALS:
METHODOLOGIES, CHARACTERIZATION, AND APPLICATIONS
Raj Kumar Golconda
Dipòsit Legal: T. 55-2013

Paper III

Analysis of linear and nonlinear optical properties of diffraction gratings inscribed on the surface of single crystals of the $KTiOPO_4$ family

G. Raj Kumar, J.J. Carvajal, M.C. Pujol, X. Mateos, M. Aguiló, F. Díaz, J.R. Vázquez de Aldana, C. Romero, C. Méndez, P. Moreno, L. Roso, J. Ferré-Borrull, J. Pallarès, L.F. Marsal, R. Macovez, J. Martorell

Proceedings of SPIE, **7728**, 77817-1-10 (2010)

UNIVERSITAT ROVIRA I VIRGILI
MICROSTRUCTURATION OF NONLINEAR OPTICAL MATERIALS:
METHODOLOGIES, CHARACTERIZATION, AND APPLICATIONS
Raj Kumar Golconda
Dipòsit Legal: T. 55-2013

Analysis of linear and nonlinear optical properties of diffraction gratings inscribed on the surface of single crystals of the $KTiOPO_4$ family

G. Raj Kumar[a], J. J. Carvajal*[a], M. C. Pujol[a], X. Mateos[a], M. Aguiló[a], F. Diaz[a], J. R. Vázquez de Aldana[b], C. Romero[b], C. Méndez[b], P. Moreno[b], L. Roso[b], J. Ferré-Borrull[c], J. Pallarès[c], L. F. Marsal[c], R. Macovez[d], J. Martorell[d]

[a]Física i Cristal·lografia de Materials i Nano materials (FiCMA-FiCNA), Univ. Rovira i Virgili (URV), Campus Sescelades, Marcel·lí Domingo, s/n, Tarragona, Spain E-43007;
[b]Servicio Láser, Facultad de Ciencias, Univ. Salamanca, Salamanca, Spain E-37008;
[c]Dept.d'Enginyeria Electrónica, Univ. Rovira i Virgili (URV), Tarragona, Spain E-43007;
[d]ICFO-Institut de Ciències Fotòniques, Castelldefels, Spain E-08860

ABSTRACT

We demonstrate here that it is possible to fabricate 1D and 2D diffraction gratings on the (001) surface of $RbTiOPO_4$ (RTP) and $KTiOPO_4$ (KTP) single crystals. We analyzed the linear and nonlinear optical properties of 1D and 2D nonlinear photonic crystals. We show enhanced second harmonics when the samples were illuminated with a pulsed Nd:YAG laser, when compared to non-structured surface of the same materials and mainly there exists an asymmetry on the diffraction patterns of the second harmonic generated light, showing higher intensity in diffraction orders different to the zero order in the reflection configuration.

Keywords: RTP, KTP, Photonic Crystals, Ultrafast laser ablation, Diffraction gratings, Nonlinear diffraction

1. INTRODUCTION

Photonic crystals (PCs) have attracted widespread interest in recent years because of their ability to alter the dispersion relations of photons. PCs are the structures in which the refractive index is a periodic function in space[1] and these structures can affect the propagation of photons. This opens up a wide range of applications such as optical switches, optical transistors, possibly leading to a revolution in information technology. Among the many practical applications which are likely to be found for the unique optical properties of PCs, one of the most exciting issues resides in the possibility of obtaining a large enhancement in the nonlinear optical response within a PC one may enhance[2,3,4] phasematch[5] or hold a non-vanishing second-order interaction even if the material is centrosymmetric[6]. A PC has a periodic variation of the linear susceptibility χ^1, which is related to the index of refraction, in one, two or three dimensions. This can be done by combining high refractive index and low refractive index building blocks in a periodic structure, which is usually a challenging task. If instead of modulating periodically the linear susceptibility of the material we can modulate periodically the nonlinear susceptibility tensor χ^2 in a nonlinear optical material, we are developing a quasi phase matching (QPM) material. This concept was first referred independently by Armstrong[7], within the theoretical explanation for the application of light modulation, second harmonic and parametric conversion in dielectric media, and by Franken and Ward[8] reported about the theoretical explanation of optical harmonic generation.

In 1998, Berger[9] extended the QPM concept from one-dimension (1D) to two dimensions (2D) and proposed the idea of a new concept: a χ^2 photonic crystal or nonlinear photonic crystal (NPC) in order to contrast and compare it with a regular photonic crystal or linear photonic crystal. NPCs are the periodic dielectric materials with the modulation of nonlinear refractive index and such structures have new optical properties with improved or new functionalities that cannot be obtained by linear PCs. The 2D NPCs for instance, offer phase matching in two dimensions with the possibility to support several conversion processes simultaneously. This is an important advantage that makes a NPC more versatile as compared to a 1D QPM structure.

* joanjosep.carvajal@urv.cat; phone +34 977 55 8790; fax +34 977 55 9563

Nonlinear Optics and Applications IV, edited by Benjamin J. Eggleton, Alexander Luis Gaeta, Neil G. R. Broderick
Proc. of SPIE Vol. 7728, 772817 · © 2010 SPIE · CCC code: 0277-786X/10/$18 · doi: 10.1117/12.854729

It is well known today that the most used nonlinear optical effect, second-harmonic generation (SHG) can be achieved by many different ways depending on the geometry of the wave phase matching (e.g., birefringence-induced phase matching or QPM), input light polarization (e.g., Type I or Type II), mutual orientation of the wave vectors of interacting waves (collinear or non-collinear)[10]. Nowadays SHG, as well as other parametric processes, can be commonly realized in engineered nonlinear photonic structures with a periodic spatial modulation of the sign of the quadratic nonlinearity[9]. In the case of non-centrosymmetric crystals with significant second-order nonlinear coefficients, the phase matching conditions for processes such as second harmonic generation are not fulfilled because of material dispersion. Instead, the efficient frequency conversion in such quadratic photonic lattices is achieved by the phase-matching condition via the QPM approach,[11,12] which takes into account the reciprocal lattice vectors of the periodic structure to compensate for the wave vector mismatch in a situation where direct phase matching is not possible. Usually, QPM is realized by collinear propagation of the fundamental frequency and second harmonic beams along the QPM grating vector. However, when the fundamental beam and QPM grating vector are non-collinear, then the second harmonic beam might diffract from the χ^2 grating[13]. In linear optics it is well established that propagation of a light beam in periodic refractive index structures leads to Bragg diffration when the full vectorial phase matching condition is satisfied. Analogously, nonlinear Bragg diffraction is the interesting phenomenon for which the nonlinear analogue of Bragg´s law satisfied and it is realized at a specific angle between the beams[14], determined by the vectorial phase matching $2k_1 + G_n = k_2$, where G_n is the grating vector and k_1, k_2 are the wave vectors of the fundamental and second harmonic beams respectively. If this vectorial condition is not satisfied, nonlinear second harmonic diffraction should be observed. This phenomenon will be helpful for the of efficient generation of second harmonic and also leads to generate multi order nonlinear diffraction so that wavelength selectivity could also be possible for the application of multiplexing, multiplexing signal processing, nonlinear microscopy etc.

However, what happens when we structurate the surface of a nonlinear optical material to modulate periodically both, χ^1 and χ^2 susceptibilities? In that case we can merge the properties of a conventional linear photonic crystal with those of a nonlinear photonic crystal. Despite the interest that these synergetic structures can show, only a few works analyzed these effects on the literature. Photonic structures on nonlinear optical materials have been fabricated by field poling techniques[15], ion etching[16], electron beam lithography[17], liquid phase epitaxy[18], etc. Remarkably, it can be a promising approach to fabricate 1D and 2D photonic structures or grating by means of femtosecond laser ablation which has become increasingly important in the last few years as a result of the large amount of practical applications in surface modification or micro-structuring of dielectric materials. When intense ultra-short pulses are focused in a transparent dielectric, strong-field ionization and subsequent avalanche ionization lead to the generation of free-electron plasma. When the density of free electrons exceeds a certain threshold, enough energy is absorbed to produce macroscopic ablation[19, 20, 21]. The largest density of ionized electrons is reached only in the central part of the focal region due to the highly non-linear nature of the strong-field ionization process. Moreover the ultra-short irradiation time strongly reduces the existence of thermal effects[22] that appear when picosecond or nanosecond pulses are used, making femtosecond laser irradiation an excellent tool for the micro-structuring of dielectrics. Nonlinear optical materials have been interesting targets for femtosecond laser applications, and the integration of diffractive gratings by ultrafast laser ablation has been recently used for tailoring SHG in KH_2PO_4 (KDP)[23], $LiNbO_3$[24], and β-BaB_2O_4 (BBO)[25,26].

In this paper, we present the results of inscribing 1D and 2D photonic structures or diffraction gratings on the surface of $RbTiOPO_4$ (RTP) and KTP crystals with a different spacing ranging from 8 to 20 μm by femtosecond laser ablation. Among the various inorganic nonlinear optical crystals explored so far, KTP family has received enormous attention in the last two decades. The key to success of the KTP family is its good nonlinear optical behaviour for frequency doubling of Nd:YAG laser radiation. A crystal has to fulfill several requirements in order to be suitable for nonlinear optics. The most favorable nonlinear coefficient for both RTP and KTP is d_{33} (RTP 17.1 pm/V and KTP 16.9 pm/V)[27] which means that the most efficient conversion is achieved in the case that all radiation fields are polarized along ***c*** crystallographic direction. One of the most remarkable features of these crystals is their high laser damage threshold[28] that makes them useful in high intense ultrafast laser ablation process. The RTP and KTP materials have high transmission coefficient between 0.35 μm and 4.5 μm. In the structures generated, that combine a modulation of χ^1 and χ^2 susceptibilities we analyzed their linear and nonlinear optical properties by measuring the diffraction of fundamental and SHG beam on their surfaces.

2. EXPERIMENTAL TECHNIQUES

2.1. Crystal growth

RTP and KTP crystallize in the orthorhombic system with the *Pna*2_1 space group of symmetry[29]. These crystals melt incongruently at 1443 K[30], and 1450 K, so they cannot be grown by conventional melting methods and they have been traditionally grown by high temperature solution techniques, and more particularly by the Top-Seeded Solution Growth (TSSG) method. Around 120 g of solution were prepared by mixing the desired ratios of the corresponding oxides, K_2CO_3 or Rb_2-CO_3 and TiO_2, P_2O_5 depending on the desired crystal, in platinum cylindrical crucibles of 125 cm^3. The crystals were grown from WO_3 containing fluxes to reduce the viscosity of the flux[31]. The solution was homogenised at 50-100 K above the crystallisation temperature. We used ***c***-oriented crystal seeds for growing KTP and RTP crystals. We determined the saturation temperature of the solution by observing the growth or dissolution of the crystalline seed in contact with the surface of the solution. During the growth the crystal seed was rotated at a angular speed of 45 rpm. Growth process proceeded by decreasing the temperature of the solution by 20-50 K from the saturation temperature at a cooling rate of 0.1 K/h, depending on the size of the desired crystal. In this work, in order to obtain larger crystals, those were extracted from the solution very slowly, 0.5 mm per 12 h. At the end of the crystal growth process, the crystal was completely extracted from the solution and slowly cooled to room temperature inside the furnace.

2.2. Cutting and polishing of crystals

To prepare the samples for the fabrication and characterization of the diffraction gratings, the single crystals obtained were crystallographically oriented, cut and polished. First, the samples were cut with the correct crystallographic orientation, using a goniometer and a Struers Accutom-50 diamond saw with disks 0.12 mm thick. The samples were polished in a Logitech PM5 polisher with an oscillatory arm using alumina powders down to a grain size of 0.3 μm. The quality of the polishing was estimated using parameters such as roughness, flatness and parallelism between opposite faces of the sample measured by a Sensofar PLμ 2300 interferometric confocal microscope and a home-made self-collimator.

2.3. Ultrafast laser ablation

We fabricated 1D and 2D photonic structures on RTP and KTP nonlinear optical materials by using a commercial Ti: Sapphire oscillator (Tsunami, Spectra Physics) and a regenerative amplifier system (Spitfire, Spectra Physics) based on chirped pulsed amplification (CPA) for ultrafast laser ablation of the surface of RTP and KTP samples. The system delivers 120 fs linearly polarized pulses at 795 nm with a repetition rate of 1 kHz. The transverse mode was TEM00 and the beam width was 9 mm ($1/e^2$ criterion).
The thickness of the RTP samples was in the range 2-4 mm. They were placed on a motorized XYZ translation stage that allowed achieving optimal focusing on the surface of the target, with the (001) face of the samples perpendicular to the laser beam. We have estimated the ablation threshold fluence following the procedure described by Dumitru and coworkers[32]. The threshold fluence depends on the number of pulses per spot, resulting 1.44 ± 0.18 $J.cm^{-2}$ for 40 pulses and decreasing to 1.18±0.15 $J.cm^{-2}$ for multi shot conditions (>100 pulses) giving an incubation factor $\xi = 0.783$[33]. According to the period of the fabricated diffraction gratings, the samples were called RTP1 (15 μm) and RTP2 (20 μm). RTP1 was prepared focusing the laser beam by means of a 50 mm achromatic lens using a pulse energy of 0.78 μJ, which provided a peak fluence of ~6.1 $J.cm^{-2}$ at focus. The sample was moved following straight lines parallel to the ***b*** crystallographic axis and all across the surface, at a constant scanning speed of 130 $\mu m.s^{-1}$ avoiding the iterative passes along the same line. The pitch between the lines was set to 15 μm. For that scanning speed and focusing conditions the number of pulses contributing to the ablation of a point within the sample surface was approximately 40. For recording RTP2, the focusing optics was a 10X (0.22 NA) microscopic objective. A 6 mm diameter circular aperture was placed before the objective in order to slightly increase the spot size at focus. The pulse energy before the aperture was 0.27 μJ leading to a peak fluence at focus of ~3.2 $J.cm^{-2}$. The writing procedure was identical than for RTP1 but now the scanning speed was set to 75 $\mu m.s^{-1}$ and the separation between lines was 10.5 μm and 9.5 μm alternatively. Under these conditions, the number of pulses contributing to the ablation of a point within the sample surface was around 55.
We followed a similar procedure for the fabrication of two different 2D structures on the surface of KTP crystals. The thickness of the KTP samples was in the range 3-4 mm and the laser beam was focused by a 10X objective lens with NA 0.30. We have written a 2D structure consisting of two perpendicular arrays of grooves, parallel to the ***a*** and ***b***

crystallographic axes, respectively (sample KTP1). It was achieved by moving the sample with a constant speed of 75 μm/s which means a number of pulses per spot (Ø~ 3 μm) of 40. A circular aperture 6 mm and some neutral filters were placed before the focusing lens in order to reduce the pulse energy to 0.48 μJ by and to produce a lattice pitch of 8.54 μm. We followed similar procedure for the fabrication of a grid of circular pores with a pitch of 8.85 μm (sample KTP2). In this case, the sample was moved to the selected positions and then irradiated with 100 pulses. Again, a circular aperture of 5.5 mm and some neutral filters were placed before the focusing lens in order to reduce the pulse energy to 0.39 μJ and achieve the desired pore diameter. The total processed area was 3 x 3 mm^2 and took approximately 8.5 h. in both cases.

3. CHARACTERIZATION OF THE PHOTONIC STRUCTURES FABRICATED BY ULTRAFAST LASER ABLATION

3.1. Micro-structure Analysis

We recorded micrographs of the samples after ultrafast laser ablation in a FEI QUANTA 600 scanning electron microscope (SEM) on top and lateral views. Figure 1 shows top views of the different samples recorded for different magnifications.

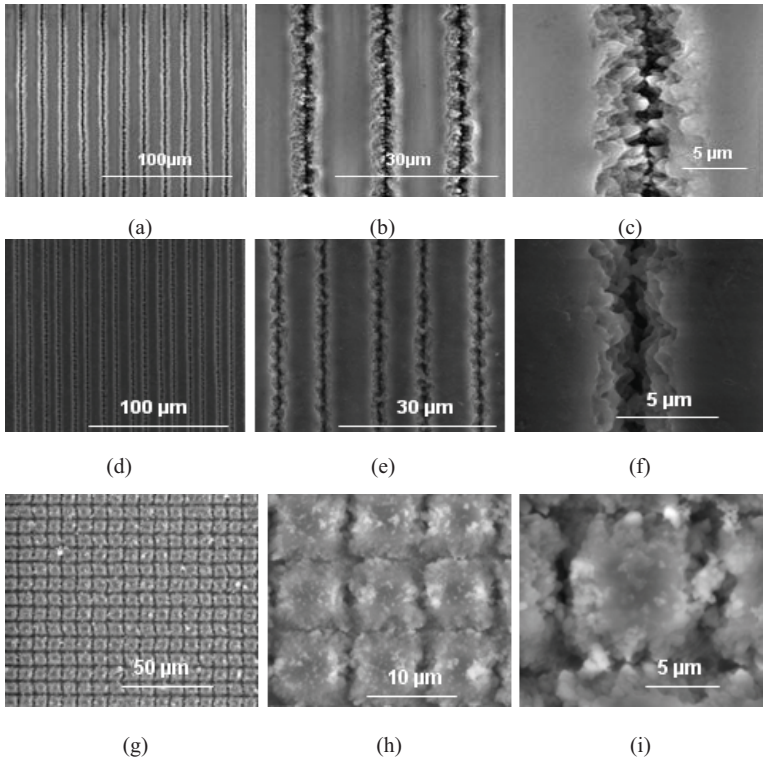

UNIVERSITAT ROVIRA I VIRGILI
MICROSTRUCTURATION OF NONLINEAR OPTICAL MATERIALS:
METHODOLOGIES, CHARACTERIZATION, AND APPLICATIONS
Raj Kumar Golconda
Dipòsit Legal: T. 55-2013

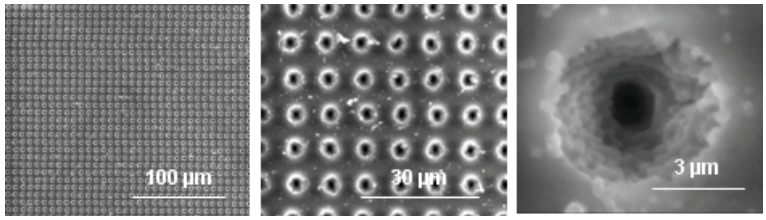

(j) (k) (l)

Figure 1. Tope views of the diffraction gratings fabricated by ultrafast laser ablation obtained by SEM with different magnification corresponding to: (a), (b) (c) RTP1, (d), (e), (f) RTP2, (g), (h), (i) KTP1, (j), (k), (l) KTP2, (m) corresponds to the lateral view of RTP1 and (n) to the lateral view of RTP2.

Figure 1 (a) to (f) are the top views of RTP1 and RTP2 samples for different magnifications and (g) - (l) show the top views of KTP1 and KTP2 samples. The variation of the energy from pulse to pulse in the laser beam causes that the width of the grooves is not constant. These values are consistent with the fluence distribution (basically an Airy function) on the surface of the samples. In the case of RTP1, the region where the fluence exceeds the ablation threshold fluence (multishot conditions) has a diameter of approximately 5 µm whereas for RTP2 the corresponding diameter is 3.3 µm. In both cases, the agreement with the width of the grooves is really good. In the case of KTP2 sample high degree of periodicity can be observed than KTP1 due to the variation of laser fluence with different diameters of laser beam. The roughness of the perpendicular grooves of KTP1 is very high so it is difficult to determine the exact width and the lattice constant. The higher magnification images of KTP1 and KTP2 reveal that the shape of the fabricated perpendicular grooves pattern shows square shape, shown in Figure (i) and circular pore with a conical shapes shown in Figure 1(l) respectively. The width of the perpendicular grooves of KTP1 sample is 3.4 µm whereas the diameter of the pores is 3.6 µm.

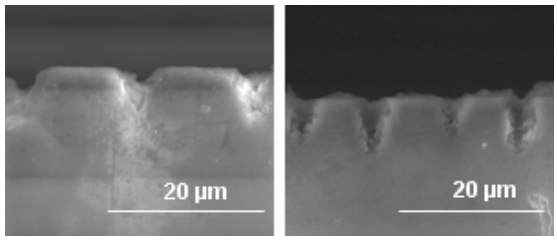

(a) (b)

Figure 2. The lateral views of the RTP samples (a) lateral view of the RTP1, (b) lateral view of the RTP2 sample.

Figure 2 (a) and (b) show the lateral views of the RTP1 and RTP2 samples. These images reveal that the roughness of the lateral walls of the grooves is very high. This roughness makes the determination of the exact width and lattice constant of these diffraction gratings difficult. The lateral views allow to determine the shape of the as fabricated channels. The grooves section is V-shaped with depths between 5 and 7 µm.
Table 1 shows the estimation of the lattice constants from optical microscope images of all the samples. The values, which are listed in table 1 in the case of RTP2 the two sub periods were estimated which are exactly coincided with a spatial period of 20 µm and the values in the case of KTP1 and KTP2 are the estimated lattice constants in axial and vertical directions of 2D structures are roughly coincided with our estimated results of SEM micrographs respectively.

Table 1. Estimated lattice constants from the optical microscope images

Sample	Lattice constant estimated from optical microscope images (µm)
RTP1	14.92
RTP2	9.4 and 10.48 (sub-periods)
KTP1	8.95 (axial), 8.91(vertical)
KTP2	9.04 (axial), 9.02 (vertical)

3.2. Determination of the lattice constant of the diffraction gratings

Since it was difficult to determine the precise lattice constant of the diffraction gratings written on the surface of the RTP and KTP samples from the SEM images as a result of the roughness of the channels, we needed to use a long range order technique to evaluate this parameter. For this purpose Bragg-diffraction spectra of these samples have been recorded by using a FT-IR spectrometer (Bruker-Vertex 70) equipped with a special attachment that allows to record the spectra by reflectivity. We used a halogen tungsten lamp as the lighting source, and we collected the intensity of the diffracted light from 7500 to 400 cm^{-1} by using a DLATGS detector. The incoming light was pointed perpendicular to the plane of the samples where 1D and 2D diffraction gratings were recorded with the fabricated pattern perpendicular to the direction of the incident beam. Several diffraction spectra were measured perpendicularly to the grooves at collection angles ranging from 24 to 60º in 2º steps. To evaluate the lattice constant, the Bragg-diffraction spectra were fitted to the 2-variable function

$$I(\lambda, \sin\theta) = \sum_{n=1}^{3} \exp - \left[\left(\sin\theta - (n\lambda/a) \right) / w_n \right]^2 \qquad (1)$$

where a is the lattice constant of the diffraction grating, n is the diffraction order, and w_n is a parameter that takes into account the width of the diffraction peaks. By fitting this function to the experimental data we obtain a robust estimation of the lattice constant of the diffraction grating, since all measurements are taken into account simultaneously. Figures 3(a) and (b) show the 2D intensity plots as a function of the wavelength and the diffraction angle of the measured data and the calculated data by the fitted function, respectively, for the diffraction grating recorded on the surface of the RTP1 sample as an example. Experimentally we observed three diffraction orders, that can be seen in the figure as dark red colour zones, with widths decreasing as the wavelength increased. The most intense peak was referred as the zero order peak and appeared in the range between 4 and 8 μm for low values of $\sin\theta$ with a lower slope. The first and second diffraction orders are observed at higher values of $\sin\theta$ with higher slopes.

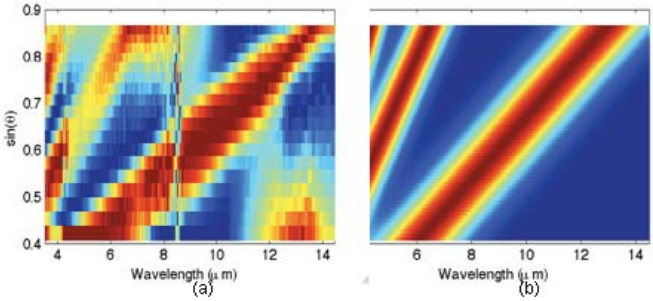

Figure 3. (a) 2D intensity plot as a function of the wavelength and the diffraction angle of the diffraction grating with a period of 15 μm recorded by ultra fast laser ablation on the surface of RTP1 sample: dark red zones represent the diffraction orders. (b) 2D plot of the fitted function to the experimental data after considering three diffraction orders.

The values estimated lattice constants of the different diffraction gratings recorded by ultrafast laser ablation from FT-IR Bragg diffraction on RTP and KTP crystals are summarized in Table 2.

Table 2. Estimation of lattice constants of the diffraction gratings by FT-IR Bragg-diffraction

Sample	Lattice constant estimated by fitting function (μm)
RTP1	14.98
RTP2	19.85
KTP1	9.1
KTP2	9

From the listed values in Table 1 and Table 2, we can observe that the estimated lattice constants from the optical microscope images of all the samples are very good agreement with the values estimated from the FT-IR Bragg diffraction measurement fitting function analysis. But in the case of RTP2 sample, the spatial period 20 μm was considered in FT-IR Bragg diffraction measurement rather than the values of the sub-periods.

3. 3. Linear diffraction properties

To check the quality of the diffraction gratings, we recorded the linear diffraction patterns generated after focusing a He-Ne laser at 632.8 nm with a power of 3 mW and a spot size of 1mm on the surface of the RTP and KTP samples in a transmission geometry by setting the incident beam perpendicular to the surface on which the diffraction grating was recorded.

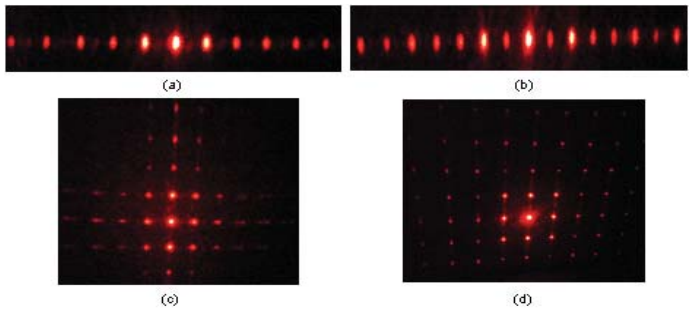

Figure 4. Linear diffraction patterns of the different diffraction gratings recorded in transmission after illuminating the sample with a He-Ne laser. (a) and (b) diffraction gratings on samples RTP1 (period 15 μm) and RTP2 (period 20 μm), respectively, (c) and (d) diffraction gratings on samples KTP1 (period 8.54 μm) and KTP2 (period 8.85 μm), respectively.

Figure 4 shows the obtained diffraction patterns for the RTP and KTP samples analysed. On the screen, ±5 diffraction orders were visible in the RTP1 sample, while ±8 diffraction orders were visible in the case of the RTP2 sample. Also in this sample, and due to the sub-period existing in the diffraction grating, we observed a modulation on the intensity of the diffraction spots. Even orders show a larger intensity than odd ones. Similarly in the case of KTP samples we observed a large number of diffraction spots. In this case the diffraction spots represent the square pattern of the diffraction grating inscribed on the surface of these samples. However, the number of diffraction spots observed for KTP1 sample, where we have a diffraction grating formed by two orthogonal arrays of grooves, is similar like KTP2 sample, where the grating is formed by circular pores forming a square grid.

In all the samples, the large number of diffraction orders that can be observed indicate the good quality of the as fabricated 1D and 2D structures, regardless the roughness of the lateral walls of the grooves that we observed by SEM and the variation of the width of the grooves with depth induced by the V-shape of the grooves.

3.4. Nonlinear diffraction properties

After checking the quality of the diffraction gratings by observing the linear diffraction patterns, we explored in the case of RTP samples, the diffraction pattern of the second harmonic generated green light, obtained after illuminating the samples at 1064 nm with a Nd:YAG laser with 7 ns pulse width and 10 Hz repetition rate in a reflection geometry. We placed the sample on a XYZ positioning stage mounted on a rotating stage to set the angle of incidence of the fundamental beam on the diffraction grating. Using the XYZ positioning stage and with the help of a CCD camera, the sample was placed close to the focal point of a 10 cm lens used to focus the laser-light pulses. The laser beam was incident on the top of the structures at a fixed angle ranging between 30º and 60º depending on the sample to avoid components of internal reflections from the other faces of the crystals in the measured diffraction patterns. The second

harmonic light generated in reflection by the samples was separated from the reflected fundamental with the use of an interference filter centered at 532 nm and measured using a photomultiplier tube that was rotated around the same rotation axis of the rotating stage on which the sample was mounted.
Several peaks were observed in the nonlinear diffraction patterns and Figure 5 shows the diffraction pattern and the intensity profile of the second harmonic generated light obtained for the RTP1 sample. We also added the intensity profile of the recorded linear diffraction pattern corresponding to the fundamental 1064 nm light for a better comparison. We observed that one of the peaks observed in the nonlinear diffraction pattern coincides with the position of the zero order peak of the linear diffraction pattern. However, while this peak is showing the maximum intensity in the linear diffraction pattern, it is not the most intense peak in the nonlinear diffraction pattern.

.

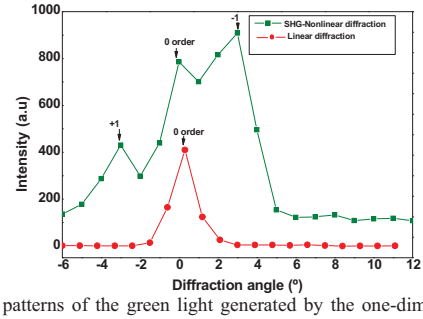

Figure 5. Intensity of the diffraction patterns of the green light generated by the one-dimensional surface relief diffraction grating versus the diffraction angle on the RTP1.The diffraction pattern of the fundamental beam is also included for means of comparison.

For the RTP1 sample, three peaks were observed on the nonlinear diffraction pattern corresponding to the zero and ±1 orders. The most interesting feature of this diffraction pattern is that the intensity of the -1 diffraction order peak is larger than the intensity of the zero order peak, while the less intense peak is that corresponding to the +1 diffraction order, generating an asymmetric diffraction pattern for the second harmonic generated green light recorded in a reflection configuration. A similar situation was observed for the rest of the samples. For instance for the KTP1 sample four circular rings were observed for the SHG light when projected onto a screen as shown in figure 6. Bright spots were observed on the intersections of these rings, but again, an asymmetry in the intensity of the different diffraction orders can be expected with peaks different from the zero order showing larger intensities.

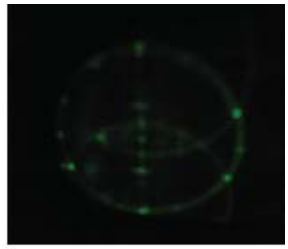

Figure 6. SHG rings by non collinear generation diffraction pattern of the green light generated by the two-dimensional nonlinear photonic crystal KTP1

Why these asymmetric diffraction patterns diffraction patterns for the SHG green light occur is not clear at present, and it is under investigation. Among the different possible explanations for these phenomena we can enumerate o-e confinement of light induced by amorphisation of the material by ultrafast laser ablation, diffracted orders coming out at grazing angles and interacting with the periodic modulation of the sample or cavity effects due to the relatively large depth and width of the grooves resulting in a stronger coupling of the incident light to the structure.

4. Conclusions

In conclusion, we have successfully fabricated 1D and 2D photonic structures or diffraction gratings on the surface of RTP and KTP nonlinear optical materials with different lattice periods by ultrafast laser ablation, and their morphology and optical studies have been analyzed precisely. In 1D diffraction gratings, despite of the roughness observed on the surface of the ablated channels, an excellent long range order was observed, reflecting the high periodicity and these structures that allowed up to 8 diffraction orders and multiple orders in 2D structures to be observed in these structures. More interestingly, the diffraction patterns of the second harmonic generated green light on the surface of these diffraction gratings and recorded in a reflection configuration, proved to be asymmetric. This indicates the possibility of splitting in space the main energies of the fundamental and second harmonic generated beams without further efforts in such structures. However, we cannot provide at present a clear explanation about why this effect is happening.

Acknowledgments

This work was supported by the Spanish government under projects MAT2008-06729-C02-02/NAN, PI09/90527, HF2008-0045, TEC2009-09551, AECID-A/016246/08, FIS2009-09522, and HOPE CSD2007-00007 and SAUUL CSD2007-00013 (Consolider-Ingenio 2010), by catalan government under projects 2009SGR235 and 2009SGR549, by Junta de Castilla y León under project GR27, and by the Research Center on Engineering of Materials and Systems (EMaS) of the URV. J.J.C is supported by the Education and Science Ministry of Spain and European Social Fund under the Ramón y Cajal program, RYC2006-858. We also acknowledge support from the Centro de Laseres Pulsados, CLPU, Salamanca, Spain.

REFERENCES

[1] Jouannopoulos J. D., Meade R. R., and Winn J. N., "Photonic Crystals, Molding the Flow of Light, Princeton", University Press, Princeton, NJ, (1995).
[2] Trull, J., Vilaseca, R., Martorell, J., and Corbalan, R., "Second harmonic generation in local modes of a truncated periodic structures" Opt. Lett. Vol.20, 1746-1748 (1995).
[3] Markowicz, P. P., Tiryaki, H., Pudavar, H., and Prasad, P.N., "Dramatic enhancement of third harmonic generation in three dimensional photonic crystals" Phys. Rev. Lett. 92, 083903(3) (2004).
[4] Torres, J., Le Vassor dÝerville, M., Coquillat, D., Centeno, E., and Albert, J. P., "Ultravoilet surface-emitted second harmonic generation in GaN one dimensional photonic crystal slabs" Phys. Rev. B, 71, 195326 (5) (2005).
[5] Martorell, J., Vilaseca, R., and Corbalan, R., "Second harmonic generation in a photonic crystal" Appl. Phys. Lett. 70, 702-704 (1997).
[6] Martorell, J., and Vilaseca, R., " Scattering of second harmonic light from small spherical particles ordered in a crystalline lattice" Phys. Rev. A, 55, 4520-4525 (1997).
[7] Armstrong, J., Bloembergen, N., Ducuing, J., and Pershan, P. S., "Interactions between light waves in a nonlinear dielectric", Phys.Rev.127, 1918-1939 (1962).
[8] Franken, P. A., and Ward, J.F., "Optical harmonics and nonlinear phenomena", Rev. Mod. Phys. 35, 23-39 (1963).
[9] Berger, V., Nonlinear photonic crystals, Phys. Rev. Lett. 81, 4136-4139 (1998).
[10] Broderick, N. G. R., Bratfalean, R. T., Monro, T. M., Richardson, D. J., and Martijn de Sterke, C., "Temparature and wavelength tuning of second , third, and fourth harmonic generation in a two dimensional hexagonally poled nonlinear crystal" J. Opt. Soc. Am. B, Vol. 19, 2263-2272 (2002).
[11] Fejer, M. M., Magel, G. A., Jundt, D. H., and Bayer, R. L., "Quasi phase matched second harmonic generation: tuning and tolerances", IEEE J. Quantum. Electron. 28, 2631-2654 (1992).
[12] Balakin, A. V., Bushuev, V. A., Mantsyzov, B. I., Ozheredov, I. A., Petrov, E. V., Shkurinov, A. P., Masselin, P., and Mouret, G., "Enhancement of sum frequency near the photonic band gap edge under the quasi phase matching conditions", Phys. Rev. E 63, 046609-466011(2001).
[13] Solomon, S., Kivshar, Y. S., "Phase matching in nonlinear χ^2 photonic crystals" Opt. Lett. 25, 1204-1206 (2000).
[14] Freund, I., "Nonlinear diffraction", Phys. Rev. Lett, 21, 1404-1406 (1968).
[15] Canalias, C., Norlof, M., Pasiskevicius, V., and Laurell, F., "A $KTiOPO_4$ nonlinear photonic crystal from blue second harmonic generation", Appl. Phys. Lett., 94, 081121(1-3) (2009)

[16] Ulliac, G., Courjal, N., Chong, H. M. H., De La Rue, R. M., "Batch process for the fabrication of $LiNbO_3$ photonic crystals using proton exhange followed by CHF_3 reactive ion etching" Opti. Mat. 31, 196-200 (2008).
[17] Coquilat, D., Vecchi, G., Comaschi, C., Malvezzi, A. M., Torres, J., and Le Vassor dýerville, M., "Enchance second-third harmonic generation and induced photoluminescence in two dimensional GaN photonic crystal", Appl. Phys. Lett., 87, 101106-7 (2005).
[18] Peña, A., Di Finizio, S., Trifonov, T., Carvajal, J. J., Aguiló, M., Pallarès, J., Rodriguez, A., Alcubilla, R., Marsal, L. F., Díaz, F., and Martorell, J., "A two dimensional KTiOPO4 photonic crystal grown using a macroporous silicon template" Adv. Mater. 18, 2220-2225 (2006).
[19] Stuart, B. C., Feit, M. D., Rubenchik, A. M., Shore, B. W., and Perry, M. D., "Laser-induced damage in dielectrics with nanosecond to sub-picosecond pulses," Phys. Rev. Lett. 74, 2248–2251 (1995).
[20] Lenzner, M., Kruger, J., Sartania, S., Cheng, Z., Spielmann, Ch., Morou, W., Kautek, G., and Krausz, F., "Femtosecond optical breakdown in dielectrics," Phys. Rev. Lett. 80, 4076–4079 (1998).
[21] Gamaly, E. G., Rode, A. V., Luther-Davies, B., and Tikhonchuk, V. T., "Ablation of solids by femtosecond lasers: ablation mechanism and ablation thresholds for metals and dielectrics," Phys. Plasmas 9, 949–957 (2002).
[22] Perry, M. D., Stuart, B. C., Banks, P. S., Feit, M. D., Yanovsky, V., and Rubenchik, A. M, "Ultrashort-pulse laser machining of dielectric materials," J. Appl. Phys. 85, 6803–6810 (1999).
[23] Méndez, M. C., Vázquez de Aldana, J. R., Torchia, G. A., and Roso, L., "Integrated-grating-induced control of second-harmonc beams in frequency doubling crystals," Optics. Letters, 30, 2763-2765 (2005).
[24] Torchia G.A, Méndez C, Arias I, L. Roso, A. Rodenas and D. Jaque, "Laser gain in femtosecond microstructured Nd^3+: MgO: $LiNbO_3$ crystals," Appl. Phys. B 83, 559-563 (2006).
[25] Romero, C., Javier R., Vázquez de Aldana, Méndez, C., and Roso, L., "Non-collinear sum-frequency generation of femtosecond pulses in a micro-structured β-BaB_2O_4 crystal," Opt. Exp. 16, 18109-18117 (2008).
[26] Li, Y., Lu, P., Dai, N., Wang, X., Wang, Y., Yu, B., Long, H., "Surface relief diffraction gratings written on β- BaB_2O_4 crystal by femtosecond pulses," Appl. Phys. B 88, 227-230 (2007).
[27] Boulanger, B., Feve, J. P., Marnier, G., Menaert, B., Cabirol, X., Villeval, P., Bonnin, C., "Relative sign and absolute magnitude of $d^{(2)}$ nonlinear coefficients of KTP from second-harmonic generation measurements ", J. Opt. Soc. Am. B, 11(5), 750 (1994).
[28] Nikogosyan, D. N., "Nonlinear Optical Crystals A Complete Survey", Springer, Berlin (2005).
[29] Carvajal, J. J., Woensdregt, C. F., Solé, R., Díaz, F., Aguiló, M., "Change in the morphology of $RbTiOPO_4$ introduced by the presence of Nb", Cryst. Growth. Des. 6, 2667-2673 (2006).
[30] Carvajal, J. J., Solé, R., Gavaldà, J., Massons, J., Aguiló, M., Diaz, F. "A new self-doubling material: $RbTiOPO_4$: (Nb, Ln)", Opt. Mater. 24, 425-430 (2003).
[31] Lliev, K., Peshev, P., Nikolov, V., Koseva, I., "Physicochemical properties of high-temparature solutions of the K_2CO_3-P_2O_5-TiO_2-WO_3 system, suitable for the growth of $KTiOPO_4$ (KTP) single crystals" J. Cryst. Growth, 100, 225-232 (1990).
[32] Dumitru, G., Romano, V., Weber, H. P.,. Sentis, M., Marine, W., "Femtosecond ablation of ultrahard materials," Appl. Phys. A 74, 729-739 (2002).
[33] Baudach, S., Bonse, J., Kruger, J., and Kautek, W., "Ultra short pulse laser ablation of polycarbonate and polymethylmethacrylate," Appl. Surf. Sci. 555, 154-155, (2000).

UNIVERSITAT ROVIRA I VIRGILI
MICROSTRUCTURATION OF NONLINEAR OPTICAL MATERIALS:
METHODOLOGIES, CHARACTERIZATION, AND APPLICATIONS
Raj Kumar Golconda
Dipòsit Legal: T. 55-2013

Paper IV

Fabrication of photonic structures in crystals of the $KTiOPO_4$ family by ultrafast laser ablation

Raj Kumar Golconda, J.J. Carvajal, M.C. Pujol, X. Mateos, M. Aguiló, F. Díaz, J.R. Vázquez de Aldana, C. Romero, C. Méndez, P. Moreno, L. Roso

Physics Procedia, **8**, 126-135 (2010)

UNIVERSITAT ROVIRA I VIRGILI
MICROSTRUCTURATION OF NONLINEAR OPTICAL MATERIALS:
METHODOLOGIES, CHARACTERIZATION, AND APPLICATIONS
Raj Kumar Golconda
Dipòsit Legal: T. 55-2013

Available online at www.sciencedirect.com
ScienceDirect
Physics Procedia 8 (2010) 126–135
Physics Procedia
www.elsevier.com/locate/procedia

VI Encuentro Franco-Español de Química y Física del Estado Sólido
VI[ème] Rencontre Franco-Espagnole sur la Chimie et la Physique de l'État Solide

Fabrication of photonic structures in crystals of the $KTiOPO_4$ family by ultrafast laser ablation

Raj Kumar Golconda[a], Joan Josep Carvajal[a*], Maria Cinta Pujol[a], Xavier Mateos[a], Magdalena Aguiló[a], Francesc Diaz[a], Javier R.Vázquez de Aldana[b], Carolina Romero[b], Cruz Méndez[c], Pablo Moreno[b], Luis Roso[b,c]

[a]*Física i Cristal·lografia de Materials i Nanomaterials (FiCMA-FiCNA), Univ.Rovira i Virgili (URV), Campus Sescelades, Marcel·li Domingo, s/n Tarragona, E-43007, Spain*
[b]*Servicio Láser, Univ.Salamanca, Salamanca, E-37008, Spain*
[c]*CLPU-Centro de Láseres Pulsados, Villamayor, Salamanca, E-37185, Spain*

Abstract

We investigate the growth and fabrication of photonic structures by ultrafast laser ablation on nonlinear optical materials of the $KTiOPO_4$ family. We studied how the ultrafast laser ablation process affected on the structure of the material by micro-Raman scattering and micro-X-ray diffraction. The modifications of the Raman frequencies and their intensities have been discussed and compared with those previously reported for unablated crystals.

Keywords: Photonic Crystals; Diffracton gratings, $RbTiOPO_4$, $KTiOPO_4$, Nonlinear optical materials, Ultrafast laser ablation.

1. Introduction

The past two decades have witnessed the intensive research efforts related to the design and fabrication of photonic crystals (PCs) [1]. From the conceptual point of view, photonic researchers are interested in manipulating the optical phenomena in confined geometries to realize more versatile and miniaturized optical devices. A PC is a material in which the refractive index is periodically modulated on a length scale comparable to the wavelength of light. With a proper design, the PCs exhibit photonic band gaps as well as acquire potential applications in light-flow manipulations [2]. A particular case of a one dimensional (1D) PC is a diffraction grating [3]. In addition to their peculiar linear properties, PCs present many interesting features for controlling the nonlinear optical interaction

* Corresponding author. Tel.: +34- 977-558-790; Fax: +34-977-559-563
Email address: joanjosep.carvajal@urv.cat

1875-3892 © 2010 Published by Elsevier Ltd.
doi:10.1016/j.phpro.2010.10.023

and alternative phase matching mechanisms [4,5]. Within a PC one may enhance [6-8], phase matching [9] or hold a non-vanishing second order interaction even if the material is centro-symmetric.

As stated before a PC has a periodic variation of the linear susceptibility χ^1, which is related to the index of refraction, in one, two or three dimensions. This can be done by combining high refractive index and low refractive index building blocks in a periodic structure, which is usually a challenging task. If instead of modulating periodically the linear susceptibility of the material we can modulate periodically the nonlinear susceptibility tensor χ^2 in a nonlinear optical material, we are developing a quasi phase matched (QPM) material. This QPM concept was first referred independently by Armstrong [10], within the theoretical explanation for the application of light modulation, second harmonic and parametric conversion in dielectric media, and by Franken and Ward that reported about the theoretical explanation of optical harmonic generation [11]. In 1998, Berger gave the idea of periodic modulation of the second order susceptibility χ^2 in multiple spatial dimensions, the so called nonlinear photonic crystals (NPC) [12], to achieve quasi phase matching in multiple spatial directions with the possibility to support several conversion processes simultaneously. Moreover, the constraints on wavelength acceptance bandwidth imposed by 1D QPM gratings can be overcome with these structures. These are important advantages that make NPCs more versatile than 1D QPM structures. However, the combination of χ^1 and χ^2 modulation simultaneously in the same material has been severely studied in the literature. That is what we pretend to do in this paper by structuring the surface of a non-linear optical material; χ^1 will be modulated periodically between the values of the material and the air, while χ^2 will be modulated periodically between the values of the material and zero. Several methods have been proposed by different groups to fabricate the 1D and 2D photonic structures. The conventional PC structures have been fabricated by ion etching [13], and direct writing [14], etc. as well as NPC structures by field poling techniques [15], electron beam lithography [16], liquid phase epitaxy [17], etc.

Ultrafast laser ablation has emerged as a technique for rapid and flexible fabrication of 1D and 2D photonic structures on hard dielectric materials and it has become increasingly important in the last few years as a result of the large amount of practical applications in surface modification or micro-structuring of dielectric materials. When femtosecond laser pulses are properly focused onto the target, the extreme short duration of the pulses facilitates material removal without imposing thermal effects on the remaining structure [18]. When intense ultra-short pulses are focused in transparent dielectrics, strong-field ionization and subsequent avalanche ionization lead to the generation of free-electron plasma. When the density of free electrons exceeds a certain threshold, enough energy is absorbed to produce macroscopic ablation. The largest density of ionized electrons is reached only in the central part of the focal region due to the highly non-linear nature of the strong-field ionization process. The application of this technique for the inscription of diffractive elements has been widely used. Both, internal and relief gratings have been designed and fabricated by direct writing with femtosecond laser pulses with arbitrarily complex geometries. Nonlinear optical materials have been interesting targets for femtosecond laser applications, and the integration of diffractive gratings by ultrafast laser ablation has been recently used for tailoring SHG in $LiNbO_3$ [19], KH_2PO_4 [20] and β-BaB_2O_4 (BBO), [21,22]. These diffractive elements allowed the multi-frequency self -converter systems and efficient second harmonic generation by non collinear phase matching and these structures show several advantages when compared to the more conventional collinear phase matching (PM) configuration [23].

Among the various inorganic crystals, the $KTiOPO_4$ (KTP) family of crystals has a unique combination of properties that makes them useful for efficient second harmonic generation from Nd doped lasers. The nonlinear optical properties of KTP and its isomorphs have been reviewed by a number of researchers and have received enormous attention in the last two decades. The key success of the KTP family is its good nonlinear optical behavior for frequency doubling of Nd: YAG laser radiation, with high non-linear optical coefficients [24,25]. One of the most remarkable features of these crystals, specially for RTP, is their high laser damage threshold [26] that makes them useful in high power laser frequency conversion. The RTP and KTP materials have high transmission coefficients between 0.35 and 4.5 μm with high thermal stability and broad angular acceptance.

Here, we present the fabrication process of photonic structures on the surface of RTP and KTP nonlinear optical crystals by means of femtosecond laser ablation. We studied the correlation between the ablation conditions,

the morphology obtained for the diffraction gratings, and the structural effects on the material, analyzed by micro-Raman scattering and micro-X-ray diffraction for a better understanding of the fabrication process.

2. Experimental techniques

2.1. Crystal growth

RTP and KTP crystallize in the orthorhombic system with space group *Pna*2_1. These crystals melt incongruently at 1443 K and 1450 K, respectively, so they cannot be grown by conventional melting methods and they have been traditionally grown by high temperature solution techniques, and more particularly by the Top-Seeded Solution Growth (TSSG) method [27]. Around 120 g of solution was prepared by mixing the desired ratios of the corresponding oxides, K_2CO_3 or Rb_2CO_3, TiO_2, and P_2O_5 depending on the desired crystal, in platinum cylindrical crucibles of 125 cm^3. The crystals were grown from WO_3 containing fluxes to reduce the viscosity of the flux [28]. The solution was homogenized at 50-100 K above the crystallization temperature. We used ***c***-oriented crystal seeds for growing RTP and KTP crystals. We determined the saturation temperature of the solution by observing the growth or dissolution of the crystalline seed in contact with the surface of the solution. During the growth, the crystal seed was rotated at an angular speed of 45 rpm. The growth process proceeded by decreasing the temperature of the solution by 20-50 K from the saturation temperature at a cooling rate of 0.1 K/h, depending on the size of the desired crystal. In this work, in order to obtain larger crystals, those were pulled from the solution during the growth process very slowly, 0.5 mm every 12 h. At the end of the crystal growth process, the crystal was completely extracted from the solution and slowly cooled to room temperature inside the furnace. To prepare the samples for the fabrication of diffraction gratings by ultrafast laser ablation, the single crystals obtained were crystallographically oriented, cut and polished.

2.2. Ultrafast laser ablation

1D and 2D diffraction gratings have been fabricated on the surface of RTP and KTP nonlinear optical materials by using a commercial Ti: Sapphire oscillator (Tsunami, Spectra Physics) and a regenerative amplifier system (Spitfire, Spectra Physics) based on chirped pulsed amplification (CPA) for ultrafast laser ablation on the surface of the samples. The laser system gives linearly polarized 120 fs pulses at 795 nm with a repetition rate of 1 kHz. The transverse mode of the beam was TEM00 and the width was 9 mm ($1/e^2$ criterion).

The thickness of the samples was in between 2-4 mm. They were placed on a motorized XYZ translation stage that allowed achieving optimal focusing on the surface of the target, with the (001) or (010) face of the samples perpendicular to the laser beam. The threshold fluence depends on the number of pulses per spot, resulting 1.44 ± 0.18 $J.cm^{-2}$ for 40 pulses and decreasing to 1.18±0.15 $J.cm^{-2}$ for multi-shot conditions (>100 pulses) giving an incubation factor $\xi = 0.783$ [29].

1D samples were fabricated on the surface of RTP crystals. According to the period of the fabricated diffraction gratings, the samples were called RTP1 (with a period of 15 μm) and RTP2 (with a spatial period of 20 μm). RTP1 was prepared focusing the laser beam by means of a 50 mm achromatic lens using a pulse energy of 0.78 μJ, which provided a peak fluence of ~6.1 $J.cm^{-2}$ at focus. The sample was moved following straight lines parallel to the ***b*** crystallographic axis and all across the surface, at a constant scanning speed of 130 $\mu m.s^{-1}$, avoiding the iterative passes along the same line. The pitch between the lines was set to 15 μm. For that scanning speed and focusing conditions the number of pulses contributing to the ablation of a point within the sample surface was approximately 40. For recording the RTP2 sample, the focusing optics was a 10X (0.22 NA) microscopic objective. A 6 mm diameter circular aperture was placed before the objective in order to slightly increase the spot size at focus. The pulse energy before the aperture was 0.27 μJ leading to peak fluence at focus of ~3.2 $J.cm^{-2}$. The writing procedure was identical than for RTP1 and the scanning speed was set to 75 $\mu m.s^{-1}$ with a separation between lines of 10.5 μm and 9.5 μm, alternatively. Under these conditions, the number of pulses contributing to the ablation of a point within the sample surface was around 55.

We followed a similar procedure for the fabrication of two different 2D structures on the surface of KTP crystals. In that case the laser beam was focused by a 10X objective lens with NA 0.30. We have written a 2D structure consisting of two perpendicular arrays of grooves, parallel to the ***a*** and ***c*** crystallographic axes, respectively

(sample KTP1). It was achieved by moving the sample with a constant speed of 75 μm/s which means a number of pulses per spot (Ø~ 3 μm) of 40. A circular aperture 6 mm and some neutral filters were placed before the focusing lens in order to reduce the pulse energy to 0.48 μJ and to produce a lattice pitch of 8.54 μm. Sample KTP2 consisted on a square array of circular holes with a pitch of 8.85 μm. In this case, the sample was moved to the selected positions and then irradiated with 100 pulses. A circular aperture of 5.5 mm and some neutral filters were placed before the focusing lens in order to reduce the pulse energy to 0.39 μJ and achieve the desired pore diameter. The total processed area was 3 x 3 mm^2 and took approximately 8.5 h to fabricate the sample in both cases.

2.3. Micro-X-ray diffraction characterization

A Bruker-AXS D8-Discover diffractometer with parallel incident beam (Göbel mirror) and vertical goniometer was used to check the crystallinity of the samples before and after the ultrafast laser ablation process. The system was equipped with a collimator for the X-ray beam of 500 μm and a GADDS detector. The GADDS detector was 30 × 30 cm^2 with a 1024 × 1024 pixel CCD sensor. Cu radiation was obtained from a copper X-ray tube operated at 40 kV and 5 mA. A 2θ scan was recorded on the samples in order to check if the crystallinity changed after the ablation process. Data were recorded in three different steps with the area detector by performing an ω-scan with a frame width of 15° in the θ range 5-45° with an integration time of 60 s/frame.

2.4. Micro-Raman scattering characterization

Micro-Raman scattering measurements were carried out using a micro-Raman system Reinshaw confocal InVia spectrometer equipped with a confocal microscope Leica 2500 and a CCD camera as detector. Micro-Raman spectroscopy is an ideal non destructive and accurate tool for the material characterization at the micron scale. Radiation of an Ar laser (λ=514 nm and 25mW) was focused by microscopic objectives (magnifications 10X, 50X, 100X) on the surface of the RTP and KTP diffraction gratings. A back scattering scheme was used to detect the Raman signal through a confocal hole, allowing the extraction of the light scattered from an extremely small region of the diffraction grating with a spatial resolution of about 1μm using the long working distance microscope objective 100X.

3. Results and discussions

3.1. Morphology of the fabricated diffraction gratings

The morphological characterization of the fabricated diffraction gratings was initially done by using the optical imaging profiler PLμ 2300.

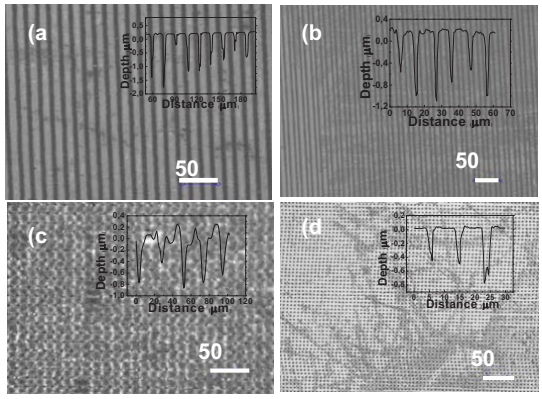

Figure1. Confocal images of the diffraction gratings fabricated by ultrafast laser ablation (a) RTP1 (2) RTP2 (c) KTP1 (d) KTP2, (inset figures: profiles of the diffraction gratings)

Figure 1 shows the confocal images of the fabricated diffraction gratings of the RTP and KTP samples. The confocal images of the diffraction gratings of all the samples were recorded with 20X microscopic objective in the long range order. In the images we can see the long range ordering and the high degree of periodicity of the diffraction gratings recorded by ultrafast laser ablation. The surface profiles of the fabricated diffraction gratings were also recorded and shown in the inset of each figure for each diffraction grating. Looking carefully at the Figure 1(b), the image to the RTP2 sample, the two different periods of the diffraction grating can be observed.

The morphological characterization of as-fabricated RTP and KTP diffraction gratings has also been done using scanning electron microscopy (SEM). The top views of the RTP and KTP diffraction gratings are shown in Figure 2 at different magnifications. Figures 2 (a) and (b) are the top views of the RTP 1D diffraction gratings and Figures 2 (c) and (d) are the top views of the 2D diffraction gratings of KTP samples, respectively. The inset Figure of each diffraction grating shows a higher magnification image of the fabricated diffraction grating by ultrafast laser ablation.

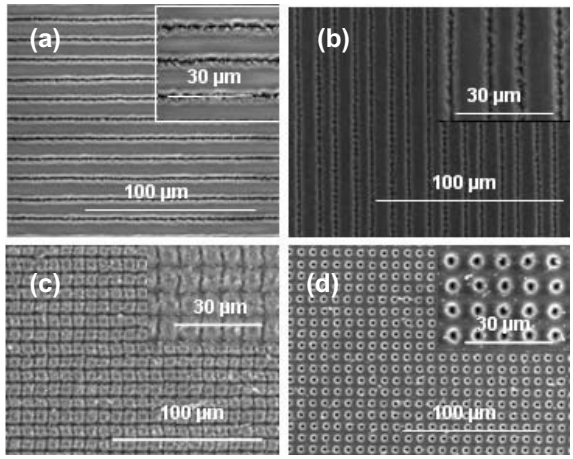

Figure 2. Top views of the diffraction gratings fabricated by ultrafast laser ablation obtained by SEM with different magnification corresponding to (a) RTP1 (b) RTP2 (c) KTP1 (d) KTP2.

We observed here that the width of the grooves is not the same for all the samples. This is due to the result of the tight focusing conditions. If the focal plane does not match the surface of the sample, even slightly, the pulse energy distribution is modified at the area where the fluence is above the ablation threshold. In the case of RTP1, the region where the fluence exceeded the ablation threshold fluence (multi-shot conditions) has a diameter of approximately 5 µm whereas in the case of RTP2, the diameter of the groove was around 3.3 µm.

In the case of KTP1 we observe that the roughness of the grooves is very high, and the squares that should be formed between the grooves are very distorted as a result of the writing procedure. This difficult the determination of the exact widths of the channels as well as the lattice period in this structure. The higher magnification images for KTP diffraction gratings show the distorted squares formed on the sample between channels and the circular pores formed on KTP1 and KTP2 diffraction gratings, respectively. The widths of the square pattern of the 2D diffraction grating is different in ***a*** and ***c*** crystallographic directions. The width of the channels along the ***a*** direction is larger than along the ***c*** direction due to the anisotropy of the material that leads to different ablation thresholds depending on the crystallographic directions in the crystal, since the laser fluence did not change during processing. The widths of the channel in KTP1, along ***a*** and ***c*** directions are 5.60 µm and 3.51µm respectively The fact that the damage threshold is different in different directions is not surprising in KTP. In this family of materials it has been found that some physical properties are quite similar when measured along the ***a*** and ***b*** crystallographic directions, and significatively different from those measured along the ***c*** crystallographic direction [30]. We also notice here that the

pulse energy was different for KTP1 and KTP2 samples that resulted in a different diameter for the pores of the KTP2 sample when compared to the width of the channels of KTP1.

Cross sections of the channels and circular pores that formed the RTP and KTP diffraction gratings are shown in Figure 3. As can be seen in these pictures, the roughness of the lateral walls is 0.4 μm, specially in the RTP samples. These images reveal that channels have a V shape and holes are conical. The depths of the grooves of RTP1 and RTP2 are 5 and 7 μm respectively.

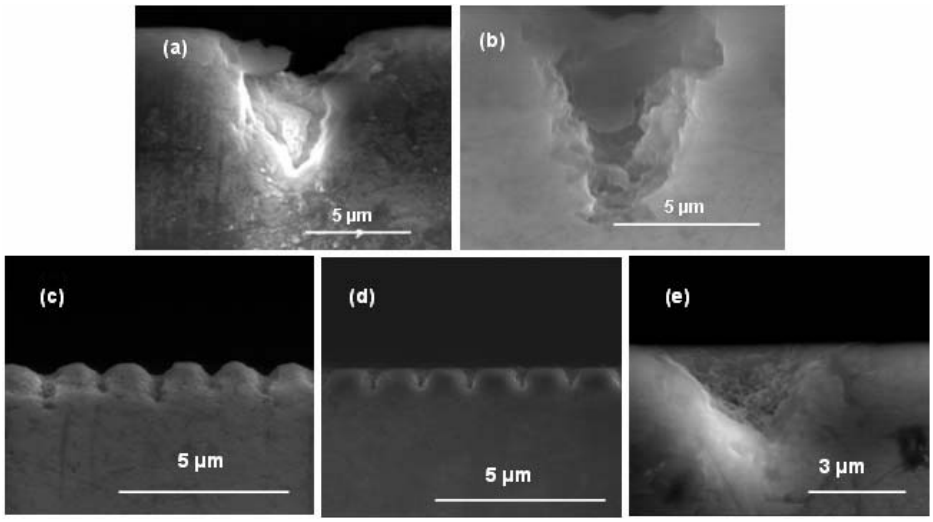

Figure 3. Cross sections of the grooves and pores inscribed in RTP and KTP diffraction gratings (a) RTP1 (b) RTP2 (c) fabricated grooves on KTP1 along ***a*** direction (d) KTP1 grooves along ***c*** direction (e) circular pore of KTP2 along ***a*** direction.

In KTP1 2D square pattern, the depths of the channels inscribed along perpendicular directions are also different as shown in Figures 3 (c) and (d) due to the material anisotropy. We observed here that the depth of the ablated channel along the ***a*** direction is 6.1 μm, while the depth of the channel along the ***c*** direction is 3.5 μm. The depth of the holes of the KTP2 diffraction grating was 4.3 μm.

2. Structural characterization

3.2.1. Micro- X-ray diffraction

We recorded the micro-X-ray diffraction patterns of the samples in order to check the variation of the crystallinity in the areas where laser ablation was performed. Figure 4 shows the results of this characterization performed on the RTP1 sample.

Figure 4 reveals only two peaks corresponding to the (001) family of planes in particular the (004) and (008) planes. Peaks marked with an arrow are artifacts due to the detection system and are not real. We observed that it exist a variation in the intensity of the peaks recorded in the processed region and in the unprocessed region of the sample. However, in opposite to what would be expected, the intensity of the X-ray diffraction pattern recorded at the processed region is higher than the intensity of the X-ray diffraction pattern measured at the unprocessed region on the surface of the RTP1 1D sample. Although the reasons for this increase in intensity are not understood at

present, these results indicate that the ultrafast laser ablation process is at least not degrading the crystalline quality of the sample.

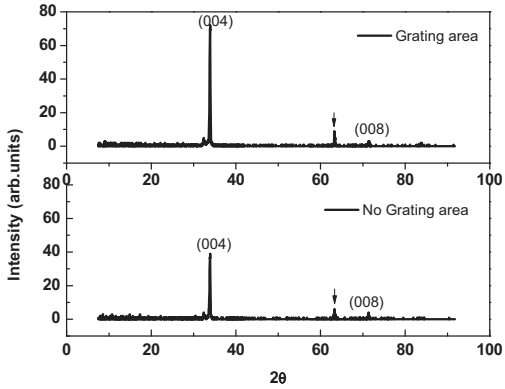

Figure 4. X-ray diffraction pattern measured on the grating area and no grating area of the RTP1 sample

3.2.2. Micro-Raman scattering

For a deeper study at a local level of structural modifications of the diffraction gratings, Raman spectra were recorded on the 1D and 2D diffraction gratings on the processed and unprocessed areas of the samples. The results are shown in Figure 5 with the micro-Raman spectra recorded at room temperature in the range of frequencies from 100 to 1200 cm^{-1} of the RTP2 and KTP2 diffraction gratings.

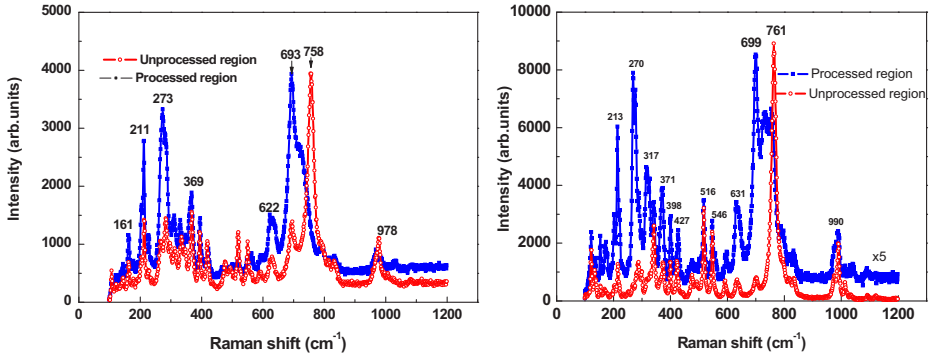

Figure 5. Raman Spectra recorded at processed and unprocessed regions of (a) RTP2 (b) KTP2

The structure of the spectra is not simple, with a large number of peaks of very different intensities. In general the Raman spectra of these materials are predominantly due to the vibrational motions of the TiO_6 octahedra and the PO_4 tetrahedra. More specifically, the regions from approximately 200-400 cm^{-1} and 600- 800 cm^{-1} are associated with TiO_6 octahedral torsional and stretching modes, respectively. The Raman bands in the 850–1200 cm^{-1} region are due to the PO_4 tetrahedra. In Figure 5(a) we observed two peaks with the strongest intensity at around 693 and 758 cm^{-1} in the processed and unprocessed regions, respectively. Other intermediate intensity peaks have been observed at 273, 369, 518, 548 and 622 cm^{-1}. As expected from the complex crystallographic structure, many

additional lines of lower intensity peaks are observed within the whole frequency range and especially below 250 cm^{-1}. However, in these peaks we did not observe a spectacular change as with the peaks appearing at 693 and 758 cm^{-1}.

The spectrum observed for the unprocessed region coincides with that reported on polarized spectra belonging to the (001) scattering configuration of the RTP crystal [31]. The peaks showing a strongest intensity in the processed region are those located at around 273, 369, 622 and 693 cm^{-1}. We pointed out that the main part of the scattered intensity (75%) arises from structures located at 211, 273, 693 cm^{-1} which are related to vibrations involving from TiO_6 octahedra. The intensity of the peaks we observed at processed region of the RTP2 diffraction grating is similar to the results obtained on the polarized spectra of the RTP sample corresponding to the (100) and (010) phonon propagation directions. The shifting of the frequency modes at unprocessed to processed regions is like the polarization of phonons is shifting from a configuration $z(yy)\bar{z}$ to $x(zz)\bar{x}$ [31].

The high intensity peak at 758 cm^{-1} at the unprocessed region of the RTP2 diffraction grating completely disappears at the processed region, and the small peak appearing at around 693 cm^{-1} at unprocessed region of the diffraction grating become the most intensity peak at the processed region. This shifting in the intensity of the Raman bands from ν_2 vibrational mode to $\nu_1$and ν_3 vibrational modes seem to indicate that the laser ablation is affecting to the orientation of the TiO_6 octahedra in the material.

Similarly we recorded the Raman spectra on the KTP2 2D diffraction grating and we observed that the peaks appearing at 699 and 761 cm^{-1} are those showing the highest intensity at processed and unprocessed regions, respectively similarly to the case of the RTP2 sample. We can observe here that all the peaks appearing at processed region are more intense than the peaks observed at unprocessed region in both RTP2 and KTP2 diffraction gratings when the conditions of recording the spectra were identical. Similar results were obtained in the case of RTP1 1D and KTP1 2D PC structures, although not shown here for the sake of brevity.

This difference between the intensity of the peaks appearing at 693 and 758 cm^{-1} in the case of the RTP2 sample, and these appearing at 699 and 761 cm^{-1} in the case of the KTP2 sample, allowed us to study if the laser ablation process only removed material from the diffraction grating or if there are internal parts of the material, that although they remained attached to the diffraction grating, they are affected by the laser ablation process. For this we scanned across the samples as shown in Figure 6 and recorded the intensity of those vibrational peaks. The plots of the intensity of these peaks are shown in Figure 6.

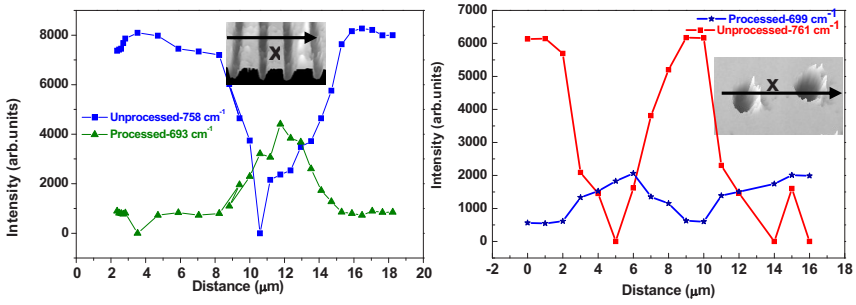

(a) (b)

Figure 6. Most Strong peaks at processed and unprocessed region, along x-axis on the surface of the diffraction grating vs intensity of the Raman signal (a) RTP2 (b) KTP2.

The features observed by the variation of intensity of the Raman scattering peaks coincides with the features inscribed with the laser during the ultrafast ablation process (grooves and pores). However, the widths of these

features described by Raman scattering (7.08 and 7 μm for RTP2 and KTP2 samples, respectively) are larger than those obtained from the profile of the grooves determined by SEM and confocal microscopy, indicating that there exist a affected region inside of the material, although it has not been ablated.

4. Conclusions

We have fabricated the 1D and 2D diffraction gratings on RTP and KTP nonlinear optical crystals by ultrafast laser ablation. We analyzed the geometrical parameters and quality of the fabricated photonic diffraction gratings by using SEM and confocal microscopy analysis. We also investigated the correlation between the affect of laser ablation on the remaining material by using micro-Raman analysis and micro-X-ray diffraction spectra. Ultrafast laser ablation did not affect to the crystallinity of the material although it seems to affect to the polarization of the structure vibrations of these materials.

Acknowledgements

This work was supported by the Spanish government under projects MAT2008-06729-CO2-02/NAN, PI09/90527, HF2008-0045, TEC2010-21574-CO2-02, Consolider Program SAUUL (CSD2007-00013) and FIS2009-09522 by catalan government under projects 2009SGR235. Junta de Castilla y León through the Program for Groups of Excellence (GR27) and from the EC's Seventh Framework Programme (LASERLAB-EUROPE, grant agreement nº 228334). J.J.C. is supported by the Science and Innovation Ministry of Spain and European Social Fund under the Ramón y Cajal program, RYC2006-858.

References

[1] Yablonovitch, Phys. Rev. Lett. 58 (1987) 2059.
[2] S. John, Phys. Rev. Lett. 58 (1987). 2486.
[3] D. Maystre, Opt.Exp. 8 (2001) 209.
[4] J. Martorell, R. Vilaseca, and R. Corbalan, Appl. Phys. Lett. 70 (1997) 702.
[5] M. Centini, C. Sibilia, M. Scalora, G. D'Aguanno, M. Bertolotti, M.J. Bloemer, C.M. Bowden, and I. Nefedov, Phys. Rev. E 60 (1999) 4891.
[6] J. Trull, R.Vilaseca, J. Martorell, and R. Corbalan, Opt. Lett. 20 (1995) 1746.
[7] P.P. Markowicz, H. Tiryaki, H. Pudavar, and P.N. Prasad, Phys. Rev. Lett. 92 (2004) 083903(3).
[8] J. Torres, M. Le Vassor dÝerville, D. Coquillat, E. Centeno, and J. Albert, Phys. Rev. B, 71 (2005) 195326.
[9] J. Martorell, and R. Vilaseca, Phys. Rev. A, 55 (1997) 4520.
[10] J. Armstrong, N. Bloembergen, J. Ducuing, and P.S. Pershan, Phys. Rev. 127 (1962) 1918.
[11] P.A. Franken,and J.F. Ward, Rev. Mod. Phys. 35 (1963) 23.
[12] V. Berger, Phys. Rev. Lett. 81 (1998) 4136.
[13] G. Ulliac, N.Courjal, H.M.H.Chong, and R. M. De La Rue, Opt. Mat. 31 (2008) 196.
[14] G. Della Valle, R. Osellame, and P. Laporta, J. Opt. A : Pure Appl. Opt. 11 (2009) 013001.
[15] C. Canalias, M. Norlof, V. Pasiskevicius, and F. Laurell, Appl. Phys. Lett., 94 (2009) 081121(1-3).
[16] D. Coquilat, G. Vecchi, C. Comaschi, A. M. Malvezzi, J. Torres, and M. Le Vassor dýerville, Appl. Phys. Lett., 87 (2005) 101106.
[17] A. Peña, S. Di Finizio, T. Trifonov, J.J. Carvajal, M. Aguiló, J. Pallarès, A. Rodriguez, R. Alcubilla, L.F. Marsal, F. Díaz, and J. Martorell, Adv. Mater. 18 (2006) 2220.
[18] M.D. Perry, B.C. Stuart, P.S. Banks, M.D. Feit, V. Yanovsky, and A. M. Rubenchik, J. Appl. Phys. 85 (1999) 6803.
[19] G.A. Torchia, C. Méndez, I. Arias , L. Roso, A. Rodenas and D. Jaque, Appl. Phys. B 83 (2006) 559.
[20] M.C. Méndez, J.R. Vázquez de Aldana, G.A. Torchia, and L. Roso, Optics. Letters, 30 (2005) 2763.
[21] C. Romero, Javier R. Vázquez de Aldana, C. Méndez, and L. Roso, Opt. Exp. 16 (2008) 1810.
[22] Y. Li, P. Lu, N. Dai, X. Wang, Y. Wang, B. Yu, and H. Long, Appl. Phys. B 88 (2007) 227.
[23] Tal Ellenbogen, and Ady Arie, Opt. Comm. 27 (2007) 423.
[24] B. Boulanger, J.P. Feve, G. Marnier, B. Menaert, X. Cabirol, P. Villeval, and C. Bonnin, J. Opt. Soc. Am. B, 11(5) (1994) 750.
[25] M.V. Pack, D.J. Armstrong, and A.V. Smith, Appl. Opt., 43, (2004) 3319.

[26] D.N. Nikogosyan, “Nonlinear Optical Crystals A Complete Survey”, Springer, Berlin (2005).
[27] J.J. Carvajal, R. Solé, J. Gavaldà, J. Massons, M. Aguiló, F. Diaz, Opt. Mater. 24 (2003) 425.
[28] J.J. Carvajal, V. Nikolov, R. Sole, Jna. Gavalda, J. masons, M. Rico, C. Zaldo, M. Aguilo, and F. Diaz, Chem. Mater. 12 (2000) 3171.
[29] S. Baudach, J. Bonse, J. Kruger, and W. Kautek, Appl. Surf. Sci. 555 (2000) 154.
[30] F.R. Wagner, A. Hildenbrand, J.Y. Natoli, M. Commandré, F. Théodore, H. Albrecht, Opt. Exp. 15 (2007) 13849.
[31] J.J. Carvajal, P. Seconds, A. Peña, J. Zaccaro, B. Boulanger, F. Diaz, and M. Aguiló, J. Phys. Cond. Matt., 19 (2007) 116214.

Paper V

Surface ablation of $RbTiOPO_4$ by femtosecond laser

G. Raj Kumar, J.J. Carvajal, M.C. Pujol, X. Mateos, J. Grau, J. Massons, J.R. Vázquez de Aldana, C. Méndez, P. Moreno, L. Roso, J. Ferré-Borrull, J. Pallarès, L.F. Marsal, M. Aguiló, F. Díaz

Optical Materials, **34**, 207-214 (2011)

UNIVERSITAT ROVIRA I VIRGILI
MICROSTRUCTURATION OF NONLINEAR OPTICAL MATERIALS:
METHODOLOGIES, CHARACTERIZATION, AND APPLICATIONS
Raj Kumar Golconda
Dipòsit Legal: T. 55-2013

Optical Materials 34 (2011) 207–214

Contents lists available at SciVerse ScienceDirect

Optical Materials

journal homepage: www.elsevier.com/locate/optmat

Surface ablation of $RbTiOPO_4$ by femtosecond laser

G. Raj Kumar [a], J.J. Carvajal [a,*], M.C. Pujol [a], X. Mateos [a], J. Grau [b], J. Massons [a], J.R. Vázquez de Aldana [c], C. Méndez [d], P. Moreno [c], L. Roso [d], J. Ferré-Borrull [e], J. Pallarès [e], L.F. Marsal [e], M. Aguiló [a], F. Díaz [a]

[a] Física i Cristal·lografia de Materials i Nanomaterials (FiCMA-FiCNA), Universitat Rovira i Virgili (URV), Campus Sescelades, Marcel·li Domingo, s/n Tarragona E-43007, Spain
[b] EUETIB, Univ. Politècnica de Catalunya (UPC), Barcelona, Spain
[c] Grupo de Microprocesado de Materiales con Láser, Univ. Salamanca, Salamanca E-37008, Spain
[d] CLPU-Centro de Láseres Pulsados, Villamayor, Salamanca E-37185, Spain
[e] Dept. d'Enginyeria Electrònica, Univ. Rovira i Virgili (URV), Tarragona E-43007, Spain

ARTICLE INFO

Article history:
Received 5 May 2011
Received in revised form 29 July 2011
Accepted 11 August 2011
Available online 9 September 2011

Keywords:
Non-linear optical materials
Ultrafast laser ablation

ABSTRACT

We report here the results obtained in surface ablation of $RbTiOPO_4$ single crystals by femtosecond laser. We fabricated and characterized one-dimensional (1D) diffraction gratings with different lattice spacings of 15 and 20 μm, and with a sub-modulation of the period introduced in the later. The optical and electronic microscopy characterization and filling factor analysis of these diffraction gratings are reported. We also show that the roughness generated on the grooves by the ablation process can be improved by chemical etching.

1. Introduction

Second harmonic generation (SHG) of laser radiation by phase matching (PM) in non-centrosymmetric crystals is commonly used for the generation of coherent sources of short-wavelength radiation. For non-linear crystals where direct phase matching is not possible, phase-matching conditions for processes such as second harmonic generation (SHG) can be fulfilled by periodically modulating the material. The periodicity of any physical property of the material introduces reciprocal lattice vectors that provide the phase matching conditions between the incident and the generated beam, a mechanism called quasi-phase matching (QPM) [1,2]. A very common means to achieve QPM is by periodic poling of non-linear material, in which case only the χ^2 tensor shows a periodic modulation, while the refractive index has no modulation whatsoever. However, if other patterning methods are employed, a modulation of the refractive index of the material, for instance, can be achieved. Such periodically modulated materials can be used to generate a non-linear optical response, even in centrosymmetric materials [3]. More interestingly, SHG in these structures may be generated through a non-collinear configuration that can provide several advantages when compared to the more conventional collinear QPM configuration, such as the automatic separation of the generated beam from the input beam [4].

$RbTiOPO_4$ (RTP) is a non-linear optical material that belongs to the family of the well known $KTiOPO_4$ (KTP). KTP is one of the materials of reference for the fabrication of solid state lasers emitting in the green region of the electromagnetic spectrum by second harmonic generation of Nd:YAG lasers [5]. RTP has, however, the advantages to respect KTP, that while presenting similar non-linear optical coefficients [6], it shows larger electro-optic coefficients [7], and a higher damage threshold than KTP [8], which makes it specially attractive for electro-optics applications.

We structured the surface of RTP single crystals by ultrafast laser ablation, forming one-dimensional (1D) surface-relief diffraction gratings. In these structures, the refractive index and the non-linear optical response of the material are periodically modulated at its surface. Such structures might have interest for the analysis of non-linear optical effects, since in these structures not only the QPM conditions can be fulfilled in the case of an external beam incident on the surface of the diffraction grating from the top half-space, but also, both the fundamental and the SH fields can be strongly localized via resonant Bloch modes of the periodic structure [9–11].

Ultrafast laser ablation is a low cost technique that provides fast procedures and one step processing. Femtosecond infrared laser pulses have been successfully applied to the micro-structuring of dielectric transparent crystals and glasses. Such pulses are focused in the material, leading to laser ablation of the exposed area with minimal mechanical and thermal deformation for the rest of the material [12]. This technique has been already used to structuring non-linear optical materials such as KH_2PO_4 (KDP) [13], $LiNbO_3$ [14], β-BaB_2O_4 (BBO) [15,16], and $LiTaO_3$ [17].

* Corresponding author. Tel.: +34 977 55 8790; fax: +34 977 55 9563.
E-mail address: joanjosep.carvajal@urv.cat (J.J. Carvajal).

0925-3467/$ - see front matter © 2011 Elsevier B.V. All rights reserved.
doi:10.1016/j.optmat.2011.08.007

In this paper, we analyze the results obtained in the structuring of the (0 0 1) surface of RTP single crystals with a femtosecond laser system forming two diffraction gratings with different grating spacings. We characterized morphologically these diffraction gratings by optical and electronic microscopy and analyzed their diffractive properties. We also smoothed the roughness generated during the ablation process by applying a chemical etching technique.

2. Experimental techniques

2.1. Crystal growth

RTP is an orthorhombic material crystallizing with the $Pna2_1$ space group of symmetry [17]. RTP melts incongruently at 1443 K [18], so it cannot be grown from its melt. The Top-Seeded Solution Growth (TSSG) technique is one of the techniques included in the high temperature solution (HTS) growth techniques. One of the advantages of crystal growth from high temperature solutions (or flux growth), is that it allows crystals to grow below their melting temperature. A vertical tubular furnace, controlled by a Eurotherm 903 controller/programmer and a platinum cylindrical crucible of 125 cm^3 has been used in the crystal growth experiments. The solution was prepared by mixing the corresponding ratios of the precursor oxides, Rb_2CO_3, TiO_2, and P_2O_5. RTP crystals were grown from WO_3 containing fluxes to reduce the viscosity of the flux and to overcome the difficulty for the structural units to reach the crystal solution interface [19]. The composition of the solution used to grow these RTP crystals was Rb_2O–TiO_2–P_2O_5–WO_3 = 42.24–16.80–18.96–20.00 mol%. A ***c***-oriented crystal seed was used for growing RTP crystals and also for the determination of saturation temperature by examining the growth or dissolution of the crystalline seed in contact with the solution surface. In all these cases, the crystal seed was placed on the surface of the solution, just in the centre of the platinum crucible. A crystal seed rotation was maintained in all cases at an angular speed of 45 rpm to favor a good homogenization of the growth solution, and avoid the formation of flux inclusions in the crystals. During the crystal growth process, the temperature was reduced by 20–30 K, depending on the size of the desired crystal, from the saturation temperature at a rate of 0.1 K/h. To obtain larger crystals, the as-growing crystals were pulled out very slowly from the solution at a rate of 0.5 mm every 12 h. Finally, when the crystal growth process was finished, the crystal was slowly extracted from the solution and slowly cooled to room temperature inside of the furnace to avoid thermal stresses that can result in cracks in the crystals.

The samples, on which the surface relief diffraction gratings were fabricated, were prepared from the single crystals obtained, by cutting and polishing them in a crystallographically oriented way. First, samples were cut with the correct crystallographic orientation to obtain surface perpendicular to the ***c***-crystallographic direction, using a goniometer coupled to a Struers Accutom-50 diamond saw with disks 0.12 mm thick. Later the samples were polished in a Logitech PM5 polisher with an oscillatory arm. This enabled accurately rotation and pressurization of the samples, depending on the hardness of the material to be polished. As abrasive substances, alumina powders of 9, 3, 1 and 0.3 μm diameters were used. The quality of the polishing was measured using parameters such as roughness, flatness and parallelism between opposite faces of the sample measured by a Sensofar PLμ 2300 interferometric confocal microscope and a home-made self–collimator.

2.2. Ultrafast laser ablation

We used a commercial Ti: Sapphire Oscillator (Tsunami, Spectra Physics) and a regenerative amplifier system (Spitfire, Spectra Physics) based on chirped pulsed amplification (CPA) for ultrafast laser ablation of the surface of RTP samples. The system delivers linearly polarized pulses of duration 120 fs at 795 nm with a repetition rate of 1 kHz. The maximum pulse energy is 1 mJ and it was reduced by means of neutral density filters and a combination of a half wavelength plate and linear polarizer in order to micro-structure the gratings with the required geometry. The transversal mode is Gaussian and beam diameter is 9 mm ($1/e^2$ criterion). Before recording the gratings, we have estimated the ablation threshold fluence for RTP following the procedure proposed by Dumitru and co-workers [21]. The threshold fluence depends on the number of pulses per spot, resulting 1.44 ± 0.18 J cm^{-2} for 40 pulses and decreasing to 1.18 ± 0.15 J cm^{-2} for multi shot conditions (>100 pulses). The value of the incubation factor was calculated, giving $\xi = 0.783$ [21].

Processing parameters were chosen to record one grating with spatial period (Λ) of 15 μm (grating RTP1) and another grating with $\Lambda = 20$ μm (grating RTP2). For recording RTP1, the pulse energy was 0.78 μJ. The laser pulses were focused by means of a 50 mm achromatic lens which provided a peak fluence of ~6.1 J cm^{-2} at focus. The sample, which was 2 mm thick, was placed on a motorized XYZ translation stage that allowed achieving optimal focusing on the surface of the target, with the (0 0 1) face of the samples perpendicular to the laser beam. The sample was moved following straight lines parallel to the ***b*** crystallographic axis and all across the surface, at a constant scanning speed of 130 μm s^{-1} avoiding iterative passes along the same line. The pitch between the lines was set to 15 μm. For that scanning speed and focusing conditions the number of pulses contributing to the ablation of a point within the sample surface was approximately 40.

For recording RTP2, the focusing optics was a 10X (0.22 NA) microscope objective. A 6 mm diameter circular aperture was placed before the objective in order to slightly increase the spot size at focus. The pulse energy before the aperture was set to 0.27 μJ leading to peak fluence at focus of ~3.2 J cm^{-2}. The writing procedure was identical than for RTP1 but now the scanning speed was set to 75 μm s^{-1} and the separation between lines was 10.5 μm and 9.5 μm alternatively. Under these conditions, the number of pulses contributing to the ablation of a point within the sample surface was around 55.

2.3. Chemical etching

Chemical etching is one of the simplest and widely applied techniques to observe ferroelectric domain structures in crystals of the KTP family. In particular molten KOH:KNO_3 mixtures have been extensively studied for this purpose in this family of materials. Here, we used this selective chemical etchant, that etches the negative (0 0 1) face of the crystal while the positive (0 0 1) face is left relatively unetched, to smooth the roughness generated by the ultrafast laser ablation process. We performed the chemical etching process by dissolving a mixture of KOH:KNO_3 2:1 M ratio in distilled water at 353 K, and immersed the diffraction gratings between 5 min and 1 h in this solution. After that, the diffraction gratings were observed again under the Scanning Electron Microscope to record the effects generated on the grooves of the diffraction gratings by this chemical etching process.

3. Results and discussion

3.1. Crystal growth of RTP single crystals

RTP single crystals with typical dimensions of 17 × 18 × 20 mm along the ***a*** × ***b*** × ***c*** crystallographic directions and a typical weight of 9.3 g were obtained from high-temperature solutions containing

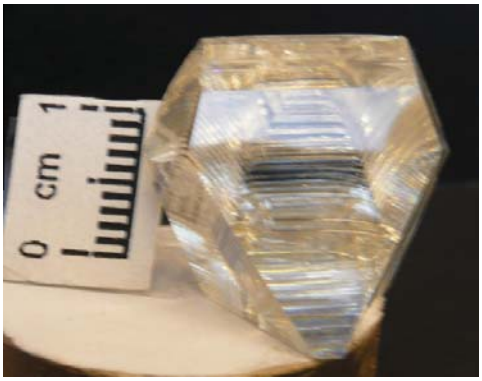

Fig. 1. $RbTiOPO_4$ single crystal obtained by Top-Seeded Solution Growth associated to a slow cooling of the solution. Pulling of the crystal from the solution was used to get a bigger crystal.

20 mol% WO_3. Fig. 1 shows an as-grown RTP single crystal. Tungsten oxide was used to decrease the viscosity of the solution of growth, that otherwise has been reported to be very high in this family of materials [22]. The composition of the solution of growth was chosen to be inside the crystallization region of RTP when a 20 mol% WO_3 was introduced in the solution [20]. The crystals were obtained by decreasing by 20–30 K the temperature of the solution starting from the saturation temperature, that was determined to be 910 K. This temperature is lower than the Curie temperature determined for these crystals, that has been determined to be 1065 K by measuring the dielectric permittivity of the crystal as a function of the temperature. This Curie temperature is lower than that measured for RTP crystals grown in solutions not containing WO_3 [23].

From these single crystals, slabs with typical dimensions $4 \times 4 \times 3$ mm along the $\boldsymbol{a} \times \boldsymbol{b} \times \boldsymbol{c}$ crystallographic axes were cut and their six faces polished to optical quality. On the (001) face of these samples is were laser ablation was performed.

3.2. Micro-structure analysis of the as fabricated diffraction gratings

The as-fabricated diffraction gratings were observed by optical microscopy. From this analysis, a long range order was observed indicating a high degree of periodicity of the two RTP samples, as can be seen in Fig. 2a and b for RTP1 and RTP2 samples, respectively.

From these figures it can be appreciated that while the periodicity was constant in the RTP1 sample with an estimated lattice parameter of 14.92 μm in average, determined after taking high magnification images of the sample, the periodicity of the RTP2 sample was sub-modulated into two different sub-periods of 9.5 and 10.5 μm approximately, inside of a longer period of 20 μm, imposed by the alternative grooves of the diffraction grating.

Micrographs of the samples were recorded in a FEI QUANTA 600 Scanning Electron Microscope (SEM) on top and lateral views to investigate the structure of the formed grooves at a local level. Fig. 3a and b shows top and lateral views, respectively, of the diffraction grating with $\Lambda = 15$ μm recorded by ultrafast laser ablation on the surface of the RTP1 sample. Fig. 3c and d shows two micrographs of the diffraction grating with $\Lambda = 20$ μm (with subperiods with lattices of 10.5 μm and 9.5 μm) recorded on the surface of RTP2 sample. The insets in Fig. 3a and c shows higher magnification images of the grating structures of RTP1 and RTP2 samples, respectively. From these micrographs we can still appreciate the high periodicity of the fabricated structures; however, the roughness of the lateral walls of the grooves was estimated to be 0.4 μm. This roughness can be a consequence of melting/vaporization and redeposition of material generated by the multipulse ablation processing, since each successive pulse would melt and vaporize the material and this would get redeposited in and around the groove, as observed in other dielectric materials [24]. Furthermore, the lateral views recorded for these two samples show that the grooves have a V shape with depths between $t = 5 \pm 0.4$ μm and $t = 7 \pm 0.4$ μm, and maximum widths of 5–5.5 μm for sample RTP1, and 3.3–3.5 μm for sample RTP2, respectively. Due to the low peak fluence used in the processing of these samples, we did not observe the formation of deposition of material at the edge of the groove, neither splattered material, as it happened with moderate peak fluences in $LiNbO_3$ [24].

These values are consistent with the fluence distribution (basically an Airy function) on the surface of the samples. In the case of RTP1, the region where the fluence exceeds the ablation threshold fluence (multishot conditions) has a width of approximately 5 ± 0.4 μm where as for RTP2 the corresponding width is 3.4 ± 0.4 μm. In both cases, the agreement with the width of the grooves is really good.

When we compare the results we obtained in RTP with those obtained in other non-linear optical materials, such as $LiNbO_3$ [24–26], $LiTaO_3$ [17] or BaB_2O_4 [16], we observed that for the wavelength and the processing conditions we used for the ablation process, similar features were observed in terms of roughness, however, deeper grooves were obtained at similar peak fluences in our case. When decreasing the peak fluence to values slightly above the ablation threshold, smoother features could be inscribed in $LiNbO_3$ [16,27], with a depth similar to those obtained in RTP, or submicrometer structures could be fabricated [26], still showing a high roughness, if the peak fluence is reduced to values close to the damage threshold.

It is well known that gratings of better quality and finer pitch can be fabricated using chemical etching techniques, becoming the standard techniques to fabricate such diffraction gratings in SiO_2 and many other materials, including $LiNbO_3$ [28].

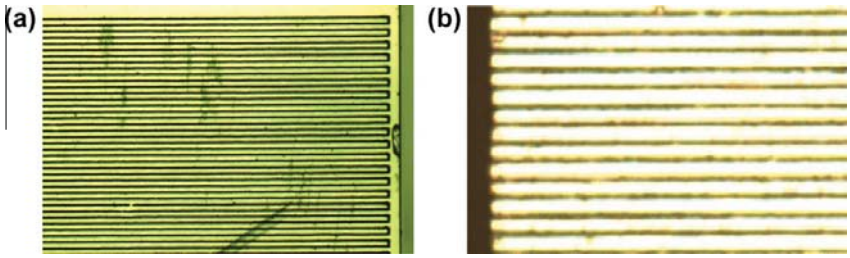

Fig. 2. Long range order optical microscope images of the RTP samples: (a) image taken with 5× objective and showing the regular pattern of the RTP 1 sample with a period of 15 μm and (b) image taken with 20× objective and showing the regular pattern of the RTP2 sample with a spatial period of 20 μm.

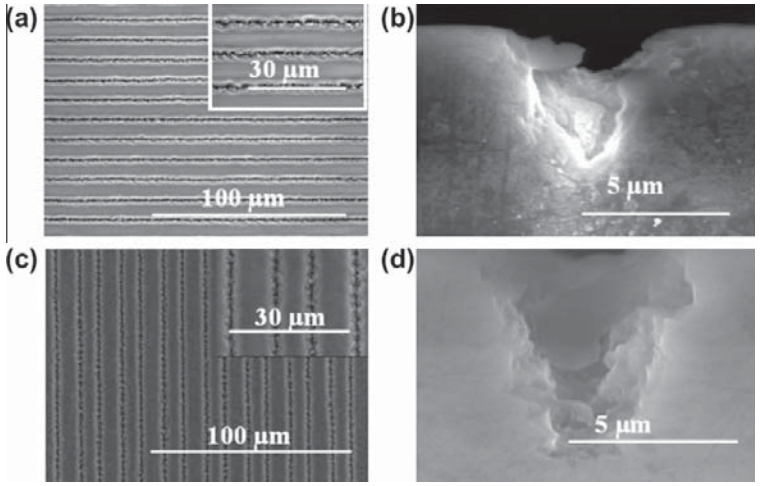

Fig. 3. SEM images recorded from the diffraction gratings fabricated by ultrafast laser ablation: (a) top view and (b) lateral view of the diffraction grating with a period of 15 μm recorded on the surface of the RTP1sample; (c) top view and (d) lateral view of the diffraction grating with a spatial period of 20 μm recorded on the surface of the RTP2 sample.

Thus, we explored the possibilities of using chemical etching to improve the quality of the diffraction gratings we fabricated on the surface of RTP by ultrafast laser ablation. Selective chemical etching in KTP and other crystals of the same family, including RTP, has been extensively studied to visualize the ferroelectric domain distribution in this family of materials [29]. This distribution of ferroelectric domains can be observed by etching the (001) face of these crystals with a mixture of KOH:KNO_3 2:1 M ratio at 353 K. Since the diffraction gratings were inscribed on the (001) face of RTP crystals we checked the possibility of using this etchant to smooth the grooves fabricated by ultrafast laser ablation.

Fig. 4 shows the results obtained in this process for the RTP2 sample using different etching times ranging from 5 min to 1 h, together with a high magnification of the as-fabricated grooves for comparison. We observed that the edge of the groove is better defined with the chemical etching and the roughness of the lateral walls of the channels is reduced. The best results were obtained for an etching time of 15 min. Beyond this etching time, the groove is becoming more and more wider when we increase the etching time, and even some of the parts of the sample not affected by the inital laser ablation process start to be affected after 1 h of exposure to the etchant. This would indicate that the sample was not single ferroelectric domain, and that for long exposure times we start to reveal the distribution of the ferroelectric domains on the surface of the sample. Also we observed that some trenches are formed at the lateral walls of the grooves by applying this etching technique. In any case, it is clear that chemical etching with KOH:KNO_3 can be used to improve the quality of the features fabricated on the (001) surface of RTP crystals by ultrafast laser ablation.

3.3. Determination of the lattice parameters of the diffraction gratings by FT-IR

Bragg-diffraction spectra of these samples have been recorded by using an FT-IR spectrometer (Bruker-Vertex 70) equipped with a special attachment that allows recording the spectra by reflectivity. We used a halogen tungsten lamp as the lighting source, and we collected the intensity of the diffracted light from 7500 to 400 cm^{-1} by using a DLATGS detector. The incoming light was pointed perpendicular to the surface of the sample where the 1D diffraction grating was recorded with the grooves perpendicular to the direction of the incident beam and several diffraction spectra were measured perpendicularly to the grooves at collection angles (θ) ranging from 24° to 60° in 2° steps. To evaluate the lattice constant, the Bragg-diffraction spectra were fitted to the 2-variable function:

$$I(\lambda, \sin\theta) \propto \sum_{n=1}^{3} \exp(-[(\sin\theta - (n\lambda/a))/w_n]^2) \quad (1)$$

where a is the lattice constant of the diffraction grating, n is the diffraction order, and w_n is a parameter that takes into account the width of diffraction peaks. By fitting this function to the experimental data we obtain a robust estimation of the lattice constant of the diffraction grating, since all measurements are taken into account simultaneously. Fig. 5a and b shows the 2D intensity plots as a function of the wavelength and the sinus of the diffraction angle of the measured data and the calculated data by the fitted function, respectively, for the diffraction grating recorded on the surface of the RTP1 sample. Experimentally, we observed three diffraction orders, that can be seen in the figure as dark red[1] color zones, with widths decreasing as the wavelength increased. The most intense peak was referred as the zero order peak and appeared in the range between 4 and 8 μm for low values of $\sin\theta$ with a lower slope. The second and third diffraction orders are observed at higher values of $\sin\theta$ with higher slopes.

The value of the lattice constant determined by this procedure was 14.98 μm for the diffraction grating recorded on the surface of RTP1 sample. This result is in good agreement with the value for the lattice constant for this sample estimated by optical and electron microscopy. For RTP2, using the same methodology, we were able to determine of the main periodicity, that was 19.85 μm. However, it has been impossible to determine the lattice constant of the two sub-periods existing in the RTP2 sample that we could observe only by optical and electronic microscopy.

[1] For interpretation of color in Figs. 1, 2, 5–10, the reader is referred to the web version of this article.

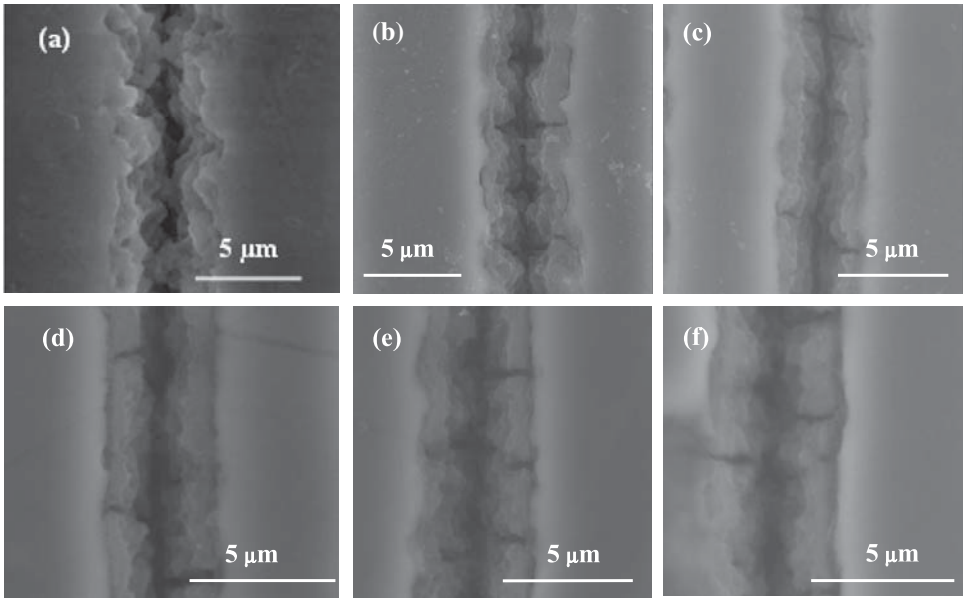

Fig. 4. SEM images of the grooves fabricated by ultrafast laser ablation after chemical attack with KOH:KNO_3 at different etching times: (a) 0 min, (b) 5 min, (c) 10 min, (d) 15 min, (e) 30 min, and (f) 1 h.

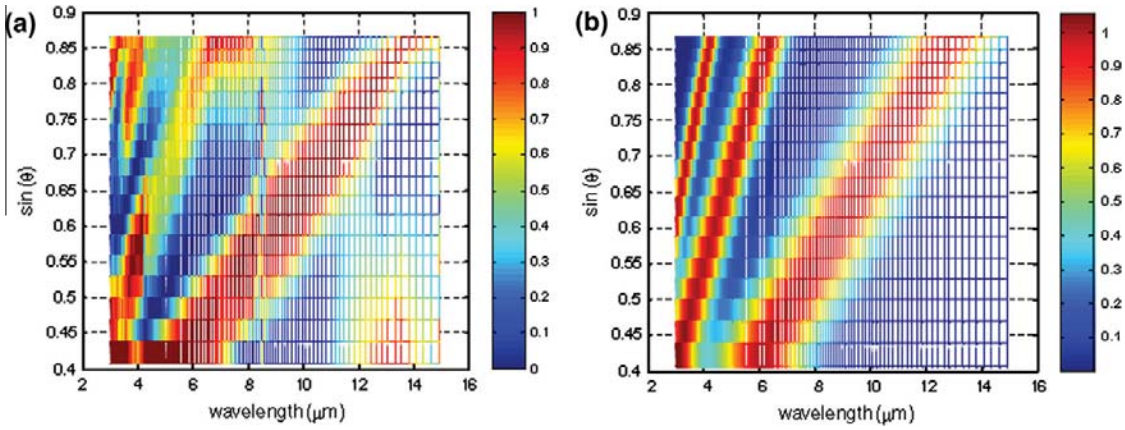

Fig. 5. (a) 2D experimental intensity plot as a function of the wavelength and the diffraction angle of the diffraction grating with a period of 15 μm recorded by ultra fast laser ablation on the surface of RTP1 sample: dark red zones represent the diffraction orders. (b) 2D plot of the fitted function to the experimental data after considering three diffraction orders.

3.4. Determination of the filling fraction of the diffraction gratings from the diffraction patterns

To check the quality of the diffraction gratings fabricated by these methods we recorded the linear diffraction patterns generated by the samples, obtained after focusing the beam of a He–Ne laser at 632.8 nm with a power of 3 mW and a spot size of ~1 mm on the surface of our samples, both in transmission and reflection geometries. In the transmission geometry the incident beam was set perpendicular to the surface of the sample on which the diffraction grating was inscribed, and the diffraction pattern was recorded at 180°. In the reflection geometry the incident beam was set to form an angle of 42° with the perpendicular to the surface of the diffraction grating to avoid additional spots on the diffraction patterns generated by internal reflections in other faces of the crystals. Fig. 6 shows the obtained diffraction patterns for the two samples analyzed.

On the screen, up to 11 diffraction orders, from −5 to +5, were visible in the transmission geometry for the RTP1 sample, while only 9 diffraction orders, from −4 to +4, were visible in the reflection geometry, as shown in Fig. 6a and b. In the RTP2 sample, even a larger number of spots could be observed, up to 15 diffraction orders, from −7 to +7, were visible in the transmission geometry, while this number was reduced to 11 diffraction orders, from −5 to +5, in the reflection geometry. Furthermore, the sub-modulation of the period of the diffraction grating is reflected in an alternation

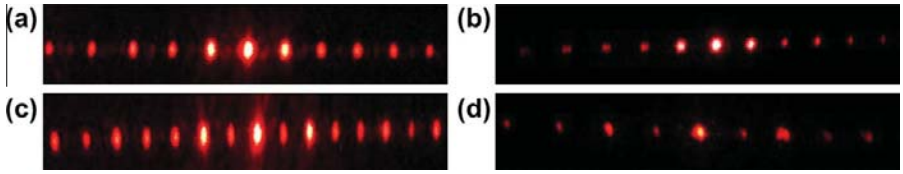

Fig. 6. Linear diffraction patterns of the different diffraction gratings recorded after illuminating the sample with a He–Ne laser: (a) diffraction grating with a period of 15 μm fabricated by ultrafast laser ablation on the surface of an RTP1 sample in transmission, and (b) in reflection geometries. (c) Diffraction grating with a spatial period 20 μm on the surface of RTP2 sample in transmission and (d) in reflection geometries.

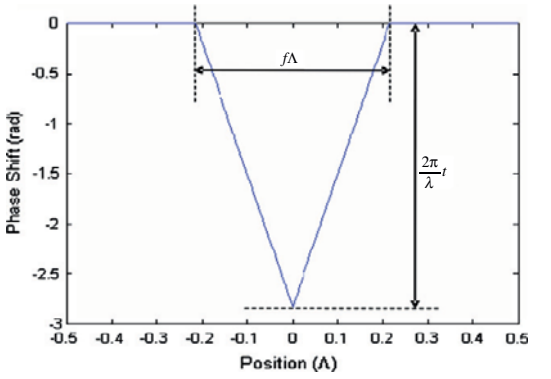

Fig. 7. Phase shift profile used to model the unit cell corresponding to the diffraction grating inscribed on the RTP1 sample, considered as a phase-only grating.

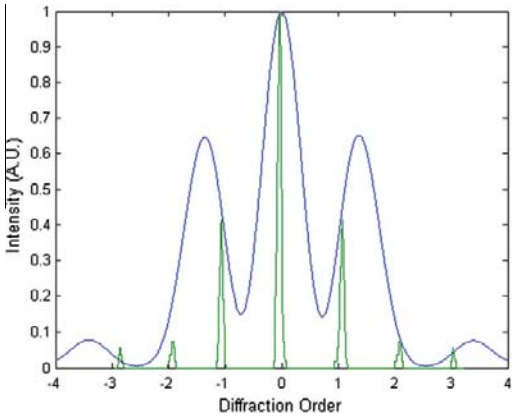

Fig. 8. Relative intensity profile of the diffraction pattern (green) and envelope profile (blue) for the RTP1 sample.

of high intensity and low intensity diffraction spots in the pattern as can be seen in Fig. 6c and d. Thus, in this way we demonstrate that these structures can work as both transmission and reflection gratings, fabricated within a single process.

The number of modes observed in these diffraction gratings are similar to those recorded previously in diffraction gratings inscribed in the surface of $LiNbO_3$ [14] and $BaBO_3$ [16] using the same methodology, indicating that the quality of the diffraction gratings in all those cases is similar.

We recorded the intensity profiles of the transmitted diffraction patterns with a charge coupled device (CCD) camera. Due to the limited dynamic range of the CCD camera we used, only the most intensity peaks of the diffraction patterns could be recorded. Diffraction patterns are sensitive to change in the periodicity of the grating or filling fraction. The filling fraction f is referred to as the fraction of the grating period that is filled with the grating material with values smaller than 1 (a value of 1 would mean that no diffraction grating exist on our sample). The analysis of the intensity profiles of the diffraction gratings can provide the characteristics of the fabricated diffraction gratings on the surface of the crystals, and can be used to determine from them the filling fraction.

In order to model the grooves with a V shape, the grating has been considered as a phase-only grating, where the grooves introduce a lower phase shift with respect to the parts of the grating without grooves. For RTP1, the phase shift profile of the unit cell is shown in Fig. 7. The position within the unit cell is expressed in terms of the lattice constant (Λ). In the figure, the different parameters describing the V-shaped grooves (f and t, where t defines the depth of the grooves) are indicated. The intensity profile of the diffraction grating on the RTP1 sample is shown in Fig. 8 together with the best fit of the experimental data, corresponding to a filling fraction $f = 0.43$ and a depth $t = 0.45\ \lambda$.

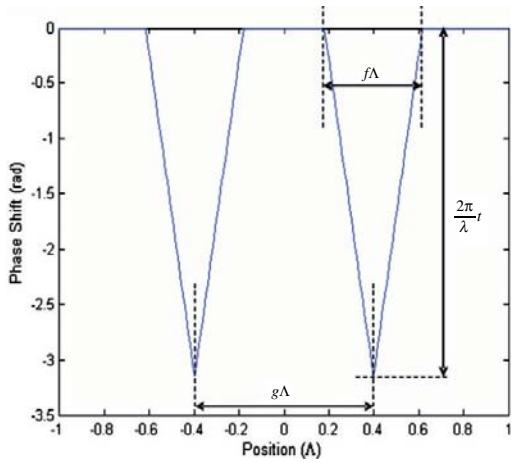

Fig. 9. Phase shift profile used to model the unit cell corresponding to the diffraction grating inscribed on the RTP2 sample, considered as a phase-only grating.

For RTP2, the profile considered to model our diffraction grating and the corresponding parameters are indicated in Fig. 9. This unit cell is periodically repeated every 2Λ. The experimental data together with the best fit are shown in Fig. 10. It is important to notice that in the case of the intensity profile of the RTP2 sample, the

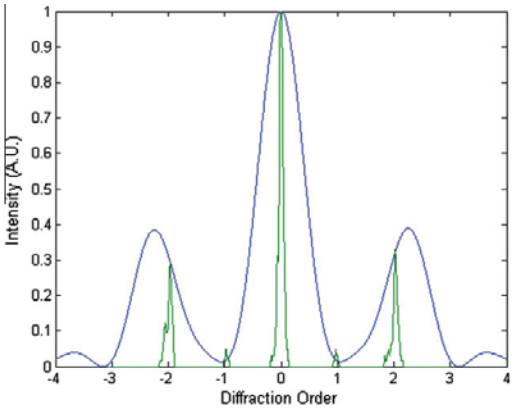

Fig. 10. Relative intensity profile of the diffraction pattern (green) and envelope profile (blue) for the RTP2 sample.

±1 order has lower intensity than the ±2 diffraction order peak. This variation in the intensity of diffraction orders were observed due to the existence of the 10.5 μm and 9.5 μm subperiodicities at the spatial period of 20 μm. The corresponding parameters for the best fit are $g = 0.92$, $f = 0.75$ and $t = 0.35\ \lambda$. The exact value for g should be 0.95, according to the subperiodicities observed in the sample. However, no reasonable fit could be obtained with this value of g, indicating also that these subperiodicities are not exact.

The profile of the envelope of the diffraction order maxima is the modulus square of the Fourier transform of the unit cell transmittance (unit amplitude and phase as indicated in Figs. 7 and 9), in the adequate scale. An analytic expression of this envelope should be very complex, difficult to obtain and very long to be included in the paper.

The diffraction efficiency for these samples was estimated by comparing the intensity recorded at the zero order with that of the incident beam. In both cases, this diffraction efficiency was found to be at around 0.1%. This value is not surprising since the measurements were not performed at the optimum wavelength for these diffraction gratings. However, comparing the quality of the diffraction gratings inscribed in RTP with those inscribed in $LiNbO_3$ for which up to a 30% diffraction efficiency has been reported [14] and those inscribed in $BaBO_3$ with diffraction efficiencies between 50% and 60% [16], one would expect to get similar values when using the optimum wavelength.

4. Conclusions

In conclusion, we have fabricated surface-relief diffraction gratings on ***c***-oriented RTP samples with different lattice constants by ultrafast laser ablation, and we characterized them morphologically and optically. The roughness observed on the surface of the channels of these diffraction gratings is similar to that observed previously in diffraction gratings fabricated on the surface of other non-linear optical materials, such as $LiNbO_3$, $LiTaO_3$ and $BaBO_3$ using the same methodology. However, the quality of the diffraction grating can be improved by using chemical etching techniques. A high number of diffraction orders were observed in the two samples analyzed, comparable to those recorded in diffraction gratings inscribed in $LiNbO_3$ and $BaBO_3$, indicating that the quality of the diffraction gratings inscribed in RTP is similar to those reported previously in other non-linear optical materials. It is obvious that the large edge roughness observed for these diffraction gratings inscribed by laser ablation on the surface of non-linear optical materials would make them more suitable for operation in the mid-infrared spectral range, were metallic rolled gratings can be fabricated in a simpler way, however, in those cases we can take advantage of the non-linear optical properties of the material to convert part of this radiation to the near-infrared or to the visible in the optimum cases.

We think that such surface-relief diffraction gratings may find potential applications in situations in which collinear phase matching configurations for SHG in non-linear optical materials cannot be achieved, such as signal multiplexing. This possibility will be analyzed in the future.

Acknowledgments

This work was partially funded by the European Commission under the Seventh Framework Program under Project Cleanspace FP7-SPACE-2010-1-GA-263044, supported by the Spanish Government under Projects PI09/90527, TEC2009-09551, AECID A/024560/09, FIS2009-09522, HOPE CSD2007-00007 and SAUUL CSD2007-00013 (Consolider-Ingenio 2010), by Catalan Government under Projects 2009SGR235 and 2009SGR549, by Junta de Castilla y León under Project GR27, and by the Research Center on Engineering of Materials and Systems (EMaS) of the URV. J.J.C. is supported by the Education and Science Ministry of Spain and European Social Fund under the Ramón y Cajal program, RYC2006-858. We also acknowledge support from the Centro de Laseres Pulsados, CLPU, Salamanca, Spain.

References

[1] J. Armstrong, N. Bloembergen, J. Ducuing, P.S. Pershan, Phys. Rev. 127 (1962) 1918.
[2] P.A. Franken, J.F. Ward, Rev. Mod. Phys. 35 (1963) 23.
[3] J. Martorell, R. Vilaseca, Phys. Rev. A 55 (1997) 4520.
[4] T.R. Zhang, H.R. Choo, M.C. Downer, Appl. Opt. 29 (1990) 3927.
[5] M.E. Hagerman, K.R. Poeppelmeier, Chem. Mater. 7 (1995) 602.
[6] M.N. Satyanarayana, A. Deepthy, H.L. Bhat, Crit. Rev. Solid State Mater. Sci. 24 (1999) 103.
[7] M. Roth, M. Tseitlin, N. Angert, Phys. Chem. 31 (2005) 86.
[8] D.N. Nikogosyan, Nonlinear Optical Crystals A Complete Survey, Springer, Berlin, 2005.
[9] A.R. Cowan, J.F. Young, Phys. Rev. B 65 (2002) 085106.
[10] R. Reinsch, M. Néviere, Phys. Rev. B 28 (1983) 1870.
[11] A.M. Malvezzi, F. Cattaneo, G. Vecchi, M. Falasconi, G. Guizzetti, L.C. Andreani, F. Romanato, L. Businaro, E. Di Fabrizio, A. Passaseo, M. De Vittorio, J. Opt. Soc. Am. B 19 (2002) 2122.
[12] M. Lenzner, J. Kruger, S. Sartania, Z. Cheng, Ch. Spielmann, G. Mourou, W. Kautek, F. Krausz, Phys. Rev. Lett. 80 (1998) 4076.
[13] C. Méndez, J.R. Vázquez de Aldana, G.A. Torchia, L. Roso, Opt. Lett. 30 (2005) 2763.
[14] G.A. Torchia, C. Méndez, I. Arias, L. Roso, A. Rodenas, D. Jaque, Appl. Phys. B 83 (2006) 559.
[15] C. Romero, J.R. Vázquez de Aldana, C. Méndez, L. Roso, Opt. Express 16 (2008) 18109.
[16] Y. Li, P. Lu, N. Dai, X. Wang, Y. Wang, b. Yu, H. Long, Appl. Phys. B 88 (2007) 227.
[17] Y. Zhang, X. Chen, H. Chen, Y. Xia, Appl. Surf. Sci. 253 (2007) 8874.
[18] J.J. Carvajal, C.F. Woensdregt, R. Solé, F. Díaz, M. Aguiló, Cryst. Growth. Des. 6 (2006) 2667.
[19] J.J. Carvajal, R. Solé, J. Gavaldà, J. Massons, M. Aguiló, F. Díaz, Opt. Mater. 24 (2003) 425.
[20] J.J. Carvajal, V. Nikolov, R. Solé, Jna. Gavaldà, J. Massons, M. Rico, C. Zaldo, M. Aguiló, F. Díaz, Chem. Mater. 12 (2000) 3171.
[21] G. Dumitru, V. Romano, H.P. Weber, M. Sentis, W. Marine, Appl. Phys. A 74 (2002) 729.
[22] K. Iliev, P. Peshev, V. Nikolov, I. Koseva, J. Cryst. Growth 100 (1990) 225.
[23] Jna. Gavaldà, J.J. Carvajal, X. Mateos, M. Aguiló, F. Díaz, Appl. Phys. Lett. 95 (2009) 182902.
[24] D.C. Deshpande, A.P. Malshe, E.A. Stach, V. Ramilovic, D. Alexander, D. Doerr, D. Hirt, J. Appl. Phys. 97 (2005) 074316.
[25] P. Galinetto, D. Ballarini, D. Grando, G. Samoggia, Appl. Surf. Sci. 248 (2005) 291.
[26] B. Yu, P. Lu, N. Dai, Y. Li, X. Wang, Y. Wang, Q. Zheng, J. Opt. A: Pure Appl. Opt. 10 (2008) 035301.

[27] A. Rodenas, J.A. Sanz García, D. Jaque, G.A. Torchia, C. Mendez, I. Arias, L. Roso, F. Agulló-Rueda, J. Appl. Phys. 100 (2006) 033521.
[28] J. Capmany, C.R. Fernandez-Pousa, E. Dieguez, V. Bermudez, Appl. Phys. Lett. 83 (2003) 5145.
[29] F. Laurell, M.G. Roelofs, W. Bindloss, H. Hsiung, A. Suna, J.D. Bierlein, J. Appl. Phys. 71 (1992) 4664.

Paper VI

Luminescent nanoparticles embedded in conical pores in $KTiOPO_4$ single crystals

R.K. Golconda, J.J. Carvajal, M.C. Pujol, X. Mateos, J. Massons, J.R. Vázquez de Aldana, C. Méndez, P. Moreno, L. Roso M. Aguiló, F. Díaz

Applied Physics Express (to be submitted)

UNIVERSITAT ROVIRA I VIRGILI
MICROSTRUCTURATION OF NONLINEAR OPTICAL MATERIALS:
METHODOLOGIES, CHARACTERIZATION, AND APPLICATIONS
Raj Kumar Golconda
Dipòsit Legal: T. 55-2013

UNIVERSITAT ROVIRA I VIRGILI
MICROSTRUCTURATION OF NONLINEAR OPTICAL MATERIALS:
METHODOLOGIES, CHARACTERIZATION, AND APPLICATIONS
Raj Kumar Golconda
Dipòsit Legal: T. 55-2013

Luminescent nano particles embedded in conical pores in $KTiOPO_4$ single crystals

R. K. Golconda, J. J. Carvajal, M. C. Pujol, X. Mateos, J. Massons, M. Aguiló, F. Díaz
Física i Cristal·lografia de Materials i Nano materials (FiCMA-FiCNA), Univ. Rovira i Virgili (URV), Campus Sescelades, Marcel·li Domingo, s/n Tarragona, E-43007, Spain

J. R. Vázquez de Aldana, C. Méndez, P. Moreno, L. Roso
Servicio Láser, Facultad de Ciencias, Univ. Salamanca, E-37008 Salamanca, Spain

We investigate here on fabrication and optical analysis of two dimensional (2D) conical pores on the surface of $KTiOPO_4$ (KTP) single crystals and embedding of Erbium (Er^{+3}) doped $KYb(WO_4)_2$ (KYbW) luminescent nanoparticles (NPs) inside the conical pores. Surface morphology, crystallinity, and micro-Raman analysis of embedded nanoparticles were analysed in detail. Embedding of RE^{+3} NPs inside KTP conical pores could be another possibility to achieve multicolour emission and also spatial and spectral control of the emitted electromagnetic radiation in micrometer scale of conical pores of an array. The obtained results are attractive for the reinforcement of rare earth based phosphor devices in the field of laser phosphor display (LPD) technology.

In the last few years, a passionate interest has been growing for controlling the electromagnetic radiation by focusing on microstructured patterns.[1] Novel ideas and approaches have been explored for enhancing and manipulating the optical properties of photonic devices by matching the periodic dimensional structures with the wavelength.[2] The optical properties of patterned materials can also be reinforced by filling the portion that has been micro or nanostructured with other materials such as polymers,[3] semiconductors,[4] molecular nanoparticle materials[5] and dye molecules.[6] A particularly interesting approach has been the control of light distribution spatially and spectrally generated by optically active trivalent lanthanide (Ln^{+3}) ions. It has been demonstrated that by embedding Ln^{+3}-doped nanoparticles into microstructured materials it might be possible to control the light spatially at the micrometer scale in a wide spectral range.[7,8]

This kind of technology might have interesting implications to reinforce an emerging technology as it is laser phosphor displays (LPD).

Several approaches have been reported for the fabrication of 2D micro-structural patterns on the surface of nonlinear optical materials, such as electric field poling techniques[9], proton exchange[10] electron beam lithography[11], liquid phase epitaxy[12] etc. Ultrafast laser ablation is a promising approach for this purpose since it allows us to fabricate deep trenches in ultra hard materials and produce high accuracy micro structure and repeatable.

$KTiOPO_4$ (KTP) crystallizes in the orthorhombic system with the non-centrosymmetric space group $Pna2_1$. It shows high nonlinear optical coefficients and has been traditionally used for frequency conversion of Nd:YAG laser radiation.[13] It also shows a wide transmission spectral range from 0.35 to 4.5 μm and a high laser damage threshold. This last property that would seem in contradiction with the microstructuring approach used in this work, is in fact an advantage for the last application of the structures we pretend fabricate, since we can increase the pump power of the luminescent nanoparticles generating brighter emissions; without damaging the base material.

Monoclinic potassium double tungstates have been chosen for their high absorption and emission cross section values of lanthanide ions, constituting suitable host materials for solid state laser applications.[14] KYbW is the best host material for doping Er^{+3} ions to obtain potential laser transitions in visible region and also produce high emission intensities due to the large absorption from Yb^{+3} ions by transferring pump energy to Er^{+3} ions. Apart from that, by embedding a high refractive index material, as it is Er^{+3}-doped KYbW nanoparticles into a lower refractive index material as it is KTP, would give an additional confinement of the emitted light that can provide even brighter emissions. Also, these composites might allow to exploit the non-linear optical properties of the base material expanding the range of emissions that can be obtained in these structures.

The KTP single crystals were grown by the Top Seeded Solution Growth-Slow Cooling (TSSG-SC) method which allows crystals to grow below their melting temperature since these crystals melt incongruently. *c*-oriented crystal seeds were used to grow KTP crystals. Details of the growth process can be found elsewhere.[15]

Ultrafast laser ablation was used to fabricate 3 × 3 mm^2 2D arrays of holes on the (001) surface of the KTP samples. Linearly polarized femto-second laser pulses at 795 nm, with a duration of 120 fs,and a repetition rate of 1 kHz, delivered from commercial Ti:Sapphire laser were used for this purpose. The irradiation fluence was reduced by means of neutral density filters and a combination of half-wave plate and a polarizer. The sample was placed on a motorized XYZ translation stage that allowed achieving optimal focusing on the surface of the target. It was scanned at a speed of 75 μm/s, and irradiated with 100 pulses with an energy of 0.39 μJ/pulse to achieve desired pore diameter and a diameter of beam was 5.5 mm. Figure 1(a) and (b) show scanning electron microscopy (SEM) images of the conical pores fabricated on the surface of KTP sample by ultrafast laser ablation. The diameter of the conical pores was 3.6 μm and the depth was around 4.3 μm. The roughness that can be observed in these images for the pores is similar to that observed in other structures fabricated on the

UNIVERSITAT ROVIRA I VIRGILI
MICROSTRUCTURATION OF NONLINEAR OPTICAL MATERIALS:
METHODOLOGIES, CHARACTERIZATION, AND APPLICATIONS
Raj Kumar Golconda
Dipòsit Legal: T. 55-2013

surface of other non-linear optical materials using the same technique.[16]

The modified sol-gel Pechini method was used to prepare 50% at. Er^{+3}-doped KYbW luminescent nanoparticles (NPs).[17] K_2CO_3, Yb_2O_3, Er_2O_3 and $(NH_4)_2WO_4$ were used as initial reagents and dissolved in concentrated HNO_3 to generate the nitrates. These salts were dissolved in distilled water and ethylenediaminetetraacetic acid (EDTA) as the complex agent in a molar ratio C_M = [EDTA]/ [METAL] = 1. Finally, we used ethylene glycol (EG) as the polymerization agent in a molar ratio C_E = [EDTA]/ [EG] = 2. After calcining the precursor powder at 1073 K for 3 h we obtained the Er^{+3}: KYbW NPs. These NPs had a diameter of around 40 nm, as determined from observation under a transmission electron microscope (TEM), a siwe much smaller than the pores we fabricated by ultrafast laser ablation on the (001) surfaces of the KTP samples.

The composites were fabricated by introducing the Er^{3+}:KYbW NPs in the holes of the KTP samples by mechanical means, and then annealing the sample at 1173 K for 5h. Figures 1(c) and 1(d) show the Er^{3+}: KYbW NPs inside the conical pores after the annealing process.

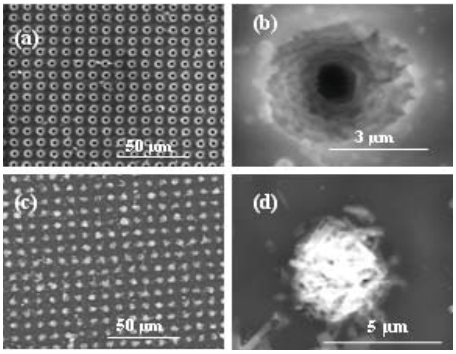

FIG. 1. (a) SEM image of a fabricated conical pores on the surface of KTP substrate (b) Higher magnification of circular pore (c) Embedded NPs inside conical pores (d) Higher magnification image of embedded NPs in conical pore.

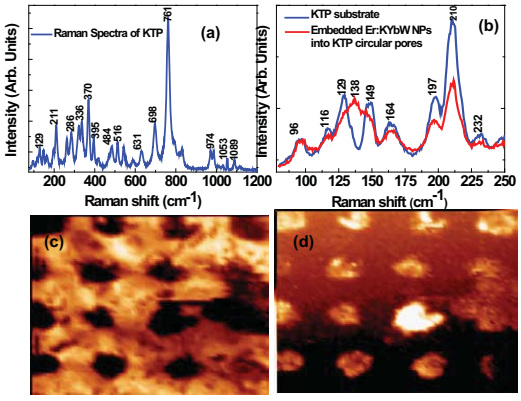

FIG. 2. (a) Micro-Raman spectra of KTP sample with conical pores (b) Micro-Raman scattering spectra of luminescent nanoparticles with and without filling the conical pores of KTP, (c) 2D micro-Raman intensity map of KTP substrate (d) 2D micro-Raman intensity map of NPs filled inside KTP conical pores after excitation.

We also confirmed that the structure of KTP substrate and embedded NPs in KTP conical pores is maintained after annealing by recording their Raman spectra. We used a micro-Raman Reinshaw confocal InVia spectrometer equipped with a confocal microscope Leica 2500 and a CCD camera as detector. The samples were excited with an Ar^+ laser (λ=514 nm, and 25 mW) focused on the sample by microscopic objectives. A backward scattering scheme was chosen to detect the Raman signal through a confocal aperture to increase the signal-to-noise ratio. Figure 2(a) shows that the micro-Raman spectra obtained for KTP substrate. The regions from 200-400 cm^{-1} and 600-850 cm^{-1} are associated with TiO_6 octahedral torsional and stretching modes, respectively. The bands in the 900 -1200 cm^{-1} region are due to the PO_4 tetrahedra. The most dominated peak observed at 761 cm^{-1}. At low band region, the Raman spectrum of Er:KYbW NPs is dominated by vibrational bands corresponding to KTP as can be seen in Figure 2(b) and the Raman mode at 138 cm^{-1} related to embedded NPs inside KTP conical pores.

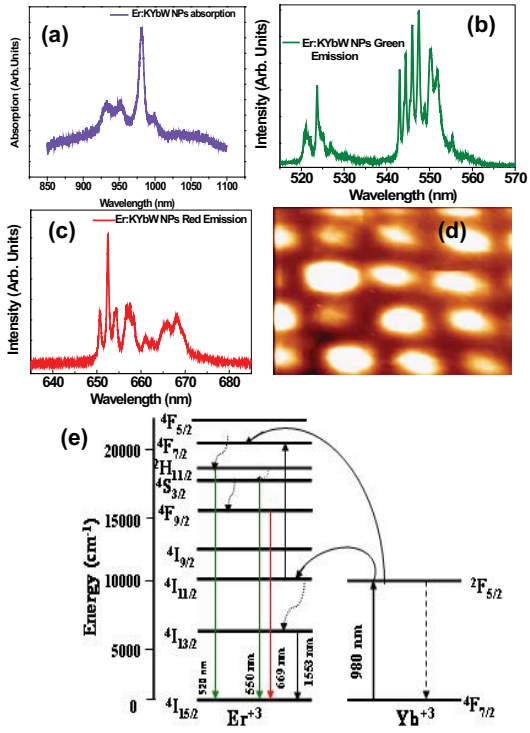

FIG. 3. (a) Optical absorption spectra of luminescent NPs embedded in conical pores corresponds to $^4F_{7/2} \rightarrow {}^2F_{5/2}$ transition (b) Green emission spectra of luminescent nanoparticles embedded in KTP conical pores corresponds to$^2H_{11/2} \rightarrow {}^4I_{15/2}$ and $^4S_{3/2} \rightarrow {}^4I_{15/2}$ transisions (c) Red emission spectra of luminescent nanoparticles embedded in KTP conical pores corresponds to $^4F_{9/2} \rightarrow {}^4I_{15/2}$, (d) 2D miscro-structure pattern of Er:KYbW luminescent NPs inside the conical pores of KTP sample.

The corresponding 2D Raman intensity maps of KTP and embedded NPs are shown in Figure 2 (c) and (d) respectively. These results indicate that both KTP and Er^{3+}:KYbW NPs have not changed their crystallographic structure during the thermal annealing applied to the sample to consolidate the structure of the composite. Also, no new compounds were formed by the interaction between KTP and the Er^{3+}:KYbW NPs at the edges of the pores.

This represents an advantage to respect previous reported similar structures, since in that case it will be easier to control the optical emission of the NPs.

We characterized the spectroscopic properties of these composites. The optical absorption of the Er^{3+}:KYbW luminescent NPs embedded in the conical pores of KTP was carried out by using a Cary 500 scan-Varian UV-Vis-NIR spectrophotometer at room temperature. Figure 3(a) shows the optical absorption of luminescent NPs embedded in KTP conical pores, with the different absorption bands corresponding to Er^{3+} and Yb^{3+}.

The green and red emissions were obtained by the process of two photon up-conversion after energy transfer from Yb^{3+},[18] as it is shown in Figure 3 (b) and (c).

Photoluminescence measurements were performed by observing the up-conversion process in Er^{3+} after direct excitation of Yb^{3+} and energy transfer to Er^{3+}. Optical excitation at the maximum of the optical absorption of Yb^{3+} was performed at 980 nm using a InGaAs diode laser. Luminescence from the embedded NPs inside the conical pores of KTP was collected and dispersed by a monochromator placed at 90º with respect to the incident laser beam. Green, and red emissions coming from Er^{3+} were observed for this sample, as can be seen in Figure 3 (e).

The transferred electrons in the $^4I_{11/2}$ level consistently increase their energy to the $^4F_{7/2}$ level, and a very fast nonradiative relaxation process took place to the $^2H_{11/2}$ and $^4S_{3/2}$ levels, where the emissions $^2H_{11/2} \rightarrow {}^4I_{15/2}$ and $^4S_{3/2} \rightarrow {}^4I_{15/2}$ take place at around 520 and 550 nm. Then, another nonradiative relaxation process takes place between the $^4S_{3/2}$ level to the $^4F_{9/2}$ level, and generates an emission at around 669 nm when it decays radiativelly to the $^4I_{15/2}$ level.

In conculsion, we have successfully grown KTP single crystals using TSSG method and fabricated the 2D micro-structure of conical pores on KTP single crystal surface by ultrfast laser ablation. The visible, IR emission and absorption of embedded luminescent NPs inside conical pores are measured and described by up-conversion energy transfer process of rare earth ions. The multicolor emission of embedded rare earth ions in a micron scale with a spatial and spectral control of emitted radiation could develop new functionalities in the field of photonics and laser phosphor display devices.

This work was supported by the Spanish government under projects, PI09/90527, HF2008-0045, TEC2010-21574-CO2-02, Consolider Program SAUUL (CSD2007-00013) and FIS2009-09522 by catalan government under projects 2009SGR235. Junta de Castilla y León through the Program for Groups of Excellence (GR27) and from the EC's Seventh Framework Programme (LASERLAB-EUROPE, grant agreement nº 228334). J.J.C. is supported by the Science and Innovation Ministry of Spain and European Social Fund under the Ramón y Cajal program, RYC2006-858.

[1]T. W. Ebbesen, H. J. Lezec, H. F. Ghaemi, T. Thio, and P. A. Wolf, Nature, **391**, 667 (1998).
[2]C. López, Adv. Mater., **15**, 1679 (2003)..
[3]K. Sasaki, S. Inoue, K. Nishio, H. Masuda, A. Otomo, and S. Yokoyama, Opt. Mat, **32**, 543 (2010).
[4]Yu. A. Vlasov, K. Luterova, I. Pelant, B. Honerlage, and V. N. Astratov, Apl. Phys. Lett., **71**, 1616 (1997).
[5]N. Gaponik, I. L. Radtchenko, M. R. Gestenberger, Y. A. Fedutik, G. B. Sukhorukov, and A. L. Rogach, Nano Lett. **3**, 369 (2003).
[6]N. Eradat, A. Y. Sivachenco, M. E. Raikh, Z. V. Vardeny, A. A. Zakhidov, and R. H. Baughman, Appl. Phys. Lett. **80**, 3491 (2002).
[7]P. Molina, M. O. Ramirez, J. V. Garcia-Santizo, S. Alvarez-Garcia, R. Pazik, W. Strek, P. J. Deren and L. E. Bausa, Appl. Phys. Lett. **95**, 051103 (2009).
[8]J. V. Garcia-Santizo, P. Molina, M. O. Ramirez, K. Lemanski, W. Strek, P. J. Deren, and L. E. Bausa, Opt.Exp. **18**, 18269 (2010).
[9]C. Canalias, M. Norlof, V. Pasiskevicius, and F. Laurell, Appl. Phys. Lett. **94**, 081121 (2009).
[10]G. Ulliac, N. Courjal, H.M. H. Chong, and R. M. De la Rue, Opt. Mat. **31**, 196 (2008).
[11]D. Coquilat, G. Vecchi, C. Comaschi, A. M. Malvezzi, J. Torres, and M. Vassor dyerville, Appl. Phys. Lett. **87**, 101106 (2005).
[12]A. Peña, S. Di Finizio, T. Trifonov, J. J. Carvajal, M. Aguiló, M. Pallarès, A. Rodriguez, R. Alcubilla, L. F. Marsal F. Díaz and J. Martorell, Adv. Mater. **18**, 2220 (2006).
[13]J. D. Bierlein and H. Vanherzeele, J. Opt. Soc. Am. B., **6**, 622 (1989).
[14]M.C.Pujol, M. Aguiló, F.Diaz and C. Zaldo, Opt. Mater., **13**, 33 (1999).
[15]A. Peña, S. Di Finizio, T. Trifonov, J. J. Carvajal, M. Aguiló, J. Pallarès, A. Rodriguez, R. Alcubilla, L. F. Marsal, F. Diaz, and J. Martorell, Adv. Mater. **18**, 2220 (2006).
[16]G. A. Torchia, C. Mendez, I. Arias, L. Roso, A. Ródenas, and D. Jaque, Appl. Phys. B **83**, 559 (2006).
[17]M. Glaceran, M. C. Pujol, M. Aguiló and F. Diaz, J. Sol-Gel. Sci. Techn, **42**, 79 (2007).
[18]X. Mateos, F. Guell, M. C. Pujol, M. A. Bursukova, R. Solé, Jna. Gavaldà, M. Aguiló, F. Diaz, and J. Massons, Appl. Phys. Lett. **80**, 4510 (2002).

UNIVERSITAT ROVIRA I VIRGILI
MICROSTRUCTURATION OF NONLINEAR OPTICAL MATERIALS:
METHODOLOGIES, CHARACTERIZATION, AND APPLICATIONS
Raj Kumar Golconda
Dipòsit Legal: T. 55-2013

UNIVERSITAT ROVIRA I VIRGILI
MICROSTRUCTURATION OF NONLINEAR OPTICAL MATERIALS:
METHODOLOGIES, CHARACTERIZATION, AND APPLICATIONS
Raj Kumar Golconda
Dipòsit Legal: T. 55-2013

Paper VII

Polycrystalline $RbTiOPO_4$ and TiO_2 formed on structured surfaces of $RbTiOPO_4$ single crystals by ultrafast laser ablation

J.J. Carvajal, R.K. Golconda, M.C. Pujol, X. Mateos, J. Massons, , J.R. Vázquez de Aldana, C. Méndez, P. Moreno, L. Roso, F. Díaz, and M. Aguiló

Cryst. Eng. Comm. (to be submitted)

UNIVERSITAT ROVIRA I VIRGILI
MICROSTRUCTURATION OF NONLINEAR OPTICAL MATERIALS:
METHODOLOGIES, CHARACTERIZATION, AND APPLICATIONS
Raj Kumar Golconda
Dipòsit Legal: T. 55-2013

UNIVERSITAT ROVIRA I VIRGILI
MICROSTRUCTURATION OF NONLINEAR OPTICAL MATERIALS:
METHODOLOGIES, CHARACTERIZATION, AND APPLICATIONS
Raj Kumar Golconda
Dipòsit Legal: T. 55-2013

Polycrystalline $RbTiOPO_4$ and TiO_2 formed on structured surfaces of $RbTiOPO_4$ single crystal by ultrafast laser ablation

J.J. Carvajal[a], R.K. Golconda[a], M.C. Pujol[a], X. Mateos[a], J. Massons[a], J.R. Vázquez de Aldana[b], C. Méndez[c], P. Moreno[b], L. Roso[c], F. Díaz[a], and M. Aguiló[a]

[a]Física i Cristal·lografia de Materials i Nano materials (FiCMA-FiCNA), Universitat Rovira i Virgili (URV), Campus Sescelades, Marcel·li Domingo, s/n Tarragona, E-43007, Spain

[b]Grupo de Microprocesado de Materiales con Láser, Univ.Salamanca, Salamanca, E-37008, Spain

[c]CLPU-Centro de Láseres Pulsados, Villamayor, Salamanca, E-37185, Spain

[*] Corresponding author: Tel.: +34 977 55 8790; Fax: +34 977 55 9563
Email address: joanjosep.carvajal@urv.cat

Abstract: We investigate the obtained results on 1D diffraction gratings inscribed on the surface of RTP crystals with different lattice spacings by ultrafast laser ablation process. The morphological and structural characterization of these diffraction gratings are analyzed by electron microscopy and X-ray diffraction analysis. The structural modifications of as-fabricated, annealed and chemically etched diffraction gratings are analyzed by Raman scattering.

Key words: Ultrafast laser ablation, Raman scattering, diffraction gratings, $RbTiOPO_4$

Since the earliest work on laser interaction with materials, femtosecond lasers have become a significant tool for micromachining of materials to fabricate waveguides [1], gratings [2], or optical data storage systems [3], among others.

Ultrafast lasers provide extremely short, high intense pulses which cause nonlinear photoionization effects and subsequent avalanche ionization that lead to the generation of a free-electron plasma in transparent dielectrics. When the density of the free electrons exceeds a certain threshold, enough energy is absorbed to produce macroscopic ablation [4]. The advantages of ultrafast laser ablation compared with other methods of micromachining, such as mechanical machining, electron- or ion-beam patterning and lithographic techniques, are that it can provide surface modification, such

as surface relief formation, or modification of refractive indices in transparent solids, with a reduced heat affected area, high speed and a non-contact nature [5]. Thus, femtosecond laser ablation has become increasingly important in the last few years owing to the large amount of practical applications and the variety of materials that can be processed, including surface modification of metals [6], polymers [7], semiconductors [8], and transparent materials [9]. Particularly, ultrafast laser ablation is a very promising method for the micro-structuration of wide band gap or hard dielectric materials which is difficult to obtain from other techniques [10].

Nonlinear optical materials are highly attracting targets for femtosecond laser processing because of their non vanishing nonlinear optical susceptibility $\chi^{(2)}$ modulation, and that can be used in frequency conversion for the potential applications in photonics [11]. These microstructured nonlinear optical materials could provide simultaneous control over the intensity, wavelength and spatial distribution of the generated frequency [12]. Up to now a few studies have been devoted to investigate these effects in micro-structured nonlinear optical materials such as KH_2PO_4 (KDP) [11], $LiNbO_3$ [14], β-BB_2O_4 [15, 16], $LiTaO_3$ [16], and more recently $RbTiOPO_4$ (RTP) [17] by ultrafast laser ablation. From these microstructured nonlinear optical materials, it has been reported that the multiple non-collinear second harmonic beams and controlled non-collinear fundamental laser beam propagation without the requirement of additional elements such as external diffraction gratings can be achieved. The micro-structured nonlinear optical materials could extend their possibilities as multi frequency self converter systems particularly in the field of telecommunications.

However, ultrafast laser ablation can also induce structural stress in these materials after the tight focusing of ultra-short intense pulses that might affect their properties. During femtosecond irradiation, very high transient temperatures in the

electron subsystem are induced. During laser pulse, the electron pressure could become dominant over the elastic pressure, initiating material expansion, and when it is stronger than the binding force, then ablation occurs. Although material ablation only takes place in the region were the beam has been focused, the surrounding material might be also affected by the shock waves produced by the femtosecond pulse. These shock waves can induce permanent structural modification of microsized dimensions that can result in and internal stress of the material [18]. The development of these internal stresses is often influenced by permanent strain resulting from the association of thermal treatment and penetration of ultra-short intense pulses through the material [19].

The stress and structural changes generated in a material can be investigated by Raman scattering [20], among other techniques. Raman scattering has proved to be a very efficient technique for structural characterization of materials, mainly because it is not destructive, its implementation is easy, it is fast and it does not require sample preparation [21]. The Raman scattered light contains information about the atomic lattice vibrations (phonons) that are selectively modified when the material is submitted to a mechanical stress. Thus, Raman scattering can allow obtaining a quantitative description of the spatial distribution of the shock wave induced permanent stress under different conditions such as pulse length and pulse energy, providing in this way additional information about the light-matter interaction during the ablation process [18]. This makes of Raman scattering one of the most effective tools for strain determination in a wide range of materials. By using micro-Raman (μ-Raman) scattering, we can establish a map of strain in the irradiated structures with a spatial resolution down to the submicrometer [22, 23].

RTP belongs to the large family of isostructural compounds to $KTiOPO_4$, that crystallize in the orthorhombic system with the $Pna2_1$ space group of symmetry [24].

These crystals are well known due to their excellent nonlinear optical properties [25, 26]. The linear and nonlinear optical properties of RTP crystals are very similar to those of KTP [27] but it is more preferable in some practical applications such as high repetition rate electro optic modulators [28], and applications that benefit from the higher laser damage threshold of RTP in front KTP [29].

In this paper, we characterized the effects that ultrafast laser ablation, under different conditions, generate in the structure of RTP single crystals using μ-Raman scattering. A layer of polycrystalline RTP has been observed to deposit on the structures generated on the surface of RTP single crystals by ultrafast laser ablation, creating a rough surface on the ablated areas. By thermal annealing, this polycrystalline RTP layer could be transformed into polycrystalline TiO_2 in the form of anatase, although a small part of rutile was also observed. By selective chemical etching, the polycrystalline RTP layer could be removed, smoothing the surface of the ablated structures and allowing to analyze the structural stress generated during the ultrafast laser ablation process.

Experimental techniques

Crystal growth.

RTP melts incongruently at 1443 K, so it cannot be grown by melting methods and it has been traditionally grown by high temperature solution techniques, such as by the Top-Seeded Solution Growth (TSSG) method [30]. Around 140 g of solution were prepared in a platinum cylindrical crucible of 125 cm^3 by mixing the desired ratios of corresponding oxides (Rb_2O-TiO_2-P_2O_5-WO_3 = 42.24-16.80-18.96-20 mol%). The crystals were grown from WO_3 containing fluxes to reduce the viscosity of the flux [31]. The solution was homogenized at 50-100 K above the crystallization temperature. RTP crystals were grown on ***c***-oriented crystal seeds. We determined the saturation

temperature of the solution by observing the growth or dissolution of the crystalline seed in contact with the surface of the solution. During the growth, the crystal seed was rotated at an angular speed of 45 rpm. We decreased the temperature of the solution by 20 K from the saturation temperature at a cooling rate of 0.1 $K.h^{-1}$, to activate the growth process. At the end of the crystal growth process, the crystal was completely extracted from the solution and slowly cooled to room temperature inside the furnace.

To prepare the samples for microstructuring by ultrafast laser ablation, the single crystals obtained were cut and polished in a crystallographically oriented manner. First, the samples were cut with the correct crystallographic orientation to obtain a surface perpendicular to the ***c***-crystallographic direction by placing them on a goniometer coupled to a Struers Accutom-50 diamond saw. As a reference to correctly orient the crystals, we used their morphology. Finally, the samples were polished in a Logitech PM5 polisher with an oscillatory arm. This enables accurately rotate and pressurize the samples depending on the hardness of the material to be polished. As abrasive substances, alumina powders with a grain size of 9, 3, 1, and 0.3 μm were used sequentially. At the end of the process we verified the correct crystallographic orientation of the sample by X-ray diffraction using a Bruker-AXS D8-Discover diffractometer equipped with parallel incident beam (Göbel mirror), vertical θ-θ goniometer, XYZ motorized stage and a General Area Diffraction Detection System (GADDS) HI-STAR detector. For the measurements we used Cu Kα radiation. The X-ray diffractometer was operated at 40 kV and 10 mA. We collected 2D X-ray diffraction patterns covering a range of 2θ between 5-85º at a distance of 15 cm from the sample. The exposure time was 10 s per frame.

A Sensofar PLμ 2300 interferometric confocal microscope and a self-collimator were used to measure the quality of the polishing using parameters such as roughness, flatness and parallelism between opposite faces of the sample. Under these conditions we fabricated a sample with a surface of 4 x 3 mm^2 perpendicular to the ***c***-crystallographic direction, with a roughness of 50 nm and a flatness of 14 m.

Ultrafast laser ablation.

Two different arrays of channels have been fabricated on the (001) surface of RTP single crystals by ultrafast laser ablation using a commercial Ti:Sapphire oscillator (Tsunami, Spectra Physics) and a regenerative amplifier system (Spitfire, Spectra Physics) based on chirped pulsed amplification (CPA). The laser system delivers linearly polarized 120 fs pulses at 795 nm with a repetition rate of 1 kHz. The transverse mode of the beam was TEM_{00} and the width was 9 mm ($1/e^2$ criterion).

The RTP samples were placed on a motorized XYZ translation stage that allowed achieving optical focusing on the surface of the target, with the (001) face of the samples perpendicular to the laser beam. The threshold fluence depended on the number of pulses per spot, resulting 1.44 ± 0.18 $J.cm^{-2}$ for 40 pulses and decreasing to 1.18±0.15 $J.cm^{-2}$ for multi-shot conditions (>100 pulses) giving an incubation factor ξ = 0.783 [32].

We prepared two different samples. RTP1 was prepared focusing the laser beam by means of a 50 mm achromatic lens using a pulse energy of 0.78 μJ, which provided a peak fluence of ~6.1 $J.cm^{-2}$ at focus. The sample was moved following straight lines parallel to the ***b*** crystallographic axis and all across the surface, at a constant scanning speed of 130 $\mu m.s^{-1}$, avoiding the iterative passes along the same line. The pitch between the lines was set to 15 μm. For that scanning speed and focusing conditions the

number of pulses contributing to the ablation of a point within the sample surface was approximately 40, thus the peak fluence used was well above the threshold fluence.

For the other sample, RTP2, the focusing optics was a 10× (0.22 NA) microscopic objective. A 6 mm diameter circular aperture was placed before the objective in order to slightly increase the spot size at focus. The pulse energy before the aperture was 0.27 μJ leading to peak fluence at focus of ~3.2 $J.cm^{-2}$. The writing procedure was identical than for RTP1 and the scanning speed was set to 75 $\mu m.s^{-1}$ with a separation between lines of 10.5 μm and 9.5 μm, alternatively. Under these conditions, the number of pulses contributing to the ablation of a point within the sample surface was around 55, and again, the peak fluence used was more than double the threshold fluence.

Morphological characterization.

Micrographs of the samples were recorded in a FEI QUANTA 600 Environmental Scanning Electron Microscope (ESEM) on top and lateral views to investigate the structures formed by ultrafast laser ablation. An ESEM is very similar to standard SEM and it has adequate performance compared with the SEM system. In this ESEM system, wet, oily, and non conductive samples can be analysed in their natural state without any prior preparation. One main advantage of using ESEM is without having to coat non-conductive samples with conducting media such as gold or silver can be examined. Moreover, it also offers high resolution secondary electron imaging in gaseous environment.

Thermal annealing.

A thermal treatment process was carried out on the RTP1 sample consisting on a heating step from ambient temperature to 1173 K at a heating rate of 15 Kh^{-1}, a

themalization step at 1173 K for 5 h, and finally a cooling step to room temperature at 15 Kh^{-1}, to avoid thermal stresses in the sample.

Chemical etching.

Chemical etching is one of the easiest and more widely applied techniques to reveal ferroelectric domain structures in crystals of the KTP family. In particular molten $KOH:KNO_3$ mixtures have been extensively studied for this purpose in this family of materials since it etches the negative $(00\bar{1})$ face of the crystal, while the positive (001) face rests relatively unetched. We explored the possibilities of using chemical etching to smooth the roughness generated by the ultrafast laser ablation process and at the same time analyze the possibilities of removing the polycrystalline layer of RTP deposited during the ultrafast laser ablation process.

We performed the chemical etching process by dissolving a mixture of $KOH:KNO_3$ 2:1 molar ratio in distilled water at 353 K, and immersing the RTP2 sample at different time intervals between 5 min to 1 h in this solution.

Micro-Raman scattering.

Micro-Raman (μ-Raman) scattering was used to analyze the effects of ultrafast laser ablation on the structure of RTP at a local level. μ-Raman scattering measurements were carried out using a μ-Raman system Reinshaw confocal InVia spectrometer equipped with a confocal microscope Leica 2500 and a CCD camera as detector. The radiation of an Ar laser (λ=514 nm and 25mW) was focused by a 100× long working distance microscopic objective on the surface of the samples. A back scattering scheme was used to detect the Raman signal through a confocal hole, allowing the extraction of the light scattered from an extremely small region of the sample with a resolution of about 0.5 μm. Approximately 75 measurements were recorded for each sample along the surface, edge, and the depth of the channels.

Results and discussions

Figure 1 present's top and lateral views of the grooves inscribed in RTP1 and RTP2 samples by ultrafast laser ablation. The width and depth of the grooves depended on the ablation parameters used in each case, such as laser fluence, pulse energy and focusing conditions of the laser beam. In the case of RTP1, grooves are wider than those fabricated in RTP2. The width of the grooves in RTP1 was 5.0 ± 1.5 μm, while in RTP2 the width of the grooves was 3.3 ± 0.5 μm. This is due to the fluence distribution (basically an Airy function) on the surface of the samples. From Figures 1 (a) and (c), it is evident that the roughness of the grooves inscribed on the surface of the samples is

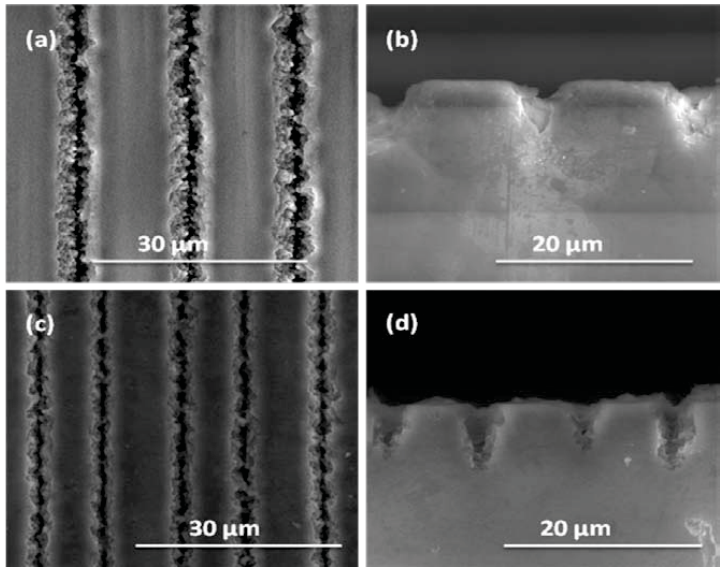

Figure. 1. SEM images of the grooves inscribed by ultrafast laser ablation on the (001) surface of RTP single crystals: (a) top view and (b) lateral view of the grooves inscribed on the surface of the RTP1 sample; (c) top view and (d) lateral view of the grooves inscribed on the surface of the RTP2 sample.

different, those inscribed on the RTP1 sample (Figure 1(a)) present a higher roughness than those inscribed on the RTP2 sample (Figure 1(c)). Thus, using a lower peak

fluence at focus and a slower scanning speed we can reduce the roughness generated on the ablated regions.

The lateral views of the grooves show that those structures present a V-shape in both cases. From Figures 1 (b) and (d), we can observe that the depths of the grooves are different depending of the ablation conditions used, which resulted in a depth of ~5 μm for RTP1, while two different depths have been observed on RTP2, ~4.5 and ~6 μm, respectively.

A complete analysis of the possible structural modifications in the ablated areas of the samples was carried out by recording the μ-Raman spectra on the ablated and unablated regions of the samples. The obtained results for RTP1 and RTP2 samples are shown in Figure 2, plotted as a function of distance along the surface covering ablated and unablated areas. In this figure it is clear the existence of a change in the intensity of some Raman peaks in the ablated and unablated areas.

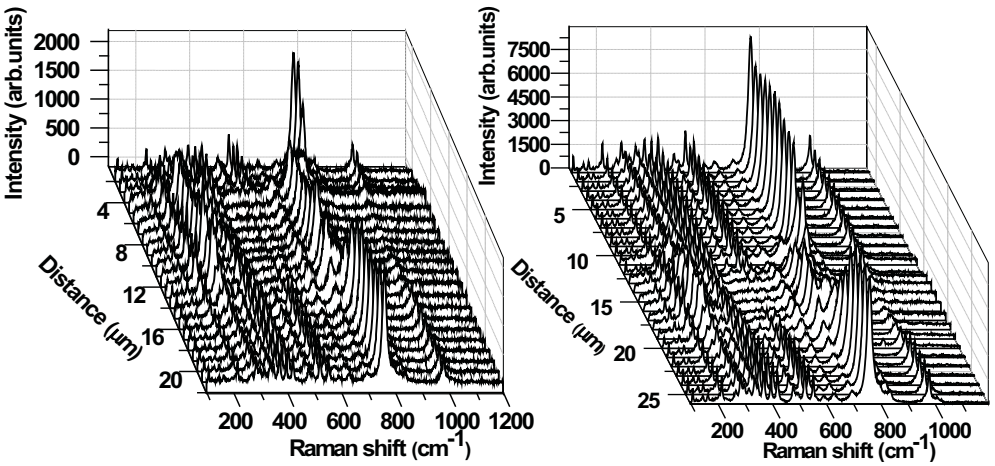

Figure 2. 3D plot of Raman spectra as a function of the distance along the surface, covering ablated and unablated areas for (a) RTP1 and (b) RTP2 samples.

A more detailed study of the differences among the recorded spectra is shown in Figure 3(a). Two different spectra are observed, that one corresponding to the ablated areas, and the other one that corresponds to the unablated areas. The main differences between them are the change of the intensity of the peaks located at 758 cm^{-1} and 978 cm^{-1} that decrease in intensity in the ablated areas, while the peak located at 693 cm^{-1} increases its intensity in these areas.

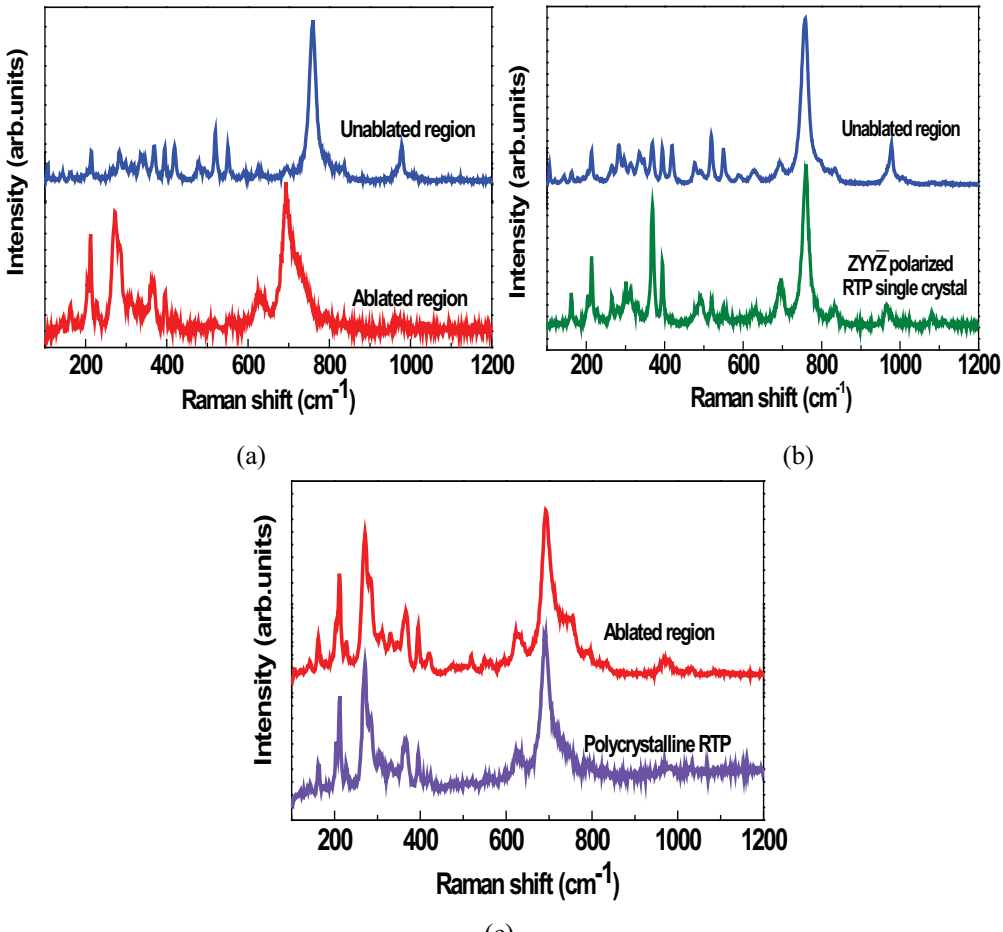

Figure 3. (a) Raman spectra recorded in the ablated and unablated areas of the RTP1 sample (b) Comparison of the Raman spectra recorded on the unablated areas with the $z(yy)\bar{z}$ polarized Raman spectra of RTP single crystals. (c) Comparison of the Raman spectra recorded on the ablated areas with the Raman spectra of polycrystalline RTP.

In general the Raman spectra of these materials are predominantly due to the vibrational motions of the TiO_6 octahedra and the PO_4 tetrahedra. [33]. The regions from 200 to 400 cm^{-1} and from 600 to 800 cm^{-1} are associated with torsional and stretching vibrational modes of TiO_6 octahedra, respectively [34]. The Raman bands in the 850 – 1200 cm^{-1} region are due to the three degenerate modes of PO_4 tetrahedra [33]. Thus, the changes observed in the spectra in the spectra affect both the TiO_6 and PO_4 groups.

The spectrum observed for the unablated region coincides with that recorded on a polarized $z(yy)\bar{z}$ configuration recorded for the RTP crystal, as can be seen in Figure 3(b). Instead, we observed that the spectra recorded for the ablated regions coincides with that of the polycrystalline RTP. Figure 3 (c) shows the comparison of the Raman spectrum recorded for powdered RTP with a grain size between 5 – 20 μm, and the Raman spectrum of the ablated regions in the single crystals. This result would indicate the formation of polycrystalline RTP in the ablated areas. The formation of polycrystalline RTP in these ablated areas might be related with the redeposition of material after the ablation process. This polycrystalline layer of RTP on the surface of the ablated areas could be formed by sublimation of the material and later condensation on the surface of the single crystal. During the ablation process we observed the ejection of high quantities of material, that with the configuration of the system we used, it can be deposited on the surface of the sample as debris. This polycrystalline layer could be part of the debris formed during the ablation process, but it is strongly attached to the surface of the grooves and could not be removed by mechanical means.

However, the most interesting aspect here is the mechanism of formation of this layer of polycrystalline RTP. As we commented in the Experimental Section, RTP melts incongruently, i.e. it decomposes before melting. Thus, the formation of polycrystalline

RTP could not be explained in terms of melting of the material and later solidification. Instead, the high energy provided by the ultrafast laser can directly sublimate the material that condensates later in colder parts of the single crystal. In fact this is the mechanism followed in the fabrication of nanoparticles of different materials by ultrafast laser ablation in a liquid environment [35]. This would be the first evidence that nanoparticles of RTP can also be formed by this mechanism, even when the material melts incongruently. In that case, since we do not use a liquid environment in which the nanoparticles can nucleate, they do it on the surface of the single crystal and they remain attached to it. This phenomenon however, was not observed in other non-linear optical materials structured by the same technique.

The change of intensity of the peak located at 758 cm^{-1} in the ablated and unablated areas allowed us to establish a profile of the area affected by the ultrafast ablation process around the ablated area. Figures 4 (a) and (b) show the intensity profile established by monitoring the change in intensity of the 758 cm^{-1} peak along 12 μm on the surface of both samples, covering in both cases ablated and unablated areas. As background in this graph we used a cross-section SEM image of the same area. As can be seen in the image, the area affected by the ablation process is wider than the ablated area in both cases. For the RTP1 sample, the profile obtained by Raman scattering is 1 μm wider at each side of the channel. This would indicate that it exist a layer of polycrystalline RTP with a thickness of ~1 μm at each side of the channel that has been deposited during the ablation process and that constitutes the important roughness observed at the edges of the grooves. Since Raman spectra were collected every 0.5 μm, this would coincide with the roughness determined from the SEM images recorded for this sample. Instead, for the RTP2 sample, the profile established from Raman scattering is more adjusted to the shape of the ablated groove. This would explain the

lower roughness observed for this sample in Figures 1 (c) and (d), although there is still a thin layer of polycrystalline RTP with a thickness of around 0.5 μm deposited on the grooves. Similar results were obtained when monitoring the intensity of the 693 cm^{-1} peak.

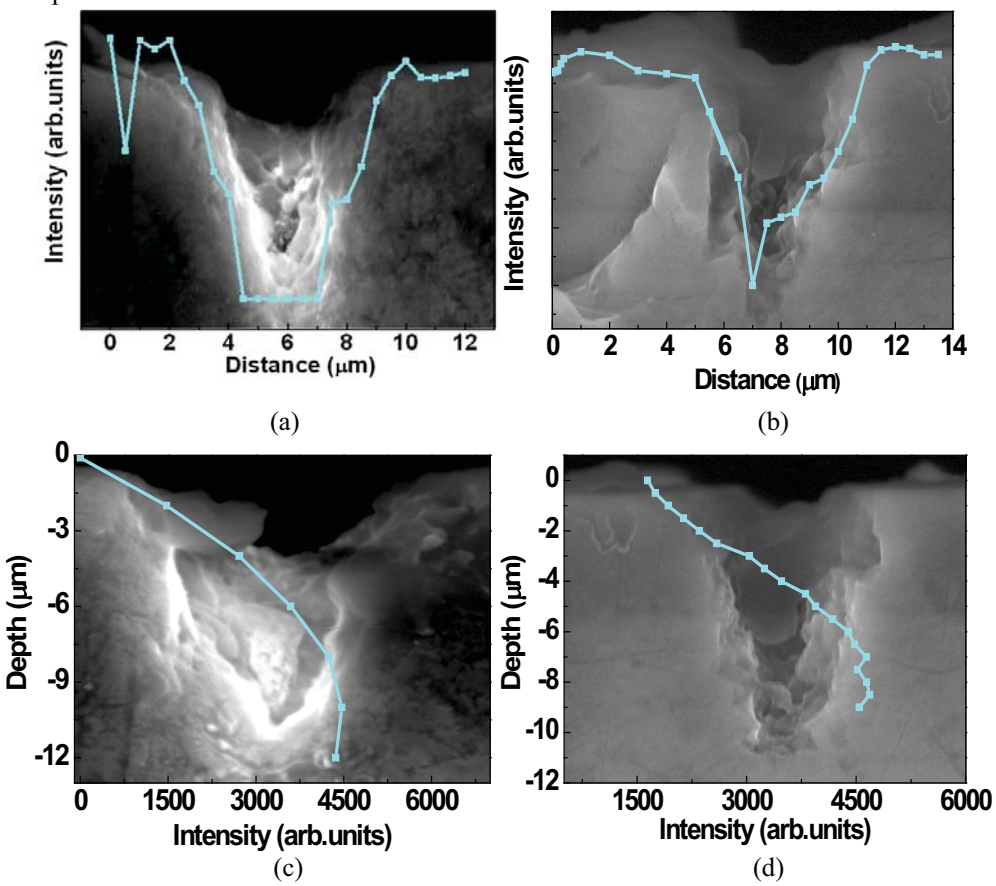

Figure 4. Variation of the intensity of the Raman peak located at 758 cm^{-1} along the surface for (a) the RTP1 and (b) RTP2 samples, and along depth for (c) the RTP1 and (d) RTP2 samples.

When we recorded the Raman spectra at different depths in the ablated and unablated areas we observed a similar situation. Two different Raman spectra were observed again: (i) that corresponding to the ablated areas that coincided with polycrystalline RTP, and (ii) that corresponding to the unablated areas, that coincided with the polarized Raman spectrum of RTP under the $z(yy)\bar{z}$ configuration. Thus,

again, by plotting the variation of the intensiy of the 758 cm^{-1} peak, we could establish a profile of the area affected by the ultrafast laser ablation that was still attached to the crystal. Figures 4 (c) and (d) show these profiles for the RTP1 and RTP2 samples together with SEM cross-section image of the channels inscribed by ultrafast laser ablation on the surface of the samples.

In Figure 5, according to the recorded Raman spectra along the depth, the affected area of the channels by ultrafast laser ablation is more than the area of the material removed. The recorded SEM images of the channels revealed that the depths of the channels were approximately 5 and 7 µm for RTP1 and RTP2 samples, respectively. The recorded intensity profiles by Raman scattering along the depth for RTP1 sample is around 1.05 µm and 1 µm for RTP2 sample at each side of the channels. The increasing of the depth inside the channels indicates that there exists a polycrystalline layer of RTP distribution around 2.75 µm and 1.25 µm for RTP1 and RTP2 samples, respectively, along the depth of the channels that has been redeposited while processing the channels by ultrafast laser ablation.

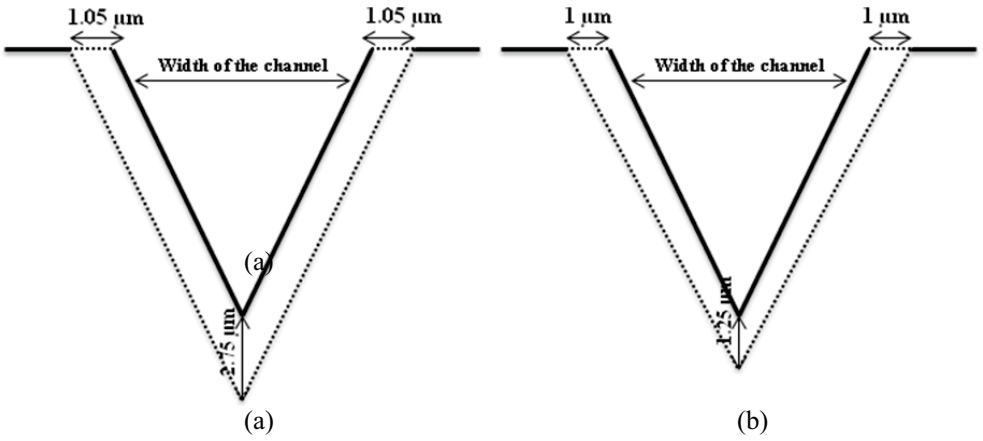

Figure 5: Schemes of the polycrystalline RTP layer formed around the ablated channels for the (a) RTP1 and (b) RTP2 samples, determined by Raman scattering.

These results allowed us to draw an scheme of the affected area of the material around the channel inscribed by ultrafast laser ablation, and that remained attached to the RTP single crystal as polycrystalline RTP material. Figure 5 shows these schemes for the RTP1 and RTP2 samples.

We explored the possibilities of removing this polycrystalline layer of RTP and the possible internal stresses generated by the ultrafast laser ablation process on the RTP samples by two different methods: (i) performing a thermal annealing of the sample and (ii) using chemical etching to selectively remove polycrystalline RTP without affecting the bulk crystal.

Thermal annealing can result in a relief of internal stresses, softening, chemical homogenizing and transformation of the grain structure into a more stable state. During thermal annealing atoms can move to more stable positions in the crystal lattice. Vacancies and interstitial defects can be eliminated and dislocations can be annihilated. To explore the effects of thermal annealing on the samples, the RTP1 sample was annealed for 5 h at 1173 K.

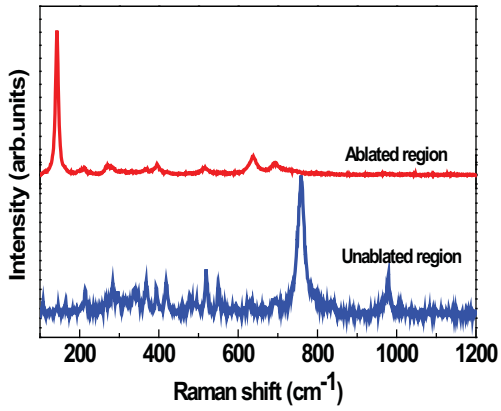

Figure 6. Raman spectra recorded at ablated and unablated regions of the RTP1 sample after performing a thermal annealing treatment at 1173 K for 5 h.

Then, we recorded again Raman scattering spectra at the ablated and unablated regions of the sample. The results are shown in Figure 6.

When this figure is compared to Figure 3(a), we can see that while the spectra recorded on the unablated areas are similar, the spectra recorded on the ablated regions are completely different. The peak located at 693 cm^{-1} is still present after the annealing process but it is not anymore the most intense peak of the spectrum, and it is replaced by a new peak at 638 cm^{-1}. Also, several new peaks with a medium intensity appear at 515, 394, 272 and 211 cm^{-1}. Although the peak located at 394 cm^{-1} could be related to the ν_2 vibration of the PO_4 group, we could not find any correlation for the other peaks in the vibrational structure of RTP.

Thus, we investigated if a new phase has been formed during the annealing process on the surface of the ablated channels. In fact, the new peaks located at 638 cm^{-1}, 515 cm^{-1} and 394 cm^{-1} correspond to the three main peaks of TiO_2 in its anatase form.

To confirm these results we recorded X-ray diffraction patterns on this area using a micro-X-ray diffractometer equipped with a 500 μm collimator, allowing us to analyze small regions of the sample. We recorded the diffraction pattern under specific conditions to avoid the diffraction of the (001) plane of the substrate, and maximizing in this way the contributions from the polycrystalline layer on the surface of the channels. After integrating the diffraction pattern for more than 3 hours, we were able to record some peaks corresponding to one or more crystalline substances, as can be seen in Figure 7. We identified these peaks corresponding to a mixture of TiO_2 in its forms of anatase and rutile, and a minority phase corresponding to polycrystalline RTP. The diffraction powder reference patterns for these substances from the JCPDS database: 00-021-1272 file for anatase, 01-086-0148 for rutile, 01-072-3660 file for RTP, are also included in the figure for a better identification of the diffraction peaks. The most

intense peak corresponds to anatase, indicating that this is the majority phase in the mixture, in agreement with the Raman spectra recorded, while RTP and rutile are present in a lower quantity.

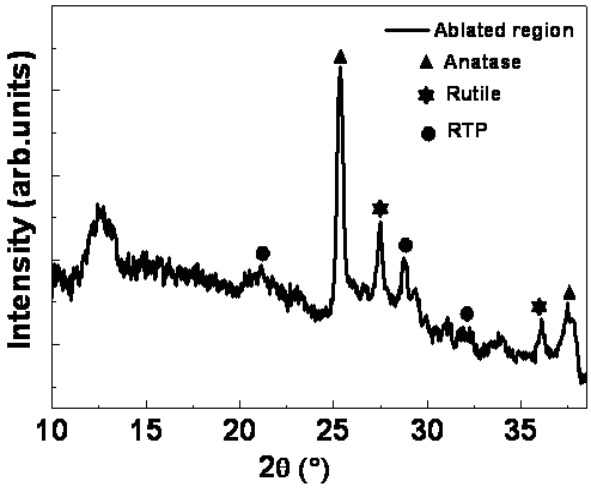

Figure 7. X-ray diffraction pattern obtained on the surface of the RTP1 sample. The reference patterns for anatase, rutile and RTP are also shown with a corresponding symbol for a better identification of the crystalline phases present in the sample.

The presence of TiO_2 is not surprising since it is one of the products formed during the decomposition of the RTP [36]. However, RTP usually decomposes at temperatures above 1300 K. Then, it is surprising that RTP starts to decompose in this case at a lower temperature (1173 K). This can be due to the process of formation of polycrystalline RTP in this case, by sublimation of the RTP single crystal and later condensation on the surface of the channels, that might modify its physical and chemical properties.

The stability of anatase is also one point that should be considered. The phase transition in TiO_2 from anatase to rutile usually happens at around 1073 K [37]. However, in particles of small sizes, surface free energy and surface stress play a crucial role in rendering the phase stability of anatase, that depending on the conditions can be stable

up to 1173 K, coexisting then with rutile [38]. This would coincide with the situation that we observed in our case. Then it seems possible that due to the lower temperature at which it happens the decomposition of RTP in this case, we can stabilize the anatase phase, while in our previous studies [36], we could only observe the formation of rutile, since the RTP decomposed at much higher temperatures.

In that case, by plotting the intensity of the peak appearing at 142 cm^{-1} in the Raman spectra we could analyze which is the thickness of the TiO_2 layer around the ablated and annealed grooves. Figure 8(a) shows the difference in intensity of this peak along the surface of the RTP1 sample after annealing, covering ablated and unablated areas. Figure 8(b) shows the same results but as a function of depth. In both cases we added as background for these profiles a SEM cross-section image of the sample after annealing for a better comparison of the real width of the grooves and the thickness of the TiO_2 layer surrounding them.

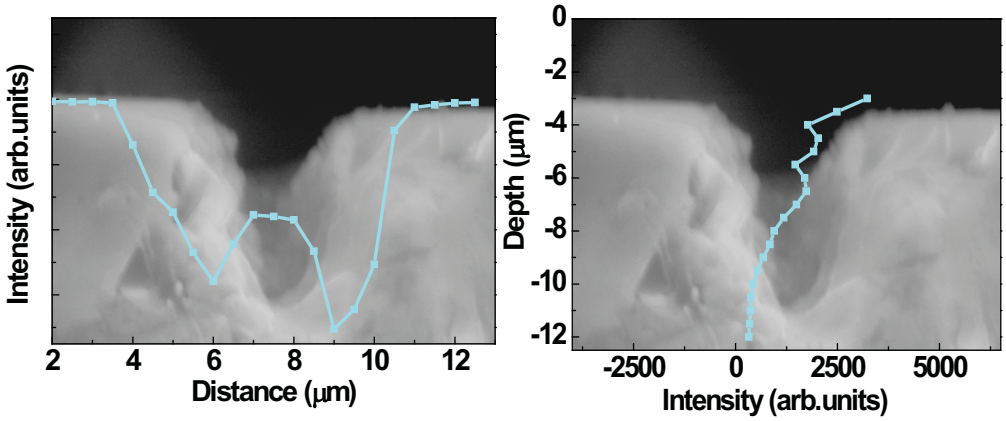

(a) (b)

Figure 8. Variation of the intensity of the Raman peak located at 142 cm^{-1} (a) along the surface and (b) along depth for the RTP1 sample.

In Figure 8, we observed that the width of the channels from the recorded profiles from Raman scattering spectra is more than the width of the channels determined from SEM images. The profile obtained by Raman scattering is 0.5 μm wider at each side of the

channel. This would realize that the surface roughness at the edges of the channels is increased due to the longer annealing time.

In Figure 8 , the difference in the intensity of the Raman peaks appeared at processed and unprocessed region along the depth of the channels of annealed sample establish a profile from the recorded Raman spectra. The profile of the obtained Raman spectra shows that the depth of the channels of annealed sample is more than the determined depth of the channels from SEM images. The recorded profile from Raman spectra shows the depth around 2 µm inside the channels.

These results allowed us to propose the following schematic view of the ablated grooves of the RTP1 sample after annealing (see Figure 9).

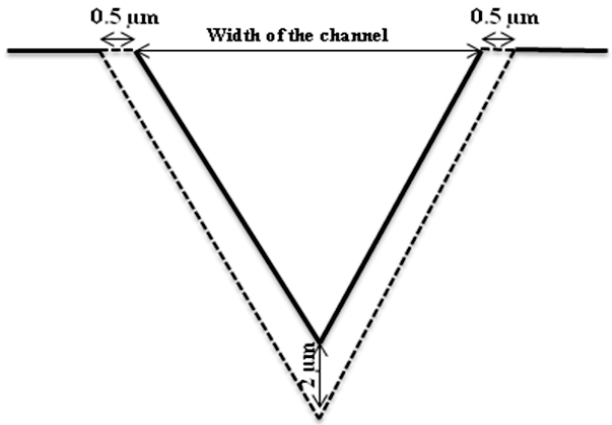

Figure 9. Schematic view of the distribution of polycrystalline layer of TiO_2 along the width and depth of the channels in the RTP1 sample after annealing.

From Figure 5(a) and Figure (9), it is observed that, the width of the channels was increased around 0.4 µm and the depth of the channels was increased up to 2 µm. These results indicate that the thickness of the TiO_2 formation around the channels after annealing process. Since thermal annealing did not reduce the roughness observed on the surface of the ablated grooves, we analyzed if it would be possible to remove the polycrystalline layer of RTP by a selective chemical etching process, and the influence that this process can have in reducing the roughness of the surface of the ablated

channels. To do that, we etched the surface of the RTP2 sample with a mixture of $KOH:KNO_3$ dissolved in distilled water at 353 K and during different time intervals from 5 min to 1 h. Although this mixture has been used specially to reveal ferroelectric domains in crystals of the KTP family, we expect that this etchant can etch more selectively polycrystalline RTP than the rest of the bulk crystal. In this way we would remove the layer of polycrystalline RTP deposited by the ultrafast laser ablation process on the surface of the ablated channels, and reduce then the roughness observed on these channels, without affecting the rest of the sample.

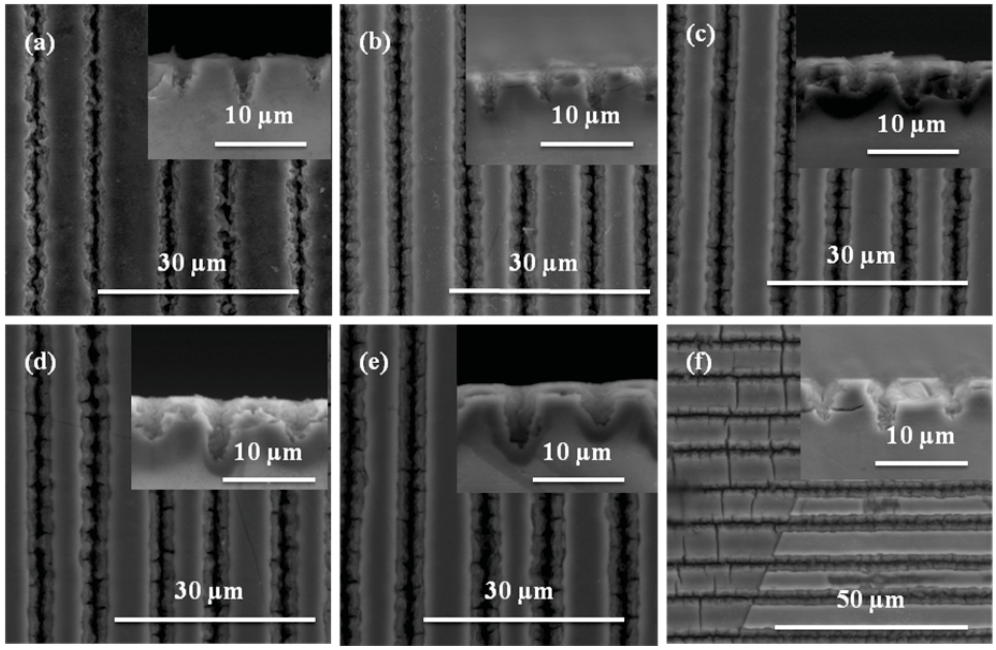

Figure 10. SEM images (top view and cross-section) of the RTP2 sample after chemical etching at different time intervals. (a) 0 min (b) 5 min (c) 10 min (d) 15 min (e) 30 min (f) 1 h ; inset figure represents the cross view image of corresponding image at different etched time.

During the process and after each etching period, we analyzed how the morphology of the fabricated channels changed by recording SEM images and recorded Raman spectra of the ablated and unablated areas to follow the evolution of the

polycrystalline RTP layer. We observed that between 5 and 15 minutes of etching, the roughness of the channel walls reduced significantly, as can be seen in Figure 10. After that, we did not observe a further improvement on the roughness of the surfaces but instead, we observed a widening of the channels, and for etching times higher than 30 min we started to observe the ferroelectric domain structure on the surface of the sample, revealing that this sample was not constituted by a single ferroelectric domain. Comparing this last image with the initial one of the sample prior to the etching process (see Figure 1(c)), we could not observe any difference in the grooves ablated in areas corresponding to different ferroelectric domains, indicating that the ultrafast laser ablation process is effective for both ferroelectric domain types.

In order to understand structural changes in the chemically etched RTP2 sample, we recorded the Raman spectra at ablated and unablated regions of the sample. The results are shown in Figure 11. This figure shows that the Raman peaks that appear in the spectra recorded for ablated and unablated areas are located at the same positions (see Figure 11(a)), indicating that the RTP polycrystalline layer has been removed. Thus, the reduction of the roughness of the edges of the grooves that we observed on the

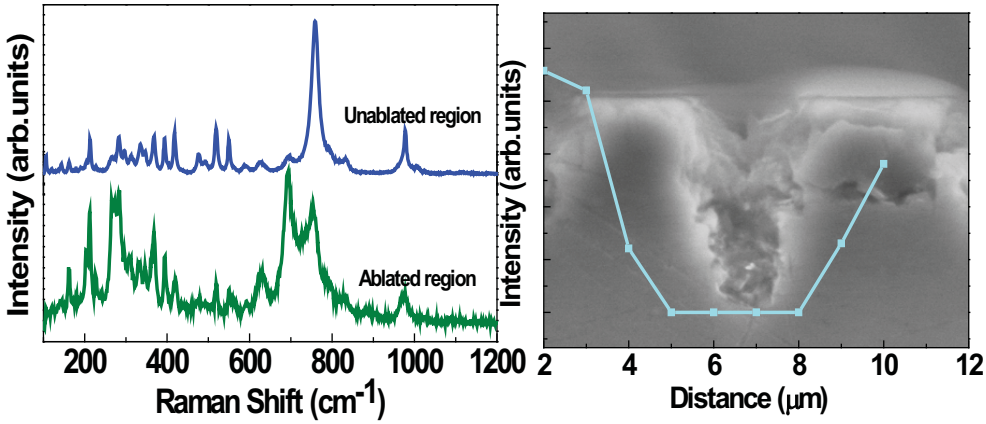

(a) (b)

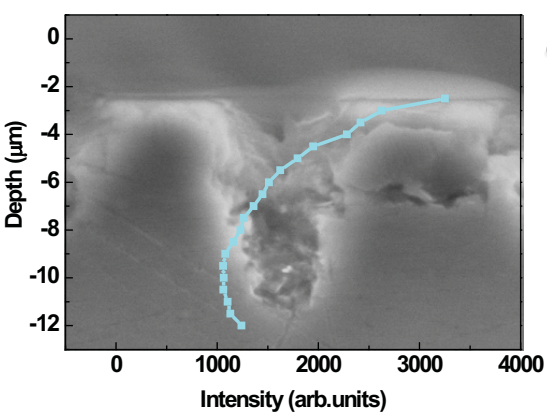

(c)

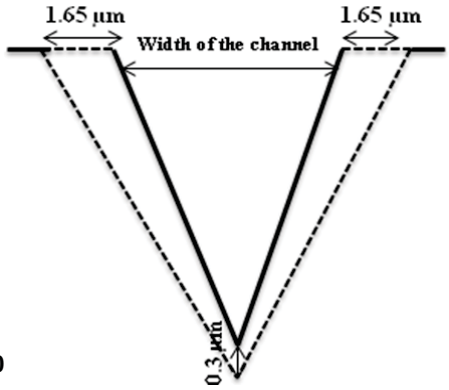

(d)

Figure 11. (a) Raman spectra recorded at ablated and unablated areas of the RTP2 sample after chemical etching (the spectra should be shifted in height). Intensity profiles of the peak located at 758 cm^{-1} (b) along the surface and (c) along depth for this sample. (d) Schematic view of the distribution of structural stress on the sample.

SEM images is associated with the removal of the RTP polycrystalline layer, indicating that this polycrystalline layer was responsible for the roughness observed in the ablated areas.

However, the slight increase in intensity of the peak located at 693 cm^{-1} in the ablated region and the slight decrease of intensity of the 758 cm^{-1} peak, indicate some orientational changes in the crystal structure in the areas in the proximity of the ablated region. These orientational changes lead to a mixture of Raman spectra corresponding to different scattering geometries [39]. In fact, a more detailed analysis of the origin of the 693 cm^{-1}, reveals that this signal is related to the ν_2 vibration mode of the TiO_6 octahedron in the $z(yy)\bar{z}$ polarized Raman spectrum of RTP [40]. However, it is also related to the ν_1 and ν_3 vibration modes of the TiO_6 octahedron in the $x(yz)\bar{x}$, $y(xx)\bar{y}$, and $y(zz)\bar{y}$ polarization configurations for the same crystal, where it corresponds to the most intense peak of these spectra. Thus, apart from the deposition of a polycrystalline layer of RTP on the surface of the ablated channels, ultrafast laser ablation induces a

permanent local stress of micrometric dimension produced by the shock waves generated during the femtosecond pulse [39, 41]. This induced permanent local stress was probably present in the samples all the time, but it was masked by the presence of the polycrystalline RTP layer.

Then, similarly to what we did with the Raman spectra corresponding to the polycrystalline RTP layer, we used the change of intensity of the peaks located at 758 cm^{-1} at the ablated and unablated regions of the sample to obtain the profile of the area affected by this permanent local stress around the ablated channel. This profile is shown in Figure 11(b) as a function of the distance on the surface, while Figure 11(c) shows the same profile as a function of depth.

The obtained width of the etched channels from Raman scattering spectra is around 3.3 μm and the width of the etched channels is 1.65 μm at each side of the channels. This analysis revealed that even though the polycrystalline layer was completely diminished, the width of the channels was increased by etching process.

Acknowledgements:

This work was supported by the European Union under the Seventh Framework Programme under project Cleanspace, FP7-SPACE-2010-1, the Spanish government under projects, PI09/90527, TEC2010-21574-CO2-02, MAT2011-29255-C02-02 and by the Catalan government under project 2009SGR235.

References:

[1]. K.bMiura, J. Qiu, H. Inouye, T. Mitsuyu, and K. Hirao, Appl. Phys. Lett. 71, (1997) 3329.

[2]. P.J.Scully, D. Jones, D.A.Jaroszynski, J.Opt.A, 5, (2003) S92.

[3]. E.N.Glezer, M. Milosavljevic, L. Huang, R. J. finlay, T.H. Her, J. P. Callan, E. Mazur, Opt. lett. 21, (1996) 2023.

[4]. J.R.Vazquez de Aldana, C. Mendez, and L. Roso, Opt. Exp. 14, (2006) 1329.

[5]. M.D. Perry, B.C.Stuart, P.S. Banks, M.D. Feit, V. Yanovsky, and A.M. Ruben chick, J. Appl. Phys., 85, (1999) 6803-6810.

[6]. M.Feuerhake, J. H. Klein-Wiele, G. Marowsky, P. Simon, Appl. Phys. A. 67 (1998) 603.

[7]. S. Kuper and M. Stuke, Appl Phys. Lett. 54, (1989) 4.

[8]. G. Herbst, M. Steiner, G. Marowsky, and E. Matthias, Mater. Res. Soc. Symp. Proc. 397, (1996) 69.

[9]. K. Kawamura, T. Ogawa, N. Sarukura, M. Hirano, and H. Hosono, Appl. Phys. B, 71, (2000) 119.

[10]. I.H. Chowdhury, A.Q. Wu, X. Xu, Am. Weiner, Appl. Phys. A 81, (2005) 1627-1632.

[11]. B. Yu, P. Lu, N. Dai, Y. Li, X. Wang, Y. Wang, and Q. Zheng, J. Opt. A. Pure Appl. Opt. 10, (2008) 35301.

[12]. J. Lamela, A.Rodenas, D. Jaque, and F. Jaque, G.A. Torchia, C. Mendez ç and L.Roso, Opt.Express. 15, (2007) 3285.

[13]. C. Mendez, J. R. Vazques de Aldana, G. A. Torchia, and L. Roso, , Opt. lett. 30, (2005) 2763.

[14]. . G.A. Torcha, C. Mendez, I. Arias, L.Roso, A. Rodenas, D. Jaque, Appl. Phys. B. 83, (2006) 559,.

[15]. Y.Li, P. Lu, N. Dai, X. Wang, Y. Wang, B. Yu, and H. Long, Appl Phys. B 88, (2007) 227.

[16]. Y. Zhang, X. Chen, H. Chen, Y.Xia, App. Surf. Sci. 252, (2007) 8874.

[17]. G. Raj Kumar, J.J. Carvajal, M.C. Pujol, X. Mateos, J. Grau, J. Massons, J.R. Vázquez de Aldana, C. Mendez, P. Moreno, L. Roso, J. Ferre-Borrul, J. Pallares, L.F. Marsal, M. Aguiló, and F. Díaz, Opt. Mater. 34, (2011) 207214.

[18]. A. Rodenas, J.A. Sanz García, D. Jaque, G.A. Torchia, C. Mendez, I. Arias, L. Roso, F. Agulló-Rueda, J. Appl. Phys. 100 (2006) 033521.

[19]. Y. Bellouard, T. Colomb, C. Depeursinge, A. A. Said, M. Dugan, P. Bado, Proc. SPIE, 6108-21, (2006) 1-9.

[20]. R. Ossikovski, Q. Nguyen, G. Picardi, J. Schreiber, J. Appl. Phys. A 103, (2008) 93525.

[21]. Raman Scattering in Material science, Springer Series in Material science, 42, Springer verlog, Berlin, (2000).

[22]. . F. Dombrowski, I. De Wolf, and B. Dietrich, Appl. Phys. Lett. 75, (1999) 2450.

[23]. V. Poborchii, T. Tada, and T. Kanayama, Appl. Phys. Lett. 89, (2006) 233505.

[24]. P.A. Thomas, S.C. Mayo, B.E. Watts, Acta. Crystallogr. B48, (1992) 401.

[25]. R. Masse, J.C. Grenier, Bull. Soc. Fr. Mineral Crystallogr, 94, (1971) 437.

[26]. G.D.Stucky, M.L.F. Phillips, T.E. Gier, Chem. Mater. 1, (1989) 492.

[27]. M.V.Pack, D. J. Armstrong, and A.V. Smith, Appl. Opt. 43, (2004) 3319.

[28]. E. Lebiush, R. Lavi, Y.Tsuk, N. Angert, A. Gachechiladze, M. Tseitlin, A. Zharov, M. Roth, Advanced solid state lasers, 2000.

[29]. D. N. Nikogosyan, Nonlinear optical crystals A complete Survey, Springer, Berlin, 2005.

[30]. L.K. Cheng, J.D. Bierlein, A.A. Ballman, J.Crystal Grwoth, 110, (1991) 697.

[31]. J.J. Carvajal, V. Nikolov, R. Solé, Jna. Gavaldà, J. Massons, M. Rico, C. Zaldo, M. Aguiló, F. Díaz, Chem. Mater. 12, (2000) 3171.

[32]. S. Baudach, J. Bonse, J. Kruger, and W. Kautek, Appl. Surf. Sci. 555 (2000) 154.

[33]. G.E. Kugel, F. Bréhat, B. Wyncke, M.D. Fontana, G. Marnier, C. Carabatos-Nedelec, J. Mangin, J. phys. C: Solid State Phys., 21, (1988) 5565.

[34]. B. Mohamadou and G.E. Kugel, Phys. Stat. Sol (b) 195, (1996) 97.

[35]. M.Glaceran, M.C.Pujol, M. Aguilo, F.Diaz, J.Sol-gel Science and Tech. 42 (2007) 79-88.

[36]. J.J. Carvajal, R. Solé, Jna. Gavaldà, J. Massons, F. Díaz, M. Aguiló, Chem. Mater. 15 (2003) 2730.

[37]. P.S. Ha, H.J. Youn, H.S. Jung, K.S. Hong, Y.H. Park, K.H. Ko, J. Colloid Interf. Sci. 223 (2000) 16.

[38]. Y. Djaoued, S. Badilescu, P.V. Ashrit, D. Bersani, P.P. Lottici, J. Robichaud, J. Sol-gel Sci. Technol. 24 (2002) 255.

[39]. A. Rodenas, J.A. Sanz García, D. Jaque, G.A. Torchia, C. Mendez, I. Arias, L. Roso, F. Agulló-Rueda, J. Appl. Phys. 100 (2006) 033521.

[40]. J.J. Carvajal, P. Segonds, A. Peña, J. Zaccaro, B. Boulanger, F. Díaz, M. Aguiló, J. Phys.: Condens. Matter 19 (2007) 116214.

[41]. M.S. Anzer, M.A. El-Ashry, L.R. Dosser, K.E. Hix, J.F. Maguire, B. Irwin, Appl. Surf. Sci. 162 (2005) 242.

UNIVERSITAT ROVIRA I VIRGILI
MICROSTRUCTURATION OF NONLINEAR OPTICAL MATERIALS:
METHODOLOGIES, CHARACTERIZATION, AND APPLICATIONS
Raj Kumar Golconda
Dipòsit Legal: T. 55-2013

UNIVERSITAT ROVIRA I VIRGILI
MICROSTRUCTURATION OF NONLINEAR OPTICAL MATERIALS:
METHODOLOGIES, CHARACTERIZATION, AND APPLICATIONS
Raj Kumar Golconda
Dipòsit Legal: T. 55-2013

Paper VIII

Interparticle energy migration-mediated upconversion in oxide nanoparticles

Joan Josep Carvajal, Raj Kumar Golconda, Maria Cinta Pujol, Xavier Mateos, Maria de la O Ramírez, Luisa Bausá, Marco Bettinelli Magdalena Aguiló, Francesc Díaz

Advanced Materials (to be submitted)

UNIVERSITAT ROVIRA I VIRGILI
MICROSTRUCTURATION OF NONLINEAR OPTICAL MATERIALS:
METHODOLOGIES, CHARACTERIZATION, AND APPLICATIONS
Raj Kumar Golconda
Dipòsit Legal: T. 55-2013

Submitted to ADVANCED MATERIALS

DOI: 10.1002/adma.((please add manuscript number))

Interparticle energy migration-mediated upconversion in oxide nanoparticles

By *Joan Josep Carvajal**, *Raj Kumar Golconda*, *Maria Cinta Pujol*, *Xavier Mateos*, *Maria de la O Ramírez, Luisa Bausá*, *Marco Bettinelli*, *Magdalena Aguiló*, and *Francesc Díaz*

In the last years, lanthanide (Ln)-doped luminescent nanoparticles have converted in versatile targets for many different research areas, such as bioimaging,[1] biological labeling[2], solar energy conversion,[3] color display[4], optoelectronics[5], sensor technology[6], and data storage[7], among others.

Upconversion (UC) luminescent nanoparticles are a particularly interesting class of these Ln-doped luminescent nanoparticles, that allow convert long wavelength excitation radiation into short wavelength output radiation, attracted the interest of many scientists in the fields of physics, chemistry, and materials and life sciences because of their broad potential applications. The mechanism of UC, proposed initially by Bloembergen in 1959[8], and discovered in the mid-1960s by Auzel[9], primarily originates from intra-configurational $4f^n$ electron transitions within the localized Ln dopant ions. UC is a process in which the sequential absorption of two or more photons in the near infrared (NIR) lead to the emission of light in the visible region of the electromagnetic spectrum, mainly through mechanisms of excited state absorption (ESA) or energy transfer upconversion (ETU) using physically existingintermediary energy states of Ln ions[10]. UC combines the benefits of high conversion efficiencies without the need for intense coherent excitation sources, with the advantages of large anti-Stokes shifts, sharp emission bandwidths, and long exited-state lifetimes.

However, efficient upconversion is generally restricted to Er^{3+}, Tm^{3+} and Ho^{3+} activators, characterized by ladder-like arranged energy levels essential for facilitating the successive photon absorption and energy transfer steps[11]. When co-doped with Yb^{3+}, the large absorption cross section of this ion allows for its use as a photosensitizer to overcome the difficulty associated with the rather smaller absorption cross section of Er^{3+}, Tm^{3+} or Ho^{3+} due to the dipole-forbidden nature of intra-4f transitions[11]. Thus, Er^{3+}-Yb^{3+} and Tm^{3+}-Yb^{3+} co-doped systems remain as the key constituents for the majority of UC materials for blue, green, and red UC luminescence.

Novel UC mechanisms have been ideated to overcome such a limitation, like the energy migration-mediated upconversion (EMUC)[12]. Here, a sensitizer ion (Yb^{3+}) is used to harvest pump photons and subsequently promote a neighboring accumulator ion (Tm^{3+}) to excited states. Then, a migratory ion (Gd^{3+}) extracts the excitation energy from high-lying energy states of the accumulator, followed by random energy hopping through the migratory ion sublattice and trapping of the migrating energy by an activator ion. One of the main benefits of choosing Gd^{3+} as the migratory ion is the relatively large energy gap between the $^8S_{7/2}$ ground state and the first excited state ($^6P_{7/2}$), higher than 3×10^4 cm^{-1}. This leads to minimized

J. J. Carvajal*, G. Raj Kumar, M. C. Pujol, X. Mateos, M. Aguiló, F. Díaz
Física i cristal·lografia de materials i Nanomaterials, Universitat Rovira i Virgili, Campus Sescelades, Marcel·li Doming, s/n, 43007 Tarragona, (Spain)
(*) Email: joanjosep.carvajal@urv.cat

M. O. Ramírez, L. E. Bausa
Departamento de Fisica de Materiales, Universidad Autonoma de Madrid, 28049 Cantoblanco Madrid, (Spain)

M. Brettinelli
Dipartimento Scientifico e Tecnologico, Universta de Verona and INSTM, Udr Verona, Ca´Vignal, Strada Le Grazie 15, I-37134 Verona, (Italy).

energy losses caused by multiphonon emission and cross-relaxation[13]. As a result, tunable UC emissions have been demonstrated for activators without long-lived intermediary energy states, such as Eu^{3+}, Dy^{3+} and Tm^{3+} in $NaGdF_4$[12]. The only restriction in this process is that to regulate energy exchange interaction between the accumulator and the activator, the sensitizer/accumulator and the activator have to be spatially confined in different spatial regions to eliminate deleterious cross-relaxation phenomena. Thus, core-shell structures or different particles have been used for this purpose. Here we investigate the possibilities of the interparticle EMUC mechanism in oxide systems. In particular, $KGd(WO_4)_2$ and Gd_2O_3 have been chosen as host materials for their probed efficiency in UC processes[14,15], their relatively low phonon energies (600 cm^{-1} phonon cut-off for Gd_2O_3[16], the benefit of the existing Gd^{3+} sublattice that can be used for fast energy migration, and the fact that the lowest excited level for this ions ($^6P_{7/2}$) is located in the UV spectral region, where most of the lanthanide ions have overlapping absorption bands. Two different kinds of nanoparticles where synthesized for these materials. The first ones were co-doped with Yb^{3+} (sensitizer) and Tm^{3+} (accumulator). The second ones were only doped with Eu^{3+} (activator). In this way we provided two spatially separated regions for the sensitizer/accumulator and the activator ions. We obtained efficient EMUC in Eu^{3+}:Gd_2O_3 nanoparticles. But instead of favouring the red emission at around 620 nm, as in the case of Eu^{3+}:$NaGdF_4$[12], here we observed an extraordinary enhancement of the emission at 675-735 nm corresponding to the $^5D_0 \rightarrow {}^7F_3, {}^7F_4$ observed in the case of transitions of Eu^{3+} . We also observed the total suppression of Tm^{3+}, a fact that was not even observed in the case of Eu^{3+}:$NaGdF_4$[12], indicating that the energy migration mechanism is more efficient in this oxide system. In Eu^{3+}:$KGd(WO_4)_2$ nanoparticles instead, the Eu^{3+} red emission had a very low intensity, and could not dominate the emission spectra in front of the blue and red emissions of Tm^{3+}. We correlated this behavior with the Gd^{3+}-Gd^{3+} interionic distance in these structures, since it seems that Gd^{3+}-Gd^{3+} energy transfer is dominated by exchange interaction[17]. We synthesized 45 at.% Yb^{3+} and 1 at. % Tm^{3+} doped Gd_2O_3, 10 at.% Yb^{3+} and 5 at. % Tm^{3+} doped $KGd(WO_4)_2$ nanoparticles, and 5 at. % Eu^{3+} doped Gd_2O_3 and $KGd(WO_4)_2$ nanoparticles by the modified sol-gel Pechini method[18]. We mixed Yb^{3+},Tm^{3+}:Gd_2O_3/Eu^{3+}:Gd_2O_3 and Yb^{3+},Tm^{3+}:$KGd(WO_4)_2$/Eu^{3+}:$KGd(WO_4)_2$ nanoparticles in four different ratios ranging from 1/0 to 1/8 in weight, and we recorded the emission spectra of the different blends of nanoparticles after excitation at 980 nm with a Ti:Sapphire laser to analyze the efficiency of the EMUC process in these systems. **Figure 1** shows representative SEM and TEM images of the luminescent nanoparticles as well as as the blends we prepared with them. While Yb^{3+}, Tm^{3+}:$KGd(WO_4)_2$ nanoparticles as well as the blends we prepared with them. While Yb^{3+},Tm^{3+}:$KGd(WO_4)_2$ nanoparticles show a shape with smooth edges and round forms and size around 100-120 nm (see Figures 1 (a) and (e)), Yb^{3+},Tm^{3+}:Gd_2O_3 nanoparticles show a more facetted morphology with smaller sizes of the order of 30-40 nm (see Figures 1 (b) and (f)). Since we used the same synthesis parameters (calcination temperature and time, basically) for these two systems, it seems that this methodology allows us to obtain smaller nanoparticles for simpler oxide systems. However, the Pechini sol-gel method is one of the most effective techniques to obtain nanoparticles of complex oxide structures.

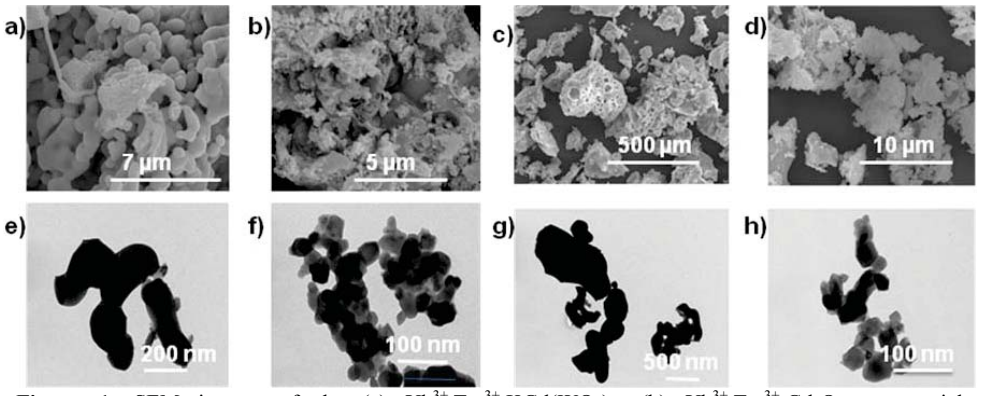

Figure 1. SEM images of the (a) Yb^{3+},Tm^{3+}:$KGd(WO_4)_2$, (b) Yb^{3+},Tm^{3+}:Gd_2O_3 nanoparticles, (c) Yb^{3+},Tm^{3+}:$KGd(WO_4)_2$/Eu^{3+}:$KGd(WO_4)_2$, and (d) Yb^{3+},Tm^{3+}:Gd_2O_3/Eu^{3+}:Gd_2O_3 nanoparticles mixed blends. TEM images of (e) Yb^{3+},Tm^{3+}:$KGd(WO_4)_2$, (f) Yb^{3+},Tm^{3+}:Gd_2O_3 nanoparticles, (g) Yb^{3+},Tm^{3+}:$KGd(WO_4)_2$/Eu^{3+}:$KGd(WO_4)_2$, and (h) Yb^{3+},Tm^{3+}:Gd_2O_3/Eu^{3+}:Gd_2O_3 nanoparticles mixed blends.

This is one of the main reasons why we have chosen this technique to synthesize the nanoparticles in this work.

After preparing the Yb^{3+},Tm^{3+}:$KGd(WO_4)_2$/Eu^{3+}:$KGd(WO_4)_2$ and the Yb^{3+},Tm^{3+}:Gd_2O_3/Eu^{3+}:Gd_2O_3 blends of nanoparticles, adding ethanol and using ultrasonication for a better mixing, we recorded again some SEM and TEM pictures, and we observed that the aspect of the samples is similar to that observed before, as can be seen in Figures 1 (c-d) and (g-h).

Figure 2 shows the X-ray diffraction patterns taken from the different nanoparticles obtained in this work. All the peaks in the diffraction patterns recorded for Yb^{3+},Tm^{3+}:$KGd(WO_4)_2$ and Eu^{3+}:$KGd(WO_4)_2$ nanoparticles could be indexed following a monoclinic cell with space group C2/c, in good agreement with the reference pattern JCPDS No. 89-6489, as expected[19]. From the other side, all the peaks in the diffraction patterns recorded for Yb^{3+},Tm^{3+}:Gd_2O_3 and Eu^{3+}:Gd_2O_3 nanoparticles were indexed following a cubic cell with space group Ia3, according to the reference pattern JCPDS No. 12-0797[20]. No other peaks corresponding to additional phases were observed demonstrating high purity of the prepared phases and suggesting that the Ln dopants occupy chemical substitutional sites.

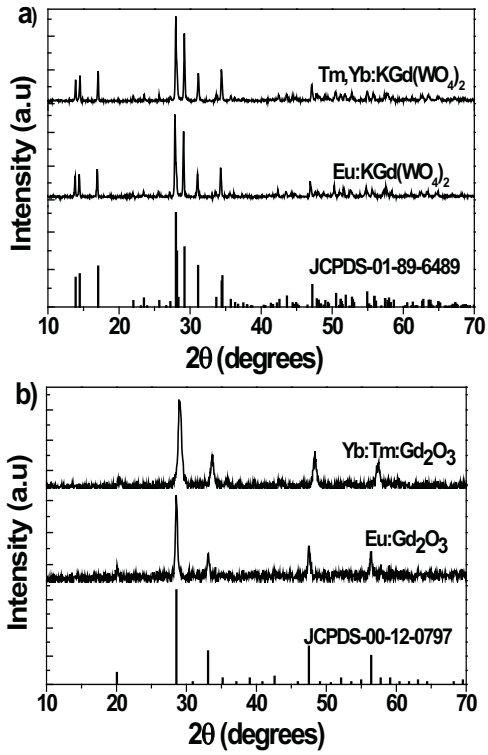

Figure 2. X-ray diffraction patterns of (a) the Yb^{3+},Tm^{3+}:$KGd(WO_4)_2$ and Eu^{3+}:$KGd(WO_4)_2$ and (b) Yb^{3+},Tm^{3+}:Gd_2O_3 and Eu^{3+}:Gd_2O_3 nanoparticles with their corresponding JCPDS standars for comparison

Figures 3 and 4 shows the emission spectra recorded for the different blends of luminescent nanoparticles prepared in this

work after pumping them at 980 nm with a Ti:sapphire laser. In the case of Yb^{3+},Tm^{3+}:$KGd(WO_4)_2$/Eu^{3+}:$KGd(WO_4)_2$ mixed nanoparticles, we explored the ratios from 1:0 to 1:8. As can be seen in Figure 3(a), the blue emission at 472 nm associated to the $^1G_4 \rightarrow {}^3H_6$ transition from Tm^{3+}, and the red emission centered at 650 nm and corresponding to the $^1G_4 \rightarrow {}^3F_4$ transition of Tm^{3+} dominate the spectra for all the mixtures analyzed. However, by taking a closer look at the spectra (see **Figure 3(b)**) we can see that the characteristic red emission from Eu^{3+} due to the $^5D_0 \rightarrow {}^7F_2$ transition starts to appear between 610-622 nm for a ratio equal to

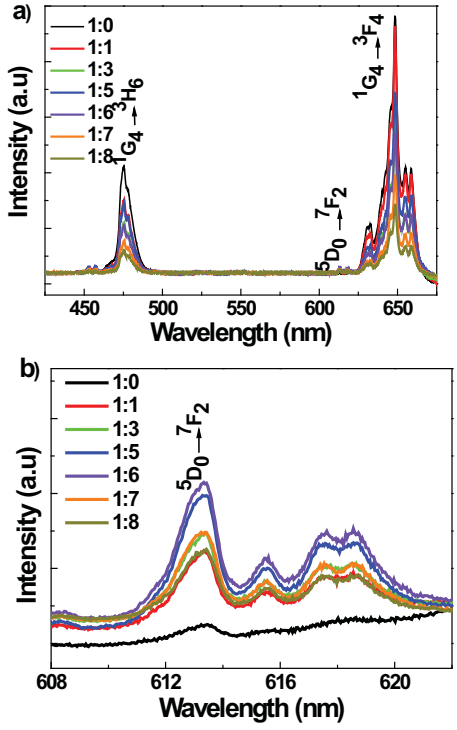

Figure 3. (a) Emission spectra of the Yb^{3+},Tm^{3+}:$KGd(WO_4)_2$/Eu^{3+}:$KGd(WO_4)_2$ mixed nanoparticles blends for different ratios ranging from 1/0 to 1/8. (b) Magnification of the range of wavelengths between 610-622 nm, showing the red emission generated by Eu^{3+} in these blends.

1:1. Then, by increasing the concentration of Eu^{3+}:$KGd(WO_4)_2$ nanoparticles, the intensity of this emission increases up to a ratio of the mixture equal to 1:6, that shows the maximum intensity. After that, if we still increase the concentration of Eu^{3+}:$KGd(WO_4)_2$ nanoparticles, the intensity quickly decreases again.

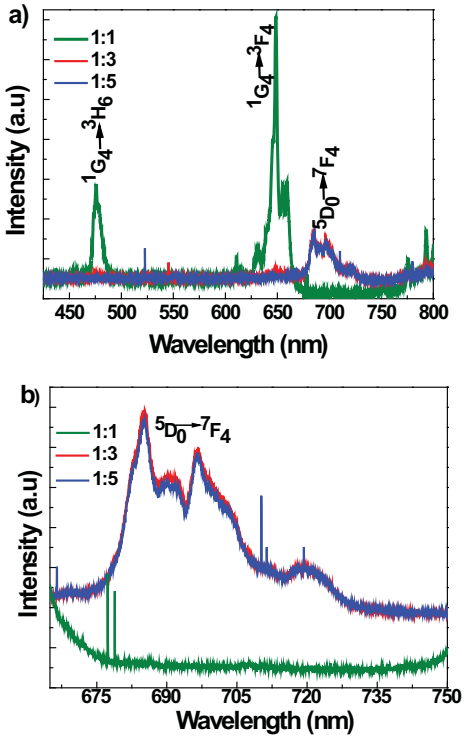

Figure 4. (a) Emission spectra of the Yb^{3+},Tm^{3+}:Gd_2O_3/Eu^{3+}:Gd_2O_3 mixed nanoparticles blends for different ratios ranging from 1/1 to 1/5. (b) Magnification of the range of wavelengths between 665-750 nm, showing the red emission generated by Eu^{3+} in these blends.

The situation is totally different for the Yb^{3+},Tm^{3+}:Gd_2O_3/Eu^{3+}:Gd_2O_3 system. As we can see in Figure 4(a), for low Yb^{3+},Tm^{3+}:Gd_2O_3/Eu^{3+}:Gd_2O_3 ratios (1/1), the emission spectra is dominated by the blue and red emissions of Tm^{3+}. However, when we increase the ratio to 1/3, a new peak located between 675 and 735 nm appears, which we considered is due to the $^5D_0 \rightarrow {}^7F_3$ and $^5D_0 \rightarrow {}^7F_4$ transitions of Eu^{3+} in these crystals[21], while the intensity of the $^1G_4 \rightarrow {}^3H_6$ (blue) and $^1G_4 \rightarrow {}^3F_4$ (red) transitions of Tm^{3+} decreases substantially. If we increase the concentration of Eu^{3+}:Gd_2O_3 nanoparticles still further, for a ratio of 1/5, the deep red emission originating from Eu^{3+} is the only emission

observed in the spectra, while the other emissions arising from Tm^{3+} are totally quenched. This can be seen in a more detailed view in **Figure 4(b)**. increase the concentration of Eu^{3+}:Gd_2O_3 nanoparticles still further, for a ratio of 1/5, the deep red emission originating from Eu^{3+} is the only emission observed in the spectra, while the other emissions arising from Tm^{3+} are totally quenched. This can be seen in a more detailed view in **Figure 4(b)**.

Thus, in this system it is possible to pump effectively Eu^{3+} by using the strategy of interparticle energy migration upconversion. This process starts by pumping Yb^{3+}, than then transfers its energy to Tm^{3+}, and after different excited state absorption processes, Tm^{3+} transfers its energy to Gd^{3+}, that finally excites Eu^{3+}. Figure 5 shows an schematic view of the energy levels and electronic transitions involved in this process when we only have Yb^{3+}, Tm^{3+} doped nanoparticles, and when we add nanoparticles doped with Eu^{3+} in the case where the matrix host contains Gd^{3+}.

This is the first time that this mechanism has been observed in oxide systems, and opens the door to new investigations using these systems to tune the color emission of the nanoparticles by upconversion processes.

The different behaviour between the two systems analyzed can be found in the dependence of the exchange migration probability (EMP) with the distance between the active ions of the material[22]. This EMP is in fact proportional to an exponential that comprises the interionic distance (R) between the ions that participate in the energy migration mechanism and the Bohr radius (r_0) in the following way:

$$EMP \propto \exp(-2R/r_0)$$

We took R as the distance between two Gd^{3+} ions in the $KGd(WO_4)_2$ and the Gd_2O_3 structures, since the gadolinium lattice is the responsible for transferring the energy from one particle to the other. For $KGd(WO_4)_2$, the Gd^{3+}-Gd^{3+} distance takes a value of 4.1 Å, while in Gd_2O_3 it is reduced to 3.6 Å. We considered r_0 as 0.3 Å, since this is a reasonable value for lanthanide ions[23]. Thus, with these considerations, we can calculate that the

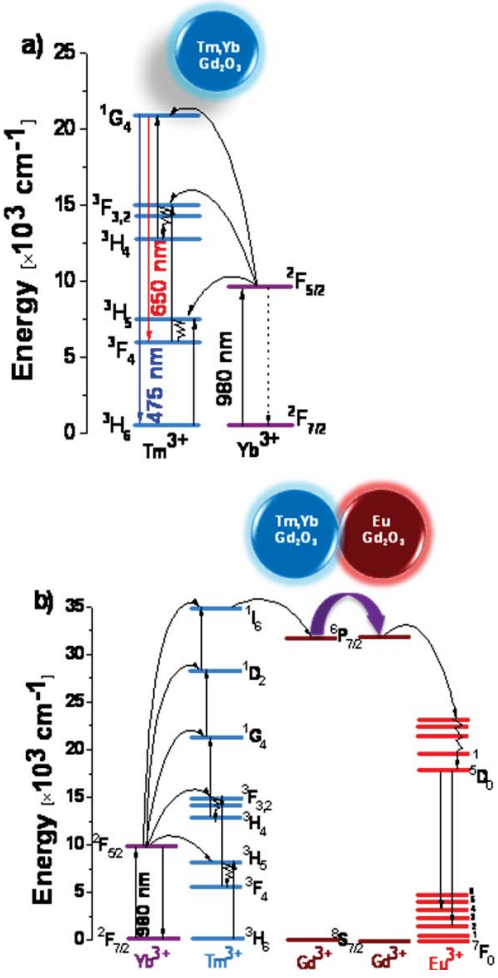

Figure 5. (a) Proposed energy transfer mechanism in Yb^{3+}, Tm^{3+} doped nanoparticles. (b) Proposed energy transfer mechanism between Yb^{3+},Tm^{3+}:Gd_2O_3 nanoparticles and Eu^{3+}:Gd_2O_3 nanoparticles

EMP is around 29 times faster in Gd_2O_3 than in $KGd(WO_4)_2$. This would explain why the Eu^{3+} emission can dominate the spectra for the Yb^{3+},Tm^{3+}:Gd_2O_3/Eu^{3+}:Gd_2O_3 system, while it is seen as a low intensity emission in the

Yb^{3+},Tm^{3+}:$KGd(WO_4)_2$/Eu^{3+}:$KGd(WO_4)_2$ system.

From another site, to give an explanation about why in the Yb^{3+},Tm^{3+}:$KGd(WO_4)_2$/Eu^{3+}:$KGd(WO_4)_2$ system, Eu^{3+} is emitting through the $^5D_0 \rightarrow {}^7F_2$ transition while in the Yb^{3+},Tm^{3+}:Gd_2O_3/Eu^{3+}:Gd_2O_3 system it emits through the $^5D_0 \rightarrow {}^7F_4$ transition, we should take into consideration the position of the Eu^{3+} states in these systems in relation with the valence and conduction bands of the host. Although the position of these electronics levels has been established previously in the literature for $KGd(WO_4)_2$[24] no data are found for Gd_2O_3, hampering us from taking a conclusion.

In conclusion, we successfully probed the EMUC concept in oxide nanoparticles. In particular, mixed nanoparticles blends of Yb^{3+},Tm^{3+}:Gd_2O_3/Eu^{3+}:Gd_2O_3 nanoparticles synthesized by the modified Pechini method show efficient deep red emission from Eu^{3+} after pumping at 980 nm, while the blue and red emissions from Tm^{3+} are effectively avoided. This opens up the possibility to expand this approach to other activator ions without resonant energy levels with Yb^{3+} in oxide nanoparticles, such as Tb^{3+}, Dy^{3+} or Sm^{3+}, allowing the generation of green, yellow and red emissions, among others from these ions after pumping Yb^{3+} at around 980 nm. This approach, provides a versatility to upconversion nanoparticles of oxide systems that might expand the already wide range of applications of this kind of systems, since we can construct novel luminescent nanoparticles with high designability and tunability. This might impulse the use of these nanoparticles in fields such as biolabelling, color displays or optoelectronics, among others.

Experimental Section

Synthesis of Ln-doped oxide nanoparticles: To prepare luminescent nanoparticles K_2CO_3, Yb_2O_3, Tm_2O_3, Eu_2O_3, Gd_2O_3 and ammonium paratungstate $(NH_4)_2WO_4$ materials were used and dissolved in concentrated HNO_3 at room temperature. The nitrate solution was totally evaporated maintaining the solution temperature at around 373 K. We used ethylenediaminetetraacetic acid (EDTA) as complex agent and ethylene glycol (EG) as polymerization agent. The nitrates salts were dissolved in an aqueous solution with a molar ratio of EDTA to metal cations [EDTA]/METAL = 1. In this way, the EDTA forms complexes with the metal cations. Further, EG was added to the mixture in a molar ratio [EDTA]/EG = 2, and then heated on a hot plate under constant stirring. When the water was removed, an esterification reaction began forming a polymeric viscous gel, where the cations are randomly dispersed in an organic network. The gel was calcinated at 573 K, generating a brown powder (precursor powder). Finally, the obtained precursor powders were calcined at 1073 K for 2 h to obtain the nanocrystalline products Yb^{3+},Tm^{3+}:$KGd(WO_4)_2$, Yb^{3+},Tm^{3+}:Gd_2O_3, Eu^{3+}:$KGd(WO_4)_2$ and Eu^{3+}:Gd_2O_3.

Preparation of the mixed nanoparticles: We prepared two different sets of samples by mixing Yb^{3+},Tm^{3+}:$KGd(WO_4)_2$ nanoparticles with Eu^{3+}:$KGd(WO_4)_2$ nanoparticles, and by mixing Yb^{3+},Tm^{3+}:Gd_2O_3 nanoparticles with Eu^{3+}:Gd_2O_3 nanoparticles in different weight ratios ranging from 1/0 to 1/8. To mix the nanoparticles we formed a suspension of the nanoparticles in ethanol and mixed them in an ultrasonic bath for 10 min.

Microscopy characterization: The morphology, and size distribution of the nanoparticles and the mixed nanoparticles blends was characterized using a scanning electron microscope Jeol JSM 6400 and a transmission electron microscope JEOL JEM-1011 with a Mega View III Soft Imaging System.

X-ray powder diffraction: X-ray powder diffraction patterns were recorded using a Bruker-AXS D8-Discover diffractometer with a parallel incident beam (Göbel

mirror) and vertical goniometer. Cu Kα radiation (λ = 0.154247 nm) was obtained from an X-ray tube operated at 40 kV and 40 mA. Measurements were taken in the 2θ angle range between 10º and 70º with a step size of 0.02º and an integration time of 16 s.

Luminescence spectra: Emission spectra were recorded in a confocal microscope after excitation at 980 nm with a Ti:sapphire laser.

Acknowledgements:

This work was supported by the European Union under project CLEANSPACE FP7-SPA-2010-263044, by the Spanish government under projects PI09/90527, TEC2010-21574-CO2-02, and MAT2011-29255-C02-02, and by the Catalan Authority under project 2009SGR235.

---

[1] R. Kumar, M. Nyk, T.Y. ochulachanskyy, C.A. Flask, P. N. Prasad, *Adv. Funct. Mater*. **2009**, *19*, 853.

[2] B. Dong, B. Cao, Y. He, Z. Liu, Z. Li, Z. Feng, *Adv. Mater*. **2012**, *24*, 1987.

[3] B. M. Van der Ende, L. Aartsa, A. meijerink, *Phys. Chem. Chemi. Phys*. **2009**, *11*, 11081.

[4] W. S. Song, K. H. Lee, Y. R. Do, H. Yang, *Adv. Funct. Mater*. **2012**, *22,* 1885.

[5] H. Guo, X. F. Wang, J. D. Chen, F. Li, *Opt. Express*. **2010**, *18*, 18900.

[6]. S, Wilhelm, T. Hirsch, E. Scheucher, T. Mayr, O. S. Wolfbeis, *Angewandte Chemie-Int. Ed*. **2011** *50*, A59-A62.

[7] A. Bednarkiewicz, D. Wavrzynczyk, A. Gagor, L. Kepinski, M. Kurnatowska, L. Krajczyk, M. Nyk, M. Samoc, W. Strek, *Nanotechnology*, **2012**, *23*, 145705.

[8] N. Bloembergen, *Phys. Rev. Lett*. **1959**, *2*, 89.

[9] F. Auzel, *C.R. Acad. Sci. (Paris*), **1966**, *262*, 1016.

[10] F. Auzel, *Chem. Rev*. **2004**, *104* 139-173.

[11] J. F. Suyver, A. Aebischer, D. Biner, P. Gerner, J. Grimm, S. Heer, K. W. Krämer, C. Reinhard, H. U. Güdel, *Opt. Mater*. **2005**, *27*, 1111-1130.

[12] F. Wang, R. Deng, J. Wang, Q. Wang, Y. Han, H. Zhu, H. Zhu, X. Chen, X. Liu, *Nat. Mat*. **2012**, *10*, 968.

[13] R. T. Wegh, H. Donker, K. D. Oskam, A. Meijerink, *Science,* **1999***, 283*, 663.

[14] H. Guo, N. Dong, M. Yin, W.P. Zhang, L. R. Lou, S. D. Xia, *J. Phys. Chem. B*., **2004**, *108,* 19205.

[15] X. M. Han, G. F. Wang, T. Tsuboi, *J. Cryst. Gro*wth, **2002**, *242*, 412-420.

[16] S. Gai, P. Yang, D. Wang, C. Li, N. Niu, F. He, X. Li, *Cryst. Eng. Comm*, **2011**, *13*, 5480.

[17] G. Blasse, *Mater. Chem. Ph*ys. **1987,** *16*, 201.

[18] M. Galceran, M. C. Pujol, M. Aguiló, F. Díaz, *J. Sol-gel Sci. Technol.* **2007**, *43*, 79.

[19]. M. C. Pujol, M. Rico, C. Zaldo, R. Solé, V. Nikolov, X. Solans, M. Aguiló, F. Díaz, *Appl. Phys. B: Lasers Opt.* **1999***, 68,* 187.

[20] Natl. Bur. Stand. (U.S.) Monogr. 25 **1962**, *25,* 16.

[21] V. Pelova, K. Kynev, T. Petrova, Tz. Piperov, *Cryst. Res. Technol*. **1998**, *33*, 125.

[22] G. Blasé, K. A. Gschneider Jr, L. Eyring *Handbook on the physics and chemistry of rare earths, Chapter 34*, , North-Holland Publishing Company, **1979**.

[23] B. Di Bartolo, *Energy transfer processes in condensed matter, Plenum*, **1983,** 130.

[24] P. Boutinaud, M. Bettinelli, F. Díaz, *Opt. Mater*. **2010**, *32*, 1659.

UNIVERSITAT ROVIRA I VIRGILI
MICROSTRUCTURATION OF NONLINEAR OPTICAL MATERIALS:
METHODOLOGIES, CHARACTERIZATION, AND APPLICATIONS
Raj Kumar Golconda
Dipòsit Legal: T. 55-2013

Paper IX

Multi-color emission from luminescent nanoparticles embedded into micro-structures of $KTiOPO_4$ for RGBY laser phosphor display devices

R.K. Golconda, J.J. Carvajal, M.C. Pujol, X. Mateos, J. Massons, A. Ruiz de la cruz, J.S. Céspedes, M. Aguiló, F. Díaz

Advanced Functional Materials (to be submitted)

UNIVERSITAT ROVIRA I VIRGILI
MICROSTRUCTURATION OF NONLINEAR OPTICAL MATERIALS:
METHODOLOGIES, CHARACTERIZATION, AND APPLICATIONS
Raj Kumar Golconda
Dipòsit Legal: T. 55-2013

UNIVERSITAT ROVIRA I VIRGILI
MICROSTRUCTURATION OF NONLINEAR OPTICAL MATERIALS:
METHODOLOGIES, CHARACTERIZATION, AND APPLICATIONS
Raj Kumar Golconda
Dipòsit Legal: T. 55-2013

Multi-color emission from luminescent nanoparticles embedded into micro-structures of $KTiOPO_4$ for RGBY laser phosphor display devices

R.K. Golconda, J.J. Carvajal[*], *M.C. Pujol, X. Mateos, J. Massons, A. Ruiz de la cruz, J.S. Céspedes, M. Aguiló, and F. Díaz*

Abstract: Luminescent nanoparticles are key components for the development of multifunctional devices and the success of many lighting and display systems. We demonstrate here that an approach for developing transparent emissive high resolution RGBY laser phosphor displays by embedding upconverting luminescent nanoparticles into the micro-meter size conical pores inscribed on the surface of optical materials. The multi-color emissions from luminescent nanophosphors can be achieved by exciting single NIR wavelength at 980 nm rather than using expensive UV pump sources.

Key words: Ultrafast laser ablation, $KTiOPO_4$, up-conversion, luminescent phosphors

1. Introduction

Display technology plays a crucial role in how information is conveyed. A picture is a worth of thousand words, so display technology simplifies information sharing. The cathode ray tube (CRT), that used scanning electron beams in a vacuum tube to excite color phosphors on the screen to emit colored light was the first device which revolutionized the display industry. However, the use of CRTs placed severe technical limitations, such as the difficulty to set possible geometric configurations of electron gun axis and aperture positions in the CRT displays.

R.K. Golconda, J.J. Carvajal[*], M.C. Pujol, X. Mateos, J. Massons, M. Aguiló, F. Díaz
Física i cristal·lografia de materials i Nanomaterials, Universitat Rovira i Virgili, Campus Sescelades, Marcel·li Domingo, s/n, 43007 Tarragona, Spain.
(*) Email: joanjosep.carvajal@urv.cat

A. Ruiz de la cruz, J.S. Céspedes
Laser Processing group, Instituto de Optica (CSIC), Serrano 121, 28006 Madrid, Spain

Tel: +34-977558790, Fax: +34-977558563

A vast research on display technology has developed displays that surpass CRTs parameters such as picture quality, size, and power consumption. Liquid crystal displays (LCD) devices replaced CRTs due to their light weight, low operating power, and compact design. Thus, this technology allowed designing numerous devices such as cell phones, laptops and many small screened electronics. Display technology has extended to design other display devices, such as plasma displays, light emitting diodes (LEDs) displays, and field emission displays (FEDs). The modern displays have direct configuration where the screen itself contains light emitting color pixels to directly form color images on the screen.

Transparent emissive displays are among the key issues in the fields of next-generation information displays. Currently, the emissive layers with a typical thickness of 20-40 μm are formed using micrometer-sized phosphor particles[1], leading to

substantial light scattering in the layers and a total opacity. Introduction of thin-film phosphors deposited by different technologies, such as vacuum, sol-gel or solution processes, may significantly improve the visible transparency of emissive layers. However, such thin-film phosphors posses processing difficulties, such as high-temperature post-annealing to activate the luminescent centers, which limits the choice of substrates that are compatible with the high-temperature annealing[2,3] An alternative to develop partially transparent displays might be the structuration of the layer of phosphors at the micrometer scale forming thin stripes or more complex structures, such as two-dimensional (2D) ordered arrays. This strategy provides two advantages. From one side, we can fabricate partially transparent emissive displays, since it exists a free transparent space in between the structured phosphor layer. From the other side, we can fabricate high resolution displays, since the pixel size can be as small as the structures designed on the phosphor layer.

From another side, a lot of effort has been deposited on developing flexible transparent emissive layers consisting of either multilayered nanophosphors or nanophosphor-embbedded polymer composites [4-6]. However, such displays suffer from two basic problems. First, the brightness that can be achieved with such displays is limited, since the pump power that can be used to pump the phosphors is limited by the stability of the polymer used as substrate. From the other side, most of the phosphors used in such displays are typically pumped in the UV, which also reduces the operative lifetime of the phosphors and the polymers since UV light can degrade them both.

A significative research line has been the development of laser phosphor displays (LPD) consisting on a phosphor panel (display screen) that comprises a substrate on which parallel phosphor stripes are made of different phosphors that emit in red, green and blue (RGB) colors by absorbing light at a particular excitation wavelength in the UV, emitted by a laser engine. By varying the amount of light emitted from the three primary colors, that can be controlled by the power of the pumping laser, can provide a full color image. Finally, the system contains a laser module that is used to project and scan the laser beam onto the screen, producing color images generated by the phosphor stripes deposited on the substrate[7]. However, the commercially available systems of this kind are pumped with UV lasers, so these LPD suffer not only from limited lifetime due to the degradation of the phosphors used, but also from a high cost due to the expensive prizes of UV lasers with a certain power.

We propose an alternative to develop new partially transparent emissive displays for LPDs, by using high refractive index optically active lanthanide ion-doped nanoparticles, emitting in the red, green and blue regions of the electromagnetic spectrum by upconversion processes after excitation in the near IR (NIR). We propose to embed these nanophosphors in two-dimensional (2D) ordered microstructures inscribed on a lower refractive index non-linear optical substrate with a high laser damage threshold. This would provide the possibility of using high pumping power and at the same time the possibility to confine the emitted light to the cavity formed by the inscribed microstructures, providing brighter emissions from the phosphors. Apart from this, the use of microstructured non-linear optical substrates might provide multifunctional devices capable to generate additional electromagnetic

radiations through nonlinear optical processes.

So far, many techniques have been proposed to microstructurate non-linear optical materials such as the electric field poling technique[8], lithography based processes[9], or liquid phase epitaxy[10], among others. Nowadays, ultrafast laser ablation has attracted a lot of attention to fabricate 1D and 2D microstructures on the surface of hard dielectric materials, including non-linear optical materials, since this process offers low cost, fast procedure and one step processing producing high accurate microstructures[11,12].

We chose potassium titanyl phosphate ($KTiOPO_4$ or KTP) as the non-linear optical material to constitute the substrate of our LPDs. It belongs to the orthorhombic system with the space group of symmetry $Pna2_1$[13]. These crystals show large nonlinear optical coefficients, large electro-optic coefficients, good phase-matchability, and high optical homogeneity with appropriate transparent wavelength range from 0.3 to 4.5 μm[14], but most interestingly, they show a high laser damage threshold of around 1.5-2.2 GW cm^{-2} in the NIR[15] that allows us to increase substantially the pumping power used in conventional laser phosphor displays to obtain a high brightness.

As upconverting phosphors we propose to use nanoparticles of the monoclinic phase of potassium rare earth double tungstates, $KRE(WO_4)_2$ (RE = Yb^{3+},Gd^{3+}, rare earth), which is widely known as an important host material for lanthanide active ions (Er^{3+}, Tm^{3+}, Ho^{3+}) for solid state laser applications due to the high absorption and emission cross sections of these ions in these materials[16]. These materials crystallize[17] with the space group of symmetry $C2/c$. We prepared Er^{3+}:$KYb(WO_4)_2$, Tm^{3+}:$KYb(WO_4)_2$ and Ho^{3+},Yb^{3+}:$KGd(WO_4)_2$ nanocrystals for the generation of green, blue and yellow light, respectively, through up-conversion processes. Ytterbium ions present a broad band absorption in the 900-1000 nm spectral range, which is suitable for pumping through commercially available InGaAs laser diodes. This ion shows a higher absorption cross section than Er^{3+}, Tm^{3+} or Ho^{3+}. Thus, it can be used as a sensitizer for these ions. Energy transfer occur efficiently from Yb^{3+} to any of the other optically active lanthanide ions with which we doped our nanoparticles. Red light through up-conversion processes can be obtained in Er^{3+}-Yb^{3+} co-doped systems, by increasing the Er^{3+} concentration and favoring in this way the red emission from Er^{3+} instead the green one[18]. However, in monoclinic double tungstates the green emission from Er^{3+} is the most efficient, and it is difficult to obtain red light through up-conversion processes in this family of materials. This is why we have replaced monoclinic double tungstates by Gd_2O_3 nanocrystals co-doped with Er^{3+} and Yb^{3+}.

Thus, by filling the 2D squared arrays of ordered pores we inscribed on the surface of KTP single crystals with these nanoparticles we can generate RGBY up-conversion LPDs. Groups of pores have been filled with a different kind of luminescent nanoparticles, so we control also spatially where every different color of light is generated.

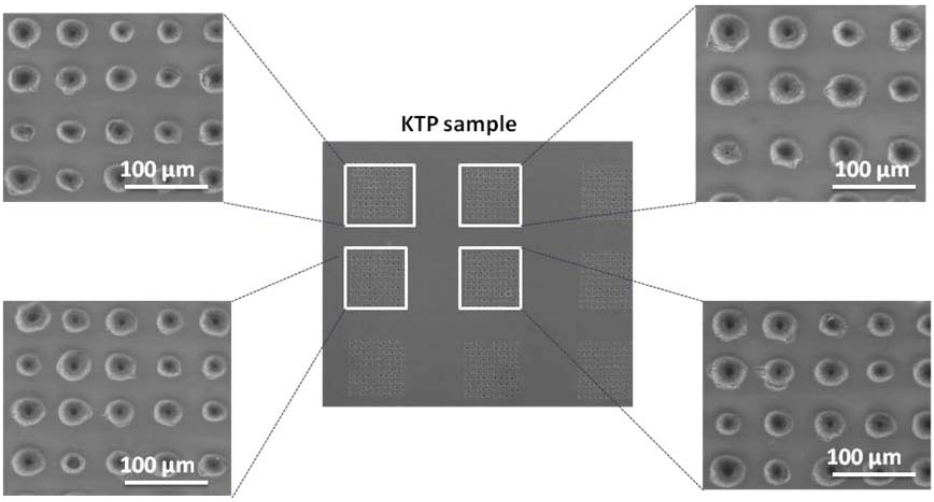

Figure 1: The SEM micrograph of conical pores inscribed on the surface KTP sample. The higher maginification images corresponding to the each set of inscribed conical pores.

2. Results and Discussion

2.1 Fabrication of the structures substrates

KTP bulk single crystals have been grown by the Top-Seeded Solution Growth-Slow Cooling (TSSG-SC) technique. Because these crystals melt incongruently[19], they cannot be grown by conventional melting methods. After growth, KTP crystals have been sliced in pieces perpendicular to the ***c*** crystallographic direction with a typical thickness of 1.5 – 2 mm. The typical area of the samples was 10 × 10 mm^2 along the ***a*** and ***b*** crystallographic directions. Those crystal slides were polished to a high optical quality using Alumina powders. After polishing, we used the ultrafast laser ablation technique to fabricate conical pores on the (001) surface of the KTP samples.

We used a pulsed Ti:sapphire fs laser amplification system (Tsunami and Spitfire from Spectra-Physics) for ultrafast laser ablation. The system delivers fs laser pulses at 799 nm with 120 fs pulse duration at a repetition rate of 1kHz. The beam wavefront was controlled by a spatial light modulator (Hamamatsu X8267) before focusing on the surface of the sample. This allowed us designing the intensity profile of the focused beam. The sample was placed on a motorized 3-axis XYZ motorized translation stage that allows us to achieve optimal focusing on the surface of the sample. A 2D square ordered array of conical pores was fabricated on the surface of KTP sample, focusing the laser beam by means of a 7.5 cm focusing lens using the pulse energy of 300 uJ. In this work, 9 different sets of 100 conical pores each were fabricatedby varying the laser pulse irradiation time from 1 to 10 sec. In all the sets of the 2D square ordered array of conical pores, the same pulse energy was used. Also, in each set, the 100 holes were fabricated with one laser shot.

Figure 1 shows the scanning electron microscope (SEM) image of the 2D square ordered array of conical pores on the surface of the KTP sample by ultrafast laser ablation. High magnification images are shown for the sets chosen to be filled with the

luminescent nanoparticles. SEM micrographs reveal that the fabricated micro-structures have a high degree of periodicity. The diameter of the conical pores was different not only at every different set of holes due to the change of laser irradiation while processing the sample, but also inside a set, due to the accuracy limit of the spatial light modulator. These images show that the diameter of the conical pores is around 28 μm, and the periodicity of the 2D array is around 50 μm. However, when we analyze the roughness at the edges of the conical pores, it is very small.

2.2 Crystal structure and size of nanophosphors.

The modified sol-gel Pechini method is used to synthesize Er^{3+}:$KYb(WO_4)_2$, Tm^{3+}:$KYb(WO_4)_2$, Ho^{3+},Yb^{3+}:$KGd(WO_4)_2$ and Er^{3+},Yb^{3+}:Gd_2O_3 nanocrystals. Stoichiometric amounts of the component were first converted to their nitrate forms by dissolution in concentrated HNO_3. Later the excess of HNO_3 was evaporated to obtain nitrate precipitates by slow heating. In the next step, an aqueous solution of ethylenediaminetetraacetic acid (EDTA), used as a chelating agent, was added to the nitrate precipitates in a molar ratio C_M= [EDTA]/[METAL] = 1 to prepare metal-EDTA complexes. Afterwards, ethylene glycol (EG), used as the sterification agent, was added in amolar ratio C_E = [EDTA]/[EG] =2. The resulting solution was heated slowly to obtain the precursor resin, which is a rigid polyester net that reduces any metal segregation. Finally, the precursor powders were calcined at 1073 K for 2 h to obtain the luminescent nanoparticles. The structural characterization of the as prepared luminescent nanoparticles was carried out by X-ray powder diffraction. Figure 2 shows the X-ray powder diffraction patterns of synthesized nanoparticles. Figure 2(a) shows the powder diffraction patterns of $KRE(WO_4)_2$ nanoparticles. For comparison we added the X ray powder diffraction pattern of KYbW. All these nanoparticles show the same diffraction peaks, corresponding to the C2/c phase.

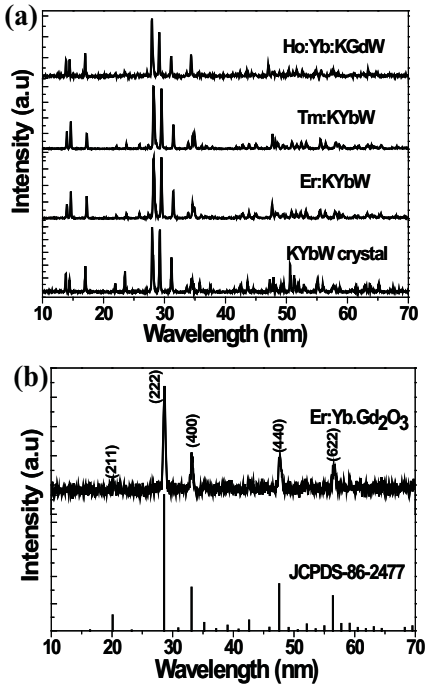

Figure 2: Figure 1: XRD spectra of as prepared luminescent nanoparticles (a) Double tungstate nanoparticles (b) Er:Gd_2O_3 nanoparticles

Figure 2(b) shows the X-ray diffraction spectra of Gd_2O_3 doped with Er lanthanide ion. The typical diffraction peaks of cubic Gd_2O_3 with space group

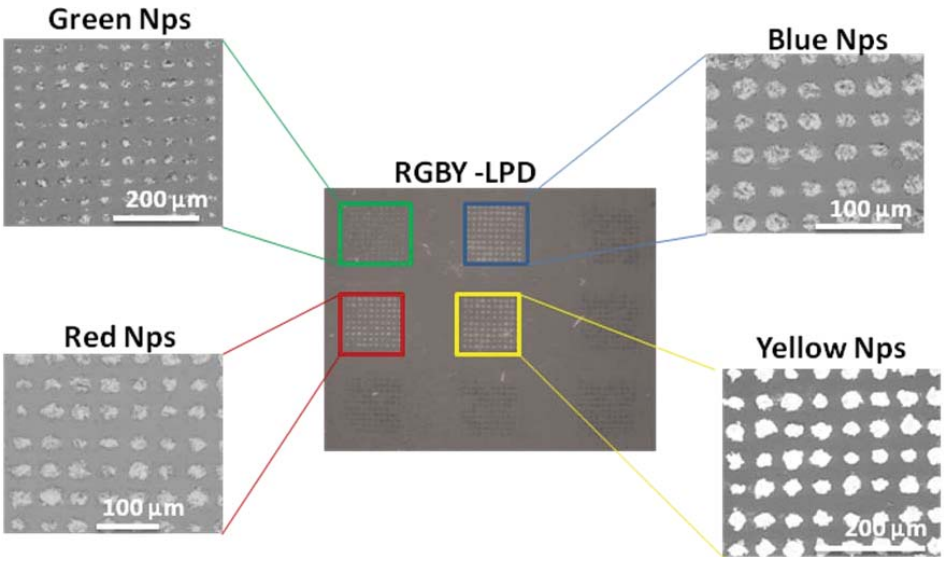

Figure 3. SEM images of different set of conical pores after filling and annealing the sample.

Ia3 are shown and the most dominant peak was observed at (222). In this figure we added the X-ray diffraction pattern corresponding to the Gd_2O_3 phase, according to the JCPDS file 86-2477 [20].

The size of the particles was estimated from transmission electron microscopy (TEM) images. It was found to be around 40 nm.

2.3 Fabrication and spectroscopic characterization of the LPDs.

The 4 different types of luminescent nanoparticles were introduced in 4 different sets of 2D square ordered array of conical pores by mechanical means separately. After filling each of those sets of pores with the corresponding luminescent nanoparticles, the sample was annealed at 1173 K for 3 h. The SEM micrographs of the KTP sample with the nanoparticles inside the pores after annealing are shown in Figure 3. Each set of hole is labeled according to the color of the emission generated by the luminescent nanoparticles with which it was filled.

The photoluminescence measurements of the LPDs were performed by optical excitation at the maximum of the optical absorption band of Yb^{3+} ions at 980 nm (with an associated energy of 10204 cm^{-1}) using a Ti:Sapphire laser. The emitted photons were collected and dispersed by a monochromator placed at 90º with respect to the incident laser beam.

In Er^{3+}-Yb^{3+} systems, the green emission obtained after infrared pump can be attributed to an up-conversion energy transfer process of Er^{3+} sensitized by Yb^{3+} involving two or three photons. These absorption-emission mechanisms associated with the up-conversion energy transfer process depend strongly not only on the pumping wavelength and pumping power, but also on the nature of the crystalline matrix. The green emission can also be linked to a cooperative sensitization, in which the simultaneous interaction of two excited Yb^{3+} ion produces the excitation of Er^{3+}. The electrons of Yb^{3+} are excited to $^2F_{5/2}$ level after absorbing a photon at 980 nm. After that, they transfer part of

UNIVERSITAT ROVIRA I VIRGILI
MICROSTRUCTURATION OF NONLINEAR OPTICAL MATERIALS:
METHODOLOGIES, CHARACTERIZATION, AND APPLICATIONS
Raj Kumar Golconda
Dipòsit Legal: T. 55-2013

energy to the electrons of Er^{3+}, that promate to the $^4I_{11/2}$ energy level. Then, a second photon at 980 nm is absorbed by Yb^{3+} promoting again its electrons from the fundamental $^2F_{7/2}$ level to the excited $^2F_{5/2}$ level. Then, a second photon at 980 nm is absorbed by Yb^{3+} promoting again its electrons from the fundamental $^2F_{7/2}$ level to the excited $^2F_{5/2}$ level. Then, energy can be transferred again to Er^{3+} that consistently increases the energy of its electrons from the $^4I_{11/2}$ level to the $^4F_{7/2}$ level. A very fast nonradiative relaxation took place to the $^4S_{3/2}$ and $^2H_{11/2}$ levels, where the transitions $^2H_{11/2} \rightarrow {}^4I_{15/2}$ and $^4S_{3/2} \rightarrow {}^4I_{15/2}$ take place at around 520 and 550 nm. From the $^4S_{3/2}$ level a nonradiative relaxation can also take place to the $^4F_{9/2}$ level, and generates an emission in the red region of the electromagnetic spectrum at around 669 nm ($^4F_{9/2} \rightarrow {}^4I_{15/2}$). The corresponding green emission spectrum recorded for the Er^{3+}:$KYb(WO_4)_2$ nanoparticles is shown in **Figure 4 (a)**. The red emission spectrum recorded for the Er^{3+},Yb^{3+}:Gd_2O_3 nanoparticles is shown in **Figure 4(d)**.

Similarly, in the case of Tm^{3+} doped systems, the Yb^{3+} ion absorbs radiation at 980 nm, and it transfers its energy to the Tm^{3+} ion. In that case, the energy transfer promotes the electrons of Tm^{3+} to the $^3H_5$ level and then relaxe down through a nonradiative process to the $^3F_4$ energy level. This level has a relatively long lifetime, and it allows another nearby Yb^{3+} ion to absorb another photon and transfer its energy to the Tm^{3+} so that its electrons can promote to the higher excited state $^3F_2$. After another internal relaxation to the $^3H_6$ level, Tm^{3+} ion receives another energy transfer process to reach the higher level $^1G_4$, from which emission at 475 nm can be obtained

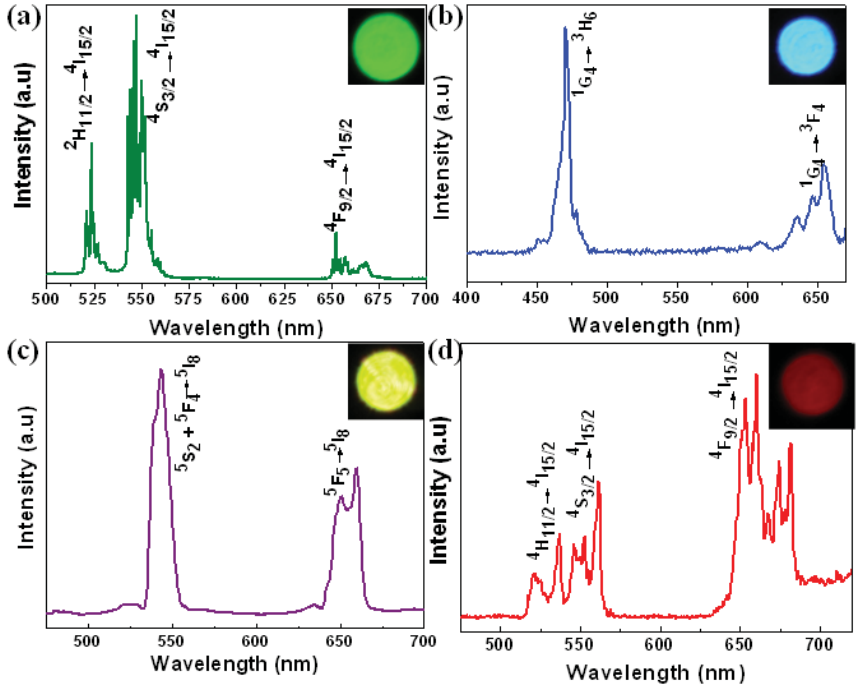

Figure 4. The recorded emission spectra of luminescent nanocomposites (a) Er:KYbW (green) (b) Tm:KYbW (blue) (c) Ho:Yb:KGdW (yellow) (d) Er:Yb:Gd_2O_3 (red)

from the $^1G_4 \rightarrow {}^3H_6$ transition. From another side, the transition $^1G_4 \rightarrow {}^3F_4$ generates also red light at around 660 nm. The corresponding emission spectra of the Tm^{3+}:$KYb(WO_4)_2$ nanoparticles is shown in **Figure 4(b)**.

The photoluminescence from the Ho^{3+},Yb^{3+}:KGdW nanoparticles after Yb^{3+} excitation generated yellow light. In this case, the absorbed energy of Yb^{3+} ions is transferred to the $^5I_6$ level of Ho^{3+}, which experiences excited state absorption with the energy of pump photons to the $^5S_2$ + $^5F_4$ levels. At this stage, a small part of the electrons excited in the $^5S_2$ level are relaxed to the $^5F_5$ level from where photons at 580 nm are generated. The red photons are generated by the transition from the $^5F_3$ level to the upper stark level of the $^5I_7$ level with an associated wavelength of 680 nm. The emission spectrum of Ho^{3+},Yb^{3+}:$KGd(WO_4)_2$ nanoparticles is shown in **Figure 4 (c)**.

The energy levels of these ions, together with the different absorption, emission and energy transfer processes involved in the upconversion processes are presented in **Figure 5**.

We also performed photoluminescence measurements on the surface of the KTP sample where the luminescent nanoparticles are embedded. In these measurements, we used again optical excitation at the maximum of the optical absorption of Yb^{3+} ions at 980 nm using a Ti:Sapphire laser. The sample was placed on the 2D stage, perpendicular to the direction of the incident NIR laser radiation. The sample was moved slowly to the position where the different nanoparticles are located. Images of the emission at each set of embedded luminescent nanoparticles were recorded with the help of a CCD camera both with the lights of the laboratory on and off. These images are also shown in **Figure 5**, showing the multicolor emissions that can be obtained with these LPDs.

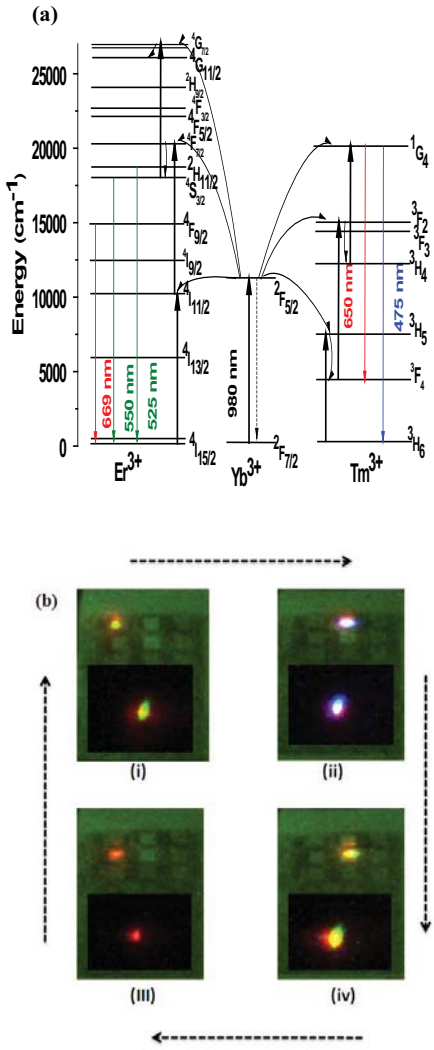

Figure 5. (a) Energy diagram of Er:Tm:Yb system (b) The recorded CCD images of the multicolor light emission different luminescent composites (i) Green (ii) Blue (iii) Yellow (iv) Red, inset figure shows the corresponding CCD image of light emissions recorded from luminescent nanocomposites.

Excitation of upconversion luminescent nanocomposites using NIR wavelength posseses several advantages in the applications for luminescent displays, including an excellent signal-to-noise

ratio, improved detection sensitivity and excitation with a low power NIR laser that is compact and inexpensive. The conventional techniques used for these applications have several limitations. For instance, the excitation of luminescent nanoparticles by UV radiation results in some limitations such as small penetration depth inherent to the short wavelength excitation light and possible damage of both, substrates and phosphors.

In conclusion we successfully fabricated RGBY multicolor laser phosphor displays through upcoversion processes after excitation in the NIR based on microstructured KTP substrates with luminescent nanoparticles embedded in the 2D square ordered arrays of pores inscribed by ultrafast laser ablation on the surface of the substrates.

Acknowledgement

This work was supported by the European Union under the Seventh Framework Programme under project Cleanspace, FP7-SPACE-2010-1, the Spanish government under projects, PI09/90527, TEC2010-21574-CO2-02, MAT2011-29255-C02-02 and by the Catalan government under project 2009SGR235.

References:

[1]. H. Zhu, E. Zhu, H. Yang, L. Wang, D. Jin, K. Yao, J. Am. Ceram. Soc. **2008,** *91,* 1682.

[2]. X. Hu, S. Yan, L. Ma, G. Wan, J. Hu, *Powder Technol*. **2009**, *192* 27.

[3]. P. Yang, Z. Quan, C. Li, Z. Hou, W. Wang, J. Lin, *J. Solid State Chem*. **2009**, *182*, 1045.

[4]. A.S.S. de Camargo, L.A.O. Nunes, D.R. Ardila, J.P. Andreeta, *Opt. Lett*. **2004**, *29* 59.

[5]. H. Zhu, H. Yang, D. Jin, Z. Wang, X. Gu, X. Yao, K. Yao, *J. Nanopart. Res.* **2008**, *10* 1149.

[6]. C.C. Wu, K.B. Chen, C.S. Lee, T.M. Chen, B.M. Cheng, *Chem. Mater.* **2007**, *19*, 3278.

[7]. R.A. Hajjar, David Kent, Phillip Malyak, laser displays using phosphor screens emitting visible colored light, patent-20090174632, 2009.

[8]. C. Canalias, M. Norlof, V. Pasiskevicius, and F. Laurell, *Appl. Phys. Lett*. **2009**, *94,* 081121.

[9]. D. Coquilat, G. Vecchi, C. Comaschi, A.M. Malvezzi, J. Torres, and Le Vassor dýerville, *Appl. Phys. Lett*. **2005**, *87*, 101106.

[10]. A. Peña, S. Di Finizio, T. Trifonov, J.J. Carvajal, M. Aguiló, J. Pallarés, A. Rodriguez, Alcubilla, *Adv. Mater*. **2006**, *18*, 2220.

[11]. I.H. Chaowdhury, A.Q. Wu, X. Xu, A.M. Weiner, *Appl. Phys. A* **2005**, *81*, 1627.

[12]. G.A. Torchia, C. Mendez, I. Arias, L. Roso, A. Ródenas, D. Jaque, *Appl. Phys. B* **2006**, *83*, 559.

[13]. J.J. Carvajal, C.F. Woensdregt, R. sole, F.Díaz, M. Aguiló, *Cryst. Growth. Des*. **2006**, *6*, 2667.

[14]. B. Boulanger, J.P. Feve, G. Marnier, B. Menaert, X. Cabirol, P. Villeval, C. Bonnin, *J. Opt. Soc. Am. B*, **1994**, *11*, 750.

[15]. P. Yankov, D. Schumov, A. Nenov, A. Monev, *Opt. Lett*. **1993***, 18***,** 1771.

[16]. A.A. Kamaskii, Crystalline lasers: Physical processes and operating schemes, CRC, Press, New York, **1996**.

[17]. C. Pujol, M. Aguilo, F. Diaz and C. Zaldo, *Opt. Mater.* **1999**, *13*, 33.

[18]. D. Solis, E. De la Rosa, O. Meza, L.A. Diaz-Torres, P. Salas, C. Angeles-Chavez, *J. Appl. Phys*. **2010**, *108*, 023103.

[19]. J.J. Carvajal, R. Solé, J. Gavalda, J. Massons, M. Aguiló, and F. Díaz, *Opt. Mater*. **2003**, *24*, 425.

[20]. Z. Xu, J. Yang, Z. Hou, C. Li, C.Zhang, S. Huang, J. Lin, *Mater. Res. Bullet.* **2009**, *44*, 1850.

UNIVERSITAT ROVIRA I VIRGILI
MICROSTRUCTURATION OF NONLINEAR OPTICAL MATERIALS:
METHODOLOGIES, CHARACTERIZATION, AND APPLICATIONS
Raj Kumar Golconda
Dipòsit Legal: T. 55-2013